

**THUNDERSTORMS & ELEMENTARY  
PARTICLE ACCELERATION**  
10 YEARS OF TGE OBSERVATION ON ARAGATS



*Edited by A. Chilingarian  
Cosmic Ray Division  
A. Alikhanyan National Laboratory  
Yerevan Physics Institute*

*SEPTEMBER 17-20  
**2018**  
NOR AMBERD  
ARMENIA*





*Proceedings of International Symposium*

**TEPA 2018**  
**Thunderstorms and Elementary**  
**Particle Acceleration**

*10 Years of TGE Observation on Aragats*



**Nor-Amberd, Armenia**  
**September 17 - 20**

**Edited by A. Chilingarian**

Cosmic Ray Division  
A. Alikhanyan National Laboratory  
(Yerevan Physics Institute)



Published by CRD  
Cosmic ray division, A. Alikhanyan National Laboratory  
Alikhanyan Brothers Street 2, Yerevan, Armenia

©All rights reserved by **CRD**  
<http://aragats.am>

Printed by **TIGRAN METS**  
2, Arshakouniats Avenue, Yerevan, Armenia  
Tel. (37410) 521 775

**ISBN ?? INSPIRE ? March 2019**

Copies 150  
Pages 164

## INTERNATIONAL SCIENTIFIC ADVISORY COMMITTEE

- **Ashot Chilingarian**, Yerevan Physics Institute, Armenia, chair
- **Michail Panasyuk**, Moscow State University, Russian Federation, co-chair
- **Lev Dorman**, Israel Cosmic Ray Center and Emilio Segré Observatory, Israel
- **Joseph Dwyer**, Space Science Center (EOS) and Department of Physics University of New Hampshire, USA
- **Gerald Fishman**, NASA-Marshall Space Flight Center, Huntsville, AL, USA
- **Hartmut Gemmeke**, Karlsruhe Institute of Technology, Germany
- **Johannes Knapp**, DESY Zeuthen, Germany
- **Alexandr Lidvanski**, Nuclear Physics Institute, Russian Academy of Science, Russian Federation
- **Jean Lilensten**, Institut de Planétologie et d'Astrophysique de Grenoble, France
- **Bagrat Mailyan**, Florida Institute of Technology, Melbourne, FL, USA.
- **Evgeny Mareev**, Institute of Applied Physics, Nizhny Novgorod, Russian Federation
- **Razmik Mirzoyan**, MPI, Munich, Germany
- **Yasushi Muraki**, STE laboratory, Nagoya University, Japan
- **Michail Panasyuk**, Moscow State University, Russian Federation, co-chair
- **Vladimir Rakov**, University of Florida, USA
- **David Smith**, University of California, Santa Cruz
- **Marco Tavani**, INAF and University of Rome "Tor Vergata", Italy
- **Tatsuo Torii**, Japan Atomic Energy Agency, Tsuruga, Japan
- **Harufumi Tsuchiya**, Cosmic Radiation Laboratory, Riken, Japan.
- **Lev Zeleny**, Space Research Institute, Russian Academy of Sciences, Russian Federation

**From the editor:**  
**Thunderstorms and Elementary Particle Acceleration (TEPA-2018)**

*10 Years of TGE Observation on Aragats*

The high-energy atmospheric physics (HEAP) is a rather new scientific discipline aimed to classify and explain thunderstorm correlated fluxes of electrons and gamma rays in the Near-Earth space (terrestrial gamma flashes, TGFs) in the troposphere (gamma glows) and on the earth's surface (thunderstorm ground enhancements, TGEs). All three types of experiments (in space, in troposphere, and on earth's surface) are accompanied with observations of lightning flashes and atmosphere electrification: TGEs and gamma glow - by detecting electric fields on the earth's surface and high in the atmosphere; TGFs - by making synchronization with worldwide lightning location networks and by optical observations of lightning flashes by orbiting high-frequency cameras. The central engine initiating the TGE is believed to be the Relativistic Runaway Electron avalanches (RREA) which accelerate and multiply seed electrons from an ambient population of cosmic rays (CR) in the large-scale strong atmospheric electric fields, initiating a minute-long burst of radiation and electrons (sometimes also neutrons) with energies up to many tens of MeV. The complementary mechanism, Modification of electron energy spectra (MOS), leads to enhancement of gamma radiation from the atmosphere even in the weak electric fields. These enhancements can last for a very long time, up to hours. The recent observations of numerous TGFs, TGEs, and gamma glows prove that RREA and MOS are robust and realistic mechanisms for explaining HEAP physics. Models using CERN GEANT4 code and CORSIKA code from Karlsruhe Institute of Technology (now both supplemented by the atmospheric electric field option) support in situ measurements of electron and gamma ray energy spectra.

The 7-th edition of TEPA symposia hold in Nor Amberd in September 2018, coincides with 10 years of TGE observations on Aragats. Nearly 500 TGEs detected at Aragats during last 10 years can be widely used for the validation of models aimed to explain high-energy phenomena in the atmosphere. The ground-based experiments have a huge advantage upon the space and atmospheric ones, because a "beam" of electrons is located directly above the particle detectors, and, usually on distances of few tens of meters. Thus, on Aragats, it was possible to measure the RREA avalanches initiated by a single CR electron, estimate the energy spectra of TGE electrons and gamma rays, and perform well synchronized measurements of lightning discharges and particle fluxes, explaining the phenomenon of the abrupt decline of high-energy part of TGE and get clues in the dynamics of atmospheric electric fields.

The problem of thundercloud electrification is one of the most difficult ones in atmospheric physics. The structure of electric fields in the atmosphere still escapes from the detailed in situ measurements. Few balloon flights although providing us with overall knowledge on possible structures and strengths of the atmospheric electric fields, cannot reveal the dynamics of the intracloud electric field. Observing TGE origination and decline simultaneously with atmospheric discharges we can understand how the charge structure of the cloud is changing during a thunderstorm and how lightning itself is originated.

Physicists and students from Russia, US, Italy, Japan, and Armenia discuss these and other problems of high-energy physics in the atmosphere through the 4-day long meeting. During a visit to the Aragats high-mountain research station, numerous particle detectors, lightning sensors, and field meters were demonstrated, the measurements of which are jointly analyzed to reveal the relationships between atmospheric discharges and particle fluxes.

In the proceedings, 17 reports are collected, some of them are already published, and some are submitted for publication. We compile all under one cover to have a comprehensive picture of advances in the high-energy atmospheric physics reported at the TEPA-2018.



**Prof. Ashot Chilingarian**, born 18 May 1949, is the Head of Cosmic Ray Division (CRD) of A.Alikhanyan National laboratory (Yerevan Physics Institute, YerPhI).

Prof. Chilingarian earned his Ph.D. in 1984 and Doctorate of Science in Physics and Mathematics in 1991 from YerPhI. Prof. A. Chilingarian has a vast experience in cosmic ray physics, machine learning, multivariate statistical data analysis, space weather, and atmospheric electricity. He has made a substantial contribution to the measurement of cosmic ray composition and energy spectrum using facilities on Mt. Aragats (MAKET experiment), Armenia and in Karlsruhe, Germany (KASKADE experiment). He developed advanced analysis methods for the photon shower identification in gamma ray astronomy, which substantially enhanced the sensitivity of the gamma ray imaging techniques. Prof. Chilingarian creates the Aragats Space Environmental Center (ASEC) and Armenian geophysics measurements network. He founded the worldwide network of new particle detectors for researches in space weather and solar physics, named SEVAN (Space Environment Viewing and Analysis Network). Nodes of the SEVAN network are now operating in Armenia, Bulgaria, Croatia, Slovakia, and Czech Republic (2 nodes will be installed in 2019 in DESY Zeuthen and Hamburg). His group discovers simultaneous fluxes of electrons, gamma rays, and neutrons correlated with thunderstorms proving the existence of the new high-energy phenomenon in the atmosphere (so-called Thunderstorm Ground Enhancements - TGEs).



Outside his field, Prof. Chilingarian has been interested in applying his data analysis methods to pattern recognition and genome analysis. In 2000-2001 he collaborated with the Huntsman cancer institute in Utah, USA to develop multivariate methods of DNA microarray data treating based on quantification of different types of gene expression in normal and tumor-affected tissues. This work culminated in a patent application by Utah University.

In 80-ths Prof. A. Chilingarian developed methodology of machine learning for high-energy physics and astrophysics experiments. He is the author of the ANI (Analysis and Nonparametric Inference) computer code library. He introduced the "multidimensional nonlinear cuts" method for analyzing data from the Atmospheric Cherenkov Telescopes. The methodology of the event-by-event analysis of the Extensive Air Shower experiments provides the estimation of energy spectra for separate groups of the primary nucleolus and partial energy spectra of primary cosmic rays. The group he led discovers the highest energy protons (with energies greater than 20 GeV) accelerated in the vicinity of the Sun on 20 January 2005 during Ground Level Enhancement event N 69.

Prof. Chilingarian has authored more than 350 scientific publications and served on many international scientific and editorial boards. He wins World Summit on Information Society award (Geneva, 2003) in the category of e-science; Armenia president award in Physics (2013); and Armenian Engineers and Scientists of Americas (AESA's) Scientist of the Year Award (2017). Prof. Chilingarian is fellow of the American Physical Society (APS).

The Space Education center (master courses) established by Prof. Chilingarian in YerPhI for a new generation of students has a special emphasis on participation in current international research projects of CRD. Prof. Chilingarian is professor at National Research Nuclear University MEPhI and he is leading a Russian National Foundation project in the Space Physics Research Institute of Russian Academy of Science. Also, he assists in the Scientific Advisory Committee of the EU project in the Czech Republic.



# CONTENTS

<b>Catalog of 2017 Thunderstorm Ground Enhancement (TGE) Events Observed on Aragats</b> .....	1
<i>A. Chilingarian, H. Mkrtchyan, G. Karapetyan, S. Chilingaryan, B. Sargsyan, A. Arestakesyan</i>	
<b>On the Origin of the Low-Energy Gamma Ray Flux of the Long-Lasting Thunderstorm Ground Enhancements (LL TGEs)</b> .....	15
<i>A. Chilingarian, A. Avetisyan, G. Hovsepyan, T. Karapetyan, L. Kozliner, B. Sargsyan, M. Zazyan</i>	
<b>Structures of the Intracloud Electric Field Supporting Origin of Long-Lasting Thunderstorm Ground Enhancements</b> .....	25
<i>A. Chilingarian, G. Hovsepyan, S. Soghomonyan, M. Zazyan, M. Zelenyy</i>	
<b>On the Origin of Particle Fluxes from Thunderclouds</b> .....	42
<i>A. Chilingarian, S. Soghomonyan, Y. Khanikyanc, D. Pokhsraryana</i>	
<b>Long lasting low energy thunderstorm ground enhancement sand possible Rn-222 daughter isotopes contamination</b> .....	51
<i>A. Chilingarian</i>	
<b>Monitoring of the Atmospheric Electric Field and Cosmic-Ray Flux for the Interpretation of Results in High-Energy Astroparticle Physics Experiments</b> .....	61
<i>A. Chilingarian, J. Knapp, M. Zazyan</i>	
<b>Termination of Thunderstorm Ground Enhancements by Lightning Discharges</b> .....	65
<i>A. Chilingarian, Y. Khanikyants, S. Soghomonyan</i>	
<b>Recovery of Electrical Structure of the Cloud with use of Ground-Based Measurement Results</b> .....	75
<i>E. Svechnikova, N. Ilin, E. Mareev</i>	
<b>Modelling of the Electron Acceleration and Multiplication in the Electric Fields Emerging in Terrestrial Atmosphere</b> .....	80
<i>A. Chilingarian, M. Zazyan, G. Karapetyan</i>	
<b>Mapping Observation Project of High-Energy Phenomena during Winter Thunderstorms in Japan</b> .....	85
<i>Y. Wada, T. Enoto, Y. Furuta, K. Nakazawa, T. Yuasa, T. Matsumoto, D. Umemoto, K. Makishima, H. Tsuchiya, GROWTH collaboration</i>	
<b>Recent Results from the Pierre Auger Observatory on Lightning Related Events</b> .....	93
<i>R. Colalillo, for the Pierre Auger Collaboration</i>	
<b>An Automatic Algorithm for the Recovering of TGE Differential Energy Spectra</b> .....	97
<i>G. Hovsepyan</i>	
<b>Recovering the Information on Atmospheric Discharges from Interferometric Data</b> .....	100
<i>A. Kiselyov, M. Dolgonosov, S. Soghomonyan, V. Karedin</i>	
<b>Monte Carlo Simulation of the Relativistic Feedback Discharge Model (RFDM)</b> .....	103
<i>E. Stadnichuk, M. Zelenyy, M. Dolgonosov, A. Nozik</i>	
<b>Electrification of the Lower Dipole: Scenarios of TGE Initiation</b> .....	107
<i>A. Chilingarian</i>	
<b>Influence of the Barometric Effect on the Surface Particle Detectors Count Rates</b> .....	111
<i>T. Karapetyan, B. Sargsyan</i>	
<b>Thunderstorm Electric Field Structural Features and Lightning Initiation Problem</b> .....	118
<i>I. Iudin, V. Rakov, A. Syssoev, A. Bulatov</i>	
<b>List of Participants</b> .....	137
<b>Gallery</b> .....	138

## Catalog of 2017 Thunderstorm Ground Enhancement (TGE) Events Observed on Aragats

*A. Chilingarian<sup>1,2,3</sup>, H. Mkrtchyan<sup>1</sup>, G. Karapetyan<sup>1</sup>, S. Chilingaryan<sup>1</sup>, B. Sargsyan<sup>1</sup>, A. Arestakesyan<sup>1</sup>*

<sup>1</sup>*Alikhanyan National Lab (Yerevan Physics Institute), Yerevan 0036, Armenia*

<sup>2</sup>*National Research Nuclear University MEPhI (Moscow Engineering Physics Institute), Moscow 115409, Russian Federation*

<sup>3</sup>*Space Research Institute of RAS, Moscow, Russia*

**Abstract:** The natural electron accelerator in the clouds above Aragats high-altitude research station in Armenia operates continuously in 2017 providing more than 100 Thunderstorm Ground enhancements (TGEs). Most important discovery based on analysis of 2017 data is observation and detailed description of the long-lasting TGEs (LL TGE).

We present TGE catalog for 2 broad classes according to presence or absence of the high-energy particles. In the catalog was summarized several key parameters of the TGEs and related meteorological and atmospheric discharge observations. For both classes (composed as 2 separate tables), the selection criteria were a peak significance as minimum 4 standard deviations from the mean value of time series measured just before a TGE ( $>4\sigma$ ). The statistical analysis of the data collected in tables reveals the months when TGEs are more frequent, the daytime when TGEs mostly occurred, the mean distance to lightning flash that terminates TGE and many other interesting relations. Separately was discussed the sharp count rate decline and following removal of high-energy particles from the TGE flux after a lightning flash. The used methodology of data analysis provides tools to integrate a multitude of particle and geophysical observations into a system that fully utilized the scientific potential of investigated physical phenomena. ADEI multivariate visualization and statistical analysis platform make analytical work on sophisticated problems rather easy; one can try and test many hypotheses very fast and come to a definite conclusion allowing crosscheck and validation

### INTRODUCTION

In recent years, the interest in using cosmic rays for obtaining information on atmospheric and extra-atmospheric processes is rapidly growing. Cosmic rays are modulated by the solar bursts and can be used as messengers carrying information on upcoming space storms. Precise and continuous monitoring of the secondary cosmic rays with networks of particle detectors can reveal the danger of agents of solar activity (Interplanetary coronal mass ejections and solar energetic proton events). Recently it was discovered that fluxes of cosmic rays detected on the earth's surface also carry information on the parameters of atmosphere, primarily on very difficult to measure atmospheric electricity. Fluxes of gamma rays and electrons carry information on high-energy processes in the atmosphere and on the net potential of atmospheric electric fields related to emerging positive and negative charged layers in thunderclouds. In the thunderclouds, seed electrons from the ambient population of cosmic rays are accelerated and form electron-gamma ray avalanches, directed either downwards to the Earth's surface or upwards into open space, depending on the direction of the electric field. Intense fluxes of gamma rays observed in space are called Terrestrial Gamma Flashes [1-3], in the atmosphere, they called gamma glows [4-7], on the ground - Thunderstorm Ground Enhancements [8-14]. In the TGEs, also neutron fluxes were observed [15-17]. The duration of particle fluxes of the atmospheric origin ranges from milliseconds to minutes and hours and consists of billions of particles [18 - 19]. To explain very large intensity of gamma ray bursts observed by the orbiting gamma ray observatories, models were introduced suggesting a new source of seed electrons from very large electric fields in the vicinity of normal intra-cloud lightning leaders [20].

Runaway Breakdown (RB, [21]), also referred to as Relativistic Runaway Electron Avalanche (RREA, [22-23]), is the main theoretical scheme satisfactory explaining electron accelerators operated in the clouds. Recently the

RB/RREA mechanism was supplemented by a new source of the electrons, accelerated in streamer tips of a developing lightning leader [24]. Electrons are accelerated up to characteristic energies of  $\sim 65$  keV and then runaway [25]. In any case, the lower dipole of the thundercloud formed by main negative charge and lower positive charge layer (LPCR) plays a key role in the downward electron acceleration, and the structure of electric field in the lower part of the thundercloud is crucial for lightning flash development.

However, due to the scarcity of measurements and poor knowledge of the electric structures in the thundercloud, including the lower dipole where electron acceleration took place and lightning activity occurred, both phenomena are not well understood until now. Thunderstorms are a major player in the global atmospheric electrical circuit, the main components of which are the ionosphere, clear air, conducting earth, thunderstorms (especially the electric charge structure inside the storm) and lightning [26]. The atmospheric electric fields and atmospheric discharges in last decades were intensively investigated using radars, 3D lightning mapping arrays, worldwide lightning location networks, observations of wideband electric field waveforms, and by the wideband and narrowband VHF interferometer systems, all-synchronous with measurements of near-surface electric field changes. The lower dipole was the main source of lightning flashes on Aragats as well as on the Tibetan plateau. In [27] was established that larger than usual LPCR prevents negative cloud-to-ground lightning flashes (-CG) to occurred, and only in the late stage of the storm -CG discharges could be triggered frequently. Nag and Rakov describe various scenarios of atmospheric discharges dependent on the maturity of LPCR [28]. In [29] was stated that negative CG usually started as an inverted-polarity intracloud discharge partly neutralized the lower positive charge so that a hole in the positive charge region

was formed and eventually led to a negative CG. In turn, the intense TGE can provide enough ionization to facilitate intracloud discharge and usually discharges occurred just after the maximum of particle flux [30]. Thus, lightning flashes and TGEs are interconnected phenomena and should be studied comprehensively. H.Tsuchiya in [31] suggested that warm winds moved from the sea originate winter thunderstorms in Japan with short-lived tripole structures appeared in a thundercloud and accelerated CR electrons toward the bottom positive layer. Chilingarian and Mkrtchyan in [32] mentioned that only after the creation of the lower dipole in the thundercloud electrons can be accelerated and particle flux can be directed downward. In this paper the correlations between thundercloud electrification (near-surface electrical field and type of lightning discharge) and measured particle fluxes were studied, thus invoking in the atmospheric electricity research a new type of key evidence—temporal evolution of the TGEs, presenting and classifying simultaneous measurements of the particle fluxes, disturbances in the near-surface electrical field, and lightning flashes of different types. In [33], it was mentioned that downward electron-accelerating electric field can be formed by the main negative charge in the cloud and its mirror image in the ground. This field is influenced by other charges in the cloud (and their images) and can be locally enhanced by the LPCR in the cloud and positive corona space charge near the ground. In [34] were considered different scenarios of lower dipole development assuming TGE and near-surface electric field observations. They mention that electron acceleration could take place between the LPCR and a negative charge layer above the LPCR and between negatively charged cloud base without any LPCR structure. Thus, there are different scenarios of TGE initiation and corresponding lightning type occurrence. However, they are dependent on each other and should be analyzed together for scrutinizing the structure and evolution of the lower dipole.

In our recent papers [35, 36] we outline and classify TGE subsample abruptly terminated by the lightning flash. We found that nearly (~75%) of TGEs abruptly terminated by lightning flashes are associated with –CG flashes and normal-polarity intracloud flashes, signaling that charge of the main negative region is rather large and the lightning leader preferably makes its path to the upper positively charged region. Another ~25% of TGEs abruptly terminated by lightning flashes are associated with inverted-polarity intracloud flashes (IC) flashes and hybrid flashes (inverted-polarity ICs followed by -CGs).

Appropriate scientific infrastructure and analysis methodology responding to these challenges was developed at the Cosmic Ray Division (CRD, [37]) of A. Alikhanyan National Scientific Laboratory (Yerevan Physics Institute). Based on continuous monitoring of particle fluxes, electric fields, and meteorological conditions on Aragats Mountain we present a catalog containing explanatory data on the TGEs and related measurements of corresponding key atmospheric parameters, measurements of near-surface electric fields and atmospheric discharges.

Aragats is a circular, shield-like mountain composed of both lavas and tufa. There are four summits: North (the highest, 4090 m), West (4080 m), South (3879 m), and East (3916 m) forming the rim of a volcanic crater. The Aragats research station of the Cosmic Ray Division (CRD) of the Yerevan Physics Institute is located at flat highland of the volcanic origin on 3200m altitude near large ice lake Kari

(latitude: 40.4713°N, longitude: 44.1819E). At the Aragats station, the average winter temperature is -15°C, with the minimum reaching down to -40°C. The average summer temperature is 12°C with the maximum reaching up to 20°C. The average wind velocity in summer is 6 m/s, and in the winter, it is 10 m/s occasionally reaching as high as 25 m/s. Snow covers the ground 250 days a year with an average depth of 165 cm. Research stations are accessible by a car (Aragats - from May to November, Nor Amberd whole year).

CRD operates on Aragats and Nor Amberd research stations the networks of detectors registering electrons, muons, gamma rays and neutrons round the clock, providing important information on various geophysical processes. Methods for visualization and analysis of multidimensional data are successfully used to research solar-terrestrial connections and high-energy phenomena in the terrestrial atmosphere. Multivariate analysis of variations of electric and geomagnetic fields, radiation, and particle fluxes can provide new information on the development of thunderstorm in the atmosphere. Such analysis presents a challenge due to the large quantity of acquired data. A huge amount of time series should be processed and identified near on-line for forecasting and alert issuing, as well as for the reports and scientific papers. Usually, researchers have no time to access archives if the data stream is pressing and new interesting events appear each new day.

To support researcher in data mining and finding “new physics” a multivariate visualization platform should be supplemented with tools of the statistical analysis (histograms, moments, correlations, comparisons); figure preparation; archiving, i.e. with a data exploration system. We connect the online stream of “big” data from ASEC to an exploration system developed in a collaboration with Karlsruhe Institute of Technology (KIT). The Advanced Data Extraction Infrastructure [38] helps researchers in exploring and understanding solar-terrestrial connections, solar modulation effects as well as in understanding high-energy phenomena in the atmosphere. A user-friendly interface interactively visualizes the multiple time-series and selects relevant parameters for different research objectives. Time series from different domains are joining for multivariate correlation analysis. The developed software links a multitude of particle and geophysical observations into an integrated system and provides analysis tools and services to fully utilize the scientific potential of current space weather/geophysical observations. In this way, we try to fully utilize the new concept of “big” data when an enormous amount of relevant observations culminates in the “new” physics unprecedentedly fast and precise.

## RESULTS

### *Long Lasting Low Energy Thunderstorm Ground Enhancements (LLL Tge)*

Hundreds of TGEs were observed at the Aragats research station in Armenia during the last 10 years. Numerous particle detectors and field meters are located in three experimental halls as well as outdoors; the facilities are operated all year round providing continuous registration of the time series of charged and neutral particle fluxes on different time scales and energy thresholds. In 2017, Aragats facilities register more than 100 TGEs, most of them originate in cumulonimbus clouds due to charge separation triggered by the moisture updraft of orographic and lake effects see Fig.1.

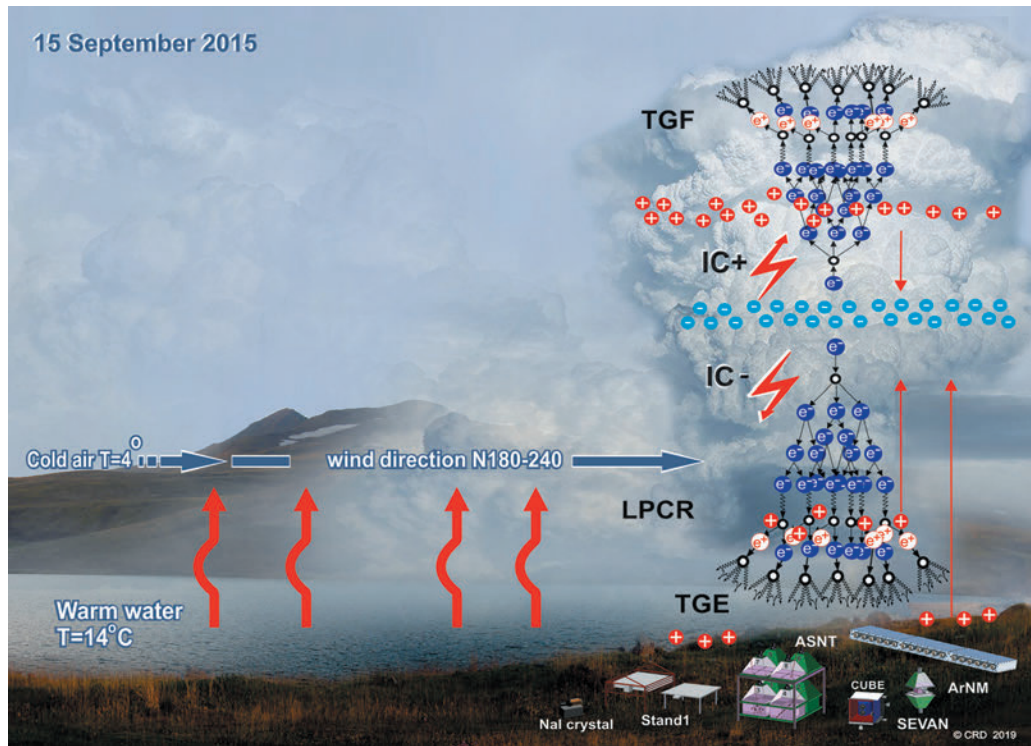


Figure 1. The lake-effect: cloud origination due to an updraft of the moisture brought by wind from the warm lake surface.

In the right side of Fig. 1, we present electron- gamma ray avalanche developed in the lower dipole of the thundercloud formed by the main negative charged region in the middle of the cloud and its mirror on the earth's surface (long red arrow) and/or by the same negative charged region with LPCR (short red arrow).

In Fig. 2 we present the time series of the particle detector counts and occurrences of lightning flashes inside radii of 10 km. The bottom curve was measured by 3 cm thick one m<sup>2</sup> area plastic scintillator; the upper curve – by 20 cm thick 0.25 m<sup>2</sup> area plastic scintillator. The energy threshold of the first scintillator is ~3 MeV, of the second ~6 MeV. In the top of Figure, the distance to lightning flash is depicted. The total number of registered lightning with distances to the detector site less than 10.5 km was 1450; thus, the frequency of lightning flashes nearby Aragats station was in 2017 ~5 per km<sup>2</sup> per year.

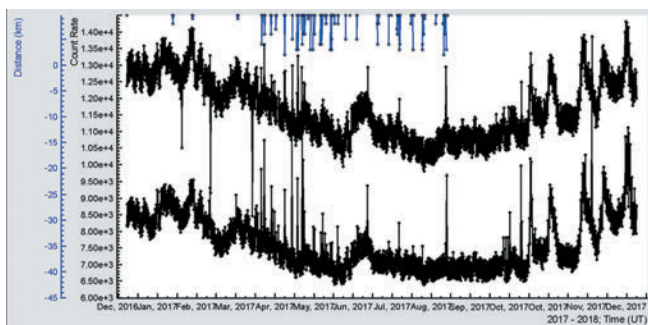


Figure 2. The time series of the particle detectors count rates: top curve – upper scintillator of the STAND3 detector; bottom - thick scintillator of the CUBE detector. In the top – the distance to atmospheric discharges (indicated by the line segment ending) occurred nearer than 10.5 km from the detector site of measured by the EFM-100 electric mill produced by the Boltek company.

We can notice in the rather coherent time series (correlation of time series is ~98%) multiple small and large coincided surges that are more frequent in the spring. In the next Figures, we demonstrate zoomed versions of these surges, i.e. TGEs lasting from a minute to several hours.

In Fig. 3 we show one of the TGE events, occurred on May 7, the month of the maximal thunderstorm and TGE activity. The one-minute time series are measured by a large (12 x 12 x 25 cm) NaI crystal located under the roof of the experimental hall; disturbances of near surface electric field and distances to the lightning flashes are measured with electric mills; and the outside temperature and dew point used for calculation of the distances to the cloud base are continuously measured by the Davis automated Weather station. The pattern of TGE is rather complicated, demonstrated several peaks and deeps directly related to the disturbances of the near surface electric field (superposition of the electric fields induced by several charged layers in the thundercloud). The first peak (from the left) started at ~9:00 UT and prolonged to ~11:30 demonstrating sharp surge at 9:57. The sharp particle outburst occurs when the near-surface field was in the deep negative domain (~-30kV/m) for ~20 minutes from 9:40 to 10:00.

The calculation of the height of the cloud base uses the assumption that the air temperature drops 9.84 C° per 1000 m of altitude and the dew point drops 1.82 C° per 1000 meters' altitude. In WEB there are several calculators for the approximation of the altitude of a cloud (see, for instance, <http://www.csnetwork.com/cloudaltcalc.html>).

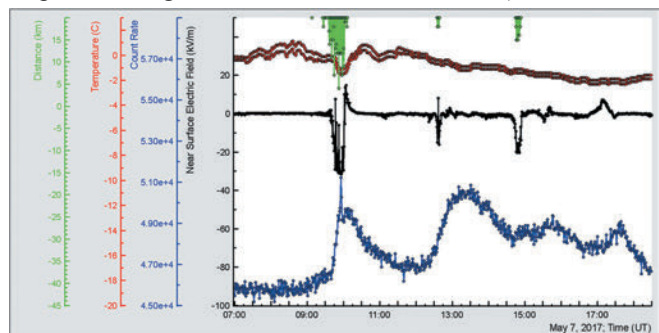
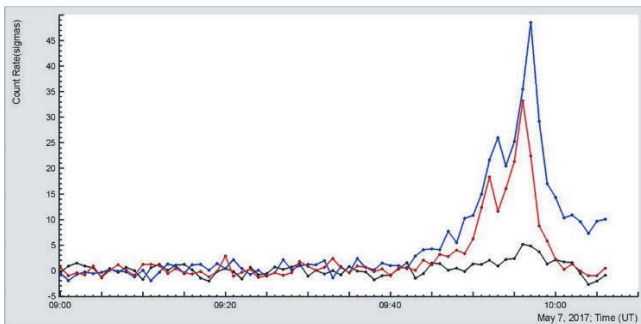


Figure 3. In the bottom – one-minute time series of NaI crystal (energy threshold 0.3 MeV); in the middle - disturbances of near surface electric field; on the top - outside temperature, dew point and distance to the lightning flash.

The simplified estimate consists in the multiplying of spread (the difference between temperature and dew point) measured in  $^{\circ}\text{C}$  by 122 m. With this approach, we estimate the height of the cloud during the sharp peak to be  $(-1.2 - -1.6) * 122 \sim 50$  m. Relative humidity of  $\sim 97\%$  also signaled the low cloud base. During the spring storms when clouds were, “sitting” on the station, the height of cloud base was 25-50 m during TGEs and RH was 96-98%. The nearest lightning flash was registered on 3.0 km from detector site.

The second peak started at 12:05 is much smoother and no sharp outbursts occur; the electric field is in the negative domain of  $\sim -14$  kV/m for 5 minutes (12:35 – 12:40) only.

In Fig. 4 we show the time series of so-called p-values of the peak significance test (number of standard deviations from the mean value of time series measured just before a peak to the peak value). The integral of normal Gaussian distribution from the p-value to infinity equal to a chance probability that observed peak is a fluctuation of background only and not a genuine effect.



**Figure 4.** Time series (in the number of  $\sigma$ ) of 1, 3 and 5 cm thick  $1\text{ m}^2$  area plastic scintillators. Energy threshold correspondingly  $\sim 0.8$ , 3 and 5 MeV.

The p-value is the most convenient measure of the reliability of detected peaks in a time series. Large p-value corresponds to small chance probabilities that the observed peak is a background fluctuation and not a genuine signal. Therefore, we can safely reject the null hypothesis (background fluctuation) and confirm the TGE existence. Very large p-values not only prove the unambiguous existence of a particle flux from the cloud but also serve as a comparative measure of the TGE significance provided by different detectors. We show the time-series of particle count rates in p-values for comparative purposes only. Comparison of the detectors with different sizes and different energy threshold in absolute counts make no sense because all structure will be smoothed when measurements will be scaled in the picture. No structures for detectors with small count rates will be seen. However, showing time series in the p-values, as we see in Fig. 4. reveals the structures even for scintillators with large energy threshold shown along with detectors with low energy threshold (the absolute count rates of both are drastically different). The mean value of the time-series is calculated with one-third of the time shown in the picture (the right third of the whole X-axes).

In Fig. 4 we show timeseries of one-minute counts of three plastic scintillators with different energy thresholds. The 1-cm thick scintillator located outdoors near MAKET experimental hall has the lowest energy threshold ( $\sim 0.7$  MeV), and correspondingly – the highest p-value of  $47\sigma$ . The lowest p-value of  $5.5\sigma$  shows 5 cm thick scintillator located in the MAKET building (energy threshold  $\sim 7$  MeV).

In Fig. 4 as well are seen 2 nearby peaks in the TGE. 1-minute time series cannot provide all details for exploring emerging structures in the particle flux; therefore, in Fig. 5 we show the one-second time series of the same-type 1-cm

thick plastic scintillator, along with disturbances of electric field measured at Aragats and Nor-Amberd stations (distance between stations  $\sim 13$  km).

The rise of count rate started at 9:50, followed by a sharp decrease related to the nearby lightning flash occurred at 9:52:45. The polarity of lightning at Aragats was negative, increasing from  $-30$  kV/m to  $-5$  kV/m (amplitude 25 kV/m); polarity of lightning in Nor Amberd was positive, decreasing from  $20$  kV/m down to  $-30$  kV/m (amplitude 50 kV/m). Thus, polarity was reversed in Nor Amberd; we identify this kind of lightning flashes as a normal-polarity IC. Such a type of lightning flashes is observed in Aragats quite often. It can be considered as an evidence of mature LPCR, providing large potential drop for electron acceleration and preventing lightning leader to reach the ground. An example of such a flash (not associated with TGE termination) was shown in Figures 8 and 9 of Chilingarian et al., 2017. Due to the low height of the cloud, the reversal distance is small, and  $\sim 13$  km between Aragats and Nor Amberd stations is sufficient to detect apparent polarity reversal.

To find out the origin of the count rate decline we measure differential energy spectra of the TGE with the network of large NaI crystals. In Fig. 6 we show differential energy spectra of the gamma ray flux from the start (Fig. 6a) to the first maximum at 9:52 (Fig. 6b) terminated by the lightning flash at 9:52:45; then we show the second maximum at 9:56 (Fig. 6d) decaying at 10:58 (Fig. 6f). From Figs 6b and 6c, we see that lightning “kills” flux of high-energy particles (HEP). Before lightning flash, the maximal energy reaches 30 MeV (Fig. 6b) and after lightning (Fig. 6c) only 6 MeV. We can see from Fig. 6 that for the smaller peak maximal energy reaches  $\sim 30$  MeV, and for the second, larger –  $\sim 40$  MeV. It is worth to note that for the NaI crystals maximal achievable energy that can be recovered by the energy release histograms is  $\sim 50$  MeV. The intensity of higher energies is so small that ever large NaI crystals hardly will detect at least 5 particles in the histogram bins above 50 MeV. Therefore, inherent background fluctuation will not allow reliable energy recovering. Another spectrometer with larger size (Aragats Solar neutron telescope, ASNT) is used for attaining TGE energies up to  $\sim 100$  MeV.

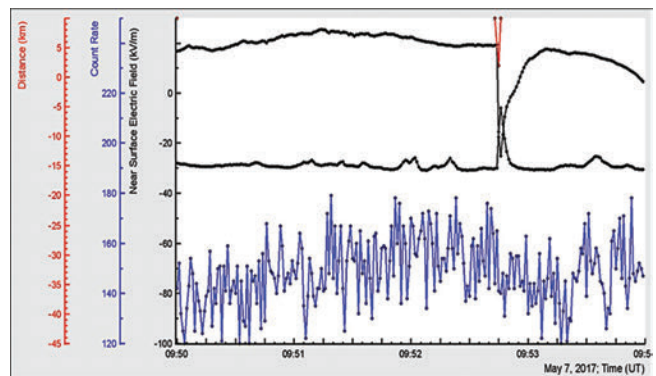


**Figure 5.** From top to bottom: distance of lightning flash to Aragats station; disturbances of near-surface electric field measured in Nor Amberd and Aragats; one-second time-series of the one-cm thick outdoor plastic scintillator.

Another important question in the establishing of long lasting TGE as the radiation of Radon progenies contributing to the TGE flux in the low energy domain (below 3 MeV). Nonstable nuclides comprise a significant portion of the low energy gamma ray flux measured by particle detectors and spectrometers at Aragats station. Fair-weather (background) low energy gamma ray spectra measured on Aragats is a mixture of the continuous spectrum produced by galactic

(and, sometimes, also solar) cosmic rays in interactions with the atmosphere and emission lines of long-lived nonstable nuclides that originated in violent mergers in the Universe ( $^{238}\text{U}$ ,  $^{235}\text{U}$ ,  $^{232}\text{Th}$ , etc.). The half-life of the radon isotope  $^{222}\text{Rn}$  is 3.82 days thus it can be transported to the atmosphere due to the diffusion mechanism. Although we demonstrate that the hypothesis of the precipitation as a source of gamma ray radiation initiated TGE is not valid [39], it was proposed that Rn-222 can be concentrated in the clouds above Aragats research station and radiation of its daughter isotopes can lead to the observed prolonged low energy part of TGE [40]. To identify the role of the gamma radiation from Radon progenies in the long lasting TGE flux, differential energy spectrum was measured with various spectrometers, including precise  $3'' \times 3''$  NaI(Tl)

spectrometer of ORTEC firm (FWHM  $\sim 7.7\%$  at 0.6 MeV). Measurements demonstrate that Radon progenies radiation significantly contributes to the “Winter TGEs” in the energy range below 3 MeV [41]. However, both Monte Carlo simulations [42,43] and measurements of gamma ray flux with large detector setups demonstrate that TGEs are originated in the intracloud electric fields. Modeling with the Weather Research and Forecasting (WRF) code uncovers the existence of charged layers above the station simultaneously with TGE detection [44]. Thus, the electrical origin of both low energy and high-energy parts of TGEs is supported by theory, modeling and observations of particle fluxes, electric fields, atmospheric discharges and hydrometeor concentrations (microphysics).

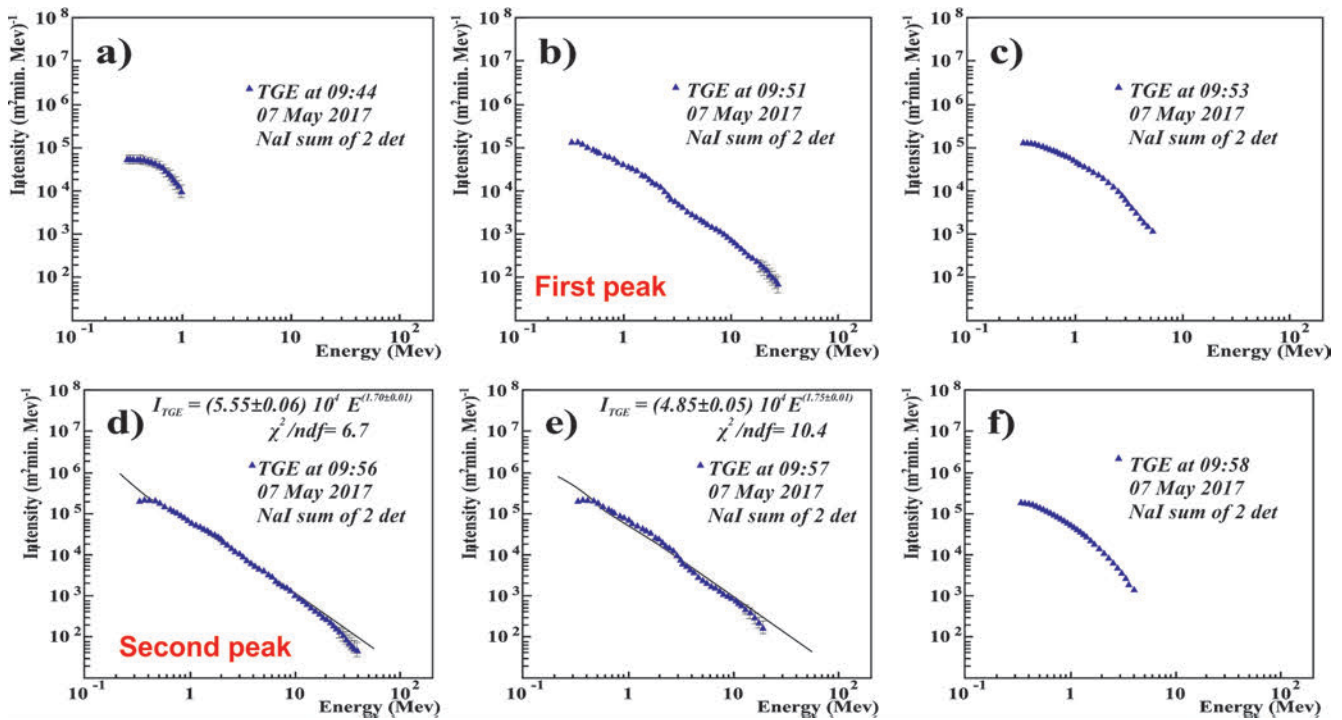


Figure 6. Differential energy spectra of the 7 May TGE measured by the NaI crystals (NN1 and 2).

#### STATISTICAL ANALYSIS OF TGE EVENTS OBSERVED IN 2017

We present TGE catalog for 2 broad classes according to presence or absence of the high-energy particles ( $>3$  MeV). In Tables 1 and 2 we summaries several key parameters of the TGEs observed in 2017 and related meteorological data. For both Tables, the selection criteria were a peak significance as minimum 4 standard deviations from the mean value of time series measured just before a peak. In the first column, we put the date of the TGE and time of the occurrence of the largest peak (the NaI scintillator one-minute time series was used for the peak identification, energy threshold  $\sim 0.3$  MeV); in the second column – occurrence time of the second peaks (if any); In 3-6 columns – the significances of the peaks (in percent/and in number of standard deviations) for particle detectors with different energy threshold:

- first NaI crystal, energy threshold 0.3 MeV;
- NaI crystal with energy threshold 3 MeV;
- The upper plastic scintillator of the STAND1 stacked detector located outdoors nearby MAKET experimental hall (energy threshold  $\sim 0.8$  MeV);

- The upper scintillator of SEVAN detector located in MAKET hall, energy threshold 7 MeV.

In columns 7-10, we show the duration of TGE observed by all 4 mentioned above detectors; all durations are calculated from the start of the enhancement of count rate until its recovery to pre-TGE value. In the 11-th column we show the distance to lightning flash (if any) estimated by the EFM-100 electric mill; in the 12-th column- distance to the cloud base calculated from outside temperature and dew point; in the 13-th – outside temperature. And in last 2 columns - the maximal negative strength of the near-surface electrostatic field measured during TGE and amplitude of electrostatic field changes. In 2017 Aragats facilities register more than 100 TGEs, proving that Mount Aragats is a stable electron accelerator for atmospheric high- energy physics research [45]. TGEs varied significantly in intensity and continuation; nonetheless, we can outline some newly discovered features of the TGE, and confirm Aragats 10-year observations. Catalog (Tabs 1and 2) contains useful information for further comparisons of time series and discovering of new correlations.

Table 1. TGE events containing High-Energyparticles

Date by NaI <sub>0.3</sub> UT	Peaks 2nd, 3rd by NaI <sub>0.3</sub> UT	%Nσ				ΔT (min.)				Dist to flash (km)	Dist. to cloud base (m)	Temp. (°C)	-E (kV/m)	ΔE (kV/m)
		Eth(NaI) ~0.3 MeV	Eth(NaI) ~3 MeV	E <sub>th</sub> (Stand) ~0.7MeV	E <sub>th</sub> (Sevan) ~7MeV	NaI <sub>0.3</sub>	NaI <sub>3</sub>	STAND	SEVAN					
Apr. 7 14:20	-	7/16	12/7	16/17	3.5/4.4	180	10	180	10	3	134	-3.1	24	65
Apr. 9 11:00	-	12/21	12/7	18/19	5/6	20	25	15	20	11	85	-4.8	22	33
Apr. 9 12:00	-	15/27	19/11	24/21	7/9	50	25	30	20	12	85	-4.1	29	40
Apr. 14 12:00	-	13/22	12/9	17/18	4.5/7.6	150	3	104	3	3	37	-0.6	18	39
Apr. 15 11:52	-	13/22	7/5	15/15	3/4	220	15	180	20	12	36	-0.3	26	28
Apr. 16 15:00	-	8/18	6.4/4	14.5/16	3/4	130	20	130	20	6	85	-3.4	24	39
Apr. 23 21:08	-	10/20.5	9/8	23/26.5	3/4	120	15	140	5	4	49	-1.6	27	73
Apr. 23 23:58	-	5/7	11/6	16/9	3/4	100	10	150	10	7	49	-1.6	42	73
Apr. 24 1:46	-	2.6/4	10.6/8	10.9/6.4	-	10	5	20	-	4	49	-2.2	34.5	52
Apr. 29 11:54	-	15/28.3	27.5/17.4	48.2/47	7.9/9	136	22	134	21	4	37	-0.6	22.8	58
May 3 01:08	-	8.5/10	13.2/10.6	23.8/21.2	5/6.8	170	25	30	27	16	37	0.2	31	36
May 3 13:53	13:59	42.7/48	73.3/39.5	45/38	7.2/8.4	110	4	120	22	3	50	0.4	22.9	70
May 6 12:40	-	11.1/21.5	26/17.9	44/36	8.8/10.8	231	45	220	30	3	98	0.7	33.8	80
May 6 14:00	-	14.4/15	9.5/5.6	27/17	3.8/4.3	95	20	25	10	10	60	0.1	40	54
May 7 9:56	9:53	11.4/21.7	09/10	40/30	4.3/4.8	120	5	120	20	4	50	-1	26	58
May 8 0:0	-	4/6.9	11.3/8.2	25.8/23.1	4.3/5.2	51	21	83	21	7	61	-2.4	21.2	67
May 14 14:48	-	11.7/15.7	14.2/8.9	15.8/16.9	-	100	15	110	-	3	159	1.9	19.5	60
May 19 17:13	-	5.9/5.1	8.3/5	9.8/5.4	3.2/4.2	139	30	112	31	2	159	2.1	23.6	64
May 20 02:25	3:49	11/21	4.5/3.1	18/13.4	3/4.4	180	8	190	15	9	25	1.8	19	24
May 20 7:50	-	10.4/18.6	7.1/4.9	4.7/4.8	-	80	5	85	-	6	37	2	22	36
May 21 14:15	-	6/5	10/6	22/16	4/5.5	170	15	25	20	7	49	-1.2	30	43
May 26 16:49	17:25	2.4/4.7	5.5/3.7	-	3.7/4.7	110	16	-	13	2	159	2.8	29.1	61
May 27 14:25	15:18	1/6.7	7/4	-	3.1/4.2	136	10	-	11	2	49	1.1	29.7	74
June 1 4:23	5:18	8/17	7/4.1	13/16.2	-	106	10	10	-	16	150	-0.3	32.9	58
June 1 08:16	9:06	8.9/15.4	7.5/5.1	10/13	4.1/5.7	155	20	19	19	12	120	0.7	19.6	51
June 15 23:56	-	3/4	4.5/4	-	3/4.5	70	20	-	30	14	135	2.8	17	25
June 21 20:53	-	8.4/17.2	3.4/3.5	06/13.0	2.4/3.8	140	-	138	-	7	219	4.1	9.56	33
June 22 13:52	14:12,14:16	7.5/16.2	15.1/10.1	18.1/23	10.4/14.9	165	42	130	41	7	170	4.4	32.4	54
July 7 13:23	13:44,13:49	6/10	6/4	-	3/5	123	20	-	20	5	280	7.2	15	43
July 15 6:28	6:57, 8:00	23/11	15.6/10.7	-	7/9.6	180	-	-	13	6	195	7.8	16.8	32
July 24 18:40	18:54	13/16	9/6	-	4/6	180	15	-	20	9	220	7	22	51
July 31 16:04	16:09	23/49	16/12	45/41	5.8/8.2	240	6	273	14	8	130	7.4	24	31
Aug. 17 11:00	-	4.9/7.2	5.5/8.8	7/6.1	4.2/5.3	90	8	73	7	5	268	7.6	23.6	42
Aug. 17 18:55	18:57	19.8/46	52.7/32.5	6/5.6	16.4/27	210	6	180	14	2	200	8.4	21	49
Sept. 29 21:52	-	12/22	7/5	12/21	6.1/8.1	120	4	11	18	16	25	0.4	15	25
Oct. 1 5:58	-	8/20	13/9	14/9	7/9.3	60	6	12	13	15	200	2.9	22	44
Oct. 1 20:33	-	16.6/21.8	5/3.5	21.3/13.2	3/5	140	10	135	5	5	85	0.7	26	53
Oct. 2 8:04	-	7/12	11/7	18/15	7/11	60	5	60	4	16	50	-0.7	21	42
Oct. 10 12:18	-	4.9/11	6.5/4.3	9.3/10.8	9.5/13	110	15	85	10	2	85	1.3	14	36
Oct. 10 14:08	14:10	10/13.7	25/20	13/11	12.8/12.4	120	8	155	15	2	150	0.5	22	48
Oct. 10 22:04	22:12	6.3/11	12.5/8	12/16.4	8/10	160	15	160	20	13	37	-0.2	8	22
Nov. 7 7:12	8:00,08:30	7/8.5	6/7.4	-	-	191	188	-	-	19	25	-0.2	10.4	32
Nov. 8 5:30	-	5/5.9	6.2/7.1	3.8/3.5	-	107	120	104	-	21/1	25	-0.1	9.8	16
Nov. 30 3:45	-	7/12	9.5/14.5	51/49	11.1/19	124	150	180	24	14	98	-7.2	5.38	15

Table 2. TGE events that do not contain High-Energyparticles

Date by NaI <sub>0.3</sub> UT	Peaks 2nd, 3rd by NaI <sub>0.3</sub> UT	%Nσ				ΔT (min.)				Dist to flash (km)	Dist to cloud base (m)	Temp. (°C)	-E (kV/m)	ΔE (kV/m)
		E <sub>th</sub> (NaI) ~0.3 MeV	E <sub>th</sub> (NaI) ~3 MeV	E <sub>th</sub> (Stand) ~0.7MeV	E <sub>th</sub> (Sevan) ~7MeV	NaI <sub>0.3</sub>	NaI <sub>3</sub>	STAND	SEVAN					
Apr. 8 14:00		5.2/11	-	6/7.5	-	480	-	310	-	13	85	-4.7	9	22
Apr. 9 21:02		3/4.5	-	-	-	65	-	-	-	12	60	-3.8	24	37
Apr. 17 16:41	-	6.7/7.7	-	12/7.7	-	80	-	100	-	4	85	-2.3	28	43
Apr. 30 13:53		2.9/5.8	-	4.6/4.8	-	160	-	30	-	23	49	0.5	22	22
May. 5 11:25		8.4/12.7	-	-	-	160	-	-	-	4	134	0.5	30	41
May 6 02:10		6.7/10.8	-	8.1/9	-	140	-	300	-	16	37	-0.7	22	24
May. 6 09:10		21.9/30	-	18.4/18.5	-	160	-	240	-	33	60	0.4	11	19
May 8 13:46		9/10	-	13/12	-	240	-	160	-	5	25	-0.1	7.5	8
May 9 16:26		12/27	-	14/14	-	160	-	120	-	16	60	1.4	14	38
May 10 14:10		2.3/4.4	-	-	-	25	-	-	-	7	160	2.9	11	20
May 10 20:31		3.1/4	-	4/4.6	-	80	-	70	-	20	200	3	7	20
May 10 22:21		8.5/11	-	10/10	-	90	-	100	-	6	170	2.8	11	32
May 12 14:06		7/17.6	-	9.4/12	-	60	-	90	-	3	195	1.6	23.6	62
May 14 8:53	8:56	7.6/13.2	-	7.5/11.3	-	105	-	180	-	24	110	1.5	7.8	14.5
May 14 13:22		4.3/7.9	-	16.9/16.4	3.4/4.5	90	-	70	15	16	85	1.9	24	28
May 15 12:05		12.3/8.5	-	18.2/19.7	3.7/4.7	278	-	267	32	7	85.4	-0.1	34.7	69.4
May 19 13:48	13:51	4.6/7	-	50/66	-	30	-	12	-	10	120	3.8	21	46
May 19 15:34	15:39	4/4	-	6/3.5	-	56	-	54	-	6	130	2.9	18.5	35
May. 22 14:57		5.1/11.7	5/3.0	37.9/23.4	4.7/6.7	80	10	38	13	5	48.8	-0.1	21.5	42
May 23 07:55		16/30	-	15/13	-	360	-	120	-	6	61	-0.4	16	16
May. 23 13:35	14:17	8.7/12.5	-	8.5/9.5	-	160	-	200	-	-	85	1.4	3	7
May 23 20:26		8.8/16.9	-	-	-	360	-	-	-	23	37	-0.8	6.9	18
May 24 15:18		2.3/4.6	-	-	-	120	-	-	-	10	37	-1.3	12	12
May 27 3:36		11.8/15.4	-	-	-	100	-	-	-	16	37	-0.1	11	15
May 29 5:14		3/6	-	-	-	30	-	-	-	15	120	-0.2	16	22
May 29 16:30		2/4.5	-	4.5/5	-	65	-	60	-	12	310	4	18	50
June 6 17:35		2.7/4	-	5.5/4.7	-	104	-	199	-	3	790	8.1	22.8	43
June 11 15:30		3.3/6	-	4.2/5.4	-	99	-	132	-	27	350	4.7	3	7
June. 12 15:22	16:30	3.8/7.3	4/3.0	5/5.3	-	131	8	180	-	20	180	4	12.3	32
June 16 10:56		10/12.5	-	7/10	-	200	-	180	-	25	110	2	14	24
June 20 10:23		8/15	-	4/5.4	-	110	-	180	-	27	120	6	5	10
June 20 12:55		7/21	-	5/6.5	-	80	-	60	-	14	300	7	5	21
June 29 09:25		17.2/23.7	-	-	-	300	-	-	-	4	330	8.4	23	49
July 13 10:12		6.9/9.2	-	-	-	210	-	-	-	6	160	9.6	7	20
July 13 13:51		11.8/15.7	-	-	-	110	-	-	-	10	240	7.5	3.5	16
July 13 18:18		11.7/15.5	-	-	-	180	-	-	-	18	120	4.7	5	17
July 14 16:17		3.5/7.3	-	-	-	160	-	-	-	25	440	9.3	16	16
July 15 16:16	18:00	4.7/4	-	-	-	63	-	-	-	5	232	7.6	18.2	34.5
July 15 18:21		4.8/9.2	-	-	-	160	-	-	-	6	250	7.1	25	46
Aug. 2 9:25		15/10	-	8.2/7.7	-	60	-	150	-	7	500	13	2	15
Aug. 2 10:20		21/14.4	-	-	-	250	-	-	-	10	610	15	7	16
Aug. 10 9:20	10:28	10.1/9.5	-	-	-	180	-	-	-	6	780	12.4	11.9	35

Aug. 11 10:00	11:11	7.7/9	-	4/2.8	-	558	-	75	-	7	561	12.9	4.8	14
Aug. 15 10:34		8/8.4	-	7/5.7	-	40	-	40	-	25	340	10.4	4	8
Aug. 15 11:36	11:49	10.6/11	5/3.6	14/11	-	70	8	60	-	14	270	4	5	31
Aug. 15 12:51		19/20	-	25/20	-	35	-	40	-	7	290	10.7	3.6	16
Aug. 15 13:55		22/24	-	29/23	-	55	-	35	-	12	270	10.2	7	21
Aug. 16 0:00	1:16	16.3/35	-	21/29	-	383	-	393	-	16	195	8.2	23.7	54
Aug. 27 22:46		6/9	-	7/8	-	130	-	110	-	16	720	9.9	19	34
Sept. 27 15:37	-	12/24.4	-	19.3/28.2	3.2/4.2	140	-	150	13	4	219	3.2	22.3	41
Sept. 28 15:10		2.1/4.3	-	3.4/4.7	-	120	-	75	-	25	170.8	2	0.8	1.5
Sept. 28 19:17		3/5.9	-	4.3/5.5	-	33	-	42	-	20	110	0.6	15	17
Sept. 28 17:59		2.5/4.8	-	2.9/3.8	-	60	-	45	-	25	134	1.2	10.5	17
Sept. 29 18:40		13/26	-	13/12	-	100	-	95	-	17	25	0.3	7	24
Sept. 29 20:20	20:37	6/13	-	12/10	-	50	-	105	-	14	37	0.3	12	21
Oct. 1 17:58		20/26.6	4/2.7	22/12.6	6-Apr	150	10	140	10	10	85	17	24	36
Oct. 1 17:58		20.3/28.6	5.4/3	20.1/26.5	3.8/6.9	150	10	140	10	10	85	1	17	24
Oct. 2 06:59		13/17	-	11/14	2.6/4	70	-	60	15	15	25	-0.6	13	25
Oct. 2 9:33		12/15	-	8.2/11	4/6.4	90	-	20	25	12	37	0	19	45
Oct. 28 10:30		16.2/29	-	11.6/15.2	-	370	-	339	-	33	85.4	-1.4	0.5	2.3
Nov. 29 18:00		3.6/7.1	3.4/7.5	-	-	81	203	-	-	33	85.4	1.18	1.23	43

In Fig. 7 we show distribution of TGE significances for different particle detectors. Obviously, detectors with lower energy threshold demonstrate highest significances.

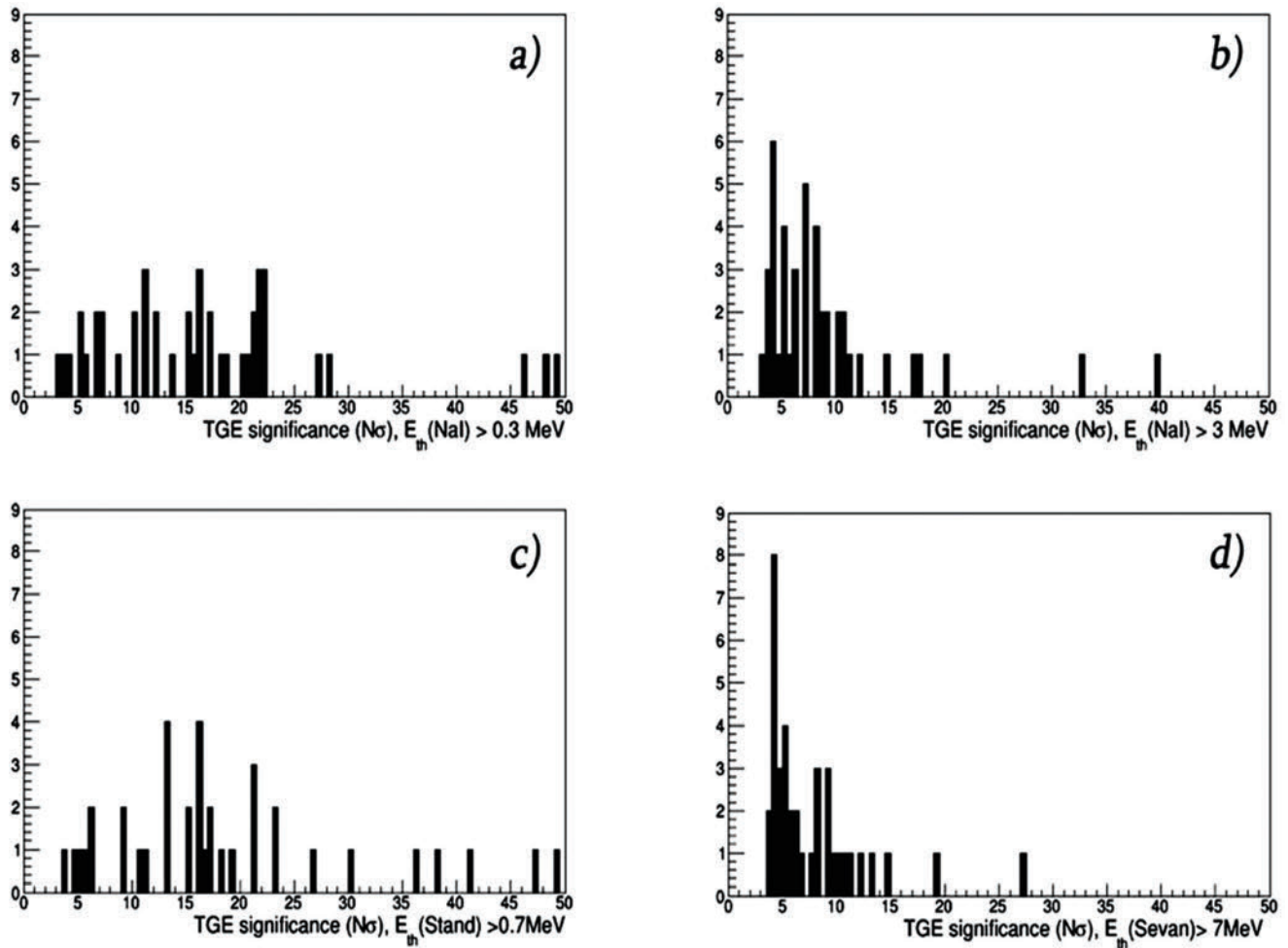


Figure 7. Statistical significance of TGE events containing HEP (44 selected events) registered by particle detectors with different energy thresholds.

In Fig. 8 we demonstrate the duration of TGE events and distance to the lightning flash that terminates TGE. In Fig. 8a and 8c by bold black we denote TGE events with HEP, by gray – without HEP. Apparently, events containing HEP are shorter in duration, because the probability of lightning is higher.

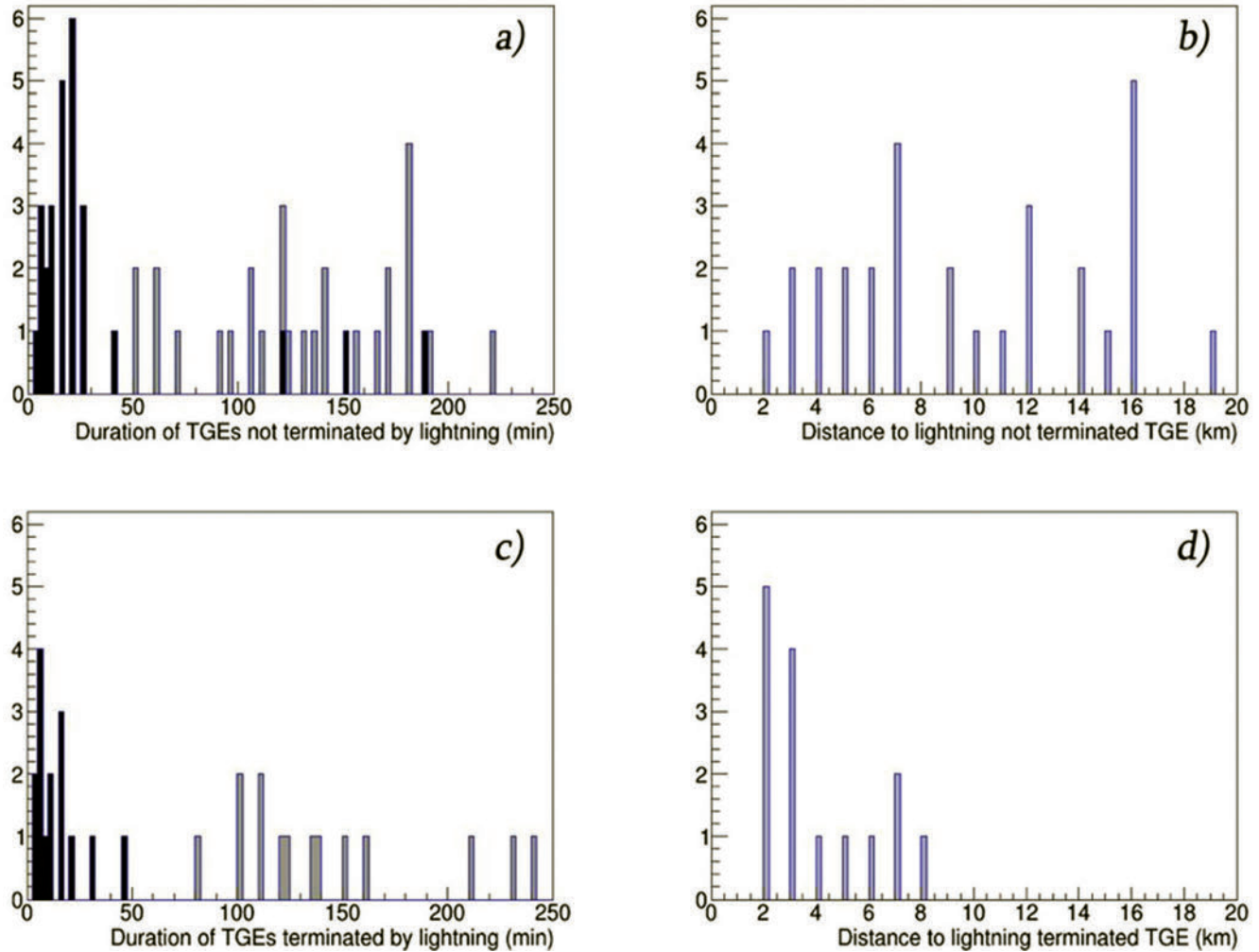


Figure 8. Duration a), c) and distances b), d) of TGEs terminated and not terminated by the lightning flash. Black –measured by NaI detector with  $E_{th} > 3$  and gray- with  $E_{th} > 0.3$ .

In Figs. 8b and Fig. 8d we show the distance to lightning flash for both kinds of TGE events. Only nearby lightning flashes ( $< 10$  km) terminate the particle flux.

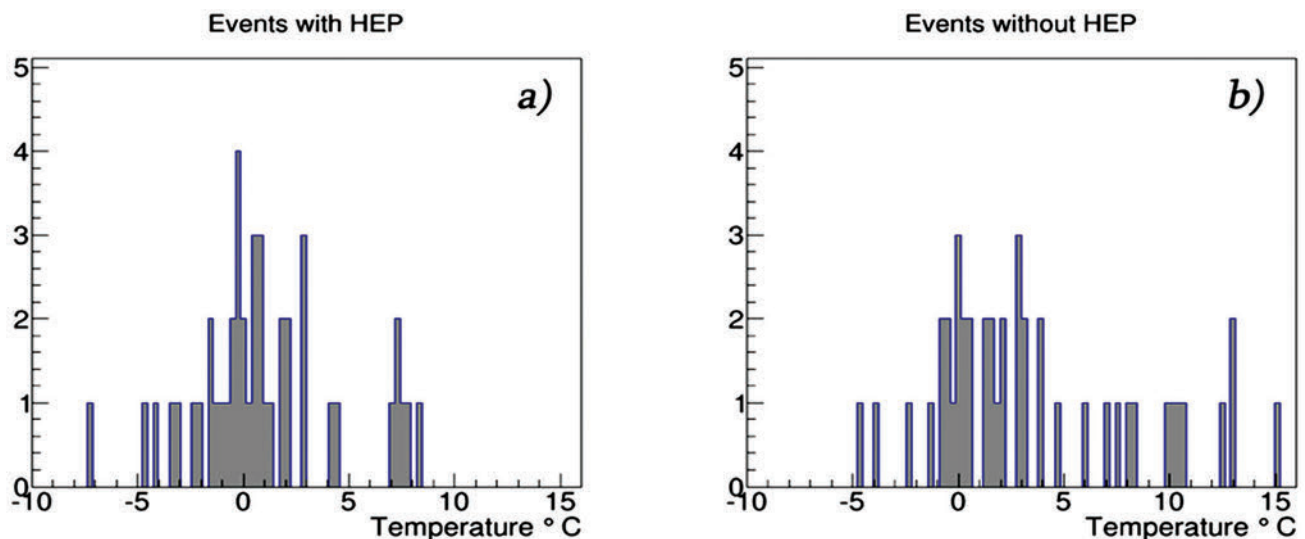


Figure 9. Outside temperature during TGE events with and without HEP.

In Fig. 9 we show the distribution of outside temperature for events containing HEP (9a) and without HEP (9b). Distribution of duration of TGE with HEP is more compact comparing with distribution of TGE without HEP. Most of largest TGEs occurred when temperature is with in  $-3 - +3^{\circ}\text{C}$ .

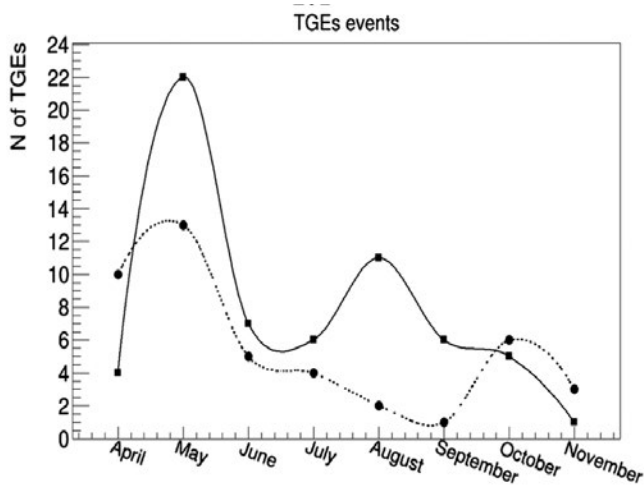


Figure 10. Distribution of TGEs by months. Solid line - TGEs without HEP; dotted line- with HEP

In Fig. 10 we can see that both kinds of TGEs are strongly peaked in May, when the temperature fluctuates around 0 C° and clouds are very low above surface. In June – July number of TGE declines to recover for TGEs containing HEP in August (start of autumn on Aragats), and in October for TGEs without HEP.

In Fig. 11 we show the daily frequencies of TGE occurrence. Maximal frequency was observed at 18-19 local time (UT+4).

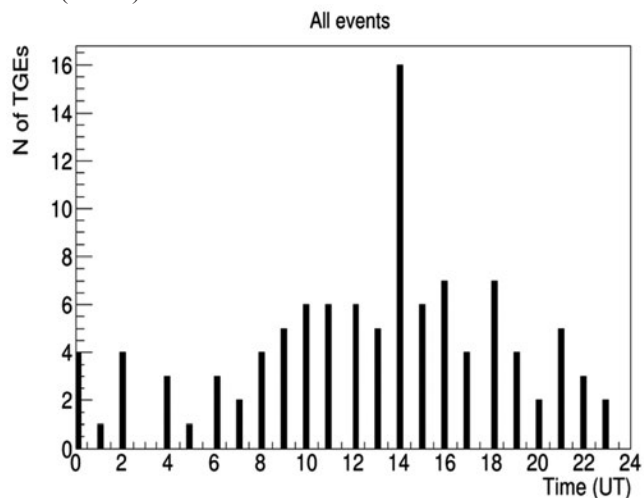


Figure 11. TGE "daily wave"; frequencies of TGE occurrence during the day time.

## DISCUSSION

We publish the first TGE event catalog. TGE events are very rare and usually, in publications, only one-two observed events are analyzed and discussed. For the first time, we present the statistical analysis of the whole TGE collection observed on Aragats mountain in April-November 2017. The natural electron accelerator in the clouds above Aragats station operates continuously in these months providing more than 100 TGEs. All TGEs were analyzed and classified according to the presence or absence of high-energy particles. We present the distribution of the TGE events by months of the year and by hours of the day. The maximal frequency of TGEs occurred in May and at 14:00 UT (18:00 local time). Strong TGEs happened mostly when the outside temperature is in the (-3 – 3) C° limits. Only lightning flashes within 10 km can terminate TGE.

Based on our analysis, we can outline new findings made in 2017 and confirm our previous conclusions from

the decade of observations. Most important finding based on analysis of 2017 data is observation and description of the *long-lasting TGE (LL TGE)*; TGE started with low energy flux of several tens of minutes, turning to short (1-5 minutes) intense peak containing high-energy particles; the decay of TGE extended several hours. LL TGE is related to development in the thundercloud strong positive electric fields accelerating electrons downward in the direction of earth. The flux of high-energy particles from the avalanches reaches detectors on earth's surface and originates bursts of intensity. High-energy part of TGE is extending few minutes and usually abruptly terminated by a nearby lightning flash. Thus, in 2017 we discover the "threshold" nature of the high-energy emission from thunderclouds. Lightning flashes that occurred within 10 km, dropping the electric field within the dipole, and terminate the acceleration of electrons to high energies. The long-lasting part of TGE is connected with Compton scattered gamma rays from remote avalanches and with bremsstrahlung emission of electrons gaining additional energy from the intracloud electric fields (MOS process, [42]). The gamma radiation from the Radon daughters brought by rain also can contribute to the low energy part of TGE. Mentioned results confirm our statement about "radioactive" thunderclouds full of enhanced fluxes of electrons, gamma rays and neutrons [36]. Raw data that was summarized in tables 1 and 2 is available via the ADEI interactive WEB platform (<http://adei.crd.yerphi.am/adei>); slides of each-month analysis of TGE data are located in CRD seminars site (<http://www.crd.yerphi.am/Slide>).

## METHODS

Neutral and charged particle fluxes are measured on Aragats with various elementary particle detectors. Count rates are measured with plastic scintillators, proportional chambers, and NaI and CsI crystals. The data are transformed to the time series of particles intensities on different time scales from tens of milliseconds to days. Energy release histograms measured each minute with NaI crystals and every 20 seconds with 60-cm thick plastic scintillators are transformed to the differential energy spectrum of gamma rays and electrons. We measure also the near-surface electrostatic field with a network of four electric field mills, located on Aragats. The wideband fast electric field is measured by 3 circular flat plate antennas attached to fast digital oscilloscopes which are triggered by the signal from active whip antennas. The oscilloscopes are used also to record the waveforms from the particle detectors to distinguish between the genuine particle signals and the electromagnetic interferences from nearby lightning flashes.

The detector network used to measure the particle energy spectra consists of 7 NaI crystal scintillators packed in a sealed 3-mm-thick aluminum housing. The NaI crystal is coated by 0.5 cm of magnesium oxide (MgO) by all sides (because the crystal is hygroscopic) with a transparent window directed to the photo-cathode of an FEU-49 PMT, see Fig. 12. The large photocathode (15 cm in diameter) completely covers the window and provides a good light collection. The spectral sensitivity range of FEU-49 is 300–850 nm, which covers the spectrum of the light emitted by NaI(Tl). The sensitive area of each NaI crystal is ~0.0348m<sup>2</sup>. A significant amount of substance above the sensitive volume of NaI crystals (0.7 mm of roof tilt, 3 mm of aluminum, and 5 mm of MgO) removes electrons with energy lower than ~3 MeV.

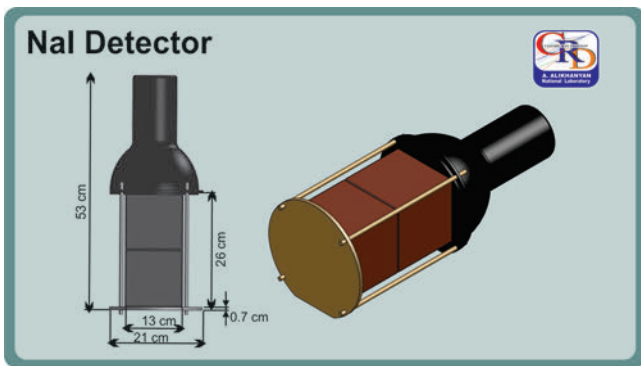


Figure 12. NaI(Tl) crystal assembly.

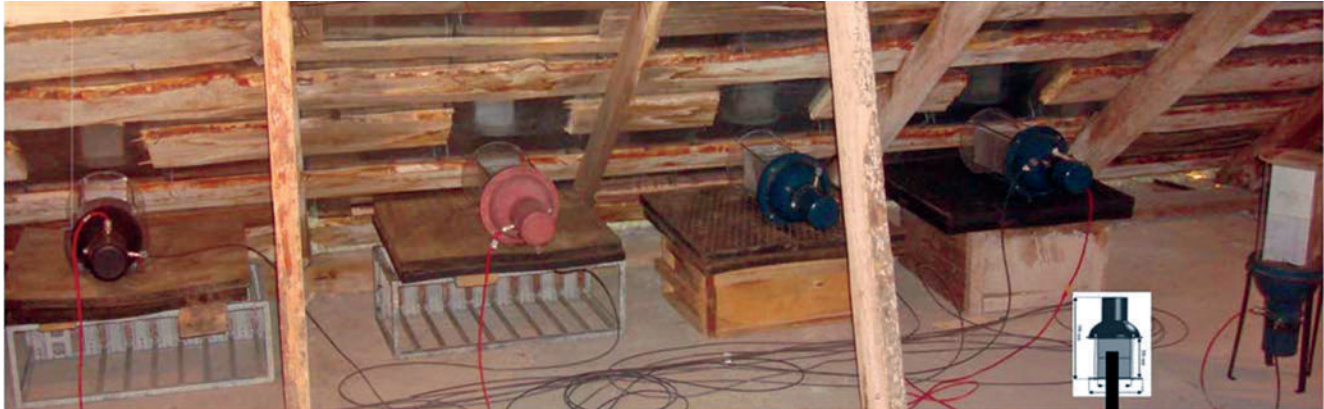


Figure 13. NaI(Tl) spectrometers installed beneath the tilted roof of the SKL experimental hall at Aragats station

The slab assembly is covered by the white paper from the sides and bottom and firmly kept together with special belts. The total thickness of the assembly is 60 cm. Four scintillators of  $100 \times 100 \times 5 \text{ cm}^3$  each are located above the thick scintillator assembly to indicate charged particle traversal and separate the neutral particles by “vetoing” charged particles (the probability for the neutral particle to give a signal in 5 cm thick scintillator is much lower than in 60 cm thick scintillator).

A scintillator light capture cone and PMT are located on the top of the scintillator housings.

The main ASNT trigger reads and stores the analog signals (PMT outputs) from all 8 channels if at least one channel reports a signal above threshold. The frequency of triggers is  $\sim 10 \text{ KHz}$  due to incident secondary cosmic rays (SCR) – products of the interaction of galactic cosmic rays with atmosphere; at the altitude of 3200 m on Aragats, the intensity of SCR is  $\sim 500 / \text{m}^2/\text{sec}$ . The flux of particles from thundercloud (TGE) can be 5 times larger than SCR (background) intensity.

Huge advantage of ASNT is large size of detector ( $4 \text{ m}^2$ ) that gives possibility to register TGE particles up to 100 MeV; to measure separately gamma ray and electron energy spectra and - angles of particle incidences.

A 52 cm diameter circular flat-plate antenna was used to record the wideband (50 Hz to 12 MHz) electric field waveforms produced by lightning flashes. The antenna was followed by a passive integrator (decay time constant  $\sim 3 \text{ ms}$ ); the output of which was connected via a 60 cm double-shielded coaxial cable to a Picoscope 5244B digitizing oscilloscope. The antenna calibration for electric field amplitude is presently not available, so the amplitude of recorded waveforms is given in voltage units of oscilloscope. The oscilloscope was triggered by the signal from a commercial MFJ-1022 active whip antenna that covers a

The energy resolution of spectrometers is  $\sim 30\%$  at 662 KeV. The big advantage of used large NaI crystals is the possibility to measure high-energy particles. Large count rate allows reliably measure rather weak flux of high-energy electrons and gamma rays – up to 50 MeV.

The NaI(Tl) spectrometers are located just below the tilted roof of the SKL experimental hall on Aragats station, at 3200 m above sea level (Fig.13). The pulses from photomultiplier (PMT) optically connected to the crystal are fed through a preamplifier to an amplitude-to-digital converter (ADC).

frequency range of 300 kHz to 200 MHz. The record length was 1 s including 200 ms pre-trigger time and 800 ms post-trigger time. The sampling rate was 25 MS/s, corresponding to 40 ns sampling interval, and the amplitude resolution was 8 bit. The trigger out pulse of the oscilloscope was relayed to the National Instruments (NI) myRIO board which produced the GPS time stamp of the record (detailed description of our fast data acquisition system based on the NI myRIO board can be found in Pokhsrlyan, 2015). The flat-plate and the whip antennas were installed at the same location, within 80m of particle detectors and two electric field mills. The distance from the antennas to third field mill was 270 m. The near-surface electrostatic field changes were measured by a network of five field electric mills, three of which were placed at the Aragats station, one at the Nor Amberd station at a distance of 12.8 km from Aragats, and one at the Yerevan station, at a distance of 39.1 km from Aragats. The distances between the three field mills at Aragats were 80 m, 270 m, and 290 m. The electrostatic field changes were recorded at a sampling interval of 50 ms. The lightning optical image is captured by a video camera at a frame rate of 30 frames/s. We used also data from the World-Wide Lightning Location Network (WWLLN), which detects very low frequency (VLF, 3-30 kHz) emissions from lightning. Electric mills also provide estimates of the distance to lightning.

The relationship between the electrification of a thundercloud, lightning activity, broadband radio emission and particle fluxes can be immediately evaluated by researchers using an advanced multidimensional visualization system ADEI (*Advanced Data Extraction Infrastructure*). ADEI is a WEB data analysis platform to handle large amounts of data stored for a long time assessable for users worldwide. The overall time interval of measurements is  $\sim 20$  years, and the frequency of data stream from particle detectors now reaches hundreds of KHz.

Interactive tools are working in real time and quickly extract important information from this huge amount of data and provide users with analysis tools. To achieve this, the ADEI constantly monitors incoming data flows, performs preprocessing and caches important information in the database.

With the ADEI system, a catalog of TGE events registered in 2017 for two broad classes of events depending on the presence or absence of high-energy particles ( $> 3$  MeV) was compiled. The summary tables 1 and 2 show several key parameters of the TGE, and associated meteorological data. In Fig. 15, we show frames visualizing several data analysis options.

In the frames a1, a2, 13 we show the large TGEs registered in 2017 with various particle detectors. The energy threshold of detectors varies from 0.3 to 7 MeV. Thus, the few minute peaks, corresponding to particle avalanches accelerated electrons to energies up to 50 MeV demonstrate all detectors. The long-lasting, low energy part – only particle detectors with low energy threshold.

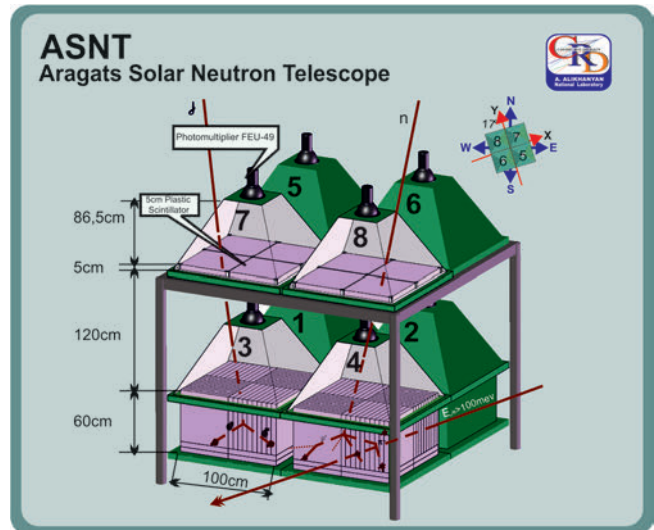


Figure 14. Assembly of ASNT with the enumeration of 8 scintillators and orientation of detector axes relative to the North direction.

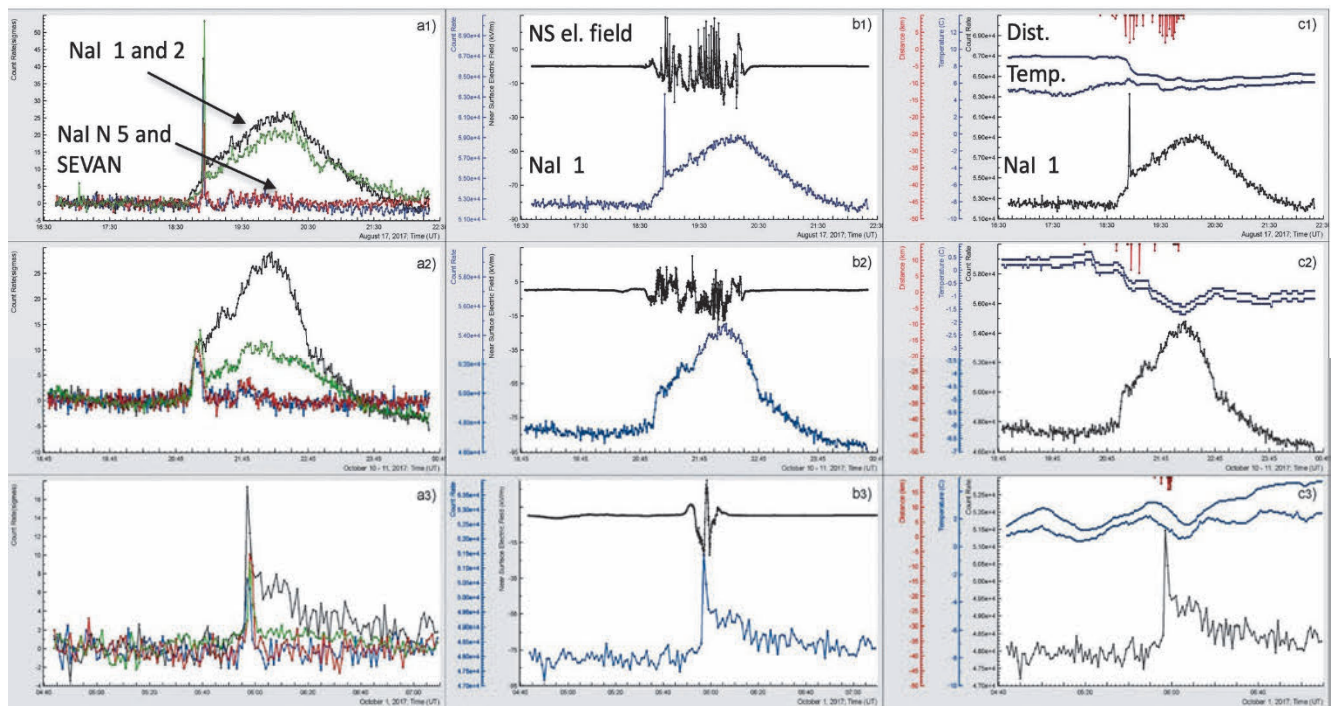


Figure 15. Visualization of the information on TGE observed in 2017 and posted in Tables 1 and 2.

To visualize all very different count rates in one and the same frame we use p-values instead of absolute values of count rates. In frames b1, b2, b3 we show relation of the same TGEs (now count rates are in the absolute numbers) to disturbances of the near surface electric field. All TGE are related to the large disturbances reaching 20kV/m. The corresponding strong electric field in the thunderclouds originate electron – gamma ray avalanches, in which electrons are accelerated and multiplying.

In frames c1, c2, c3 we show the relation of meteorological parameters to TGEs. In the middle of frames, we locate outside temperature and dew point. The rough estimate of cloud base height made with these parameters proves a rather close location of thunderclouds on Aragats (50–200 m) in Summer-Autumn season [36]. The distance to lightning flash is shown in the top of frames. The close lightning flashes (2–5 km) from detector site prove the strong electric field above Aragats station.

#### ACKNOWLEDGMENTS

Authors would like to thank the staff of the Aragats Space Environmental Center for the uninterrupted operation of Aragats research station facilities. Authors thank G.Hovsepyan for preparing Fig. 6.

Work was supported by Russian Science Foundation grant (project No. 17-12-01439).

The data for this paper are available on the WEB page of the Cosmic Ray Division (CRD) of the Yerevan Physics Institute, <http://adei.crd.yerphi.am/adei>. Figures from the paper can be easily reproduced with embedded multivariate visualization on-line program ADEI [38].

#### REFERENCES

- [1] Fishman G. J., Bhat P. N., Mallozzi v, et al. Discovery of intense gamma ray flashes of atmospheric origin, Science 264, 1313 (1994).

- [2] Briggs M.S., Connaughton V., Wilson-Hodge C., et al. Electron-positron beams from terrestrial lightning observed with Fermi GBM, *Geophys. Res. Lett.* 38, L02808 (2011).
- [3] Tavani, M. et al. (AGILE team), Terrestrial gamma-ray flashes as powerful particle accelerators. *Phys. Rev. Lett.* 106, 018501 (2011).
- [4] McCarthy, M. P. & Parks, G. K. Further observations of X-rays inside thunderstorms. *Geophys. Res. Lett.* 97, 5857–5864 (1985).
- [5] Eack, K. B., Beasley, W. H. & Rust, W. D. et al. Initial results from simultaneous observations of x rays and electric fields in a thunderstorm. *J. Geophys. Res.* 101, 29637–29640, (1996).
- [6] Kelley, N. A., Smith, D. M., Dwyer, J. R. et al. Relativistic electron avalanches as a thunderstorm discharge competing with lightning, *Nature communications* 6 Article number: 7845 (2015).
- [7] Kochkin P, van Deursen P. J., Marisaldi M., et al., In-Flight Observation of Gamma Ray Glows by ILDAS, *JGR, Atmosphere*, 122, 12,801–12,811 (2017).
- [8] Alexeenko, V. V., Khaerdinov, N. S. & Lidvansky, A. S. et al. Transient Variations of Secondary Cosmic Rays due to Atmospheric Electric Field and Evidence for Pre-Lightning Particle Acceleration. *Physics Letters A.* 301, 299–306, doi:10.1016/S0375-9601(02)00981-7 (2002).
- [9] Chilingarian, A., Daryan, A. & Arakelyan, K. et al. Ground-based observations of thunderstorm-correlated fluxes of high-energy electrons, gamma rays, and neutrons. *Phys. Rev. D* 82, 043009
- [10] Chilingarian, A., Hovsepyan, G. & Hovhannisyan, A. Particle bursts from thunderclouds: natural particle accelerators above our heads. *Phys. Rev. D: Part. Fields* 83(6), 062001, (2011).
- [11] Torii, T., Sugita, T. & Kamogawa, M. et al. Migrating source of energetic radiation generated by thunderstorm activity. *Geophys. Res. Lett.* 38, L24801–n/a, (2011).
- [12] Tsuchiya, H., Enoto T., Iwata K., et al. Hardening and termination of long-duration g rays detected prior to lightning. *Phys. Rev. Lett.* 111, 015001 (2013).
- [13] Kudela, K., Chum, J., Kollárik, M., Langer, R., Strhářský, I., & Baše, J. Correlations between secondary cosmic ray rates and strong electric fields at Lomnický štít. *Journal of Geophysical Research: Atmospheres*, 122, 10, 70010,710, (2017).
- [14] Kuroda, Y., Oguri, S. & Kato, Y. et al. Observation of gamma ray bursts at ground level under the thunderclouds. *Physics Letters B* 758, 286–291, (2016).
- [15] Gurevich, A. V. et al. Strong flux of low-energy neutrons produced by thunderstorms. *Phys. Rev. Lett.* 108, 125001 (2012).
- [16] Tsuchiya, H., Hibino K., Kawata K., et al. Observation of thundercloud-related gamma rays and neutrons in Tibet. *Phys. Rev. D* 85, 092006 (2012).
- [17] Chilingarian, A., Bostanjyan, N., & Vanyan, L. Neutron bursts associated with thunderstorms. *Physical Review D: Particles and Fields*, 85(8), 085017.
- [18] Mailyan B.G., Briggs M.S., Cramer E.S., et al., The spectroscopy of individual terrestrial gamma-ray flashes: Constraining the source properties, 121, 11,346–11,363, (2016).
- [19] Chilingarian A., Hovsepyan G., Mailyan B., In situ measurements of the Runaway Breakdown (RB) on Aragats mountain, *Nuclear Inst. and Methods in Physics Research, A* 874,19–27 (2017).
- [20] Lu, G., R. J. Blakeslee, J. Li, D. M. Smith, et al., Lightning mapping observation of a terrestrial gamma-ray flash, *Geophys. Res. Lett.*, 37, L11806 (2010).
- [21] Gurevich, A. V., Milikh, G. M. and Roussel-Dupre´. Runaway electron mechanism of air breakdown and preconditioning during a thunderstorm. *Phys. Lett. A* 165, 463 (1992).
- [22] Babich, L. P., Donskoy, E. N., Il’kaev, R. I., Kutsyk, I. M. and Roussel-Dupre´, R. A. 2004 Fundamental parameters of a relativistic runaway electron avalanche in air. *Plasma Phys. Rep.* 30, 616–624.
- [23] Dwyer, J. R. A fundamental limit on electric fields in air. *Geophys. Res. Lett.* 30 (20), 2055 (2003).
- [24] Xu, W., S. Celestin, and V. P. Pasko, Source altitudes of terrestrial gamma-ray flashes produced by lightning leaders, *Geophys. Res. Lett.*, 39, L08801 (2012).
- [25] Xu, W., Marshall, R. A., Celestin, S., & Pasko, V. P., Modeling of X-ray images and energy spectra produced by stepping lightning leaders, *Journal of Geophysical Research: Atmospheres*, 122, 11,776–11,786 (2017).
- [26] Qie, X. S., ZHANG Y., YUAN T., et al., A review of atmospheric electricity research in China. *Adv. Atmos. Sci.*, 32(2), 169–191, doi: 10.1007/s00376-014-0003-z (2015).
- [27] Qie, X. S., T. L. Zhang, C. P. Chen, et. al., The lower positive charge center and its effect on lightning discharges on the Tibetan Plateau. *Geophys. Res. Lett.*, 32, L05814, doi: 10.1029/2004GL022162 (2005).
- [28] Nag, A., and Rakov, V., Some inferences on the role of lower positive charge region in facilitating different types of lightning, *Geophys. Res. Lett.* 36, L05815, doi: 10.1029/2008GL036783 (2009).
- [29] Liu, D. X., X. S. Qie, L. X. Pan, and L. Peng, Some characteristics of lightning activity and radiation source distribution in a squall line over north China. *Atmospheric Research*, 132–133, 423–433 (2013).
- [30] Chilingarian A., Chilingaryan S., Karapetyan T., et al., On the initiation of lightning in thunderclouds, *Sci. Rep.* 7 (2017) 1371. <http://dx.doi.org/10.1038/s41598-017-01288-0>.
- [31] Tsuchiya, H., et al., Long-duration g ray emissions from 2007 and 2008 winter thunderstorms, *J. Geophys. Res.*, 116, D09113, doi:10.1029/2010JD015161 (2011).
- [32] Chilingarian, A. and Mkrtychyan, H., Role of the Lower Positive Charge Region (LPCR) in initiation of the Thunderstorm Ground Enhancements (TGEs), *Physical Review D* 86, 072003 (2012).
- [33] Chilingarian A., Khanikyants Y., Mareev E., et al., Types of lightning discharges that abruptly terminate enhanced fluxes of energetic radiation and particles observed at ground level, *J. Geophys. Res. Atmos.*, 122, doi:10.1002/2017JD026744 (2017).

- [34] Wada, Y., Bowers, G., Enoto, T., et al., Termination of electron acceleration in thundercloud by intracloud/intercloud discharge. *Geophysical Research Letters*, 45, 5700–5707 (2018).
- [35] Chilingarian A., Hovsepyan G., Khanikyanc Y., et al., Lightning origination and thunderstorm ground enhancements terminated by the lightning flash, *EPL* 110, 49001 (2015).
- [36] Chilingarian, Hovsepyan G., Soghomonyan S., et al., Structures of the intracloud electric field supporting origin of long-lasting thunderstorm ground enhancements, *Physical review* 98, 082001(2018).
- [37] Chilingarian, A., Arakelyan, K., Avakyan, K., et al., Correlated measurements of secondary cosmic ray fluxes by the Aragats Space-Environmental Center monitors. *Nucl. Instrum. Methods Phys. Res., Sect. A* 543 (2–3), 483–496, (2005).
- [38] Chilingaryan S., Chilingarian A., V. Danielyan, et al., The Aragats data acquisition system for highly distributed particle detecting networks, *Journal of Physics: Conference Series* 119 082001, (2008).
- [39] Chilingarian A., Long lasting low energy thunderstorm ground enhancements and possible Rn-222 daughter isotopes contamination, *Physical review D* 98, 022007 (2018).
- [40] Bogomolov V.V., Iyudin A.F., Maximov I.A., et al., Detection of Rn-222 daughter radiation during long lasting thunderstorm ground enhancements on mountain Aragats, *PRD* (2019), in press.
- [41] A.Chilingarian, A.Avetisyan, G.Hovsepyan, et al., On the origin of the low-energy gamma ray flux of the Long-Lasting Thunderstorm Ground Enhancements (LL TGEs), *Proceeding of TEPA-2018 conference*, Nor-Amberd, Armenia, 2018.
- [42] Chilingarian A., Mailyan B., and Vanyan L., Recovering of the energy spectra of electrons and gamma rays coming from the thunderclouds, *Atmos. Res.* 114–115, 1 (2012).
- [43] Chilingarian A., Zazyan M., Karapetyan G., Modelling of the electron acceleration and multiplication in the electric fields emerging in terrestrial atmosphere, *Proceeding of TEPA-2018 conference*, Nor-Amberd, Armenia, 2018.
- [44] E.K. Svechnikova, N.V. Ilin and E.A. Mareev, Recovery of electrical structure of the cloud with use of ground-based measurement results, *Proceeding of TEPA-2018 conference*, Nor-Amberd, Armenia, 2018.
- [45] Chilingarian, A., Hovsepyan, G., & Mantasakanyan, E., Mount Aragats as a stable electron accelerator for atmospheric high-energy physics research. *Physical Review D: Particles and Fields*, 93(5), 052006 (2016)

## On the Origin of the Low-Energy Gamma Ray Flux of the Long-Lasting Thunderstorm Ground Enhancements (LL TGEs)

A. Chilingarian<sup>1,2,3</sup>, A. Avetisyan<sup>1</sup>, G. Hovsepyan<sup>1</sup>, T. Karapetyan<sup>1</sup>, L. Kozliner<sup>1</sup>,  
 B. Sargsyan<sup>1</sup>, M. Zazyan<sup>1</sup>

<sup>1</sup>A. Alikhanyan National Lab (Yerevan Physics Institute), Yerevan 0036, Armenia

<sup>2</sup>National Research Nuclear University MEPhI, Moscow 115409, Russia

<sup>3</sup>Space Research Institute of RAS, Moscow 117997, Russia

**Abstract:** To identify the role of the gamma radiation from Radon progenies in Long Lasting TGE flux, differential energy spectrum was measured with various spectrometers, including precise 3" x 3" NaI(Tl) spectrometer of ORTEC firm (FWHM ~ 7.7% at 0.6 MeV). Measurements demonstrate that Radon progenies radiation significantly contributes to the count rate enhancements measured in winter 2018-2019 in the energy range below 3 MeV. However, performed Monte Carlo simulations and observation of Long Lasting TGEs with plastic scintillators of various thickness and energy thresholds shown that TGEs are originated in the intracloud electric fields. Radon progenies (mostly <sup>214</sup>Bi spectral lines) contribute to count rate in the low energy domain.

### 1. INTRODUCTION

The emerging field of High Energy Atmospheric Physics (HEAP, [1]), studies processes producing high energy particles in the terrestrial atmosphere, such as thunderstorm ground enhancements (TGEs, [2,3]), terrestrial gamma-ray flashes [4] and gamma-ray glows [5,6]. Understanding these phenomena requires developing of appropriate models of the interaction of electrons, positrons, and photons with air and electric fields [7,8,9]. It is widely accepted that all 3 processes are mainly driven by electric fields, ionization, scattering and bremsstrahlung. One of underlying processes, namely Runaway Breakdown (RB, [10]), now mostly referred as Relativistic Runaway Electron Avalanche (RREA, [11,12]) is a "threshold" process controlled by the strength of the electric field. RB/RREA is responsible for the development of electron-gamma ray avalanches in the atmosphere and, consequently, for the large-scale multiplication of the particles detected on the earth surface or observed in the atmosphere by spectrometers located on balloons and aircraft. The second process, Modification of the electron energy spectra (MOS, [13, 8]) operates on much less scales however is effective for almost all strengths of atmospheric electric fields.

Although a lot of TGEs were observed in mountain-top and sea-level experiments (see references in [14]), spatial structure of electric fields and time evolution of the electron acceleration in atmosphere are poorly understood. The "electric" origin of the ionization radiation from clouds itself is sometimes put under question. Bogomolov et al., [15] argue that the significant contribution to the low energy part of TGE spectrum was originated by the Rn-222 decay chain, including daughter isotopes <sup>214</sup>Bi and <sup>214</sup>Pb, that are clearly identified in the spectrum of the background radiation. Although we demonstrate that the hypothesis of the precipitation as a source of gamma ray radiation is not valid [16], it was proposed that Rn-222 can be concentrated in the clouds above Aragats research station and radiation of its daughter isotopes can comprise low energy part of TGE [15].

However, recent measurements by Armenian and Japanese researchers [17, 18] reveal much more details about the relations of TGEs and electric fields inside the cloud. Numerous TGEs observed on Aragats are an ideal target to investigate the source of the ionization radiation from the

clouds because low altitude of thunderclouds enables us to detect both electrons, gamma rays and neutrons simultaneously [2,3] and observe each individual avalanche originated by a CR electron (seed particle) entering high electric field region [19]. The interplay of TGEs and lightning flashes (see [20], Figs 6 and 7) shows ultimate causal relation and dependence of TGEs on atmospheric electric fields.

Nonstable nuclides comprise a significant portion of the low energy gamma ray flux measured by particle detectors and spectrometers at Aragats station. Fair weather (background) gamma ray energy spectra measured on Aragats is a mixture of the continuous spectrum produced by galactic (and, sometimes, also solar) cosmic rays in interactions with the atmosphere and emission lines of several isotopes (lines are turned to distributions with finite width dependent on the spectrometer resolution). It is very difficult to see any "isotope-produced" structures in the resulting spectra of TGE with low-resolution large size spectrometers used for the 7-24 monitoring of gamma radiation on Aragats (see details of the NaI spectrometers network on Aragats in [20,21]). To prove that TGE can originate from radioactive isotopes inside cloud it is necessary to find and enumerate peaks in TGE spectrum with high-resolution spectrometers (started to operate on Aragats in December 2018).

- Analyze the background radiation spectrum measured on Aragats and in Yerevan by precise ORTEC spectrometers;
- Investigate the fluctuations of the measurements of spectral lines <sup>214</sup>Bi (0.609 MeV) and <sup>40</sup>K (1.46MeV) with the precise spectrometer located indoors and in the open air;
- Present results of Monte Carlo modeling of the MOS process, as an origin of the long lasting TGE.
- Critically examine the methodology of energy spectra recovering and possible emerging methodical errors.
- Perform analysis of the gamma ray flux enhancements observed in Winter 2018-2019 with emphasis to most pronounced spectral lines, namely <sup>214</sup>Bi (0.609, 1.12 and 1.76 MeV).

## 2. POSSIBLE SOURCES OF LOW ENERGY (BELOW 3 MEV) GAMMA RAYS REGISTERED ON THE EARTH'S SURFACE

Natural radioactivity measured on the earth's surface can be explained by following main sources:

1. Rather stable primary particle flux coming mostly from super-novae stars' explosions in our Galaxy and from numerous extragalactic sources. Neutrinos, gamma rays, and ultra-high energy nucleons can come from very distant violent explosions in the Universe (like neutron star mergers or black hole jets). CR particles incident on earth's atmosphere originate in the atmosphere extensive air showers (EAS) containing billions of electrons, muons and gamma rays. Thus, EASs sustain rather stable energy spectra of these and another species of CR specific for each geographic coordinate (sure, meteorological effects can modify the spectra in the low energy domain).
2. Transient radiation from periodically activated solar accelerators.
3. Cosmogenic nuclides that are generated by the nuclear reactions during the interaction between cosmic radiation and stable isotopes in the atmosphere (for example,  $^{14}\text{C}$  and  $^3\text{H}$ ).
4. Long-lived nonstable nuclides ( $^{238}\text{U}$ ,  $^{235}\text{U}$ ,  $^{232}\text{Th}$ ,  $^{40}\text{K}$ , etc.) that originated in the neutron star (or neutron star and black hole) mergers. The original radionuclides disintegrate to the secondary radionuclides and form the decay chains i.e., uranium-radium decay chain (starting from  $^{238}\text{U}$  to  $^{226}\text{Ra}$ ,  $^{222}\text{Rn}$ ,  $^{218}\text{Po}$ ,  $^{214}\text{Bi}$ ...), thorium decay chain (starting from  $^{232}\text{Th}$  to  $^{224}\text{Ra}$ ,  $^{222}\text{Rn}$ ,  $^{212}\text{Pb}$ ,  $^{212}\text{Bi}$ ...), actinium decay chain (starting from  $^{235}\text{U}$  to  $^{223}\text{Ra}$ ,  $^{219}\text{Rn}$ ,  $^{211}\text{Bi}$ ...), that are present in the open air. Several isotopes emit radiation in form of gamma rays (spectral lines). However, dependent on limited resolution and sizes of spectrometers these lines broadened and are seen as more or less pronounced peaks with finite width. For the measurements with large crystals, spectral lines are smoothed and the contribution from isotope decay we can notice only as a broad bump at low energies.
5. Additional radiation from the CR electrons accelerated in the emerging in atmospheric electric fields. Gamma ray emission is governed by RB/RREA and MOS processes. Both processes originate continuous spectra of gamma rays in the energy range 0.3-100 MeV.
6. Additional radiation in the 0.3-3 MeV range from nonstable nuclides occurred during TGEs; from this process, we can expect the enhanced intensity of spectral lines.

The first manifestation of TGE is a large narrow (for the detectors with high-energy threshold) or broad (for the detectors with low energy threshold) peak in the time series of count rates of measured by particle detectors (see Figs. 4, 9 of [16]). As a rule, in the same time, we observe huge storm with many lightning flashes and disturbances of the near surface electric field above detector site (see Figs 1 and 3 of [16]). In the TGE analysis procedures, we select the minutes to recover energy spectra (usually at the location of the largest peak and around, see for instance Fig. 5 in [20]). The

techniques of differential energy spectra recovering is described in the Instrumentation section of [20]. The most important in recovering TGE energy spectra is to obtain as much as possible "pure" signal without background contamination to avoid "fake" peaks. We have to use measurements of the "stable background" just before TGE and subtract it from the minutes when the peak is detected. Then, look for the significant enhancements in the intensity of spectral lines in the obtained after subtraction histogram; make calibration; enumerate peaks position and intensity, etc. These techniques should work perfect if the background (points 1-4) is stable. Unfortunately, CR radiation (point 1) cannot be accepted as stable in low energy range (below 3 MeV). The meteorological effects (atmospheric pressure and temperature gradient in the atmosphere, see [13]) can highly change the low energy particle flux. The radiation from nonstable isotopes on earth's surface (point 4) also is very variable, changing significantly on the hour-to-hour scale due to the same meteorological effects and wind when spectrometer is located outside (the case of the spectrometer used in the [15]).

Thus, proving the origin of flux enhancement in the low-energy range is a very difficult task. Usually, we should make a trade-off between statistical significance and possible biases of background spectra estimates. Due to the small size of the NaI crystal (5 x 5 x 5 cm) of the spectrometer, 50 minutes' data collection time was required to get appropriate statistical significance [15]. During another 50 minutes, before TGE was the sample of "pure" background accumulated. However, as mentioned above, due to the high variability of isotope concentration in the air, in these 2 samples the mean intensity of the background can be different leading to "fake" peaks.

Radon ( $^{222}\text{Rn}$ ) is the immediate daughter of  $^{226}\text{Ra}$  and is continuously produced wherever  $^{226}\text{Ra}$  exists.  $^{226}\text{Radium}$  is itself nearly abundant in rocks and soils and in the materials derived from them. Because it is a noble gas, radon is relatively much more free to migrate than either its parents or daughters, all of which are metals.

The half-life of the radon isotope  $^{222}\text{Rn}$  is 3.82 days thus it can be transported to the atmosphere due to diffusion mechanism. Mean concentrations of Radium can be assumed to be constant at Aragats, near research station surrounded by rocks, however, the concentration of daughter nuclides in ambient air should follow strong variations due to fast changing meteorological conditions. The ratio of maximum to minimum of the diurnal variations of the atmospheric radon measured in four countries is approximately in the range of 2-5 [22]. The concentration of  $^{222}\text{Rn}$  in surface air was measured in 1989 at Sacavem-Lisbon, Portugal. The sampling station, located at  $38^\circ 47'N$   $09^\circ 06'W$ , concentrations of Radon highly fluctuated between 1 and  $40 \text{ Bqm}^{-3}$  [23]. The average daily course of  $^{222}\text{Rn}$  concentration measured during the years 1991-1994 in Bratislava, Slovakia has waveform with a maximum between 4 and 6 a.m and with a minimum between 2 and 4 p.m. [24]. The ratio of the maximum to minimum radon equals 1.7. The variation of the indoor Radon concentration is much smaller, being maximal in the basement and decreasing at higher floors of the building. Atmospheric radon exhibits a vertical concentration profile, which normally ranges from a maximum at the air-soil interface to an unmeasurably low value in the stratosphere [22]. The vertical profiles of  $^{222}\text{Rn}$  concentration measured by aircraft flying above the west-central portion of

the continental United States demonstrate rapidly decrease of concentration with altitude (Fig. 3 in [25]).

Thus, world data on Radon concentration in the atmosphere demonstrate large variability during the day, fast decline with altitude above earth surface and with the decrease of the outside temperature.

### 3. NATURAL GAMMA RADIATION (NGR) MEASUREMENTS ON ARAGATS AND IN YEREVAN WITH HIGH-RESOLUTION SPECTROMETERS

For the investigation of hour-to-hour variations of Radon progenies and for enumerating the spectral lines we perform monitoring of the of the NGR of Rn-222 daughter chain on Aragats and in Yerevan with ORTEC firm spectrometers [26]:

- NaI(Tl), type 905-4 (ORTEC), 3" x 3" – diameter and length), 1024 channels, very high stability, MAESTRO software for spectral lines identification. Relative energy resolution (FWHM ~ 7%)
- HPGe (High-Purity Germanium Coaxial Detector System), Model GEM15P4-70 (ORTEC). Relative energy resolution (FWHH ~ 1%)

The goal of measurement was to measure the diurnal variations of the background on Aragats in the building where the NaI network is located and outdoors near the spectrometer used to obtain the data plotted in fig 2 in [15]. In Fig. 1a we show the background spectrum measured at Aragats beneath the roof of the SKL experimental hall. In Fig. 1b we show the background spectrum measured in Yerevan indoors by high-resolution HPGe spectrometer (to be transported to Aragats in Spring 2019). The overall picture of  $^{238}\text{U}$  chain isotope gamma radiation is very well expressed by the measurements made by the HPGe spectrometer. It resolved very close  $^{214}\text{Bi}$  and  $^{214}\text{Pb}$  decay spectral lines, that NaI(TL) spectrometer cannot resolve and measured as one broad peak at 0.609 MeV (the same peak as in Fig. 2 in [15]). We will use this peak, which was claimed to have maximal significance in [15] for measurements of the diurnal variations.

The recovering of spectral lines was performed according to standard procedure used in the isotope spectroscopy [27].

After measurement of the energy spectra, we choose the spectral line and outline the energy window around the peak. Then, subtract the background measurement taken just before TGE and from the corrected in this way histogram calculate the peak area as it is demonstrated in Fig. 2C. For investigation of the diurnal and daily variations of the 0.609 MeV spectral line we omit procedures shown in Fig. A and B.

In Fig. 3 we demonstrate diurnal variations of the count rates of joint  $^{214}\text{Bi}$  and  $^{214}\text{Pb}$  decay gamma rays measured by NaI(TL) spectrometer (in the energy range 0.56-0.66 KeV). By diamonds, we show the diurnal variation of NaI (Tl) spectrometer positioned under the roof of SKL experimental hall where Aragats NaI network is located. As was demonstrated in [22] the indoor Radon concentration fluctuations have a vertical negative gradient. The fluctuations of  $^{214}\text{Bi}$  are much larger for the outdoor location of the spectrometer (relative range is ~47%); for the indoor location in highest position in the building, while the concentration is much higher but also much more stable

(asterisks, the relative range is much less ~12%). Thus, the location of the NaI network on the maximal height in the building provides minimal diurnal variations. Open air location of the same spectrometer near the spectrometer used in [15] leads to much larger diurnal variations (diamonds in Fig. 3) as it is expected from world data on Radon concentration (see references in the previous section).

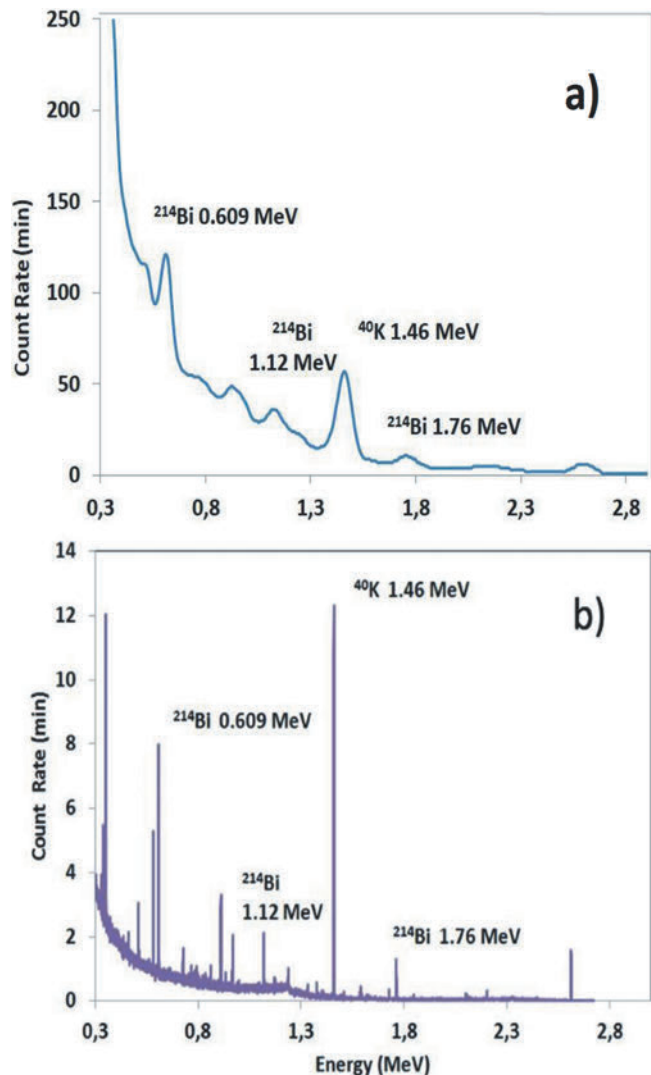


Figure 1. Indoors background gamma-ray energy spectrum measured at Aragats and in Yerevan with various spectrometers: NaI (Tl) – a) and HP Ge b).  $^{214}\text{Bi}$  spectral line (peak) will be used for the investigation of diurnal variability of Radon concentration at Aragats. We also consider Potassium  $^{40}\text{K}$  isotope as a stable spectral line used for the calibration of fast varying  $^{214}\text{Bi}$  spectral lines.

$^{40}\text{K}$ , Potassium-40 is a radioactive isotope of potassium, which has a very long half-life of  $1.25 \times 10^9$  years. It makes up 0.012% of the total amount of potassium found in nature. It decays to the gas argon-40 by electron capture with the emission of an energetic gamma ray of 1.46 MeV energy. Potassium-40 assimilated into the materials derived from rock and soil.

As we can see in Fig. 4 Potassium-40 concentration do not variate with daytime and do not depends strongly on atmospheric conditions. The fluctuations of Potassium-40 indoors and outdoors are approximately the same; the relative range is 5.8% and 3.7% correspondingly. As the 1.46 peak is always is present in the natural gamma ray energy spectrum, it can be used for the calibration purposes.

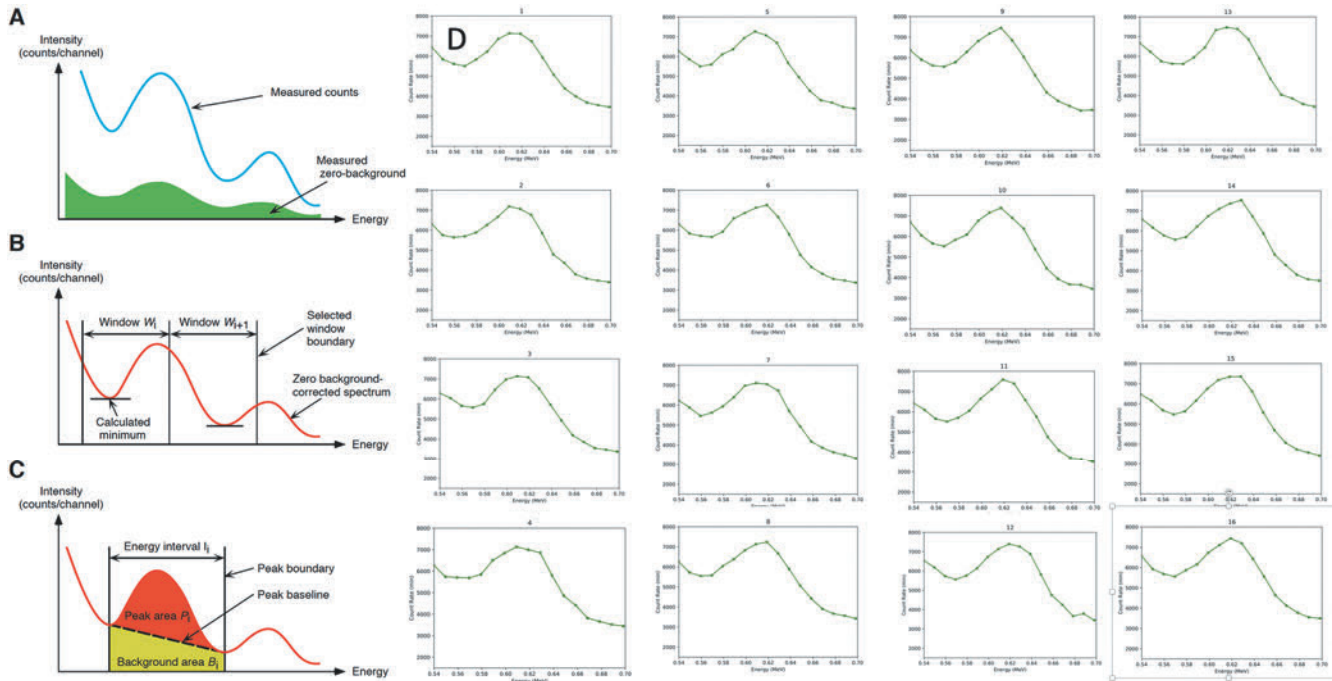


Figure 2. The cartoon of the standard procedure of the background extraction and spectral peaks area calculation (A, B, C, from [27]) and routinely numerated by the NaI (Tl) ORTEC spectrometer (D).

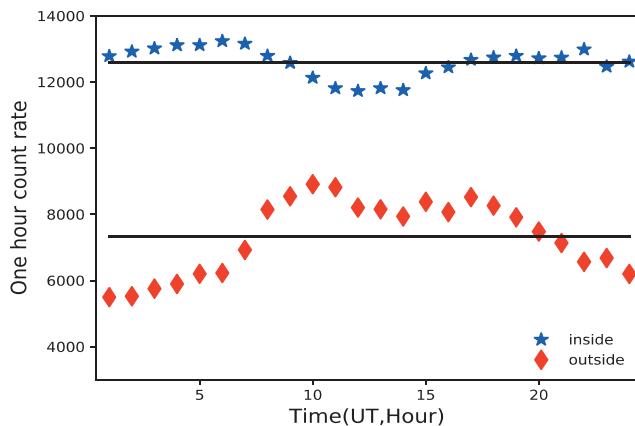


Figure 3. Diurnal variations of the intensity of the 0.609 MeV ( $^{214}\text{Bi}$ ); spectral line measured indoor and in the open air. Measurements performed in December 2018.

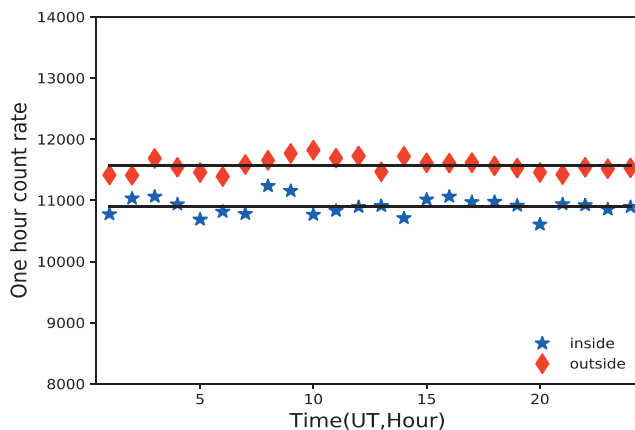


Figure 4. Diurnal variations of the intensity of the 1.46 MeV(Potassium-40); spectral line measured indoor and in the open air.

Large fluctuations of the  $^{214}\text{Bi}$  spectral line (Fig. 4) pose limitations on the possibility of physical inference on Radon origin of TGE based on the observed peak in [15]. The enhancement of the gamma ray flux registered by spectrometers (signal) started at  $t_1$  can be attributed to several physical processes, main of which are summarized in the equation one:

$$S_{t_1} = S_{AV} + S_{MOS} + S_{RN} \pm S_M \quad (1),$$

where  $S_{av}$  is an intense gamma-ray flux due to electron-ion avalanche process started in the strong atmospheric electric fields;  $S_{MOS}$  – is bremsstrahlung gamma ray flux also leased in the atmospheric electric fields of much less lengths;  $S_{RN}$  – is due to Radon daughter isotopes radiation on the clouds above the detector site, or from other yet unspecified source; and  $R_M$  – is the influence of different meteorological effects (atmospheric pressure, gradient of temperature, etc.). For identification of the possible signal from Radon progenies the statistical fluctuations can be substantial. As we demonstrate in Fig. 2 the standard technique of the spectral analysis is subtraction of the background measured separately before TGE. See equation 2, where we denote by ON the sample containing background with possible signal and by OFF “pure” background.

$$ON = S_{t_1} + B_{t_1}; OFF = B_{t_2} \quad (2).$$

However, as we can see in equation 3 by subtracting OFF sample from ON sample we do not obtain “pure” signal. For collecting enough events the time span  $\Delta t$  started at  $t_1$  and  $t_2$  is rather large (50 minutes to obtain Fig. 2 in [15]), and due to large fluctuations of the count rate measured by the gamma spectrometer located on open air (see Fig. 3b)  $B_{t_1} \neq B_{t_2}$ , see Eq. 3.

$$ON - OFF = S_{t_1} + B_{t_1} - B_{t_2} \neq S_{t_1} \quad (3).$$

Due to hourly fluctuations of the Radon concentration in the atmosphere we can obtain a “fake” signal of ~5-10% only because of difference in background samples measured at  $T_1 + \Delta t$  and  $T_2 + \Delta t$  time spans. The fluctuations of the count rate measured by the spectrometer used in [15] are large and  $^{214}\text{Bi}$  peaks are not well pronounced because of the small size of NaI(Tl) crystal used in their spectrometer. The NaI crystal is very sensitive to the temperature and responds nonlinearly on solar heating. Therefore, the energy spectra of gamma rays should be measured indoors on the highest floor of the building where Radon concentration is minimal. The NaI

network used for recovering energy spectrum is located indoors where fluctuations of background are minimal (see Fig. 3); due to large size of the NaI crystal background sample is collected during just few minutes before the event and large fluctuations are not probable; usually during TGE we register large energies of gamma rays far beyond ones possible from any radioactive decay. Additionally, to prove “electric” origin of TGE we perform a cycle of simulation experiments, described in the next section.

#### 4. MODELING OF THE RB/RREA AND MOS PROCESSES IN THE ATMOSPHERE TO REVEAL FEATURES OF THE GAMMA PHOTONS SPECTRUM MEASURED ON THE EARTH’S SURFACE

The atmospheric gamma-ray energy spectrum initiated by Extensive air showers (EAS) from usually is presented within a model based on a power-law continuum (index of -1.16 in the few MeV energy range, [28]). Gamma ray flux measurements clearly reveal the 511 keV line due to the annihilation of positrons produced in extensive air showers (EAS). After our observation of Long Lasting TGEs (LL TGEs, [17]) – hours extending flux of gamma rays observed at Aragats, we started a cycle of simulations to find out how the electric field of different strength and elongation can modify gamma ray spectrum in the atmosphere. The main goal of Monte Carlo simulations was to get answer if the MOS process [14] can provide such a long duration of gamma ray flux, or remote Extensive Cloud Showers (ECSs) can contribute to this flux, or we should consider another origin of gamma rays, say, Radon progenies gamma radiation (or all processes have a part in the additional particle flux). Thus, our simulations are always pairing with observations and with hypothesis testing.

For a new series of simulations, we use the CORSIKA package, see details of used options of CORSIKA code in [29]. From the consideration of the ~500 TGE events in the last decade, we conclude that far not all TGEs are due to the intense RB/RREA process, for instance, winter TGEs were not accompanied with thunderstorms and large disturbances of the near-surface electric field. To investigate the “small fields” effect typical for the winter TGEs, we use in simulations rather low values of the atmospheric electric fields strengths starting from 0.1 MeV/cm. The overall scheme of the simulations is presented in Fig. 5.

Each simulation set consists of  $10^6$  showers originated from vertically traversing CR electrons with energies in the interval  $1\div 300$  MeV. The differential energy spectrum of electrons follows the power law with spectral index  $\gamma = -1.21$ . Avalanche particles were followed till the Earth’s surface ( $H_{\text{obs}} = 3200$  m a.s.l.) or till their energy become less than  $E_{\text{cut}}=0.05$  MeV. Electric field  $E_z > 0$  was introduced in a kilometer above the “cloud base”  $H$ , that was changed from 50 to 1000 m.

As we can see in Fig. 5 two fields are supporting electron acceleration downwards: the field between the main negative layer and its mirror on the earth and field between the same negative layer and small positively charged layer in the bottom of the cloud. Sure, it is a highly simplified structure, however, the most intense TGEs happened when both fields are in play and their superposition exceeds the avalanche initiating threshold. In the simulation, we make no difference between these fields, assuming the existence of constant field a kilometer length with fixed prechosen strength. Both such a field elongation and strength were routinely measured in balloon flights [30,31].

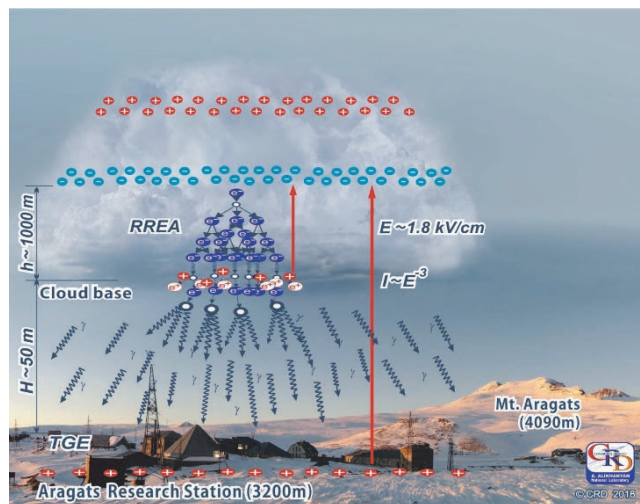


Figure 5. The scheme of electron acceleration modeling in the atmosphere.

In Tab. 1 we enumerate the gamma ray flux enhancement in the electric fields of the different strength. After reaching RB/RREA threshold the number of particles exponentially rose in the electron – gamma ray avalanches. However, even for the small electric field we have a significant enhancement that can be reliably registered by the spectrometers and counters located on Aragats.

Table 1. The number and relative enhancement of secondary photons reaching earth’s surface after traversing the electric field of 1 km located 50 m above Aragats research station (3200 m a.s.l.)

$E_z$ (kV/cm)	$N(E_z)$	$(N(E_z)-N(0))/N(0)$ (%)
0.	370647	0
0.1	387271	4.5
0.2	405065	9.3
0.3	425962	14.9
0.9	626225	69.0
1.7	1879136	407.0
2.0	9052389	2342.3

In Tab. 2 we post the particle flux enhancement (comparing with fair weather values) in different energy intervals. We see that most of the enhancement occurred at low energies (0.3 -2 MeV).

Table 2 Enhancement  $(N(E_z)-N(0))/N(0)$  (%) of secondary photons in different energy intervals.

$E_z$ (kV/cm)	0.3 - 2 MeV %	50 – 60 MeV %	70 – 80 MeV %
0.1	5.6	5.7	3.7
0.2	11.3	7.4	3.7
0.3	17.7	11.8	4.7
0.9	82.9	37.1	32.1
1.7	547.4	109.7	94.1
2.0	3412.3	157.3	133.9

In Tab. 3 and Fig. 6 we demonstrate the influence of electric field height on the number of additional gamma rays reaching the earth's surface. We can see that when distance of the electric field from particle detectors increases from 50 m to 200 number of additional gamma rays decreases 2 times, and – to 1000m – 3 times.

Table 3. Number of gamma rays reaching earth's surface from different heights above.

	H=0m	H=50m	H=200m	H=500m	H=1000m
$N_\gamma$	1106968	581764	466073	313161	185241

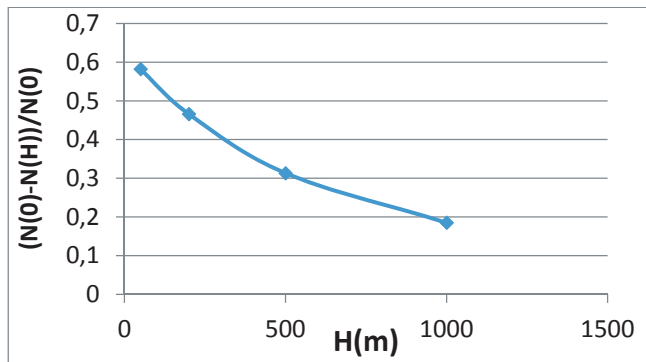


Figure 6. The percentage of gamma rays reaching the earth's surface after escaping from electric field at different heights (related to the case when the electric field is prolonged until earth surface).  $E_z=0.8kV/cm$  with elongation of 1 km.

Thus, Monte Carlo simulations demonstrate that even very small intracloud electric fields can lead to sizable enhancements in gamma photons flux in the energy range of 0.3 – 3 MeV. We assume that the electric fields in the atmosphere do not decline abruptly after cessation of the severe storm and for many tens of minutes can supply the cosmic ray electrons with additional energy that lead to the enhanced probability of radiating bremsstrahlung gamma rays.

##### 5. WINTER ENHANCEMENTS OF GAMMA RAY FLUX (“WINTER TGES”)

The winter is very severe on Aragats; the temperature at Aragats usually reach  $-20\text{ }^\circ\text{C}$  and stay deep in the negative domain till May. There is a strong positive correlation between temperature and Radon emanation: at negative temperatures Radon concentration is highly decreased [32]. The thickness of snow covering Aragats usually reaches and exceed 1.5 m. that also may affect the  $^{222}\text{Rn}$  concentration [33]. Thus, the Radon emanation in the atmosphere is suppressed in winter. On the other hand, during snow storms in presence of strong winds, radon can easily diffuse and reach particle detectors. Electric fields in Winter are very weak, there are no lightning flashes, large disturbances of near-surface electric field and bursts of high-energy particles (gamma rays and electrons with energies up to 50 MeV). Thus, we do not observe any large enhancements in winters. However, after precise scanning of the count rate monitoring results, we outline 4 events with particle flux enhancements in the NaI network. The detector network used to measure the particle energy spectra consists of 6 NaI crystal scintillators with sensitive area  $\sim 0.0330\text{ m}^2$  each ( $\sim 5$  times than ORTEC NaI). The energy resolution of spectrometers is 30-40% at 662 KeV, thus we cannot resolve  $^{222}\text{Rn}$  progenies spectral lines with these crystals. The big

advantage of used large NaI crystals is the possibility to measure high-energy particles. Large count rate allows reliably measure rather week flux of high-energy electrons and gamma rays in the energy range above 10 MeV. In Fig. 7 we present one-minute time series of four “Winters TGES” observed by NaI (TI) network. In December OTEC spectrometer was located under the roof of SKL experimental hall nearby the NaI network (Fig 7c and 7d), i.e. the  $^{214}\text{Bi}$  isotope daily variations were minimal. In January ORTEC spectrometer was moved outdoor (Fig 7a and 7b) near the spectrometer used in [15]. For outdoor location, the variation of the  $^{214}\text{Bi}$  isotope concentration is significantly larger, see Fig. 3 (diamonds). NaI network, as well as, ORTEC spectrometer operates in 2 modes: measuring energy release histograms and, also, one-minute time series of count rates. Particle flux enhancement is apparently seen in all 4 events shown in Fig. 7.

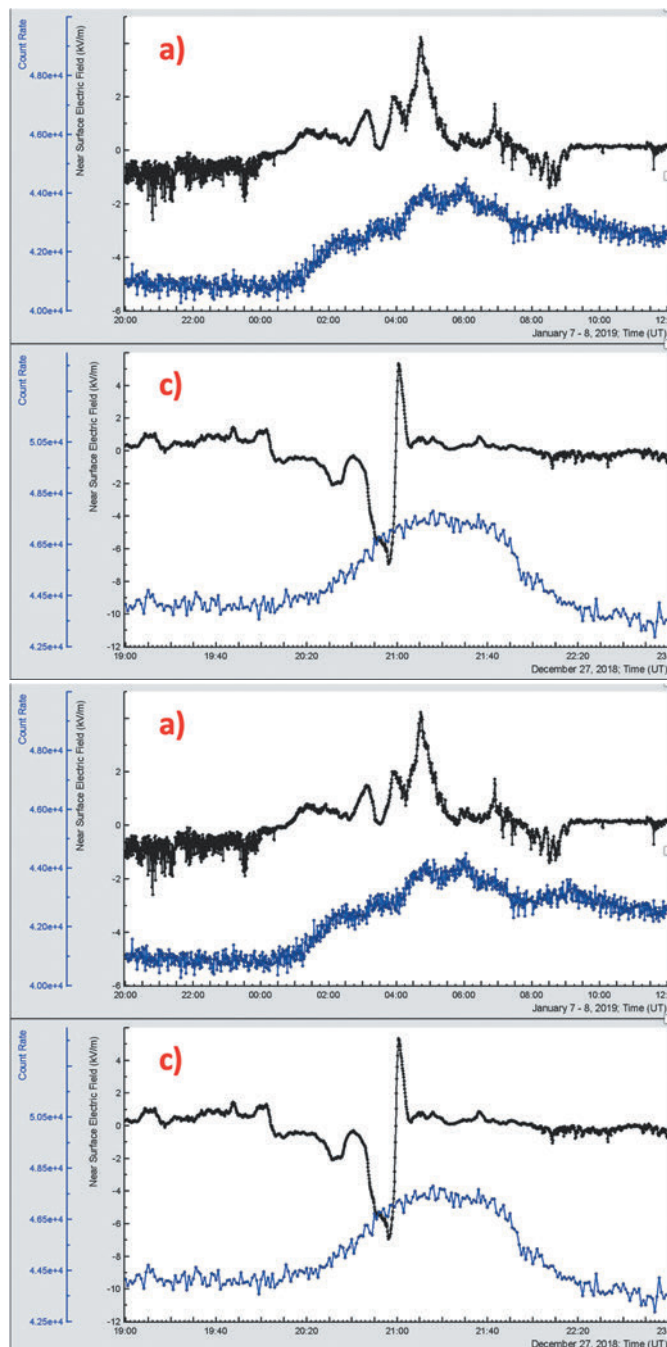


Figure 7. Winter TGE. On the top (black curves), we show disturbances of the near-surface electric field, below (blue curves) – 1-minute time-series of count rates of particle flux measured by first NaI crystal located under the roof of the SKL experimental hall on Aragats.

In Fig. 8 we demonstrate the procedure of obtaining “pure” signal and demonstrate energy spectra for all four events. Subtracting background sample, we obtain an estimate of “pure” signal used for the recovering differential energy spectra with superimposed spectral lines originated from natural isotope gamma decay. The times of background (BT1) sampling and signal + background sampling (BT2+S) were 50 minutes. The resulting signals obtained by

subtracting background from the signal + background are shown in the bottom of frames a-d of fig. 8. Obtained in a such way, peak corresponding to 0.609 KeV spectral line is seen in all 4 events. For the outdoor location of spectrometer (January events) the 0,609 MeV peak is better pronounced and the peaks corresponding to the 1.12 and 1,76 MeV also can be outlined.

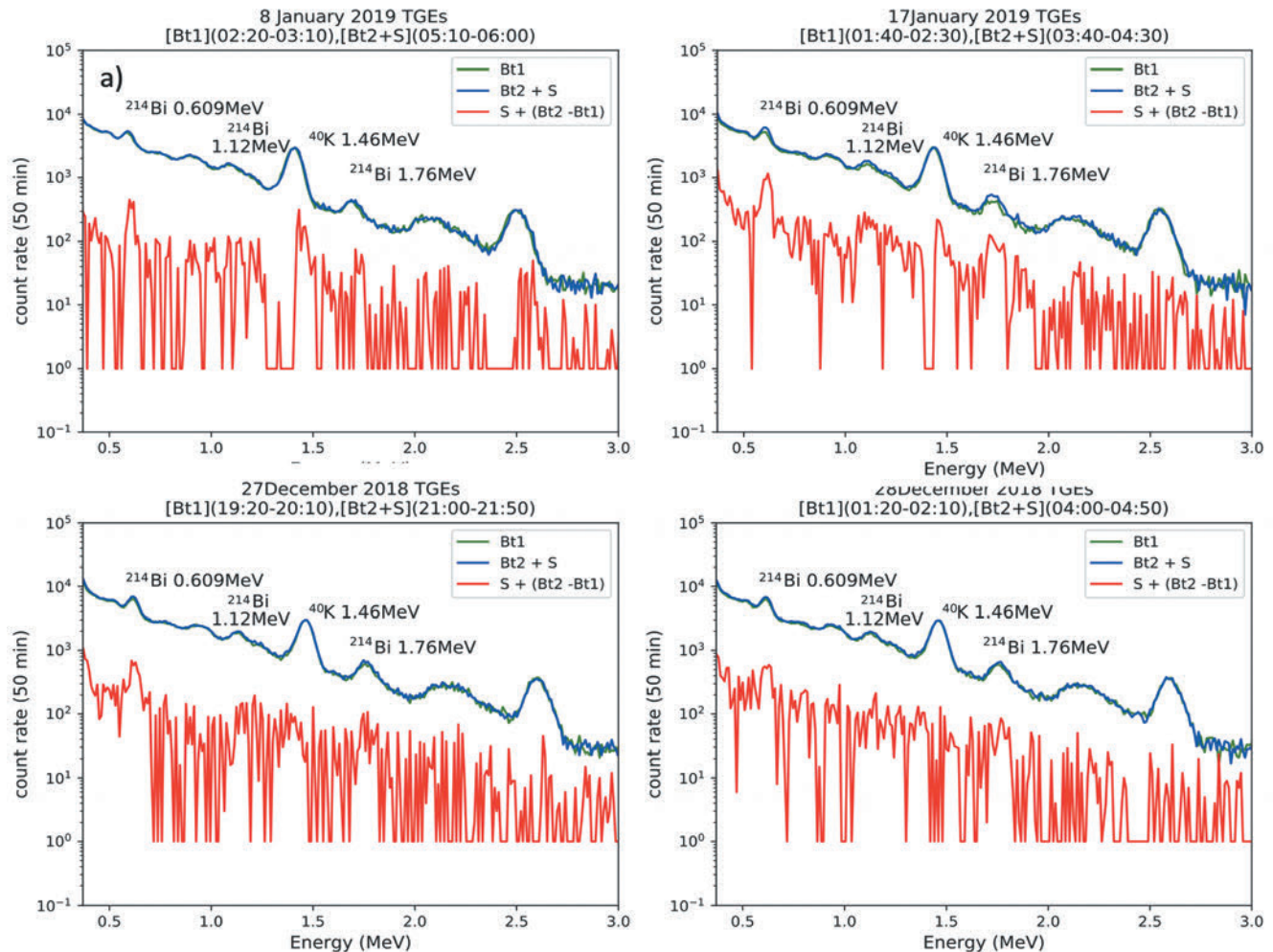


Figure 8. Differential energy spectra of the winter TGEs measured in open air (a, b) and in SKL experimental hall.

The continuum spectrum from cosmic rays is obscured by Compton scattered gamma rays escaping from the NaI crystal forming another continuum spectrum to the left of the peaks corresponding to the spectral lines. There are no peaks corresponding to the stable  $^{40}\text{K}$  line in December events (inside spectrometer location, 8c and 8d), for the outside location of spectrometer (8a and 8b) a negative/positive profile of the  $^{40}\text{K}$  line is detected. We connect this difference with high diurnal fluctuations of the isotope radiation in the open air leading to the small random shifts in the bin-to-bin population. For energies above 1,76 MeV no spectral peaks for all 4 winter TGE events are seen. Thus, the measurements performed with ORTEC spectrometer demonstrate that Radon progenies radiation overwhelmingly contributes to the “Winter TGE” events. A more detailed analysis of the  $^{222}\text{Rn}$  progenies contribution, as well as the contribution of the Compton scattered gamma ray’s spectral lines will be made after experiments with high precision HP Ge spectrometer on Aragats planned in May 2019. In the next section, we will show that particles that form TGEs have energies well above the energetic domain where isotope decays can contribute to TGE count rate, thus the origin of TGEs is connected with electron acceleration in the

intracloud electric fields and not with gamma radiation from  $^{222}\text{Rn}$  progenies.

## 6. LONG LASTING TGES MEASURED BY THE PLASTIC SCINTILLATORS

The particle flux monitoring on Aragats was performed by more than 200 detectors. Thus, we have the possibility to use several independent operated detectors to crosscheck the flux enhancements. The first long lasting TGEs observed on Aragats with 3-cm thick and 1 m<sup>2</sup> area plastic scintillator in 2015 were reported in [34], see Figs 7, 9, 10. We estimate energies of gamma rays responsible for the long-lasting enhancement with the notion of the “effective energy threshold” for gamma ray measurements introduced in [21]. According to this method the energy threshold of 3-cm thick plastic scintillator is  $\sim 3\text{MeV}$  (see Fig 10 of [21]). The contamination to TGE of Radon progenies decay gamma rays as we demonstrate in the previous section is essential for energies below 3 MeV. Thus, the TGE observed by the 3-cm thick plastics can originate from intracloud electric fields only (MOS process). To confirm this observation, we present in Fig. 9 the same TGE measured by other scintillators: the 1 cm thick scintillator of the CUBE array

(effective energy threshold  $\sim 1$  MeV) and by 25 scintillators of GAMMA surface array, 5-cm thick and  $1\text{ m}^2$  area each (effective energy threshold  $\sim 5$  MeV). The TGE presented in Fig. 9 well coincide with TGE published in 2016 and the enhancement of the count rate is proportional to the effective energy threshold.

In Figs. 10 and 11 we present another TGEs measured by plastic scintillators along with disturbances of the near-surface electric field obtained by the EFM-100 electric mills of the BOLTEK company. In both upper pictures 10a and 11a we see that both TGEs are directly related to the large disturbances of the electric field. In Figs. 10b and 11b we demonstrate the TGE as measured by the NaI crystals and by plastic scintillators. The shapes of all curves measured by detectors with different energy thresholds are very similar, thus, we can conclude that the physical mechanism responsible for the TGE initiation is one and the same. And as the energy threshold of plastic scintillators (middle scintillator of STAND1, the lower curve in Fig. 10b and middle scintillator of STAND3, the lower curve in Fig. 11b) is above 3 MeV we can confirm the “electric” origin of the shown TGEs. In Figs 10 and 11 we can also see that enhancement of count rate starts simultaneously with disturbances of the electric field. For the TGE measured on May 30 (Fig. 11) abrupt rise in NaI crystal count rate coincides with the sharp decrease of electric field and occurrence of high-energy particles in the TGE.

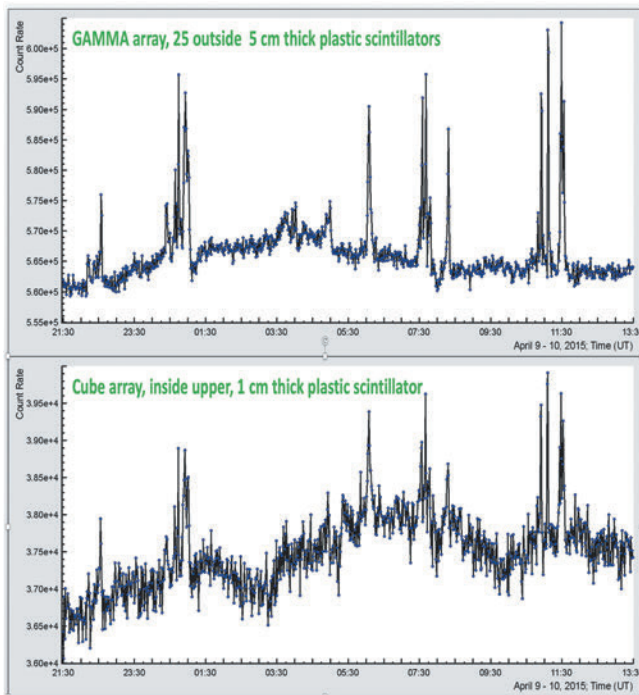


Figure 9. The TGE measured by the 1-cm thick and  $1\text{ m}^2$  area plastic scintillator (upper of indoor CUBE detector) and by the 5-cm thick and  $25\text{ m}^2$  area plastic scintillators of GAMMA experiment.

In Fig 12 we demonstrate the 3-minute time series of the maximal energies measured during the particle flux enhancement on 17 January, 2019 and during TGE occurred on March 4, 2016. In previous section, we explain 17 January event by the  $^{222}\text{Rn}$  progenies gamma radiation and in Fig. 12a we can see that the maximal energy of the spectra measured each 3 minute are beyond 3 MeV. On the other hand, the analogical time series of the TGE measured on 30 May 2018 demonstrate that many of the maximal energies are well above the 3 MeV, reaching 30 MeV during short high-energy particle burst originated by the electron-gamma ray avalanche in the thundercloud above detectors.

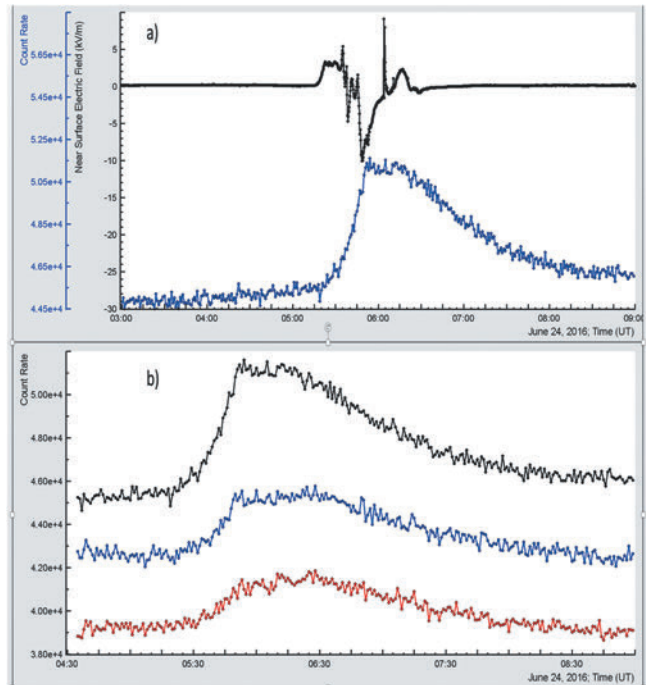


Figure 10. The disturbances of the electric field and count rate measured by the large crystal of NaI network (a); Comparison of the count rate time series measured by the same crystal and two 1 cm thick and  $1\text{ m}^2$  area vertically stacked plastic scintillators of the STAND1 detector located outdoors nearby MAKET experimental hall (b).

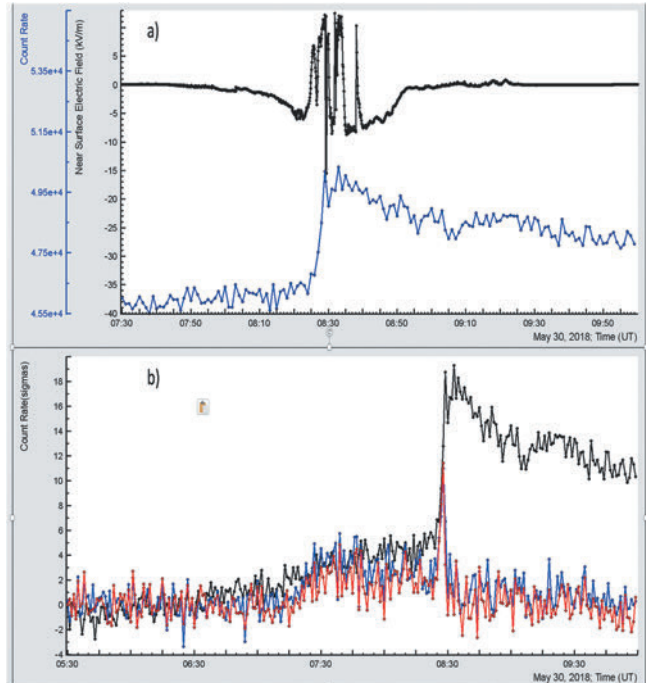


Figure 11 The disturbances of electric field and count rate measured by the large crystal of NaI network (a). One-minute count rates of the same NaI crystal and count rates of the upper and middle of vertically stacked scintillators of the STNAD3 detector located indoors in the SKL experimental hall (b). The count rate in the frame b) is shown in the number of standard deviations from the mean count rate measured before TGE to fit in one picture time series of 2 detectors that are significantly different in the count rates.

Thus, the electric nature of TGEs can be derived from the observations with plastic scintillators of various thickness and different energy thresholds, as well as, by observing energy spectra prolonged far beyond 3 MeV. The particle flux enhancement in presented TGE events can be explained by the electron acceleration in the electric field in the atmosphere above particle detectors. The Radon progenies contribute to the particle flux enhancements in 0.3 – 3 MeV energetic domain only.

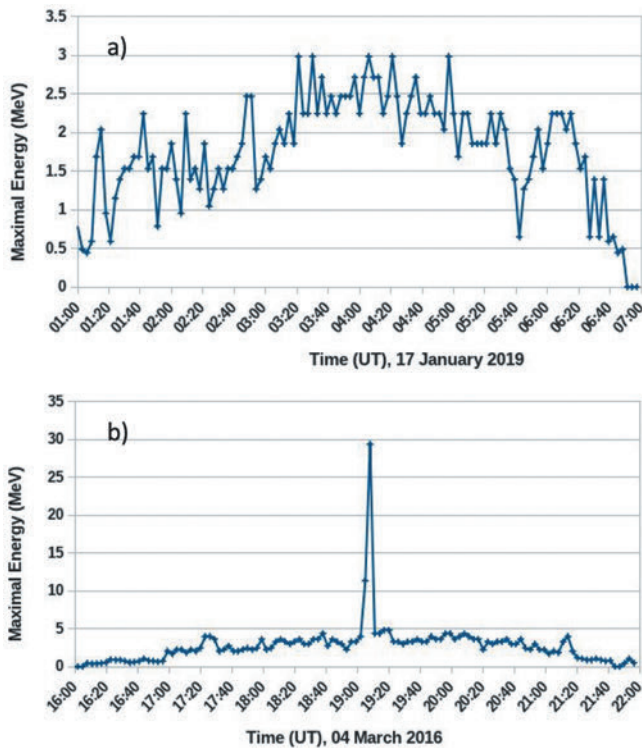


Figure 12. Differential energy spectra of recovered for several minutes of the strongest winter TGE occurred on January 17, 2019.

## CONCLUSIONS

In the December and January months of 2018/2019 winter we performed monitoring of the particle count rate with precise  $3'' \times 3''$  NaI(Tl) spectrometer of ORTEC firm (FWHM  $\sim 7.7\%$  at 0.6 MeV) and operated on Aragats recent years NaI crystals network. All spectrometers recorded prolonged periods of gamma ray enhancements. Two locations of ORTEC spectrometer were included in data analysis: under the roof of SKL experimental hall where Aragats NaI network is located and on open air nearby the spectrometer used in [15].

*The analysis of the four “Winters TGEs” allows confirming the overwhelming contribution of the gamma radiation from Radon progenies to the TGE count rate in the energy range below 3 MeV in the winter time.*

This result should be confirmed by observation of much more intense spring TGEs incorporating also precise HP Ge spectrometer. Comparing spectra measured by NaI and Ge spectrometers will allow estimating the portion of Compton scattered gamma rays forming continuous spectra on the left of the isotope gamma radiation lines.

By measurements with plastic scintillators and by performing Monte Carlo simulations we confirm “electric” nature of the long lasting TGEs. TGEs observed by the plastic scintillators demonstrate that the extended enhancements of the particle flux are related to the energies above the 3 MeV, where Radon progenies cannot contribute to the TGE counts.

CORSIKA code was used to investigate the “small fields” effect on particle detector count rates. We show that even for not very large values of the atmospheric electric fields strengths modification of the cosmic ray electron energy spectra (MOS process, [8]) lead to bremsstrahlung radiation sustaining additional gamma ray flux.

Each TGE observed on Aragats is accompanied with disturbances of the near-surface electric field and, in turn, each disturbance of electric field has its roots in the enhanced concentration of hydrometeors above the station. Modeling

with the WRF code, proves the existence of charged layers above the station simultaneously with TGE detection [35]. Thus, the electrical origin of TGE is supported by theory, modeling and observations of particle fluxes, electric fields, atmospheric discharges and hydrometeor concentrations (microphysics).

## ACKNOWLEDGMENTS

The data for this paper are available via the multivariate visualization software ADEI on the web page of the Cosmic Ray Division (CRD) of the Yerevan Physics Institute, <http://adei.crd.yerphi.am/adei>. We thank the staff of the Aragats Space Environmental Center for installing and maintenance of the Na (Tl) spectrometer of ORTEC firm and staff of Isotope Research Department for performing measurements with HP Ge spectrometer. We are thankful to Pokhsranyan David for the modernization of spectrometer software. Authors thank Ekaterina Svechnikova for modelling with WRF code density of hydrometeors above Aragats. We appreciate the support of the Russian Science Foundation Grant (Project No. 17-12-01439).

## REFERENCES

- [1] J. R. Dwyer, D. M. Smith, and S. A. Cummer, High-Energy Atmospheric Physics: Terrestrial Gamma-Ray Flashes and Related Phenomena, *Space Science Review*, 173, 133 (2012).
- [2] A. Chilingarian, A. Daryan, K. Arakelyan, et al., Ground-based observations of thunderstorm-correlated fluxes of high-energy electrons, gamma rays, and neutrons, *Phys. Rev. D* 82, 043009 (2010).
- [3] A. Chilingarian, G. Hovsepyan, and A. Hovhannisyan, Particle bursts from thunderclouds: Natural particle accelerators above our heads, *Phys. Rev. D* 83, 062001 (2011).
- [4] G. J. Fishman, P.N. Bhat, R. Mallozzi, et. al., Discovery of Intense Gamma-Ray Flashes of Atmospheric Origin, *Science*, 264, 1313 (1994).
- [5] M. McCarthy and G. Parks, Further observations of X-rays inside thunderstorms, *Geophysical Research Letters*, 12, 393 (1985).
- [6] N.A. Kelley, D.M. Smith, J.R. Dwyer, et al., Relativistic electron avalanches as a thunderstorm discharge competing with lightning, *Nature communications*, 6 (2015).
- [7] J.R. Dwyer, A fundamental limit on electric fields in air, *Geophys. Res. Lett.* 30, 2055 (2003).
- [8] A. Chilingarian, B. Mailyan, and L. Vanyan, Recovering of the energy spectra of electrons and gamma rays coming from the thunderclouds, *Atmos. Res.* 114–115, 1 (2012).
- [9] D. Sarria, C. Rutjes, G. Diniz, et al., Evaluation of Monte Carlo tools for high-energy atmospheric physics II: relativistic runaway electron avalanches, *Geoscientific Model Development, Geosci. Model Dev.*, 11, 4515 (2018).
- [10] A. V. Gurevich, G. M. Milikh, and R. A. Roussel-Dupre, Runaway electron mechanism of air breakdown and preconditioning during a thunderstorm. *Phys. Lett.* 165A, 463 (1992).
- [11] J.R. Dwyer, Relativistic breakdown in planetary atmospheres, *Physics of Plasmas*, 14, 042901 (2007).

- [12] L.P. Babich, E.N. Donskoy, I.M. Kutsyk, et al., *IEEE Trans. Plasma Sci.*, 29(3), 430 (2001).
- [13] L.I. Dorman, I.V. Dorman, Possible influence of cosmic rays on climate through thunderstorm clouds. *Adv. Space Res.* 35, 476 (2005).
- [14] A. Chilingarian, Thunderstorm ground enhancements – model and relation to lightning flashes, *J. Atmos. Solar-Terr. Phys.* 107, 68 (2014).
- [15] V.V. Bogomolov, A.F. Iyudin, I.A. Maximov, et al., Detection of Rn-222 daughter radiation during long lasting thunderstorm ground enhancements on mountain Aragats, *PRD* (2019) in press.
- [16] A. Chilingarian, Long lasting low energy thunderstorm ground enhancements and possible Rn<sup>-222</sup> daughter isotopes contamination, *Physical review D* 98, 022007 (2018).
- [17] A. Chilingarian, G. Hovsepyan, S. Soghomonyan, et al., Structures of the intracloud electric field supporting origin of long-lasting thunderstorm ground enhancements, *Physical review* 98, 082001(2018).
- [18] T. Enoto, Y. Wada, Y. Furuta et al., Photonuclear reactions triggered by lightning discharge, *Nature (London)* 551, 481(2017).
- [19] A. Chilingarian, G. Hovsepyan, and B. Mailyan, In situ measurements of the runaway breakdown (RB) on Aragats mountain, *Nucl. Instrum. Methods Phys. Res., Sect. A* 874, 19 (2017).
- [20] A. Chilingarian, Energetic radiation from thunderclouds: extended particle fluxes directed to Earth's surface, *Rendiconti Lincei. Scienze Fisiche e Naturali*, doi.org/10.1007/s12210-018-0755-y (2019).
- [21] A. Chilingarian, S. Chilingaryan, G.Hovsepyan, Calibration of particle detectors for secondary cosmic rays using gamma-ray beams from thunderclouds, *Astroparticle Physics* 69, 37 (2015).
- [22] T. Gesell, Background atmospheric <sup>222</sup>Rn, concentrations outdoors and indoors: a review, *Health Physics* Vol. 45, No. 2 (August), pp. 289 (1983).
- [23] F. Corvalno, Origins and concentrations of <sup>222</sup>Rn, <sup>210</sup>Pb, <sup>210</sup>Bi and <sup>210</sup>Po in the surface air at Lisbon, Portugal, at the Atlantic edge of the European continental Landmass. *Atmospheric Environment* 29, 1809 (1995).
- [24] I. Sýkora, M. Jeřkovský, R. Janík, et. al., Low-level single and coincidence gamma-ray spectrometry; *Journal of Radioanalytical and Nuclear Chemistry*, 276, 779 (2008).
- [25] H.E. Moore, S.E. Pet, E.A. Martell, <sup>222</sup>Rn, <sup>210</sup>Bi, and <sup>210</sup>Po, <sup>214</sup>Bi Profiles and Aerosol Residence Times versus Altitude, *JGR* 78, 7065 (1973).
- [26] I. Hossain, N. Sharip and K.K. Viswanathan, Efficiency and resolution of HPGe and NaI(Tl) detectors using gamma-ray spectroscopy, *Scientific Research and Essays* 7(1), 86 (2012).
- [27] P. Blum, *Physical properties handbook: a guide to the shipboard measurement of physical properties of deep-sea cores*, College Station, Texas, USA, <http://www-odp.tamu.edu> (1997).
- [28] J.R. Letaw, G.H. Share R.L. Kinzer et al., Satellite observation of atmospheric nuclear gamma radiation, *J Geophys Res.*, 94(A2), 1211 (1989).
- [29] A. Chilingarian, J. Knapp and M. Zazyan, Atmospheric Monitoring for High Energy Astroparticle Detectors (AtmoHEAD-2018), *EPJ Web Conf.*, v. 197 (2019).
- [30] T.C. Marshall, M. Stolzenburg, C.R.Maggio et. al., Observed electric fields associated with lightning initiation, *Geophys. Res. Let.*, L03813, (2005).
- [31] T.C. Marshall, M. Stolzenburg, P.R. Krehbiel et. al., Electrical evolution during the decay stage of New Mexico thunderstorms, *JGR* 114, D02209 (2009).
- [32] D.E. Tchorz-Trzeciakiewicz and A.T. Solecki, Seasonal variation of radon concentrations in atmospheric air in the Nowa Ruda area (Sudety Mountains) of southwest Poland, *Geochemical Journal*, 45, 455 (2011).
- [33] R. Fujiyoshi, H. Morimoto and S. Sawamura, Investigation of the soil radon variation during the winter months in Sapporo, Japan. *Chemosphere*, 47, 369 (2002).
- [34] A. Chilingarian, G. Hovsepyan, L.Kozliner, Extensive Air Showers, Lightning, and Thunderstorm Ground Enhancements, *Astroparticle Physics* 82, 21 (2016).
- [35] E.K. Svechnikova, N.V. Ilin and E.A. Mareev, Recovery of electrical structure of the cloud with use of ground-based measurement results, *Proceeding of TEPA-2018 conference*, Nor-Amberd, Armenia, 2018.

## Structures of the intracloud electric field supporting origin of long-lasting thunderstorm ground enhancements

A. Chilingarian,<sup>1,2,3</sup> G. Hovsepyan,<sup>1</sup> S. Soghomonyan,<sup>1</sup> M. Zazyan,<sup>1</sup> and M. Zelenyy<sup>3,4</sup>

<sup>1</sup>*A. Alikhanyan National Lab (Yerevan Physics Institute), Yerevan 0036, Armenia*

<sup>2</sup>*National Research Nuclear University MEPhI, Moscow 115409, Russia*

<sup>3</sup>*Space Research Institute of RAS, Moscow 117997, Russia*

<sup>4</sup>*Institute of Nuclear Research of RAS, Moscow 117312, Russia*

 (Received 15 August 2018; published 3 October 2018)

The problem of thundercloud electrification is one of the most difficult ones in atmospheric physics. The structure of electric fields in clouds escapes from the detailed *in situ* measurements; few balloon flights reveal these rather complicated structures. To gain insight into the problem of the charge structure of a thundercloud, we use new key evidence—the fluxes of particles from a thundercloud, the so-called thunderstorm ground enhancements—TGEs. TGEs originate from electron acceleration and multiplication processes in the strong electric fields in the thundercloud, and the intensity and energy spectra of electrons and gamma rays as observed on the Earth’s surface are directly connected with the atmospheric electric field. Discovery of long-lasting TGEs poses new challenges for revealing structures in the thundercloud responsible for hours-extending gamma ray fluxes. In the presented paper, we demonstrate that experimentally measured intensities and energy spectra of the “thundercloud particles” give clues for understanding charge structures embedded in the atmosphere. A rather short “runaway” process above the detector site, which is consistent with the tripole structure of the cloud electrification, is changing to a much less energetic emission that lasts for hours. Measurements of enhanced particle fluxes are accompanied by the simulation experiments with CORSIKA and GEANT4 codes.

DOI: [10.1103/PhysRevD.98.082001](https://doi.org/10.1103/PhysRevD.98.082001)

### I. INTRODUCTION

One of the main problems of the atmospheric electricity is the study of the spatial-temporal structure of the electric field in the thunderclouds. Precise measurement of the electric potential within thunderclouds is extremely difficult because of the time variability and the need to make spatially separated simultaneous measurements within the highest field regions of the storm [1]. The charge structure of a thundercloud can be viewed as a vertical tripole consisting of three charge regions. The main positive charge region is located at the top, the main negative in the middle, and an additional positive below the main negative [2]. Reference [3] observed a tripole charge structure, with a large lower positively charged region (LPCR) in the thunderclouds over the Tibetan plateau of China, and noticed that the large LPCR prevents negative cloud-to-ground (CG) flashes from occurring and, instead, facilitates inverted-polarity intracloud (IC) flashes. Different lightning scenarios that may arise depending upon the magnitude of the LPCR have been examined in [4]. Reference [5] examined different patterns of the near-surface electric field occurring during the thunderstorm ground enhancements (TGEs, [6,7]). A hypothesis that electrons of the ambient population of cosmic rays are accelerated and multiplied in the bottom dipole formed by

the main negative charge layer and the LPCR was proposed. Reference [8] also considered the electric field of the same direction formed by the main negative charge in the cloud and its mirror image on the ground.

The possibility that the intracloud electric field could be evaluated by ground-based measurements of the gamma ray and electron spectra was considered in [9]. However, there were only a few cases when electron energy spectra were measured at the ground level [10] due to fast attenuation of the electron flux in the air. Nonetheless, measured gamma ray spectra are in good agreement with the RREA model [11,12].

The relation of particle fluxes and lightning flashes also provides valuable information on the cloud electrification. During the TGE, lightning flashes are suppressed, and, when this happens, they usually abruptly terminate the high-energy particle flux [13,14]. Simultaneous detection of the particle fluxes and atmospheric discharges with microsecond time resolution on Aragats enables us to associate the lightning types abruptly terminated particle fluxes with the electric structure within thundercloud [8].

However, the TGE-electric field relation is still far from fully understood, and the study of various charge structures that can initiate the TGEs should be accompanied by Monte Carlo simulation of the passage of particles through the region of the assumed intracloud electric fields.

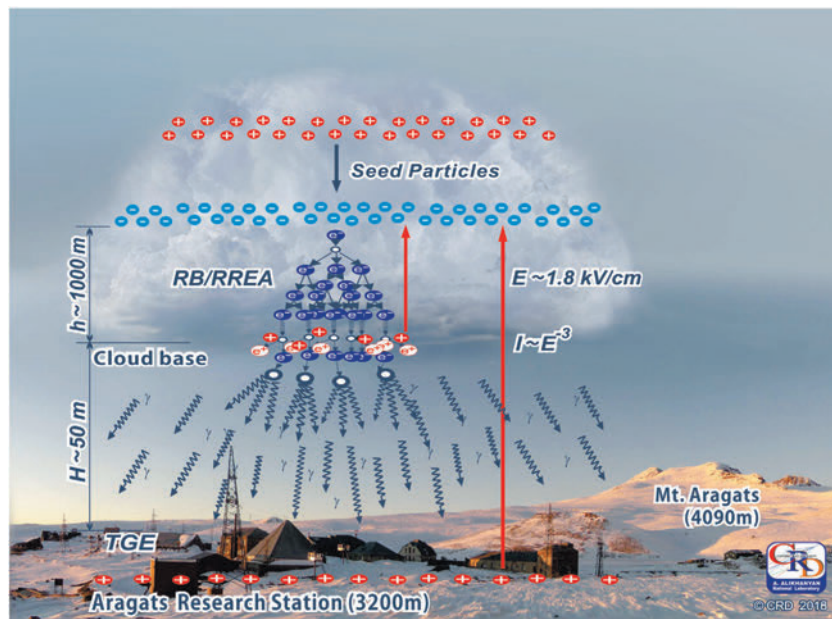


FIG. 1. Cartoon demonstrating electron acceleration and multiplication in the electric field of the lower dipole of the thundercloud and in the electric field beneath the cloud.

Thus, we use a new type of key evidence in the atmospheric electricity research, namely, the particle fluxes from the thunderclouds, to scrutinize the atmospheric electricity problem. The origin of the fluxes of electrons, gamma rays, and neutrons detected on the Earth’s surface are the runaway breakdown (RB) processes [15] now mostly referred to as relativistic runaway electron avalanches (RREA, [16,17]). The electron acceleration in the Earth’s direction is due to the electric field between the main negative charge region in the middle of the cloud and the positive charge that is induced on the ground. This field can be significantly increased by the electric field between the main negative region and the emerged lower positively charged region (LPCR) in the bottom of the cloud. The maximal intensity (and maximal energy of particles) of the TGE is observed when the strength of the total electric field in the cloud exceeds the “runaway” threshold in the atmosphere and the RB/RREA avalanches start to develop in the direction of Earth. Such a condition corresponds to the maximum dimension and charge of the LPCR; thus, the lightning leader cannot make its path through the LPCR, and cloud-to-ground flashes are suppressed [4]. The decay of the gamma ray flux and its termination by the lightning flash indicates the degradation of the bottom dipole.

In the presence of weak electric fields in the atmosphere (lower than RB/RREA threshold) when cosmic ray seed electrons cannot “runaway” and originate avalanches, the electric field effectively transfers energy to the electrons modifying their energy spectra (MOS process, [18]) and making the probability of emitting bremsstrahlung gamma rays larger. In contrast to RB/RREA, the MOS process is

dominating in the energy range above  $\approx 50$  MeV; the RREA process generates gamma rays with energies below  $\approx 50$  MeV although with a much larger count rate.

In the cartoon (Fig. 1), we show the electron–gamma ray avalanche developed in the bottom of the thundercloud above the Aragats high altitude research station of the Yerevan Physics Institute [19]. The avalanche comes out of the base of the cloud and illuminates various particle detectors, measuring count rates of charged and neutral particles and their energy. The distance to the cloud base at Aragats in the spring and autumn seasons is usually rather small  $H = 25\text{--}100$  m; in summer, it is larger,  $H = 50\text{--}500$  m. In our simulation studies of TGEs, we will assume the strength of the electric field in the cloud up to  $1.8$  kV/m and elongation up to  $1$  km. Both values are ordinary and have been measured in balloon flights [20].

The recently discovered phenomenon of long-lasting TGEs [21] gives additional clues to understanding embedded charged structures in thunderclouds. With numerous observations of TGEs in the 2017–2018 seasons and incorporated appropriate Monte Carlo simulations, we will demonstrate how intracloud electric fields originate the particle fluxes that continue for hours.

## II. DISTURBANCES OF THE NEAR-SURFACE ELECTRIC FIELD DURING TGES

The spring season on Aragats usually continues from April to middle of May. It is characterized by low-lying clouds ( $25\text{--}100$  m); high relative humidity (RH) of  $95\%\text{--}98\%$ ; large disturbances of the near-surface electric field

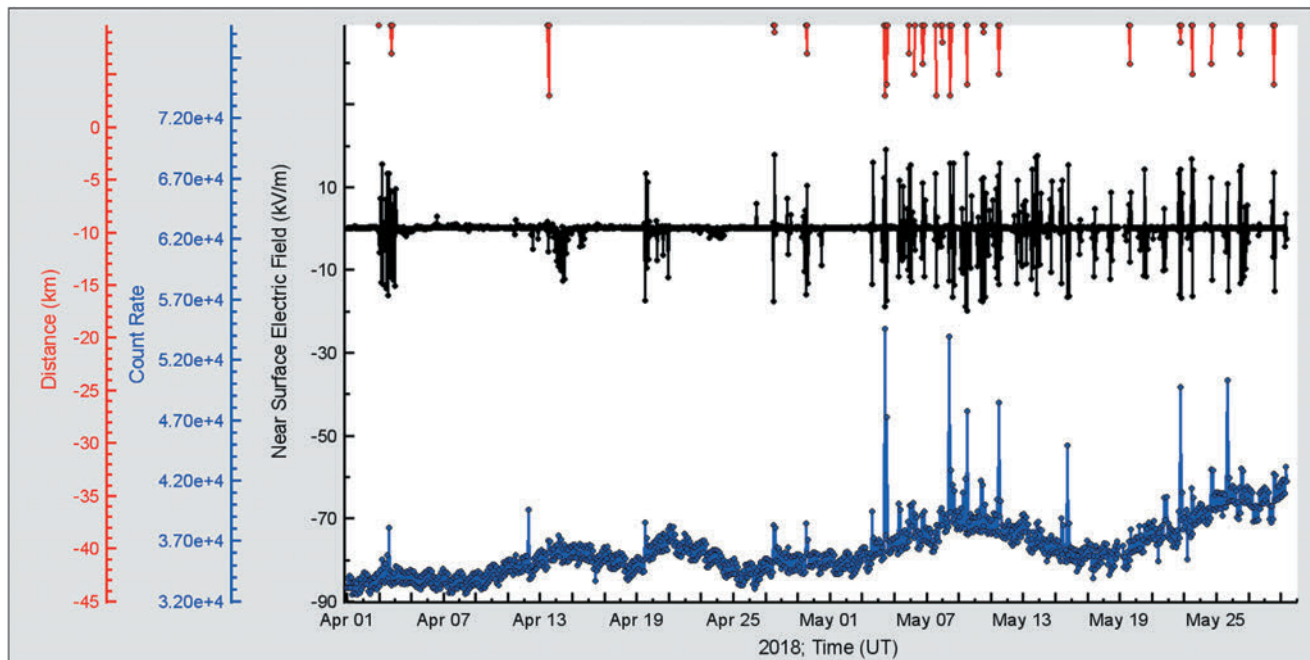


FIG. 2. At the top, vertical lines show the distance to lightning flash; in the middle, we show near-surface electric field disturbances measured by EFM-100 electric mill; at the bottom, one-minute time series of 1-cm-thick 1 m<sup>2</sup>-area outdoor plastic scintillator located outdoor nearby MAKET experimental hall.

(sometimes dropping into the negative region down to  $-30$  kV/m for several minutes); intense lightning activity (approaching the station for a few kilometers), and numerous TGEs—see Fig. 2. Large TGEs occurred usually when the outside temperature was in the range from  $-2$  to  $+2$  C° degrees.

In Fig. 2, we see that TGE activity peaked in the first days of May, providing multiple episodes of large fluxes of electrons and gamma rays. The mean count rate of the outdoor scintillator is increasing in May due to melting of the snow covering it in winter months (mean count rate is also dependent on the atmospheric pressure).

On May 22, 2018, thunderclouds approached the borders of Armenia, moving as usual from the Armenian highlands into Turkey. In Fig. 3, we show the approaching front of the storm as mapped by atmospheric discharges registered by the Boltek StormTracker lightning detector. At 16:00, the electrified clouds reached the Aragats mountain environment, inducing large disturbances of the near-surface electric field accompanied with lightning flashes; see Fig. 4.

In Fig. 4, we show the typical spring TGE with several maxima of high-energy particle (HEP) emissions, coinciding, as a rule, with the episodes when the near-surface electric field dropped into the deep negative region for at least several minutes. The emerging structures in the measured time series of the near-surface electrostatic field posted in the middle of Fig. 4 are reflecting the complicated structure of charged layers in the thundercloud. We speculate that when the mature LPCR arrives (or emerges) above

the detector location, the strength of the electric field in the lower dipole reaches the “runaway” threshold, and an unleashed electron-photon avalanche provides the maximum flux of TGEs. The intensity of the particle flux reaches the maximum if the LPCR is above the detector; when the cloud moves away from the detector site, the TGE declines.

In Fig. 4, along with the disturbances of the electric field, we also show the time-series of count rates of large NaI crystals. After the peak, the prolonged tail of the TGE is comprised of the low-energy gamma rays (with max energy 3 MeV or less). The NaI spectrometers have energy threshold of  $\approx 0.3$  MeV, besides the fifth one, whose threshold is  $\approx 3$  MeV. Thus, spectrometers with a higher-energy threshold register only peaks of TGE; they do not detect the long-lasting “pedestal” which comprises the low-energy particles.

At 20:15–22:15, without noticeable disturbances of the near-surface electric field, the NaI crystals continue to register decaying gamma ray flux. To gain insight into these two modes of the cloud radiation, we look at the electric field disturbances in more detail.

In Fig. 5, we show a zoomed version of the near surface electric field along with the count rate of the 1-cm-thick outdoor plastic scintillator (rather good coinciding with count rate of the NaI network), outside temperature, dew point, and relative humidity. From the picture, it is apparent that the most important feature, which is responsible for the particle burst, is the sufficiently long time period during which the near surface electric field remains

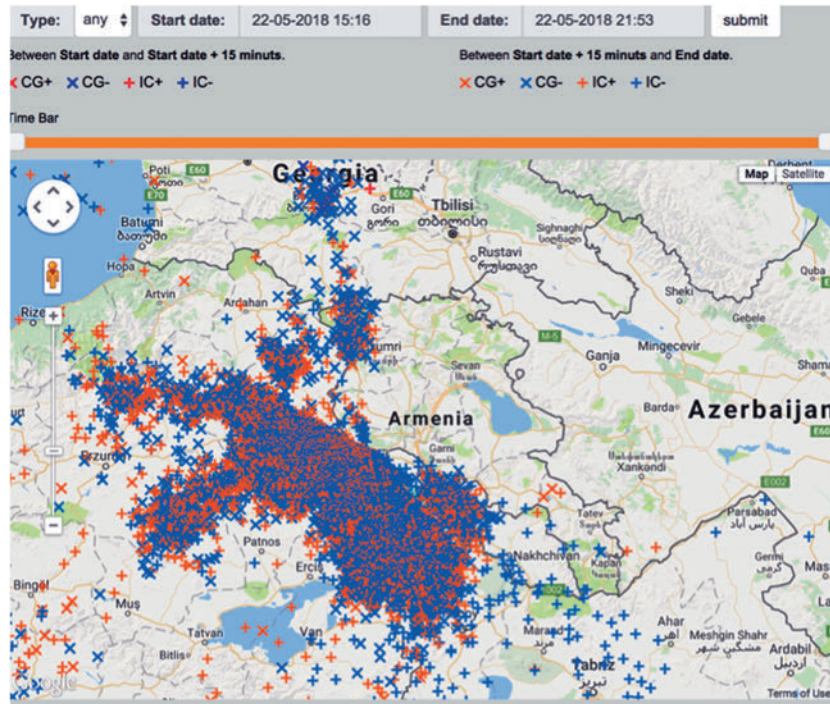


FIG. 3. The Google Map with lightning flashes shows the thunderstorm of May 22, 2018, approaching Armenia.

in the deep negative domain ( $\approx -15$  kV/m). We measure the peak significance in the units of relative enhancement (percent) and in numbers of standard deviations from the mean value measured before the TGE started (critical

value of the peak significance test,  $N\sigma$ ). The critical value (and corresponding p-value—integral of probability density distribution from the critical value to infinity) is the most comprehensive estimate of the reliability of detecting

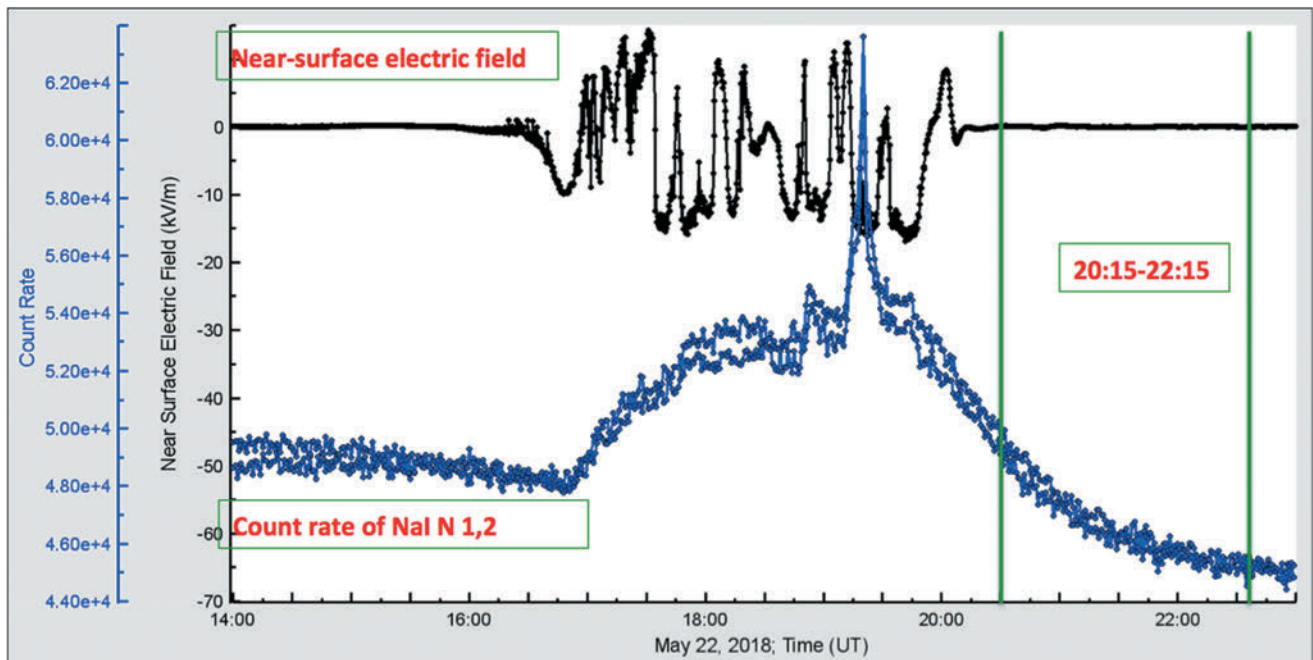


FIG. 4. LL TGE lasting approximately from 17:00 to 22:15; at the top, disturbances of the near-surface electric field measured by the EFM-100 electric mill located on the roof of MAKET experimental hall; at the bottom, one-minute time series of the NaI network’s spectrometers N 1 and 2 (energy threshold 0.3 MeV). The inset shows time series of NaI N5 spectrometer (energy threshold 3 MeV).

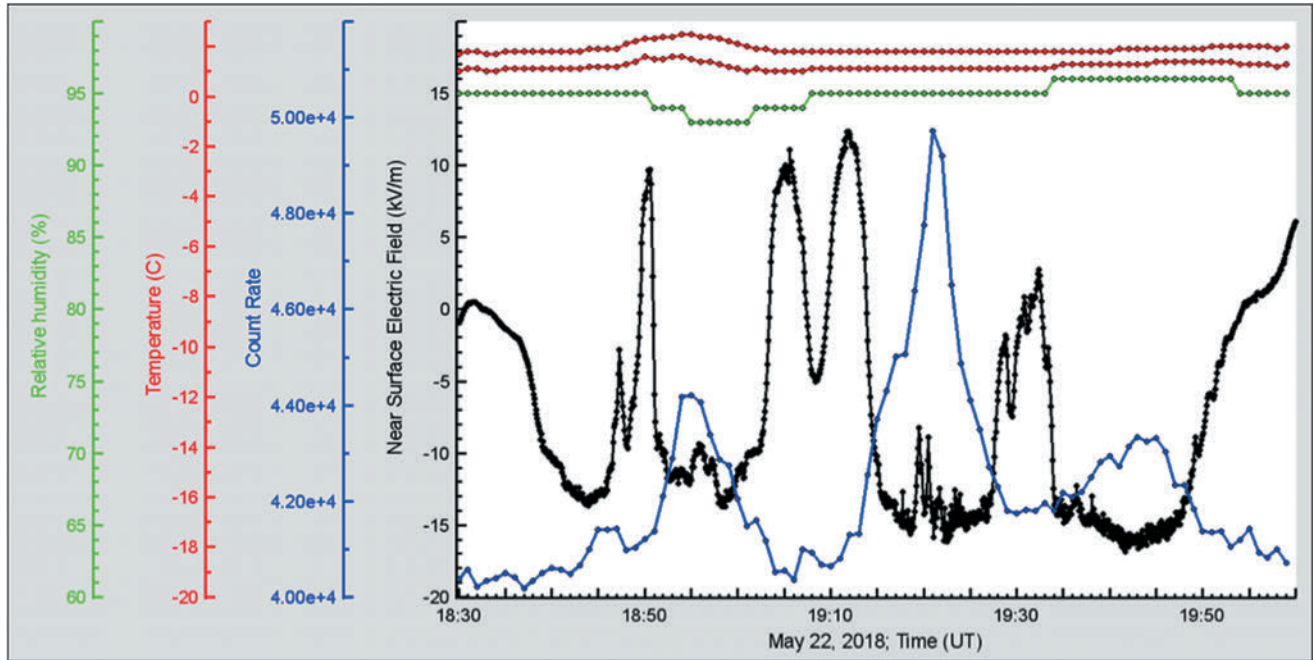


FIG. 5. Triple peak structure of HEP TGE: in the top outside temperature, dew point, and relative humidity.

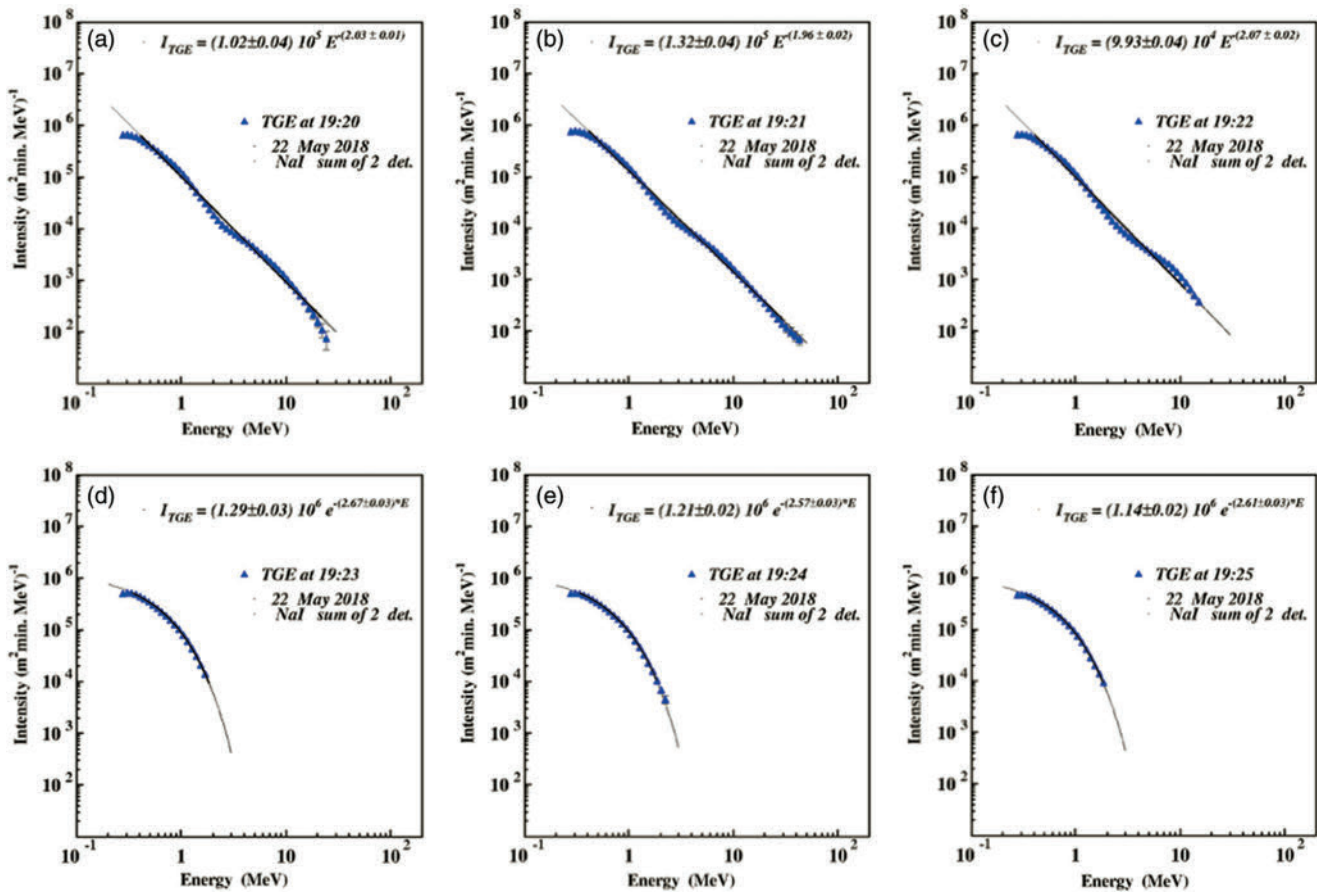


FIG. 6. The differential energy spectra of TGE particles registered by NaI network (N 1 and N 2 spectrometers); minutes 19:20–19:26.

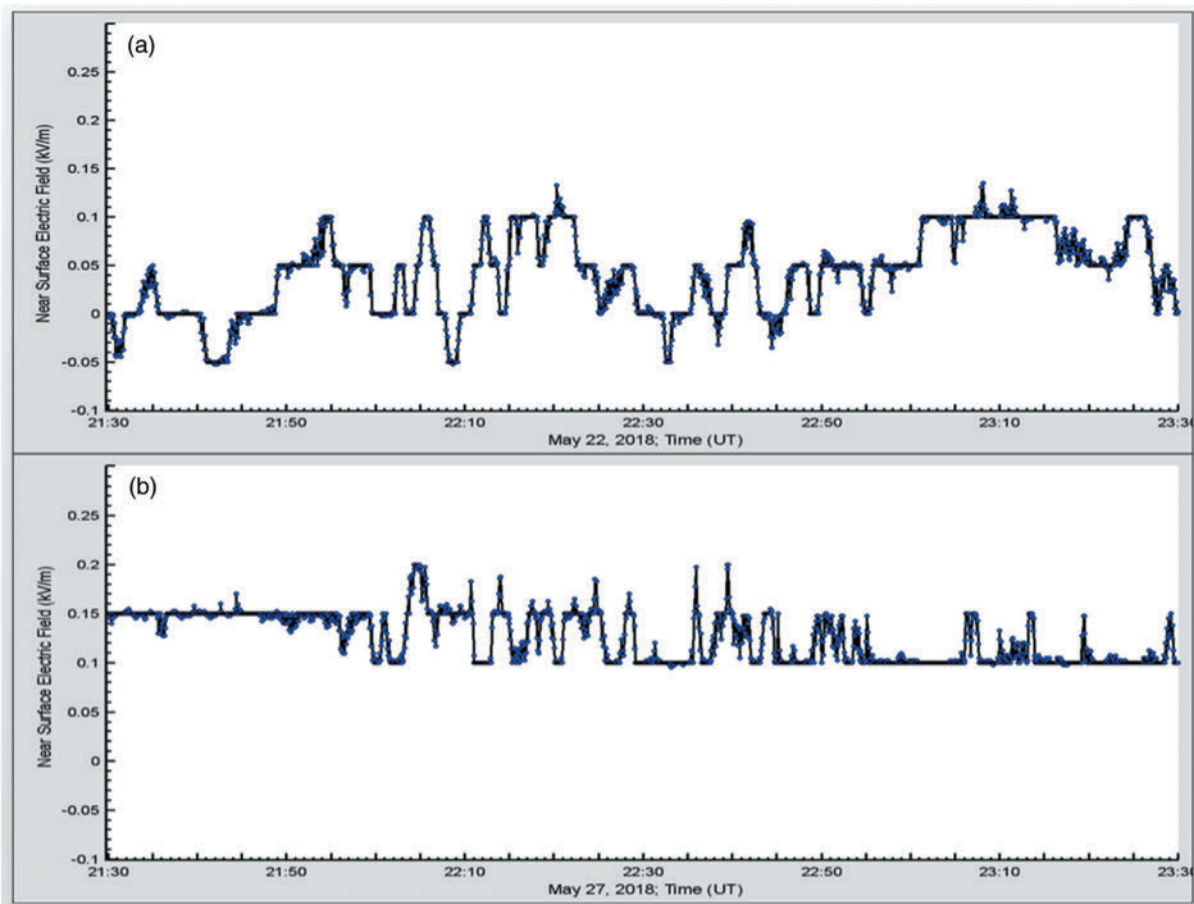


FIG. 7. The disturbances of near-surface electric field measured by EFM-100 electric mills with a sampling rate of 1 Hz on Aragats during LL TGE (6a), and during fair weather (6b).

peaks in the time-series. Large critical values correspond to small probabilities that the observed peak is a background fluctuation and not a genuine peak (TGE). Therefore, we can safely reject the null hypothesis (background fluctuation) and confirm the TGE. Very large critical values not only prove the unambiguous existence of a particle flux from the cloud but also serve as a comparative measure of the TGE observations using different detectors. During first peak (significance  $\approx 13\%/13\sigma$ ), near-surface field values were below  $-10$  kV/m at 18:52–19:01, 9 min; during middle largest peak (significance  $\approx 30\%/30\sigma$ ) at 19:15–19:28, 13 min; for the third peak (significance  $\approx 12\%/12\sigma$ ) at 19:34–19:49, 15 min. These extended periods of negative field were accompanied by small outbursts with field strength of several kV/m. We speculate that these outbursts are possibly connected with the LPCR emergence. However, outbursts are small and, therefore, the LPCR is not mature. The location of the cloud base estimated by the, so-called, “spread” parameter [22] is  $\approx 100$  m.; the relative humidity is  $\approx 95\%$ ; the maximal count rate measured by the 1-cm-thick and  $1\text{ m}^2$  area outdoor plastic scintillator reaches 50,000 per minute.

For understanding the relation between HEP bursts and long-lasting, low-energy emissions, we measure differential energy spectra during full duration of the TGE. In Fig. 6, we show the energy spectra of the LL TGE. To obtain a pure TGE signal, the cosmic ray background (containing muons, neutrons, and other energetic particles) measured at fair weather just before TGE should be bin-by-bin extracted from the histogram containing both background and additional counts from the avalanches initiated in the thundercloud. After background extraction, the histogram is fitted by an analytical distribution function (usually power law or exponential). For the recovery of the differential energy spectra measured by the NaI network, the spectrometer response function was calculated with the CERN GEANT package.

The sizeable intensity TGE was observed during 3 minutes (19:20–19:22). At the beginning [Fig. 6(a)] and in the end [Fig. 6(c)] of the high-energy TGE, the maximal energy of the flux reached 20 MeV and, at the minute of maximal flux [Fig. 6(b)],  $-40$  MeV. The particle flux was well approximated by the power law dependence with spectral index  $\approx -2$ . After fading of the high-energy particle, the shape of the flux spectrum abruptly changed to

exponential dependence with maximal energy not exceeding 3 MeV. Such an abrupt change of the flux shape spectrum and maximal energy can be connected with transient structure in the intracloud electric field. We associate it with the lower positively charged region, which significantly enhanced the total flux in the cloud for a few minutes. The charge and size of the main negatively charged region in the middle of the cloud is at least an order of magnitude larger than the charge and size of the LPCR. Thus, for a few minutes when the LCPR develops, the field in the cloud exceeds the runaway threshold, and the electrons which enter this enhanced field region are accelerated and multiplied, producing the TGE on Earth's surface. As the cloud is rather high ( $\approx 100$  m), due to the attenuation of particle flux in the air, the significance of the TGE does not exceed  $\approx 30\%$  corresponding to  $\approx 30$  standard deviations.

As we can see in Figs. 4 and 6, the gamma ray flux is lasting for hours after the disturbance of the near-surface electric field calms down. To check the exact pattern of electric field fluctuations, we compare the electric field measured by electric mill EFM-100 just after TGE and at the same time during a fair weather period. In Fig. 7(a), we can see that the disturbances measured by the electric mill during TGE are not very large, but not negligible, and have excursions to the negative domain. For the fair weather, the field value never goes below 0.1 kV/m, and variance is much smaller [Fig. 7(b)]. For the post-TGE electric field, the near-surface electric field values differ from the expected value of  $\sim 140$  V/m typical for the fair weather [Fig. 7(b)]. The electric field strength difference of the fair weather and post-TGE electric field is 0.9 kV/m. In the next section, we will analyze small disturbances of the near-surface electric field, which accompany the small TGE events.

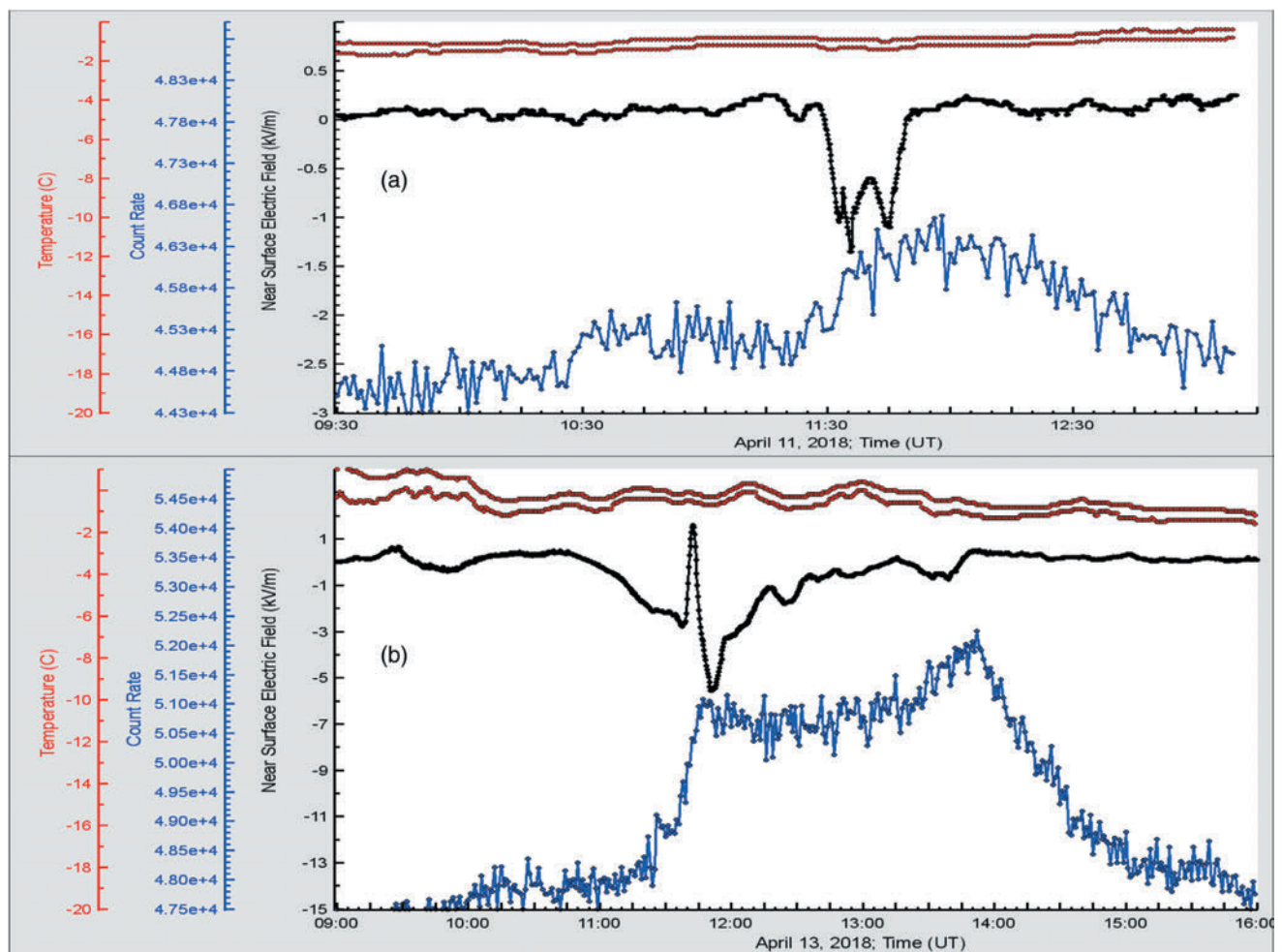


FIG. 8. Small TGEs observed in April 2018. At the top of each frame, we show outside temperature and dew point; in the middle, disturbances of the near-surface electric field; at the bottom, one-min count rate measured by the NaI crystal (energy threshold—0.3 MeV).

### III. LOW-ENERGY LONG-LASTING GAMMA RAY FLUXES FROM THUNDERCLOUDS

In the previous section, we outlined some specific characteristics of the field disturbance pattern that are supporting TGEs. The TGE observed in the low-energy particle flux is very different from the one observed in the high-energy flux. The high-energy particles (HEP) come from RB/RRE avalanches unleashed above the detector site; particles are accelerated in the lower dipole of the cloud formed by the main negative layer and emerged LPCR. As we have seen in the previous section, the necessary conditions for the high-energy particle bursts are the deeply negative near-surface electric field and the closeness of the cloud base to the Earth’s surface. During the high-energy phase of TGEs, the amplitude of disturbances of the near-surface electric field can reach 60–70 kV/m. However, we observe also the TGE events not connected with large disturbances of the electric field and lightning activity. Both the amplitude of disturbances and the significance of peaks are much smaller compared

with TGEs containing HEP. In Fig. 8, we show two such events that occurred in April 2018.

Estimated parameters for the April 11 event [Fig. 8(a)] are the following:

- (i) Duration of TGE: 11:25–12:45, 80 min;
- (ii) Duration of field disturbances 11:32–11:46, 13 min;
- (iii) Estimate of the height of cloud base:  $(-0.8-1.2) C^\circ * 122 \text{ m} \approx 50 \text{ m}$
- (iv) Relative humidity (RH)  $\sim 97\%$ ;
- (v) TGE significance (NaI crystal)  $\sim 4.8\%$  ( $10.4\sigma$ ).

TGE observed two days later was more prolonged and larger:

- (i) Estimated parameters for April 13 event [Fig. 8(a)] are as following:
- (ii) Duration of TGE: 11:25–12:45, 80 min;
- (iii) Duration of field disturbances 11:32–11:46, 13 min;
- (iv) Estimate of the height of cloud base:  $(-0.8-1.2) C^\circ * 122 \text{ m} \approx 50 \text{ m}$
- (v) Relative humidity (RH)  $\sim 97\%$ ;
- (vi) TGE significance (NaI crystal)  $\sim 4.8\%$  ( $10.4\sigma$ ).

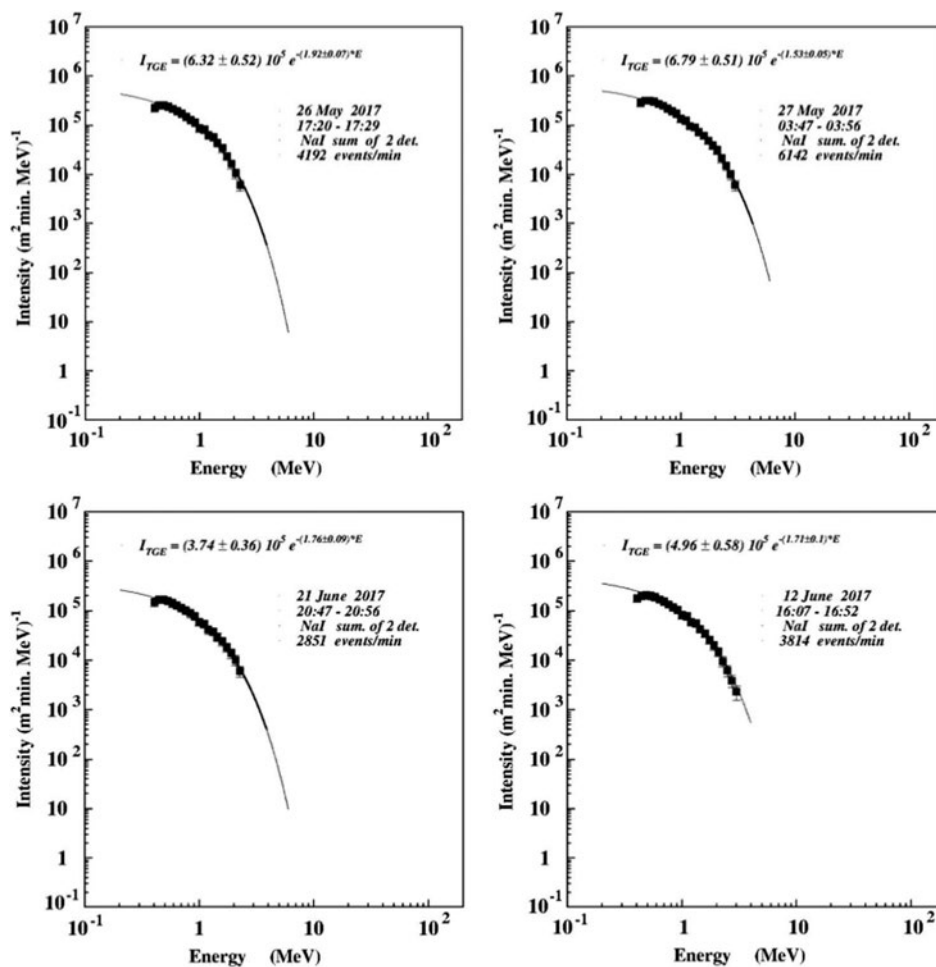


FIG. 9. Energy spectra of the TGE events coinciding with small disturbances of the near-surface electric field (possibly pure MOS process).

Neither TGE observed in April 2018 contained HEP or was accompanied by lightning activity.

Thus, there are two independent processes related to the particle fluxes from the thundercloud: the intense burst of particles from RB/RRE avalanches connected with LPCR development and prolonged low-energy gamma ray flux due to a MOS process [11]. The first one operates between the main negative charged layer and the LPCR; the second operates between the same main negative charged layer and the positive charge in the ground induced by the main negative charge. Thus, radiation processes in the clouds are not only connected with avalanches unleashing in the presence of the electric field above a threshold. Weak electric fields well below the RB/RREA initiation threshold also enhance gamma ray fluxes, although much less intensely than those with RB/RREA. Such small events can be fitted by a simple exponential dependence, with index varying from 1.5 to 1.9; see Fig. 9.

#### IV. TGES AND LIGHTNING FLASHES

In Fig. 10, we show the TGE observed by the one-cm-thick, one-m<sup>2</sup> area outdoor plastic scintillator on May 6, 2017. At 12:35, the electric field fell into the deep negative domain and remained there for  $\sim 12$  minutes. Thus, a lower dipole was formed and started to accelerate electrons downwards in the direction of the Earth. On the Earth's surface, all particle detectors register sizable TGE (the peak p-value for 1-minute count rate detected by 1 m<sup>2</sup> area plastic scintillator was  $\sim 50\sigma$ ). Two lightning flashes

terminated the particle flux at 12:42:22 count rate drops from 665 to 547 in two s and at 12:47:38 from 664 to 490 in 4 s. Both flashes were identified as a negative cloud-to-ground (CG) (see Fig. 12 and explanation in the text below). Thus, negative CG lightning partially destroyed the lower dipole; however, it was recovered in a few seconds, and the TGE was reestablished two times in five minutes.

In Fig. 11, we show the differential energy spectra as one-minute histograms slices. The arrows denote lightning flashes. Each time after lightning, the high-energy portion of the TGE is declined. Thus, the lightning flash decreases the strength of the electric field in the lower dipole and electrons cannot “run away” anymore and accelerate to tens of MeV. However, the electric field in the cloud is still sizable to enhance gamma ray radiation by the MOS process.

Electromagnetic emission produced by two mentioned lightning flashes was detected by a fast wideband (50 Hz to 12 MHz) electric field measurement system. We used a 52-cm-diameter circular flat-plate antenna followed by a passive integrator (decay time constant = 3 ms), the output of which was connected via a 60-cm double-shielded coaxial cable to a Picoscope 5244B digitizing oscilloscope. The sample interval of the oscilloscope was 40 ns, and the recorded length was 1 s. The oscilloscope was triggered by the signal from a commercial MFJ-1022 active whip antenna that covers a frequency range of 300 kHz to 200 MHz.

The fast electric field record of the first flash that occurred at 12:42:23.501 shows characteristic return stroke (RS) signatures, which are indicative of -CGs (Fig. 12).

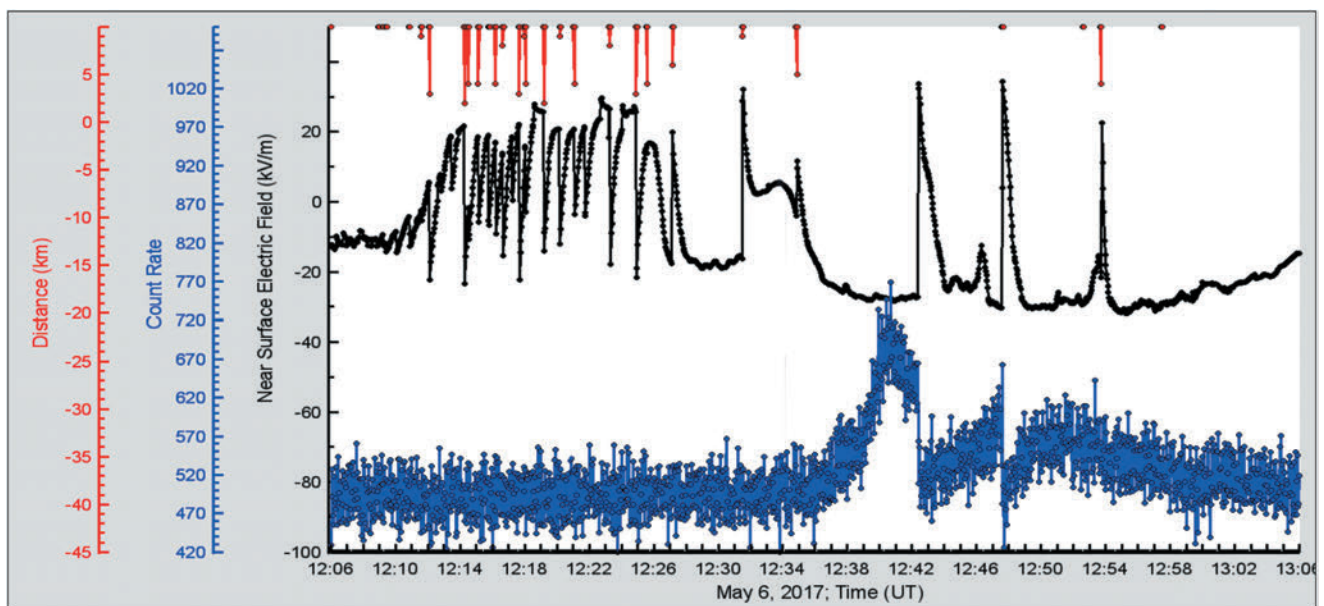


FIG. 10. From top to bottom: distance to lightning flash; disturbances of near surface electric field; one-second time series measured by 1-cm-thick outdoor plastic scintillator (energy threshold 0.7 MeV).

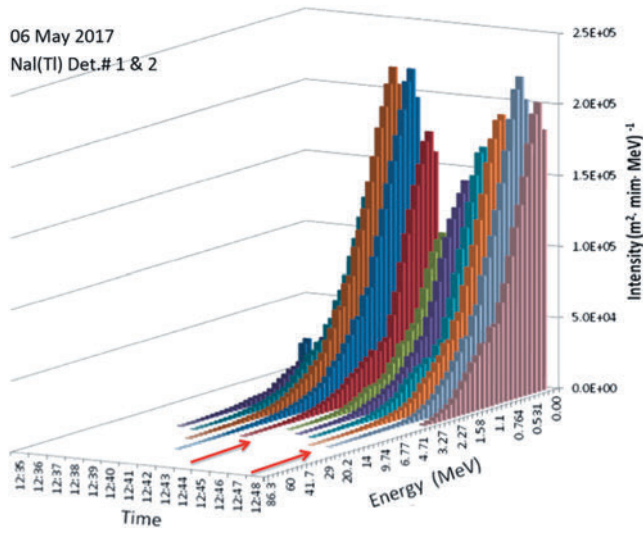


FIG. 11. The differential energy spectra measured by the NaI crystals minute-by-minute during TGE. By red arrows are denoted lightning flashes terminated high-energy particle flux.

Two RS pulses are observed at 177.6 ms and 210.8 ms after the trigger. The fast electric field record of the second flash that occurred at 12:47:36.302 also shows characteristic return stroke (RS) signatures, which are indicative of CGs. Four RS pulses are observed at 462.7 ms, 474.2 ms, 587.1 ms, and 787.6 ms after trigger; see Fig. 12.

### V. MONTE CARLO SIMULATION OF PARTICLE PROPAGATION IN THE INTRACLOUD ELECTRIC FIELD

In previous sections, we show that TGEs can last for many hours and comprise short high-energy bursts and extended lower-energy gamma ray flux. To check these findings, we performed simulations with CORSIKA and GEANT4 codes [23,24]. The theoretical bases of our simulation experiments are well-known processes of charged and neutral particle interactions with the terrestrial atmosphere and very simple models of cloud electrification. We assume the presence of the positive electric field of

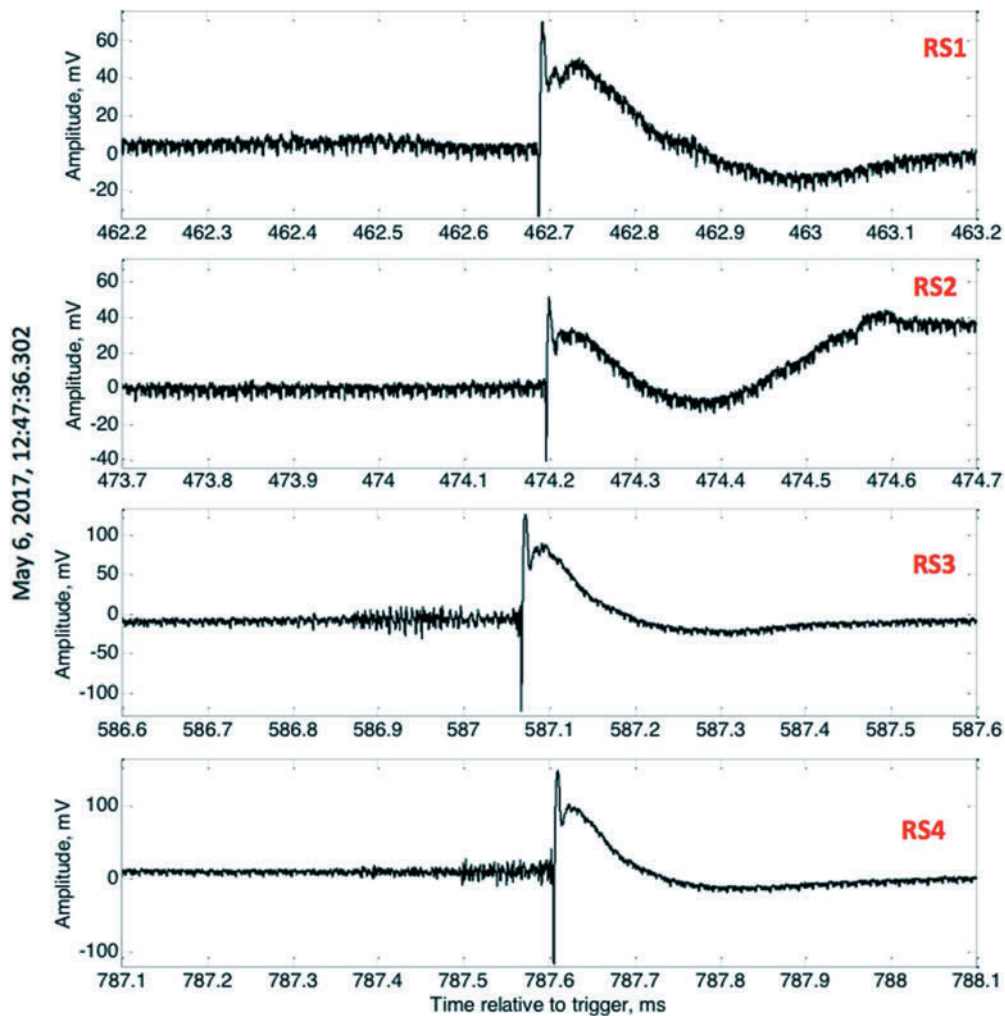


FIG. 12. Four RS pulses are observed at 462.7 ms, 474.2 ms, 587.1 ms, and 787.6 ms after trigger at 12:47:36/302.

different strength and spatial extent in the lower part of the cloud; the cloud base height was selected according to measurements on Aragats. Each simulation trial consists of  $10^8$  vertical gamma ray and electron showers with energies in the interval 1–100 MeV. The differential energy spectrum of gamma rays from the ambient population of cosmic rays follows the power law with spectral index  $\gamma = -1.42$  (on the heights 4–5 km). We follow the cascade particles till their energy is above the energy cutoff of  $E = 0.05$  MeV. The observation level  $H_{\text{obs}} = 3200$  m above sea level is the Aragats research station elevation. In Fig. 13, we show the dependence of enhanced particle flux on the strength of the electric field in the cloud changing from 0.1 to 1, 8 kV/cm. The spatial extent of the electric field was 1 km, and the height of the cloud base above the detectors was 50 m; see Fig. 1 for the arrangement of simulations.

In Fig. 13, we can see that although particle flux is dramatically enhanced by reaching the RB/RREA threshold ( $\approx 1.8$  kV/m on 4000 m height above sea level), the enhanced particle fluxes are nonetheless also evident for smaller electric fields. We assume that these electric fields originate in the cloud below the main negatively charged layer and extend to Earth's surface. Starting from the lowest tested field of 0.1 kV/m, we can see small enhancements of particle flux in good agreement with observations. Thus, the low electric fields in the atmosphere above the detector site can explain prolonged gamma radiation after the high-energy phase of TGE.

Another possible explanation of the long-lasting gamma ray flux is the detection of Compton-scattered gamma rays from the remote RB/RREA avalanches. According to our views, the RB/RREA avalanches are continuously emerging in the different parts of the thundercloud filling it with radiation [25]. To test the possibility of detecting remote RREA avalanches, we investigate the radial distribution of the gamma ray flux originated from large TGE. Each simulation set consists of  $10^8$  vertical gamma ray showers initiated by particles with energies in the interval 1–100 MeV (the differential energy spectrum was a power law, spectral index  $\gamma = -3$ ), leaving the cloud on different heights

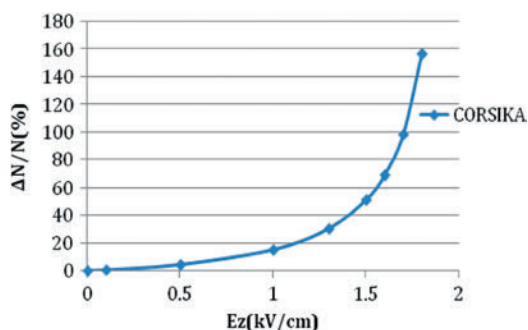


FIG. 13. Dependence of particle flux on the strength of the 1 km extended intracloud electric field.

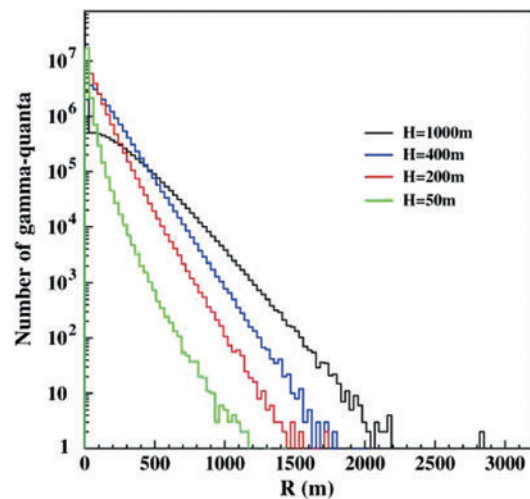


FIG. 14. Lateral distributions of gamma rays leaving thundercloud on different heights above the surface (located at 3200 m above sea level).

above Earth's surface. The particles were followed until  $H_{\text{obs}} = 3200$  m above sea level. The secondary particle energy cut was  $E = 0.05$  MeV; the lowest energy threshold of particle detectors operated on Aragats was 0.3 MeV. The cloud was located at four different heights:  $H = 50$  m, 200 m, 400 m, and 1000 m above the observation level. In Fig. 14, we show the lateral distribution of gamma rays with energies above 0.3 MeV born in the cascade initiated by gamma rays leaving the thundercloud at different heights above the particle detectors.

In Fig. 14, we can see that scattered gamma rays from RREA avalanches can barely contribute to particle flux on distances larger than 1 km. Furthermore, as we see in Fig. 15, the zenith angle distribution for such gamma rays peaked on very large angles, making registration of gamma

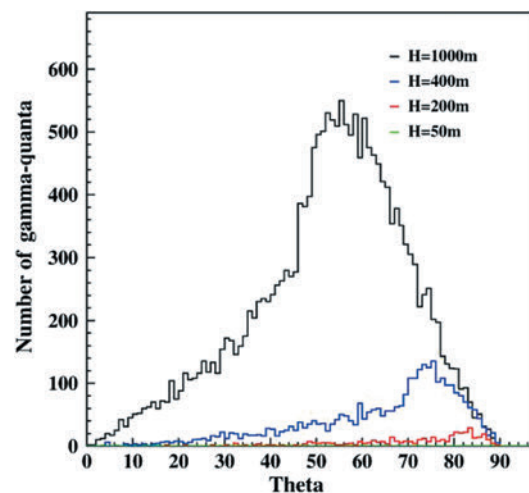


FIG. 15. Angular distributions of secondary gamma-quanta at distances  $R > 1000$  m from the shower core.

rays with stacked horizontal particle detectors very problematic.

## VI. VALIDATION OF MC SIMULATIONS

After verification of the simulation results performed by using different MC programs with the same parameters (we use CORSIKA and GEANT4 codes), the most important issue is the model validation, i.e., checking if the models used do more or less precisely describe the nature. The MC simulations described in the previous section were validated with a TGE that occurred on May 30, 2018, one of the four largest TGEs observed on Aragats in the last decade; see Fig. 16.

On May 30, the outside temperature was  $1.61\text{ C}^\circ$ , dew point  $-0.86\text{ C}^\circ$ ; thus, the estimated height of the cloud base was  $\approx 25\text{ m}$ . Very high humidity of 98% also confirms very low location of the cloud base. The huge single peak (peak value of particle flux 76,000 per m, per  $\text{m}^2$ , significance  $\approx 78\%/126\sigma$ ) shown in Fig. 16 occurred during the time span when the field was mostly in the negative domain ( $\approx 25\text{ m}$ , from 1:15 to 1:40). However, during the 4 minutes coinciding with the particle outburst, the near-surface electric field abruptly increased and remained in the positive domain. In analogy with Fig. 5, where we show the May 22 TGE, we can assume that, during this 4 minutes, a very strong LPCR was just above the detector site, producing a large electric field in the lower dipole of the cloud. Thus, the strength of the electric field in the lower dipole for a few minutes exceeded the runaway threshold

and, due to the low location of the cloud, a huge particle flux was registered.

The differential energy spectra of the May 30 TGE is posted in Fig. 17. Here, again, similar to the May 22 event (Fig. 6), we observe 3 minutes of HEP flux extrapolated with “broken” power law dependence. The power index for the low-energy (below 7–8 MeV) particle is very hard  $-1.2$ , changing after turnover to a very steep one of  $\approx -3$ . And, again, before [Fig. 17(a)] and after [Fig. 17(c)] the minute of maximal flux [Fig. 17(b)], we observe the maximal energy of 20 MeV, at maximal flux  $\approx 40\text{ MeV}$ . The difference between the May 22 and May 30 TGEs is the size of the LPCR deduced from the amplitude of the positive field excursion during the deep negative near-surface electric field. We can assume that because the distance of the cloud base is very small ( $\approx 25\text{ m}$ ) on May 30, compared with May 22 ( $\approx 100\text{ m}$ ), the influence of the LCPR on the total near-surface electric field is much larger. Thus, we have on May 30 one of the largest TGEs ever detected, with much larger intensity and significance than the May 22 TGE. We can explain the broken power law dependence as being due to a larger-than-usual LPCR that produced multiple avalanches that reached the ground and were registered. Thus, very large intensity of the TGE at energies below 8 MeV changed to an abrupt decline at higher energies (we already observed such a behavior; see Fig. 4 of [18]); the cumulative differential energy spectra measured by the MCAL calorimeter onboard the AGILE satellite also demonstrated very steep turnover at high energies [26]. After the decline of the TGE caused by the

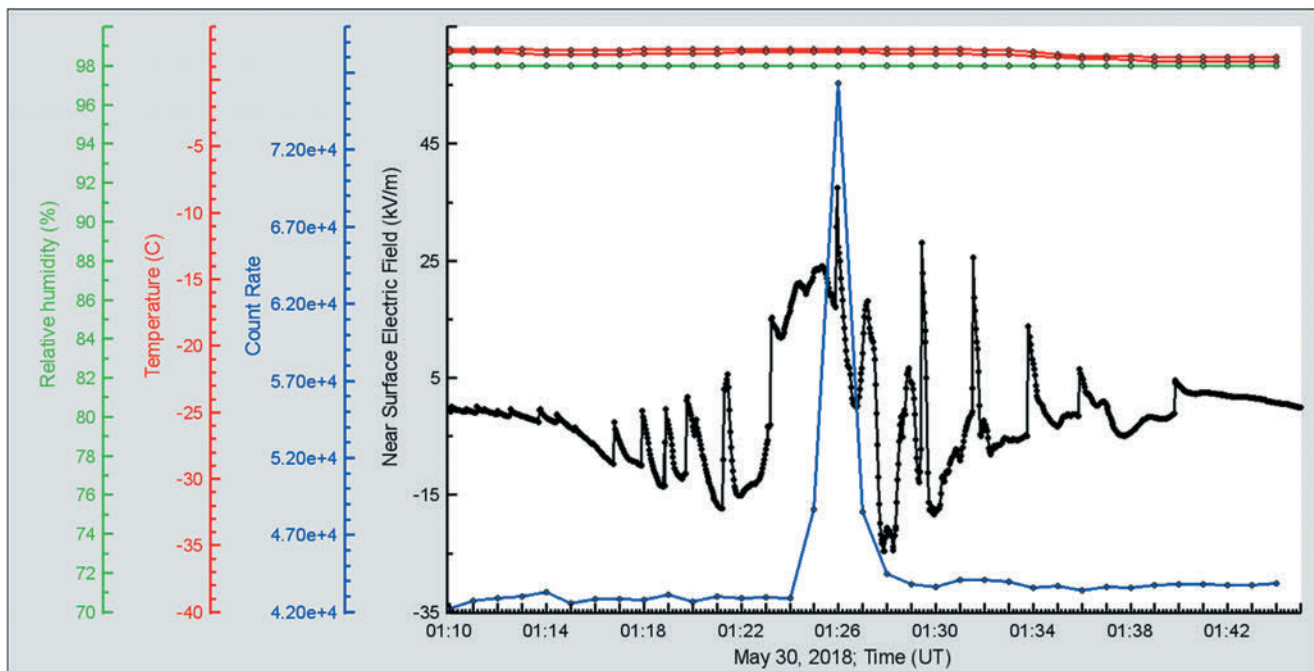


FIG. 16. Super-TGE occurred on May 30, 2018. At the top, outside temperature, dew point, and relative humidity and the middle disturbances of the near-surface electric field; at the bottom, 1-minute count rate of the 1-cm-thick  $1\text{ m}^2$ -area outdoor plastic scintillator.

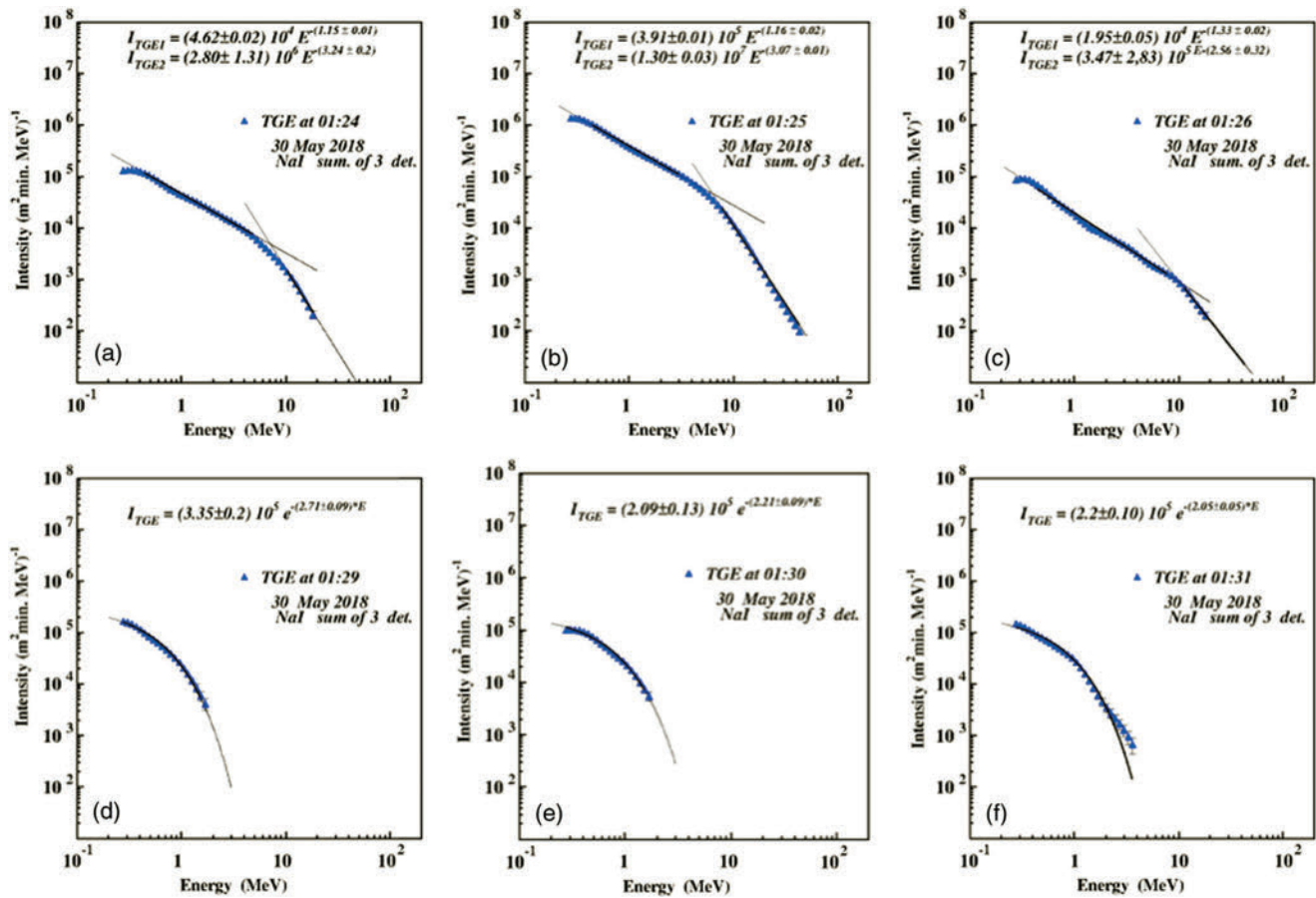


FIG. 17. The differential energy spectra of TGE particles registered by NaI network (N 1 and N 2 spectrometers); minutes 1:24–1:30.

near lightning flash, the particle flux continued for 1 hour with sizable count rate; however, the HEP particles disappeared [Figs. 6(d)–6(f)], the same as on May 22.

In Fig. 18, we show the differential energy spectra of the background gamma rays (obtained with WEB calculator PARMA/EXPACS, [27]), mostly originated from the interactions of the Galactic cosmic rays with the terrestrial atmosphere, and the spectrum measured by three large NaI crystals at 01:25 on May 30, 2018.

From the plots and from integral spectra shown in the left bottom corner, we see that overall TGE flux (mostly gamma rays with very small contamination of electrons) more than 2 times exceeds natural gamma radiation. Even after turnover (knee) at  $\approx 8$  MeV, TGE flux continues to exceed background until 20 MeV. Obtained integral spectra for 5 and 6 MeV thresholds well coincide with the fluxes observed by another particle detector—CUBE, supplied with veto effectively rejecting charged particles [28].

To gain insight into the size of the radiation-emitting region in the bottom of the cloud, we use measurements from the STAND1 particle detector network located on the

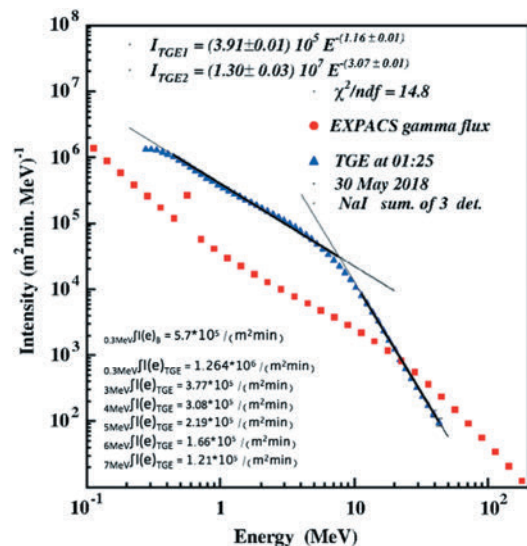


FIG. 18. Background spectrum and TGE spectrum observed on May 30, 2018. In the left bottom corner, values of integral spectrum calculated for different energy thresholds.

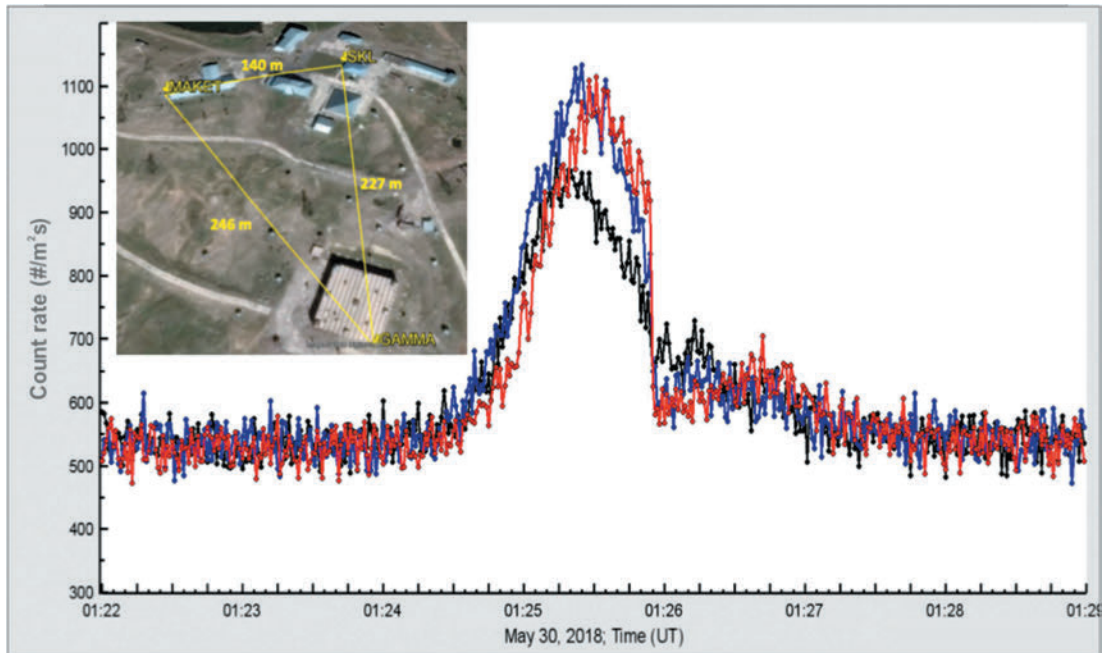


FIG. 19. One second time series of the STANd1 particle detector network count rates; in the inset, the map of detector units location.

Aragats station. In Fig. 19, we show the one-second time series of the May 30 TGE as measured by the three-cm-thick and one-m<sup>2</sup>-area outdoor plastic scintillators. The detectors are arranged in a triangle with unequal sides as shown in the inset in Fig. 19. Usually, the TGE measured by all three detectors coincides very well, as shown in the patterns of the one-second count rates displayed in Fig. 19; thus, the size of the emitting region in the cloud is rather large, exceeding at least 100 m.

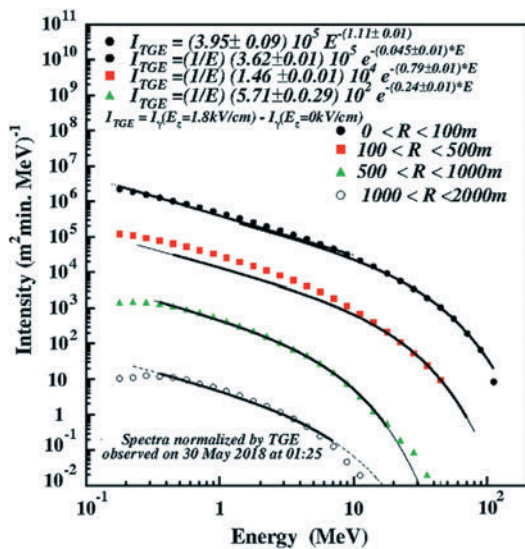


FIG. 20. Energy spectra of simulated TGE estimated by the particles fallen in the “rings” at different distances from the shower axes coincided with detector location site.

We use the recovered energy spectra at 1:25 on May 30 [Fig. 17(b)] for comparison and calibration of the simulated events containing high-energy particles. In Fig. 20, we present spectra of simulated events selected in different rings around the shower axes. We can see that, departing from the shower axes, the shape of the energy spectra become exponential and the maximal energy reduces in good agreement with observed energy spectra posted in Figs. 6, 9, and 17. We assume that when disturbances of the near-surface electric field calm down, but sizable flux of the TGE continues [see TGE intensities at 20:15–22:15, Fig. 4, and Figs. 6(d)–(f) and 17(d)–(f)], the electric field originated by the transient LPCR fades, and we can detect only low-energy gamma rays according to the MOS process and large-angle Compton scattered gamma rays.

The comparisons with simulation for such a complicated scientific domain as atmospheric electricity can provide only quantitative results. We are not aware of the localization and strength of intracloud electric fields. In simulations, we use the simplest tripole model with a uniform electric field between layers. The nature is much more complicated; nonetheless, TGEs give us new types of information (intensities and shapes of the “thundercloud” particle spectra) that overall agree with simulations.

## VII. CONCLUSIONS

Observation of numerous TGEs by the Japanese, Chinese, and Slovakian groups [28–32] proves that RB/RREA and

MOS are robust and realistic mechanisms for electron acceleration and multiplication, confirming the correctness of the model of TGE initiation [5,13,33].

However, there are observations of the alternative source of thundercloud particles.

Physicists performing experiments at the Tien-Shan Mountain Cosmic Ray Station, Kazakhstan (altitude of 3340 m), reported the existence of high-energy emissions, i.e. the electron, gamma, and neutron fluxes that are directly from the lightning bolt [34]. Another observation of the lightning-induced gamma ray flux was reported by the group from the International Center for Lightning Research and Testing [35] in North Central Florida. The authors claimed the observation of very intensive gamma ray flux was associated with upward positive leaders approaching a negative charge region. The systematic research of the lightning-related x-ray radiation was made at the Lightning Observatory in Gainesville (LOG), Florida [36]. During a thunderstorm on February 6, 2017, in Japan, a  $\gamma$ -ray flash with duration of less than one millisecond was detected at monitoring sites 0.5–1.7 km away from the lightning. The subsequent  $\gamma$ -ray afterglow subsided quickly, with an exponential decay constant of 40–60 milliseconds, and was followed by prolonged line emission at about 0.511 MeV, which lasted for a minute [37]. Authors claimed conclusive evidence of positrons and neutrons being produced after the lightning. Few bursts of gamma ray showers have been observed coincident with downward-propagating negative leaders in lightning flashes by the Telescope Array Surface Detector [38]. The authors claimed that the observed energy deposit is consistent with forward-beamed showers of  $10^{12}$ – $10^{14}$  or more primary photons above 100 keV, distributed according to a RREA spectrum. However, no model was presented to justify such a huge number of high-energy particles associated with a lightning flash.

During numerous storms observed from 2016 to 2018, we did not observe on Aragats any lightning producing relativistic particles in any of the continuously monitoring detectors. However, we do not exclude that propagation of lightning leaders and emerging of strong electric fields around leader tips can produce x rays and additional seed electrons involved in a runaway process. More registered events associated with lightning flash are needed to make a realistic model of such an exotic phenomenon.

In the present paper, we scrutinize the TGE model and propose the structure of the electric field in the thunderstorm atmosphere that accelerates and multiplies electrons, resulting in the huge particle fluxes reaching the Earth's surface.

The new key evidence, namely, intensities and energy spectra of the TGEs, along with associated disturbances of the near-surface electric field and lightning flashes, allows us to develop the comprehensive model of electric fields in the thundercloud. Discovered in 2017, long-lasting TGEs

prove that two independent mechanisms are responsible for bursts of high-energy particles and prolonged emissions of low-energy gamma rays.

HEP TGEs mostly occur when the near-surface electric field is in the deep negative domain and when the cloud base is 25–50 m above Earth's surface. The maximal energy of electrons in the RB/RREA avalanches can reach and exceed 40 MeV. Proof of the runaway process is the abrupt decline of the HEP bursts after the lightning flash, reestablished several seconds later when the electric field within the lower dipole again enhances the “runaway” threshold. Hours-long, low-energy gamma ray fluxes can be explained by the MOS process (modification of the cosmic ray electron energy spectra) in rather weak electric fields not triggering the RB/RREA process (low strength field originated between the main negative layer and its mirror on the Earth's surface).

LL TGEs start with small-intensity, low-energy gamma ray fluxes originated in weak electric fields between a mature main negative charge region in the middle of the cloud and its mirror on the Earth's surface. After several tens of minutes, or faster, with emerging of the LPCR above the detector site, the cumulative field surpasses the runaway threshold in the atmosphere, and the RB/RREA avalanches start in the cloud. If the cloud base is close to the Earth's surface (the case of Aragats storms in spring and autumn), TGE intensity can reach very high levels, exceeding the background radiation many times, and the maximal energy of the electrons and gamma rays reaches 40 MeV and more. Because the size of the LPCR is much smaller than the main negative region, the high-energy phase of the TGE is prolonged for only a few minutes, changing again to the low-energy gamma ray flux that can last for several hours.

The electron acceleration model based on the “classical” tripole charge structure of the thundercloud, which is used in our analysis [5,9,25], is the simplest one; however, we do not exclude more sophisticated scenarios of the electric field emergence in the thundercloud. Nearly (50%) of TGEs abruptly terminated by lightning flashes are associated not with cloud-to-ground but with normal-polarity intracloud flashes, signaling that charge of the main negative region is rather large and the lightning leader can make its path to the upper positively charged region. Another  $\approx 20\%$  of TGEs abruptly terminated by lightning flashes are associated with inverted-polarity intracloud flashes. Observation of the TGE-terminating inverted-polarity IC flash which occurs in the lower dipole proves that the downward electron-accelerating electric field is significantly enhanced by the field formed by the main negative charge in the cloud and the LPCR and, thus, enables the TGE development. The inverted-polarity IC flash reduces the main negative charge and, thus, leads to the reduction or elimination of this field inside the cloud. As a result, the TGE is abruptly terminated.

Numerous TGEs observed on Aragats and appropriate Monte Carlo simulations confirm our model; however, many questions remain unanswered, including

- (i) The way of LPCR development;
- (ii) The size and shape of the particle-emitting region;
- (iii) The possible changes of radio emission patterns due to TGE propagation in the atmosphere [39];
- (iv) The influence of remote lightning flashes on disturbances of the near-surface electric field;
- (v) How the intracloud electric fields can be deduced from the ground-based measurements of the near-surface electric field.

*In situ* measurements of charge and field distribution in clouds by a Lightning Mapping Array (LMA) or interferometer

facilities (operation on Aragats begins in 2018) will improve our understanding of cloud electrification.

## ACKNOWLEDGMENTS

The data for this paper are available via the multivariate visualization software ADEI on the web page of the Cosmic Ray Division (CRD) of the Yerevan Physics Institute, <http://adei.crd.yerphi.am/adei>. We thank the staff of the Aragats Space Environmental Center for the consistent operation of the Aragats research station facilities. We also thank E.Mareev and V.Rakov for useful discussions and appreciate the support of the Russian Science Foundation Grant (Project No. 17-12-01439).

- 
- [1] J. R. Dwyer, The initiation of lightning by runaway air breakdown, *Geophys. Res. Lett.* **32**, L20808 (2005).
  - [2] E. R. Williams, The tripole structure of thunderstorms, *J. Geophys. Res.* **94**, 13151 (1989).
  - [3] X. Qie, T. Zhang, C. Chen, G. Zhang, T. Zhang, and X. Kong, Electrical characteristics of thunderstorms in plateau regions of China, *Atmos. Res.* **91**, 244 (2009).
  - [4] A. Nag and V. Rakov, Some inferences on the role of lower positive charge region in facilitating different types of lightning, *GRL* **36**, L05815 (2009).
  - [5] A. Chilingarian and H. Mkrtchyan, Role of the lower positive charge region (LPCR) in initiation of the thunderstorm ground enhancements (TGEs), *Phys. Rev. D* **86**, 072003 (2012).
  - [6] A. Chilingarian, A. Daryan, K. Arakelyan, A. Hovhannisyanyan, B. Mailyan, L. Melkumyan, G. Hovsepyan, S. Chilingaryan, A. Reymers, and L. Vanyan, Ground-based observations of thunderstorm-correlated fluxes of high-energy electrons, gamma rays, and neutrons, *Phys. Rev. D* **82**, 043009 (2010).
  - [7] A. Chilingarian, G. Hovsepyan, and A. Hovhannisyanyan, Particle bursts from thunderclouds: Natural particle accelerators above our heads, *Phys. Rev. D* **83**, 062001 (2011).
  - [8] A. Chilingarian, Y. Khanikyants, E. Mareev, D. Pokhsranyan, V. A. Rakov, and S. Soghomonyan, Types of lightning discharges that abruptly terminate enhanced fluxes of energetic radiation and particles observed at ground level, *J. Geophys. Res. Atmos.* **122**, 7582 (2017).
  - [9] A. Chilingarian, G. Hovsepyan, and L. Vanyan, On the origin of the particle fluxes from the thunderclouds: Energy spectra analysis, *Europhys. Lett.* **106**, 59001 (2014).
  - [10] A. Chilingarian, B. Mailyan, and L. Vanyan, Observation of Thunderstorm Ground Enhancements with intense fluxes of high-energy electrons, *Astropart. Phys.* **48**, 1 (2013).
  - [11] A. Chilingarian, B. Mailyan, and L. Vanyan, Recovering of the energy spectra of electrons and gamma rays coming from the thunderclouds, *Atmos. Res.* **114–115**, 1 (2012).
  - [12] E. S. Cramer, B. G. Mailyan, S. Celestin, and J. R. Dwyer, A simulation study on the electric field spectral dependence of thunderstorm ground enhancements and gamma ray glows, *J. Geophys. Res. Atmos.* **122**, 4763 (2017).
  - [13] A. Chilingarian, Thunderstorm ground enhancements—Model and relation to lightning flashes, *J. Atmos. Terr. Phys.* **107**, 68 (2014).
  - [14] A. Chilingarian, G. Hovsepyan, Y. Khanikyanc, A. Reymers, and S. Soghomonyan, Lightning origination and thunderstorm ground enhancements terminated by the lightning flash, *Europhys. Lett.* **110**, 49001 (2015).
  - [15] A. V. Gurevich, G. M. Milikh, and R. A. Roussel-Dupre, Runaway electron mechanism of air breakdown and preconditioning during a thunderstorm., *Phys. Lett.* **165A**, 463 (1992).
  - [16] L. P. Babich, E. N. Donskoy, R. I. Il'kaev, I. M. Kutsyk, and R. A. Roussel-Dupre, Fundamental parameters of a relativistic runaway electron avalanche in air, *Plasma Phys. Rep.* **30**, 616 (2004).
  - [17] J. R. Dwyer, A fundamental limit on electric fields in air, *Geophys. Res. Lett.* **30**, 2055 (2003).
  - [18] A. Chilingarian, G. Hovsepyan, and L. Vanyan, On the origin of the particle fluxes from the thunderclouds: energy spectra analysis, *Europhys. Lett.* **106**, 59001 (2014).
  - [19] A. Chilingarian, G. Hovsepyan, and E. Mantasakanyan, Mount Aragats as a stable electron accelerator for atmospheric High-energy physics research, *Phys. Rev. D* **93**, 052006 (2016).
  - [20] T. C. Marshall, M. Stolzenburg, Paul R. Krehbiel *et al.*, Electrical evolution during the decay stage of New Mexico thunderstorms, *J. Geophys. Res.* **114**, D02209 (2009).
  - [21] A. Chilingarian, Long lasting low energy thunderstorm ground enhancements and possible Rn-222 daughter isotopes contamination, *Phys. Rev. D* **98**, 022007 (2018).
  - [22] A. Chilingarian, G. Hovsepyan, and B. Mailyan, In situ measurements of the runaway breakdown (RB) on Aragats mountain, *Nucl. Instrum. Methods Phys. Res., Sect. A* **874**, 19 (2017).

- [23] D. Heck, J. Knapp, J.N. Capdevielle, G. Schatz, and T. Thouw, Report No. FZKA 6019, 1998, Forschungszentrum, Karlsruhe, <https://www.ikp.kit.edu/corsika/70.php>.
- [24] S. Agostinelli, J. Allison, A. Amako *et al.* Geant4—a simulation toolkit, *NIM* **506**, 250 (2003).
- [25] A. Chilingarian, S. Chilingaryan, T. Karapetyan, L. Kozliner, Y. Khanikyants, G. Hovsepyan, D. Pokhsranyan, and S. Soghomonyan, On the initiation of lightning in thunderclouds, *Sci. Rep.* **7**, 1371 (2017).
- [26] M. Marisaldi, F. Fushino, M. Tavani *et al.*, Properties of terrestrial gamma ray flashes detected by AGILEMCAL below 30 MeV, *J. Geophys. Res. Space Phys.* **119**, 1337 (2014).
- [27] T. Sato, Analytical Model for Estimating the Zenith Angle Dependence of Terrestrial Cosmic Ray Fluxes, *PLoS One* **11**: e0160390 (2016).
- [28] T. Torii, T. Sugita, M. Kamogawa, Y. Watanabe, and K. Kusunoki, Migrating source of energetic radiation generated by thunderstorm activity. *Geophys. Res. Lett.* **38**, L24801 (2011).
- [29] H. Tsuchiya, T. Enoto, K. Iwata *et al.*, Hardening and Termination of Long-Duration Gamma Rays Detected Prior to Lightning, *Phys. Rev. Lett.* **111**, 015001 (2013).
- [30] Y. Kuroda, S. Oguri, Y. Kato, R. Nakata, Y. Inoue, C. Ito, and M. Minowa, Observation of gamma ray bursts at ground level under the thunderclouds, *Phys. Lett. B* **758**, 286 (2016).
- [31] B. Bartoli, P. Bernardini, X. J. Bi *et al.*, Observation of the thunderstorm-related ground cosmic ray flux variations by ARGO-YBJ, *Phys. Rev. D* **97**, 042001 (2018).
- [32] K. Kudela, J. Chum, M. Kollárik, R. Langer, I. Strhárský, and J. Baše, Correlations between secondary cosmic ray rates and strong electric fields at Lomnický štít, *J. Geophys. Res.* **122**, 10700 (2017).
- [33] A. Chilingarian, Long lasting low energy thunderstorm ground enhancements and possible Rn-222 daughter isotopes contamination, *Phys. Rev. D* **98**, 022007 (2018).
- [34] A. V. Gurevich, V.P. Antonova, A.P. Chubenko *et al.*, Strong Flux of Low-Energy Neutrons Produced by Thunderstorms, *Phys. Rev. Lett.* **108**, 125001 (2012).
- [35] B. M. Hare, M. A. Uman, J. R. Dwyer *et al.*, Ground-level observation of a terrestrial gamma ray flash initiated by a triggered lightning, *J. Geophys. Res. Atmos.* **121**, 6511 (2016).
- [36] S. Mallick, V. A. Rakov, and J. R. Dwyer, A study of X-ray emissions from thunderstorms with emphasis on subsequent strokes in natural lightning, *J. Geophys. Res.* **117**, D16107 (2012).
- [37] T. Enoto, Y. Wada, Y. Furuta *et al.*, Photonuclear reactions triggered by lightning discharge, *Nature (London)* **551**, 481 (2017).
- [38] R. U. Abassi, T. Aby-Zayyad, M. Allen *et al.*, Gamma-ray Showers Observed at Ground Level in Coincidence With Downward Lightning Leaders, *JGR Atmosphere* **123**, 6864 (2018).
- [39] P. Schellart, T.N.G. Trinh, S. Buitink *et al.*, Probing Atmospheric Electric Fields in Thunderstorms through Radio Emission from Cosmic-Ray-Induced Air Showers., *Phys. Rev. Lett.* **114**, 165001 (2015).

## On the origin of particle fluxes from thunderclouds

A. Chilingarian<sup>a,b,c,\*</sup>, S. Soghomonyan<sup>a</sup>, Y. Khanikyanc<sup>a</sup>, D. Pokhsraryan<sup>a</sup>



<sup>a</sup> Alikhanyan National Lab (Yerevan Physics Institute), Alikhanyan Brothers 2, Yerevan 0036, Armenia

<sup>b</sup> National Research Nuclear University MEPhI (Moscow Engineering Physics Institute), Moscow 115409, Russia

<sup>c</sup> Space Research Institute of RAS, Moscow, Russia

### ARTICLE INFO

#### Article history:

Received 26 June 2018

Revised 14 October 2018

Accepted 15 October 2018

Available online 17 October 2018

#### Keywords:

Atmospheric electricity  
 lightning physics  
 thunderstorm ground enhancements

### ABSTRACT

We present the observational data on registration of atmospheric discharges simultaneously with the detection of elementary particles obtained during thunderstorms at an altitude of 3200 m above sea level on Mt. Aragats in Armenia. Throughout the 2016 summer and 2018 spring campaigns on Aragats, we monitored lightning occurrences and signals from NaI spectrometers, plastic scintillators and Neutron Monitor proportional counters, and analyzed the shape of registered pulses. Particle detector signals were synchronized with lightning occurrences at a few nanoseconds level.

Analysis of shapes of the simultaneously detected pulses of the fast wideband electric field produced by a lightning flash and pulses from particle detectors discloses that all additional detector pulses registered during lightning flash were the electromagnetic interference signals and not particles originated directly from the lightning bolt. Thus, we observe no evidence of the direct production of electrons, neutrons or gamma rays during a lightning flash. We conclude that the entire particle fluxes detected on Aragats research station (more than 250 TGEs) can be explained by the generation of MeV electromagnetic cascades in the strong atmospheric electric fields.

© 2018 Elsevier B.V. All rights reserved.

### 1. Introduction

Copious observations of the thunderstorm ground enhancements (TGEs) [7,8], i.e. enhanced fluxes of electrons, gamma rays and neutrons detected by particle detectors located on the Earth's surface and related to the strong thunderstorms overhead, posed the question of their origin. According to the TGE initiation model [11,16], the electrical field of the lower dipole effectively transfers field energy to secondary cosmic ray electrons. Electrons generate copious gamma rays by a runaway breakdown (RB) [21], now referred mostly as relativistic runaway electron avalanches (RREA) [4,5,18]. High-energy gamma rays (with energies above 10 MeV) in interaction with atmosphere atoms generate neutrons by photonuclear reaction [10]. Large TGEs usually occurred during large negative electric fields observed near the earth's surface [9]. Multi-year observations of particle fluxes and lightning occurrences on Aragats prove that during large TGEs the lightning activity is suppressed; lightning reduces particle fluxes and does not accelerate them [12,15].

Observation of numerous TGEs by the Japanese, Chinese, and Slovakian groups [6,26,27,30,31] proves that RB/RREA process re-

liably accelerates and multiplies electrons producing numerous TGEs.

In contrast, there are observations of an alternative source of thundercloud particles.

Physicists performing experiments at the Tien-Shan Mountain Cosmic Ray Station, Kazakhstan (altitude of 3340 m) in several papers reported the existence of high-energy emissions, i.e. electron, gamma and neutron fluxes that are directly connected with yet unknown processes in the lightning bolt. Gurevich et al. [23] "report for the first time about the registration of an extraordinary high flux of low-energy neutrons generated during thunderstorms. The measured neutron count rate enhancements are directly connected with thunderstorm discharges". Gurevich et al. [25] confirm that "the intensity both of electrons and gamma rays in lightning discharge prevail the background emission by 1.5 to 2 orders of magnitude"

Another group from the Lebedev Institute in Moscow, Russian Federation, reported the emission of neutrons in the energy range up to tens of MeV in a one-meter long high-voltage discharge produced in laboratory [2]; and that "neutrons were registered within the range from thermal energies up to the energies above 10 MeV. It was found that the neutron generation takes place at the initial phase of electric discharge and is correlated with the generation of x-ray radiation" [3].

\* Corresponding author.

E-mail address: [chili@aragats.am](mailto:chili@aragats.am) (A. Chilingarian).

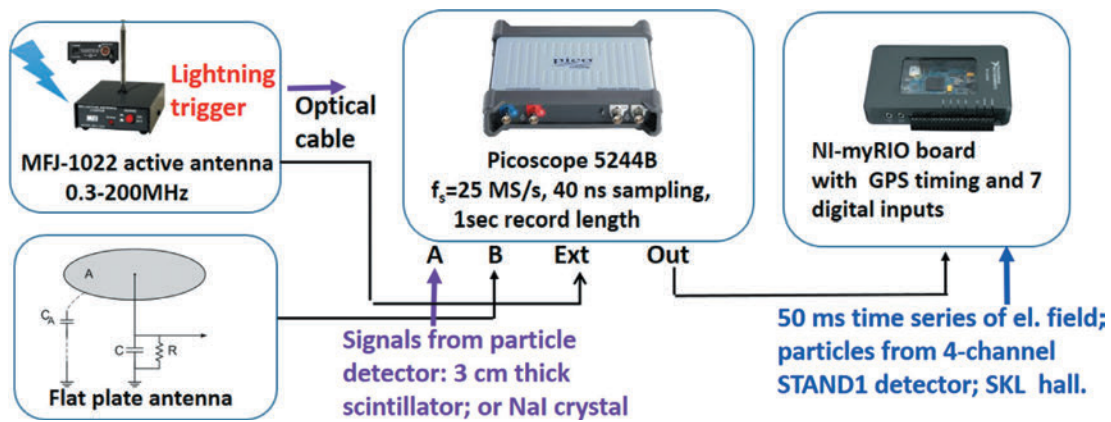


Fig. 1. The fast synchronized data acquisition (FSDAQ) system for the research of particle flux–lightning relations.

Another observation of the lightning-induced gamma ray flux was reported by the group from the International Center for Lightning Research and Testing (ICLRT) [20] in north central Florida. The gamma ray flux intensity was able to saturate the electronics throughout 50  $\mu$ s following the system trigger. The authors claim that the primary factor that triggered the very intensive gamma ray flux was the upward positive leader approaching a negative charge region.

Despite these pieces of evidence, the physical model of the particle origination in the thunderbolt is not yet well explained. Usually, the physical model is not formulated at all; the only detection of particles is described:

Ref. [24]: it is established that “the neutrons are generated during thunderstorm atmospheric discharges. Often the neutrons are emitted in short bursts; the burst width is 200–400  $\mu$ s.”

Ref. [2]: “Currently, there is no reasonable model or mechanism to explain the generation of neutron bursts during atmospheric discharge in air. A special mystery is the origin of the neutrons with energies above 10 MeV.”

The systematic research of the lightning-related X-ray radiation was made at the lightning observatory in Gainesville (LOG), Florida [29]. The 7.6 cm long cylindrical NaI (TI) scintillator, circular flat-plate antennas were used for correlated measurements of the X-ray photons, electric field, and electric field derivative. Measured X-ray radiation, lightning leader and return-stroke onset times, helped to establish a correspondence between leader steps and X-ray pulses. For 23 (8 first and 15 subsequent) strokes within 2 km of the lightning observatory in Gainesville; X-rays were detected 88% of the time. The authors present the time series of gamma ray count rates before the lightning (Fig. 5 of [29]) on a microsecond time scale.

During a thunderstorm on 6 February 2017 in Japan, a  $\gamma$ -ray flash with duration of less than 1 ms was detected at monitoring sites 0.5–1.7 km away from the lightning. The subsequent  $\gamma$ -ray afterglow subsided quickly, with an exponential decay constant of 40–60 ms, and was followed by prolonged line emission at about 0.511 MeV, which lasted for a minute [19]. Authors claim a conclusive evidence of positrons and neutrons being produced after the lightning.

Few bursts of gamma ray showers have been observed in coincidence with downward propagating negative leaders in lightning flashes by the telescope array surface detector (TASD) [1]. The authors claim that observed energy deposit is consistent with forward-beamed showers of  $10^{12}$ – $10^{14}$  or more primary photons above 100 keV, distributed according to a RB/RREA spectrum. However, no model was presented to justify such a huge amount of high-energy particles associated with a lightning flash.

In summary, two models are suggested in the literature:

- The RB/TGE model—electrons from the ambient population of CR accelerated in the strong electric field in the lower part of the cloud, runaway, generate bremsstrahlung gamma rays and the gamma rays produce neutrons via photoneuclear reactions;
- The lightning model—the electron, gamma, and neutron fluxes originate in the lightning flashes. The model of particle generation in the lightning bolt, or around the lightning bolt is yet not well specified.

To solve this controversy, we need to unambiguously answer the question: do lightning flashes emit high-energy electrons, positrons, gamma rays and neutrons with single energies of several tens of MeV? [28]. Therefore, we perform experiments with simultaneous recording of the pulse shape from particle detectors and from atmospheric discharges. During the summer 2016 to spring 2018 campaigns on Aragats completed by the staff of cosmic ray division (CRD) of Yerevan Physics Institute (YerPhi) hundreds strong storms with numerous lightning flashes were observed, and some of the most violent ones produced electromagnetic interferences (EMI) in some of the particle detectors and data acquisition electronics (DAQ). Taking as examples the huge storms occurred on Aragats we demonstrate that with new fast electronics we can reliably distinguish EMI from genuine particle registration in a variety of particle detectors that are in operation on Aragats. No particle fluxes correlated with lightning flashes were detected at Aragats during the whole time of observations.

## 2. Instrumentation

The correlation analysis of the TGEs and lightning discharges poses stringent requirements on the time resolution and synchronization of the data flow from particle detectors, near surface electric field sensors and sensors of the fast electric field. The recently developed fast synchronized data acquisition (FSDAQ) system (see Fig. 1) is triggered by a commercial MFJ-1022 active whip antenna that covers a frequency range from 300 kHz to 200 MHz. A flat-plate antenna followed by passive integrator is used to record fast electric field waveforms. The output of the integrator is directly connected to the digital oscilloscope (2-channel Picoscope 5244B) with 60 cm long RG58 coaxial cable. The data capture length is 1 s, including 200 ms pre-trigger time and 800 ms post-trigger time. The sampling rate is 25 MS/s, corresponding to 40 ns sampling interval, and the amplitude resolution is 8 bit.

The trigger output of the oscilloscope is connected to the input of GPS timing system of the national instrument’s (NI) MyRIO board. Any event recorded by the oscilloscope generates an output trigger, causing the GPS card to trigger at the same instant and produce a timestamp.

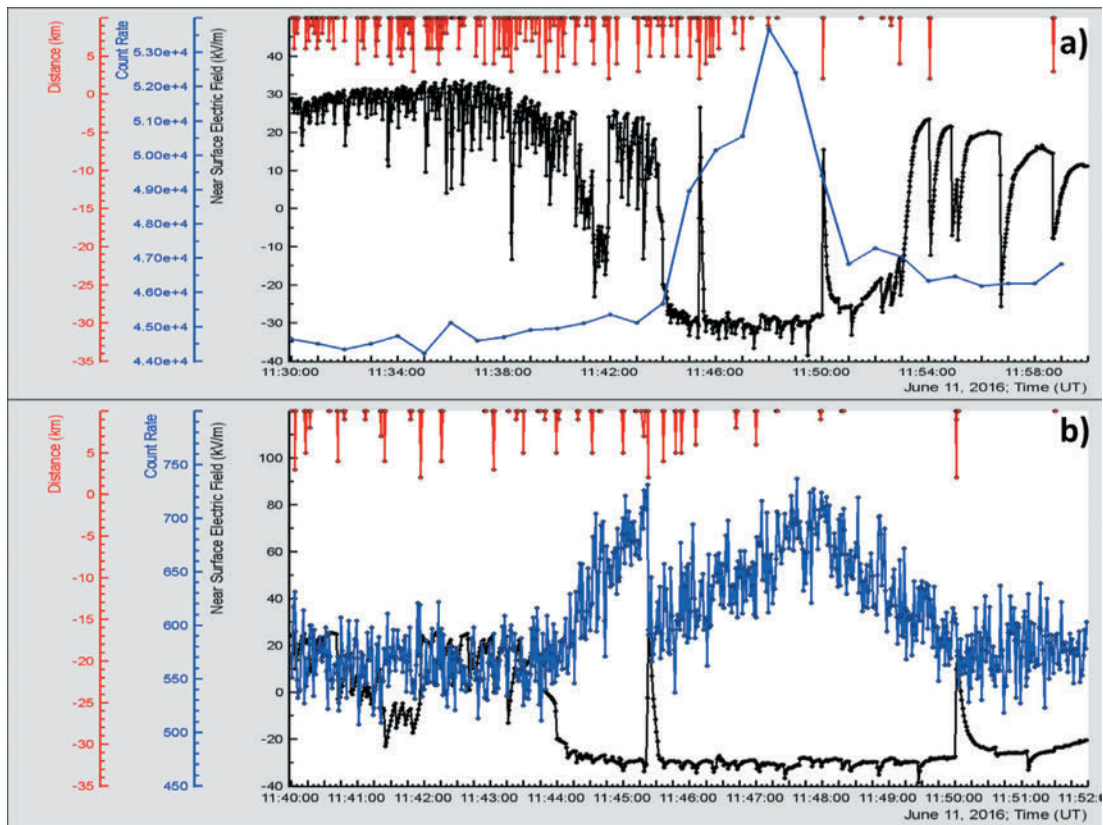


**Fig. 2.** (a) Disturbances of the near surface electrostatic field, distance to lightning and 1 min count rate of STAND1 (MAKET) upper scintillator; energy threshold  $\sim 1$  MeV; (b) 1 s time series of the 3 cm thick plastic scintillator of the same detector. A strong lightning discharge is seen as a vertical line interrupted TGE.

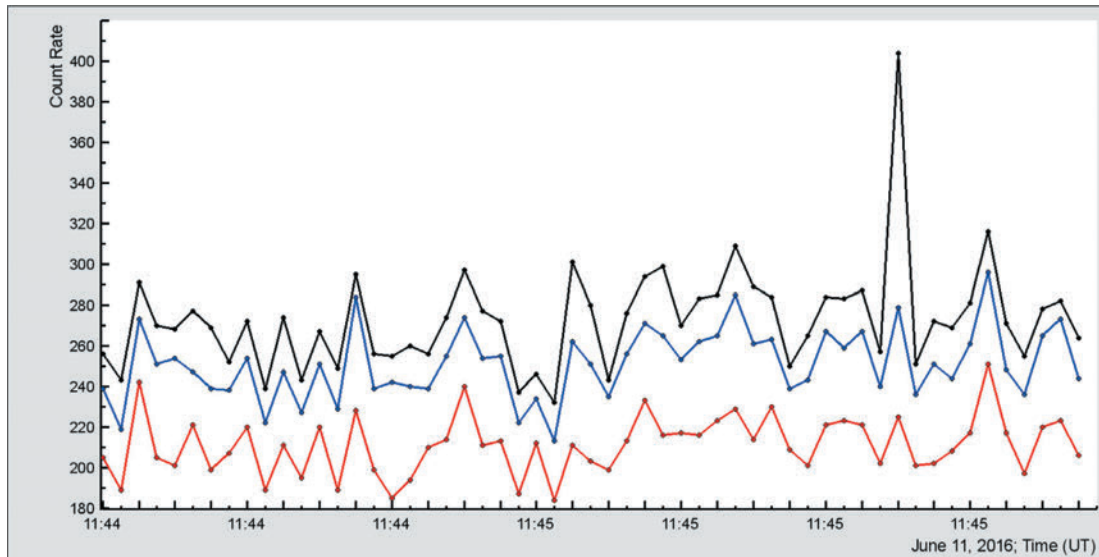


**Fig. 3.** Event on 11/6/2016, 11:44 UT. The 1 s time series of ArNM. Only time series corresponding to  $0.4 \mu\text{s}$  dead time (upper curve) demonstrates large peak due to counting multiple secondary neutrons coming within time span  $\sim 1$  ms; the time series corresponding to  $750$  and  $1200 \mu\text{s}$  dead time demonstrate no peak.

The heart of the DAQ system is the NI-myRIO board. It includes eight analog inputs, four analog outputs, 32 digital I/O lines, programmable FPGA, and a dual-core ARM Cortex-A9 processor (a high-performance processor implementing the full richness of the widely supported ARMv7-A architecture). With reconfigurable FPGA technology, we perform high-speed signal processing, high-

speed control, inline signal processing, and custom timing and triggering. For the control systems, one can also run advanced control algorithms directly in the FPGA fabric to minimize latency and maximize loop rates. "LabVIEW FPGA Module", which extends the LabVIEW graphical development platform, provides an alternative to HDL (Hardware description language) graphical programming

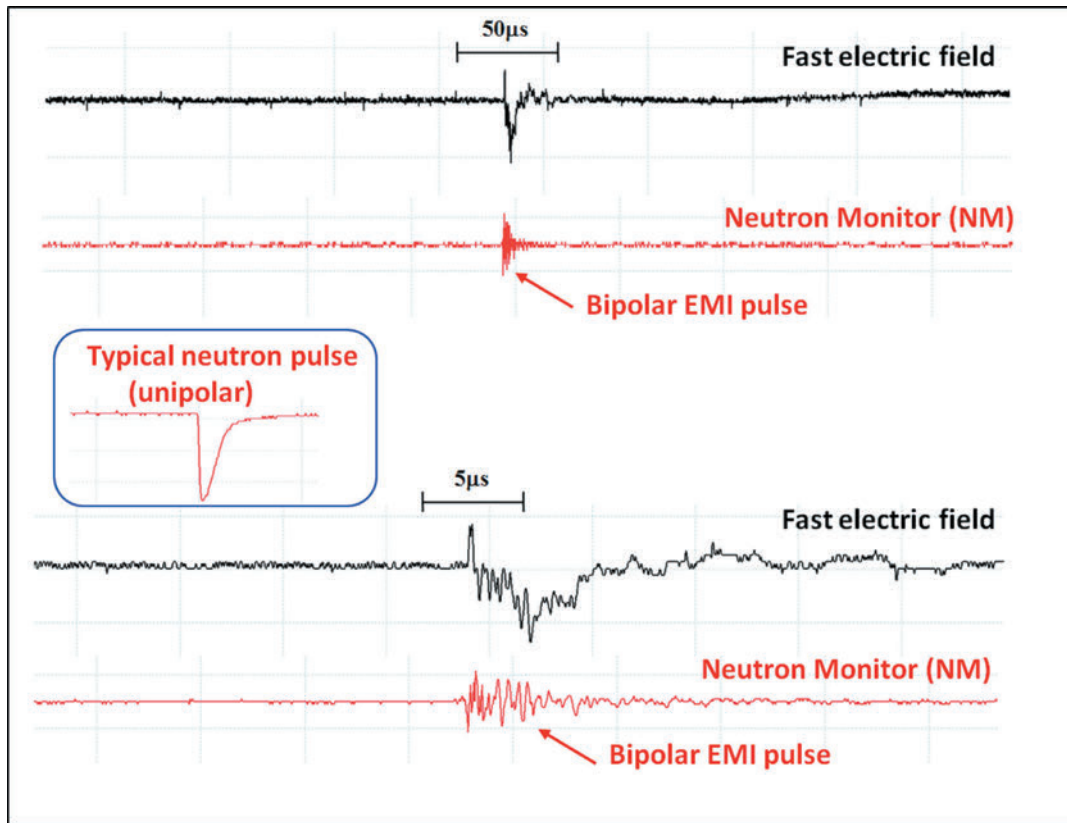


Fig. 4. Synchronized waveforms of fast electric field and neutron monitor shown in different time scales along with a typical waveform of neutron signal from the proportional counter of NM. Lightning flash occurred on 11 June 2016 at 11:44 UT.

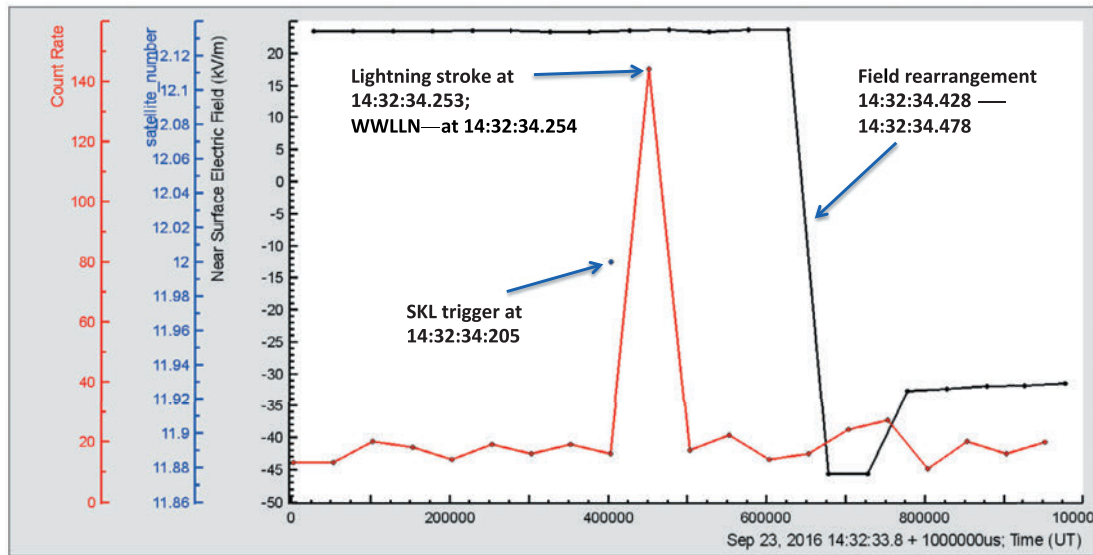
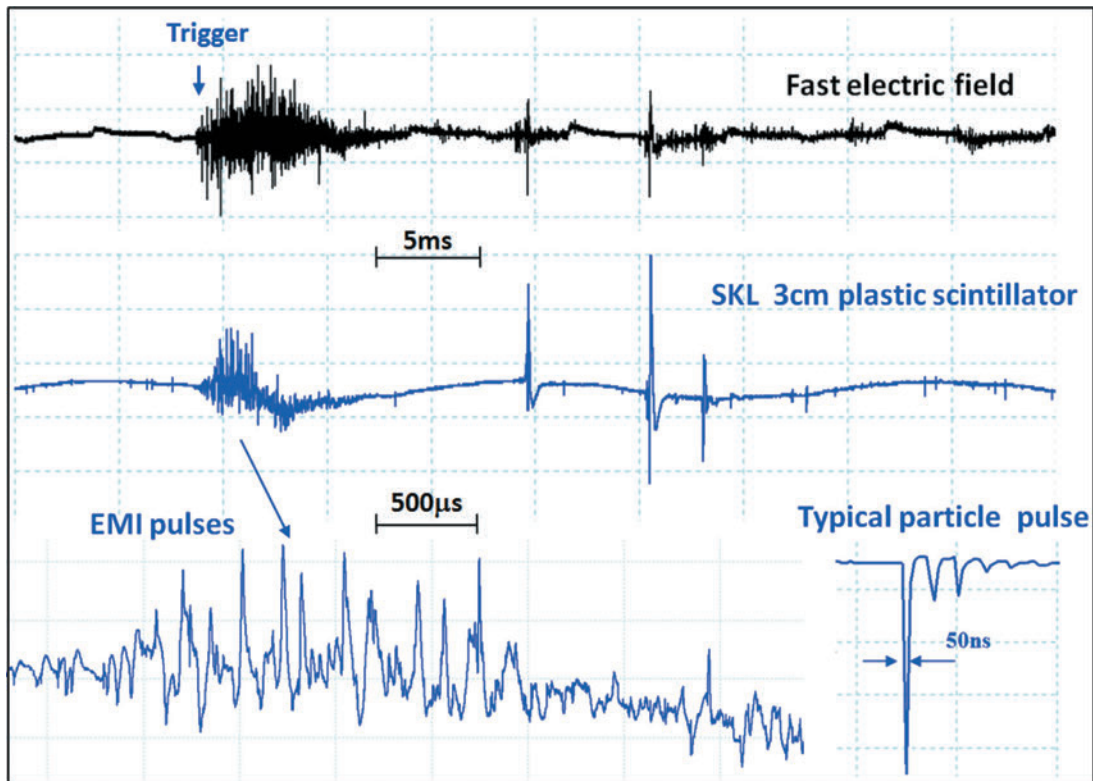


Fig. 5. 50 ms time series of the bottom scintillator of STAND1 detector and electrostatic field disturbances. The negative change of electrostatic field of 69.3 kV/m is produced by an inverted-polarity lightning flash.

approach that simplifies the task of interfacing to I/O and communicating data.

The commercial GPS receiver sends two types of data-stream to the board. The first is RS-232 ASCII data telling what time it is, at what latitude, longitude, and altitude the receiver is, and information about the satellites the receiver is using. An embedded

25 MHz counter on FPGA gives the exact time of the trigger. The 1PPS (one pulse per second) stream of the 5 V, 100 ms pulses re-sets this counter at each second. The leading edges of 1PPS signals from GPS receivers are synchronized within the accuracy of the non-military GPS system (about 100 ns). This feature allows time synchronization with 100 ns resolution.



**Fig. 6.** Typical EMI signature from atmospheric discharges in the particle detector waveform. Synchronised time-series of the pulses of fast electric field and signals from the plastic scintillator. SKL trigger occurred on 23 September 2016 at 14:32:34.205 UT.

Eight digital inputs of myRIO board are used for feeding signals from the variety of particle detectors operated on Aragats. Since the 2016 summer season, we connected to myRIO the STAND1 detector comprised of three vertically stacked plastic scintillators (thickness = 1 cm, area = 1 m<sup>2</sup>, energy threshold ~0.8 MeV) and one stand-alone plastic scintillator (thickness = 3 cm, area = 1 m<sup>2</sup>, energy threshold ~2 MeV), proportional counters of Aragats neutron monitor (ArNM) and NaI crystal based spectrometers (energy threshold ~0.3 MeV). Details on the performance of these particle detectors can be found in [13,14].

The myRIO pulse counting system can provide registration of very short time series (down to 1 ms) that enables the investigation the dynamic of TGE development and its relation to the lightning initiation (50 ms time series are stored currently).

Signals from the electric field sensor (electric mill EFM-100) were fed to the myRIO board via the TCP-IP connection (WiFi). The electrostatic field changes were recorded at a sampling interval of 50 ms; the amplitude resolution of electric field measurement was 0.01 kV/m, and the lightning location accuracy was  $\approx 1.5$  km. The firmware application provided by Boltek has a feature to share the electric field data via a network (it acts as a server for a client running under myRIO). The 8th channel is reserved for the synchronization pulse (the trigger) from a fast waveform recording device or from any of particle detectors.

At any triggering signal, the MyRio board generates a special output containing current value of particle detector counts, near-surface electric field value and precise time of arriving of the trigger signal. Thus, the fast waveform patterns are synchronized with particle fluxes and with slow (20 Hz) near surface electric field measurements.

The time series of particle detector count rates, electrostatic field measurements and service information (status of myRIO, time

delays, a number of satellites used for GPS timing), as well as the files containing digital oscilloscope data, are transferred via online PC to the MySQL database on CRD headquarters in Yerevan. All information is available via ADEI multivariate visualization code at the website <http://adei.crd.yerphi.am>; explanations are located in the Wiki section [17].

Two DAQ systems are operated independently in MAKET and SKL experimental halls on Aragats; triggers issued by both fast DAQ systems usually coincide within few ms. However, an optical link can transfer the trigger signal from SKL to MAKET experimental hall located at a distance of 100 m for the joint triggering of 2 networks of particle detectors and field meters.

### 3. *In situ* measurements of the thunderstorm particles on Aragats

Throughout this paper, we use the atmospheric electricity sign convention, according to which the downward-directed electric field or field change vector is considered to be positive. On 11 June 2016, large disturbances of the near-surface electrostatic field started at 10:45 UT (see Fig. 2(a)). The atmospheric pressure was 690.8 mbar; relative humidity—75%; wind speed 3–4 m/s; temperature  $\sim 5$  °C; no rain was registered. In Fig. 2(a) and (b) we show disturbances of the near-surface electric field; 1 min and 1 s time series of plastic scintillators of STAND1 array and distance to lightning in the top of both Fig. 2(a) and (b). Note the difference in the horizontal axes of Fig. 2(a) and (b); for 1 min time series, it is half of the hour, for 1 s time series it is 12 min. The typical shape of the electrostatic field disturbances (the electrostatic field in the deep negative domain for several minutes possibly accompanied by several short “bursts” touching positive domain and 1–2 negative lightning flashes with large amplitude) shown in Fig. 2(a)

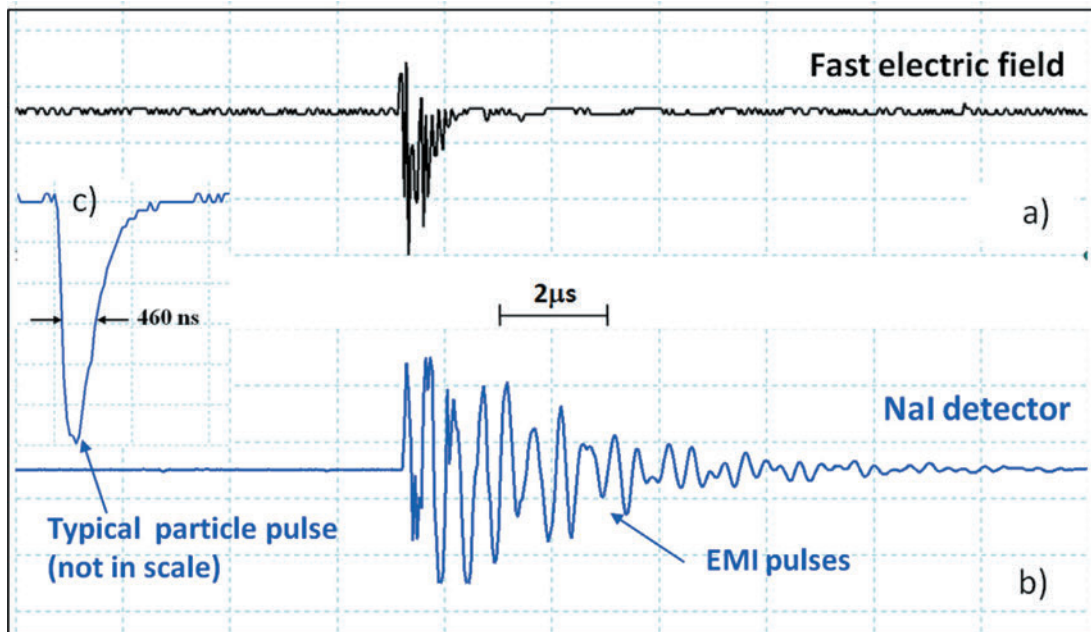


Fig. 7. Registration of the lightning flash occurred on May 15, 2016, 12:48:25. Waveforms of the fast electric field (a); NaI detector output (b); in the inset (c) is shown a typical shape of NaI detector response to an incident particle.

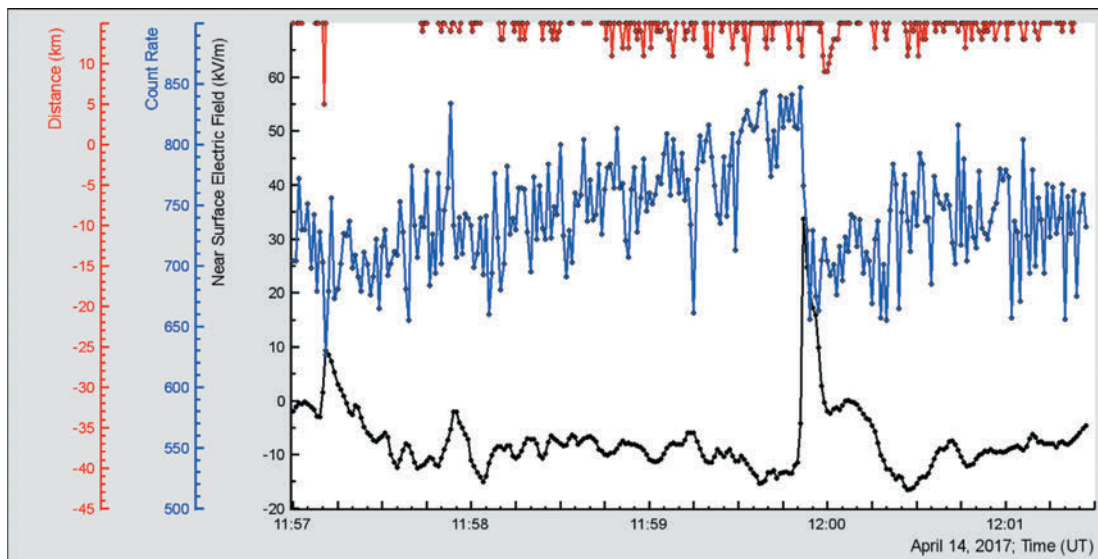
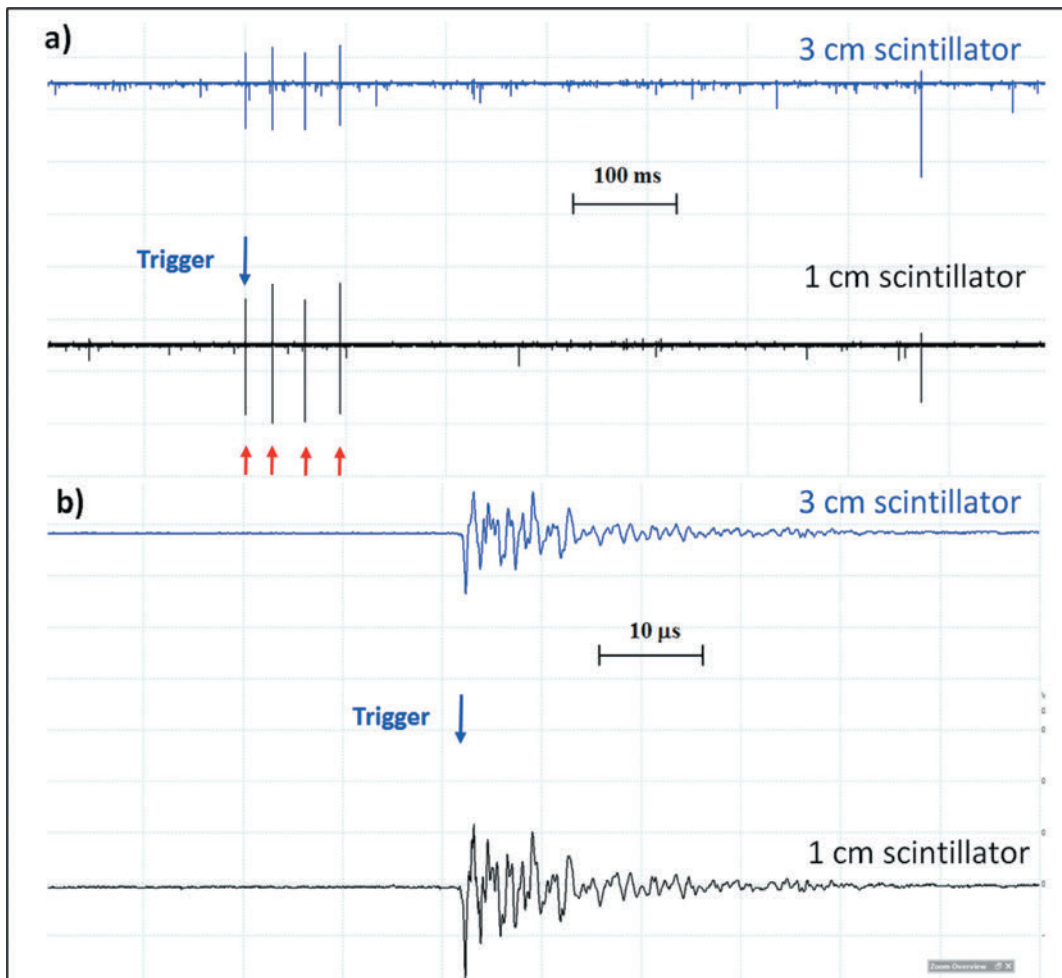


Fig. 8. TGE abruptly terminated by the lightning flash at 11:59:51.82; trigger was registered in MAKET and SKL hall at 11: 59:51.75; a surge of the electrostatic field started at 11:59:51.94; a decline of particle flux started at 11:59:51.83.

indicates the establishment of the lower dipole, which accelerates the CR electrons downwards. Accelerated electrons unleash multiple relativistic runaway avalanches measured on the earth's surface [7,8]. The enhanced particle flux (TGE) is shown in Fig. 2(a) by the 1 min time series of count rate of 1 cm thick plastic scintillator of STAND1 detector located nearby MAKET experimental hall (upper detector of 3 stacked above each other). The count rate enhancement was  $\approx 25\%$  corresponding to more than 35 standard deviations. From the recovery of the differential energy spectrum of TGE (see for instance Fig. 5 in [16]) it is apparent that after lightning flashes high-energy particle flux is totally terminated, whereas the flux of low energy particles (below 3 MeV) continues.

A strong lightning discharge that occurred at 11:45:22 abruptly terminated the TGE. However, the TGE restarted and was continuing  $\sim 4.5$  min until 11:50, when second strong lightning discharge finally terminated particle flux. The electrostatic field change caused by the lightning has a rise time of few hundreds milliseconds and recovery time of several seconds. Abrupt termination of particle flux caused by first lightning is shown in Fig. 2(b) with 1 s time series of the 3 cm thick scintillator of the same STAND1 detector. Count rate decreases from 731 at 11:45:22 down to 592 (19%) at 11:45:23. The electrostatic field starts to rise from an initial value of  $-30.6$  kV/m at 11:45:22.48, and shows a maximum of  $39.7$  kV/m at 11:45:22.58; the amplitude of field change was



**Fig. 9.** The “Shower Burst” event detected on 14 April 2017 by 1 cm thick and 3 cm thick 1 m area plastic scintillators located in the experimental hall MAKET. The signal shapes were synchronized with lightning flash (atmospheric discharge trigger was detected at 11: 59:51.75). The “bursts” are denoted by 4 small arrows in (a). The zoomed version of the first burst is shown in (b).

70.3 kV/m reached in 100 ms. Field recovery took much longer time  $\sim 10$  s.

The lightning discharge is a powerful wideband radio-wave emitter, which produces electric pulses in the cables, DAQ electronics, and power lines. To check if the registered pulses are electromagnetic interferences (EMI) or signals from relativistic particles born in the lightning bolt we performed synchronized measurements of the waveforms of fast electric field caused by atmospheric discharges and signals from particle detectors. The Aragats neutron monitor (ArNM, see details in [14]) measures the 1 s time series of count rates from 16 proportional counters filled with Boron gas. Neutrons and protons incident the detector’s 5 cm thick lead absorber generate in nuclear reactions numerous secondary neutrons, which are detected by the proportional counter.

In Fig. 3 we show three time series of detector count rates recorded with 3 different dead times. For the shortest dead time of 0.4  $\mu$ s, all secondary neutrons that enter the proportional counter are detected. For larger dead times of 750  $\mu$ s and 1250  $\mu$ s the particle count is suppressed after detecting the first neutron. Thus, a hypothetical particle burst from the lightning will be registered by ArNM as a large peak in the 1 s time series of ArNM count rate corresponding to 0.4  $\mu$ s dead time, and will not be registered with 750  $\mu$ s and 1250  $\mu$ s dead times, as it is shown in Fig. 3.

To prove that detected peak is due to burst of neutrons we need to examine the pulse shapes recorded by the oscilloscope. In Fig. 4, we demonstrate fast electric field waveforms from flat plate antenna and pulses from one of the proportional counters of ArNM and their zoomed versions. As a reference, a typical shape of the genuine neutron pulse is also shown.

By detecting the large peak at 11:45:23 in time-series of ArNM shown in Fig. 3 only, we can erroneously conclude that simultaneously with atmospheric discharge a large number of neutrons is generated in the lightning bolt. However, comparing the detailed pattern of the detected lightning bipolar pulses with the typical unipolar pulse that neutron generates on the output of the proportional counter (Fig. 4) we should reject the hypothesis of neutron production in the lightning bolt. All additional counts detected by the proportional counter at 11:45:23 are due to EMI.

On 23 September 2016 on Aragats station, a severe storm was observed with strong lightning activity and heavy rain at 13:50–14:50 UT. The temperature dropped from 3.6  $^{\circ}$ C to 1.3  $^{\circ}$ C; relative humidity was very high—98%, rain rate for 20 min touched a level of 1 mm/h. In Fig. 5 we show the trigger time, the estimated lightning flash time (by the large EMI pulse registered by one of the particle detectors) confirmed by the World-Wide Lightning Location Network (WWLLN) observation and the time series of the electric field rearrangement.

During the time span of several tens of ms after the trigger and before the lightning stroke, numerous atmospheric discharges induce plenty of pulses in a 52 cm diameter circular flat-plate antenna and simultaneously we observe bipolar pulses from particle detector (Fig. 6). A large number of bipolar “fake” signals (“trains” of pulses) from the 3 cm thick plastic scintillator of STAND1 detector mimicked a particle burst correlated with lightning. If one counts the number of particles in a burst only, it is possible to come to an erroneous inference that a registered peak is due to particles from the lightning bolt. However, the pulse from the charged particle registered by the scintillator has a typical unipolar shape (right bottom corner of Fig. 6). Using a fast digital oscilloscope, we can reliably distinguish bipolar pulses from atmospheric discharges and unipolar pulses from the particle detectors.

In Fig. 7(b) we show bipolar pulses registered by another detector, NaI crystal based spectrometer [13] produced by the strong atmospheric discharge (Fig. 7(a)). Signals from charged or neutral particles detected by NaI spectrometer are always unipolar.

Thus, we observe that all examined particle detectors (plastic scintillators, NaI crystals and proportional counters) can be triggered by a strong nearby lightning. However, by examining the shape of registered pulses we can easily discriminate EMI from the genuine particle pulse.

To confirm our results on the nature of “bursts” in the particle detectors we perform the pulse shape analysis from 3 particle detectors operated on Aragats Mountain. Two FSDAQ systems located in MAKET and SKL experimental halls separated by a distance of  $\sim 100$  m were triggered by two independent whip antennas. Several particle detectors were connected to both FSDAQ systems; data files with 1 s capture length and 40 ns sampling intervals were stored after each trigger (200 ms before and 800 ms after trigger). In April–June 2017 we detected numerous lightning flashes, which triggered the both FSDAQ systems;  $\sim 250$  joint triggers of MAKET and SKL DAQ system were registered. Careful examining of the shapes of output signals from flat plate antenna and from particle detectors proves that there was no genuine signal from any of the 3 particle detectors. All output “bursts” were bipolar and can be easily distinguished from the unipolar signals from particles traversing the detector. As an example of 2017 observations, we present the April 14 TGE, the first TGE of 2017 abruptly terminated by a lightning flash (Fig. 8). The outputs of the 2 plastic scintillators synchronized with trigger worked out by the whip antenna are shown in Fig. 9. We can detect 4 “Shower Bursts” in the Fig. 9(a); however, examining of the zoomed version shown in Fig. 9(b) proves that bi-directional signals from the DAQ electronics are EMIs and not genuine unipolar particle signals.

#### 4. Discussion and conclusion

New emerging field of atmospheric high-energy physics is still lacking firmly established theoretical model. Our paper is an attempt to clarify one of the often-discussed problems: the origin of extremely rare particle “bursts” coinciding with a lightning flash.

During numerous storms observed from 2016 summer to 2018 spring we did not observe any lightning producing relativistic particles in any of continuously monitored detectors. There were no intense particle bursts in monitored particle detectors within 200 ms before atmospheric discharge trigger and 800 ms after. However, as we mentioned, in our previous papers, we do not exclude that propagation of lightning leaders and emerging of strong electric fields around leader tips can produce X-rays and additional seed electrons involved in the runaway process.

For many years of observations, there are not more than a half-of-dozen reported events of possible lightning origin. In contrast, only on Aragats we detect hundreds of TGE events comprising of millions and millions of “ECSs”—extensive cloud showers [11];

or Micro Runaway Breakdowns (“MRBs”) [22]. All these alternative terms (Shower Burst [1], Inverse TGF [20], ECS [8], and MRB [22]) are related to one and the same entity—a runaway cascade developed in the strong electric field in the thunderstorm atmosphere. Continuum of gamma rays detected in Japan, China, Armenia, Slovakia and other countries can prolong till the return stroke and obviously include as well few gamma ray showers that coincide with the stepped leader propagation. Routinely observed copious gamma ray bursts integrated into a prolonged TGE can be explained by a standard RB/RREA theory with cosmic ray electron seeds [11,16,21].

If thunderclouds are high above particle detectors (1–2 km), like in Utah and Florida most gamma rays and all electrons are absorbed in the atmosphere. This is why the detection of TGEs at such sites is so rare. In contrast, thunderclouds at Aragats can be as low above particle detectors as 25–50 m. Only when the electric field in the cloud is extremely large the runaway electrons can collect from the electric field energy enough to unleash cascades so large, that gamma rays from RB/RREA cascades can be observed 1–2 km below the cloud on the earth’s surface. It is why the reported “lightning origin” events are so rare and so short.

To finally resolve the enigma of the lightning correlated high-energy particles we need more observation at many sites with various particle detectors and improved time resolution.

#### Acknowledgments

Authors would like to thank the staff of the Aragats Space Environmental Center for the uninterrupted operation of Aragats research station facilities. Authors are grateful to Yuri Stenkin for useful discussions and valuable comments. Work was supported by the Russian Science Foundation grant (project No. 17-12-01439).

The data for this paper are available on the WEB page of the Cosmic Ray Division (CRD) of the Yerevan Physics Institute, <http://adei.crd.yerphi.am/adei>. Figures from the paper can be easily reproduced with embedded multivariate visualization on-line program ADEI [17].

#### References

- [1] R.U. Abassi, T. Aby-Zayyad, M. Allen, et al., Gamma-ray showers observed at ground level in coincidence with downward lightning leaders, *JGR Atmos.* 123 (2018) 6864.
- [2] A.V. Agafonov, A.V. Bagulya, O.D. Dalkarov, et al., Observation of neutron bursts produced by laboratory high-voltage atmospheric discharge, *Phys. Rev. Lett.* 111 (2013) 115003.
- [3] A.V. Agafonov, V.A. Bogachenkov, A.P. Chubenko, et al., Observation of hard radiations in a laboratory atmospheric high-voltage discharge, *J. Phys. D* 50 (2017) 165202.
- [4] L.P. Babich, E.N. Donskoy, I.M. Kutsyk, et al., Comparison of relativistic runaway electron avalanche rates obtained from monte carlo simulations and from kinetic equation solution, *IEEE Trans. Plasma Sci.* 29 (2001) 430.
- [5] L.P. Babich, E.N. Donskoy, R.I. Il'kaev, I.M. Kutsyk, R.A. Roussel-Dupre, Fundamental parameters of a relativistic runaway electron avalanche in air, *Plasma Phys. Rep.* 30 (2004) 616.
- [6] B. Bartoli, P. Bernardini, X.J. Bi, et al., Observation of the thunderstorm-related ground cosmic ray flux variations by ARGO-YBJ, *Phys. Rev. D* 97 (2018) 042001.
- [7] A. Chilingarian, A. Daryan, K. Arakelyan, et al., Ground-based observations of thunderstorm-correlated fluxes of high-energy electrons, gamma rays, and neutrons, *Phys. Rev. D* 82 (4) (2010) 043009.
- [8] A. Chilingarian, G. Hovsepyan, A. Hovhannisyanyan, Particle bursts from thunderclouds: natural particle accelerators above our heads, *Phys. Rev. D* 83 (6) (2011) 062001.
- [9] A. Chilingarian, H. Mkrtchyan, Role of the lower positive charge region (LPCR) in initiation of the thunderstorm ground enhancements (TGEs), *Phys. Rev. D* 86 (2012) 072003.
- [10] A. Chilingarian, N. Bostanjyan, T. Karapetyan, L. Vanyan, Remarks on recent results on neutron production during thunderstorms, *Phys. Rev. D* 86 (2012) 093017.
- [11] A. Chilingarian, Thunderstorm ground enhancements—model and relation to lightning flashes, *J. Atmos. Solar-Terr. Phys.* 107 (2014) 68–76.
- [12] A. Chilingarian, G. Hovsepyan, G. Khanikyan, et al., Lightning origination and thunderstorm ground enhancements terminated by the lightning flash, *EPL* 110 (2015) 49001.

- [13] A. Chilingarian, G. Hovsepyan, E. Mantasakanyan, Mount Aragats as a stable electron accelerator for atmospheric high-energy physics research, *Phys. Rev. D* 93 (2016) 052006.
- [14] A. Chilingarian, G. Hovsepyan, L. Kozliner, Extensive air showers, lightning, and thunderstorm ground enhancements, *Astropart. Phys.* 82 (2016) 21–35.
- [15] A. Chilingarian, Long lasting low energy thunderstorm ground enhancements and possible Rn-222 daughter isotopes contamination, *Phys. Rev. D* 98 (2018) 022007.
- [16] A. Chilingarian, G. Hovsepyan, S. Soghomonyan, M. Zazyan, M. Zelenyy, Structures of the intracloud electric field supporting origin of long-lasting thunderstorm ground enhancements, *Phys. Rev. D* 98 (2018) 082001.
- [17] S. Chilingaryan, A. Beglarian, A. Kopmann, S. Vöcking, Advanced data extraction infrastructure: web based system for management of time series data, *J. Phys. Conf. Ser.* 219 (2010) 042034.
- [18] J.R. Dwyer, A fundamental limit on electric fields in air, *Geophys. Res. Lett.* 30 (2003) 2055.
- [19] T. Enoto, Y. Wada, Y. Furuta, et al., Photonuclear reactions triggered by lightning discharge, *Nature* 551 (7681) (2017) 481.
- [20] B.M. Hare, M.A. Uman, J.R. Dwyer, et al., Ground-level observation of a terrestrial gamma ray flash initiated by a triggered lightning, *J. Geophys. Res. Atmos.* 121 (2016) 6511.
- [21] A.V. Gurevich, G.M. Milikh, R. Rouseel-Dupre, Runaway electron mechanism of air breakdown and preconditioning during a thunderstorm, *Phys. Lett. A* 165 (1992) 463–1992.
- [22] A.V. Gurevich, K.P. Zybin, R.A. Roussel-Dupre, Lightning initiation by simultaneous of runaway breakdown and cosmic ray showers, *Phys. Lett. A* 254 (1999) 79.
- [23] A.V. Gurevich, V.P. Antonova, A.P. Chubenko, et al., Strong flux of low-energy neutrons produced by thunderstorms, *Phys. Rev. Lett.* 108 (2012) 125001.
- [24] A.V. Gurevich, V.P. Antonova, Chubenko, et al., The time structure of neutron emission during atmospheric discharge, *Atmos. Res.* 164 (2015) 339.
- [25] A.V. Gurevich, A.M. Almenova, V.P. Antonova, Observations of high-energy radiation during thunderstorms at Tien-Shan, *Phys. Rev. D* 94 (2016) 023003.
- [26] K. Kudela1, J. Chum, M. Kollárik, R. Langer, I. Strh.rsky', J. Baše, Correlations between secondary cosmic ray rates and strong electric fields at Lomnický štít, *J. Geophys. Res.* 122 (2017) 10700.
- [27] Y. Kuroda, S. Oguri, Y. Kato, R. Nakata, Y. Inoue, C. Ito, M. Minowa, Observation of gamma ray bursts at ground level under the thunderclouds, *Phys. Lett. B* 758 (2016) 286–291.
- [28] C. Köhn, G. Diniz, M.N. Harakeh, Leptons, hadrons and photons and their feedback close to lightning leaders, *J. Geophys. Res. Atmos.* 122 (2017) 1365.
- [29] S. Mallick, V.A. Rakov, J.R. Dwyer, A study of X-ray emissions from thunderstorms with emphasis on subsequent strokes in natural lightning, *J. Geophys. Res.* 117 (2012) D16107, doi:10.1029/2012JD017555.
- [30] T. Torii, T. Sugita, M. Kamogawa, et al., Migrating source of energetic radiation generated by thunderstorm activity, *Geophys. Res. Lett.* 38 (2011) L24801.
- [31] H. Tsuchiya, T. Enoto, K. Iwata, et al., Hardening and termination of long-duration gamma rays detected prior to lightning, *Phys. Rev. Lett.* 111 (2013) 015001.

## Long lasting low energy thunderstorm ground enhancements and possible Rn-222 daughter isotopes contamination

A. Chilingarian<sup>1,2,3</sup>

<sup>1</sup>*A. Alikhanyan National Lab (Yerevan Physics Institute), Yerevan 0036, Armenia*

<sup>2</sup>*National Research Nuclear University MEPhI, Moscow 115409, Russia*

<sup>3</sup>*Space Research Institute of RAS, Moscow 117997, Russia*



(Received 6 May 2018; published 11 July 2018)

Thunderstorm ground enhancements (TGEs) comprise large particle fluxes coming from the clouds that usually coincide with thunderstorms. Most of TGEs observed at the Aragats research station in Armenia during the last ten years originated from “beams of the electron accelerator” operating in the thunderclouds above the research station. Observed TGEs contain high-energy electrons and gamma rays (as well as neutrons) and usually last a few minutes. Starting from 2014, we use particle detectors tuned for the registration of lower energies particles coming from thunderclouds (starting from 0.3 MeV). In 2016, we already noticed that TGEs measured by particle detectors with a low energy threshold demonstrated a drastically larger duration. The flux of the high-energy particles (with energies up to 40 MeV) lasts 1–10 min; the lowest ones (less than 3 MeV)—more than two hours. All intense TGEs contain a high-energy peak and a prolonged low-energy extension lasting 2–3 h. In the presented paper, we describe examples of long-lasting TGEs and discuss correlations of enhanced particle fluxes with disturbances of the electric field and with precipitation.

DOI: [10.1103/PhysRevD.98.022007](https://doi.org/10.1103/PhysRevD.98.022007)

### I. INTRODUCTION

The bulk of information on particle fluxes correlated with thunderstorms (thunderstorm ground enhancements, TGEs, [1–3]) can be used to better understand the electrical structure of thunderclouds and high-energy processes in the atmosphere. In the strong intracloud electric fields, seed electrons from the ambient population of secondary cosmic rays gain such an amount of energy that they surpass the electron energy losses and “run away”, giving rise to electron-photon avalanches. Thus, the bulk of runaway electrons and gamma rays results in a runaway breakdown (RB, [4]), recently referred to as a relativistic runaway electron avalanche (RREA, [5–7]).

In the last decade, TGEs were investigated at the Aragats research station of the Yerevan Physics Institute. The Aragats research station is located at an altitude of 3200 m on the plateau near a large lake, and the height of the cloud base above the ground is typically 25–50 m in spring, increasing to 100–200 m in the summer. In the 2017–2018 campaigns on Aragats, we paid special attention to the long lasting low energy TGEs (LLL TGE). NaI spectrometers and large area plastic scintillators were used to detect enhanced fluxes of low energy fluxes (less than 3 MeV) of gamma rays. A concern is that it is very important to distinguish particle avalanches initiated by runaway electrons, from the radiation of environmental isotopes; those fluxes are also possibly increased during a thunderstorm [8,9].

Analysis of TGE data allows us to associate the particle flux enhancement with the acceleration of electrons in the strong electric fields emerging in a thundercloud [10]. However, even without noticeable disturbances of the near surface electric field, the flux of the low energy gamma rays is observed. We relate this phenomenon to the detection of Compton scattered gamma rays from remote electron-gamma ray cascades and/or randomly emerging small size stochastic electric fields above the detector site [11].

Neutral and charged particle fluxes are measured on Aragats with various elementary particle detectors. Count rates are measured with plastic scintillators, proportional chambers, and NaI and CsI crystals on the time scale from tens of nanoseconds to minutes. Energy release histograms are measured each minute with NaI crystals and each 20 s with 60-cm thick plastic scintillators. Energy release histograms are transformed to differential energy spectra using a detector response function calculated by GEANT simulations. Details of the particle detector operation and spectra deconvolution can be found in [12]. We also measure the near-surface electrostatic field with four electric field mills EFM-100 produced by the Boltek company. The stormy weather is usually accompanied by precipitation that possibly brings the radioactive isotopes, lightning flashes, strong wind, and fast changes of the atmospheric pressure. Abrupt decrease of atmospheric pressure can also increase the flux of most species of cosmic rays (although not exceeding  $\sim 0.5\%$ /mb).

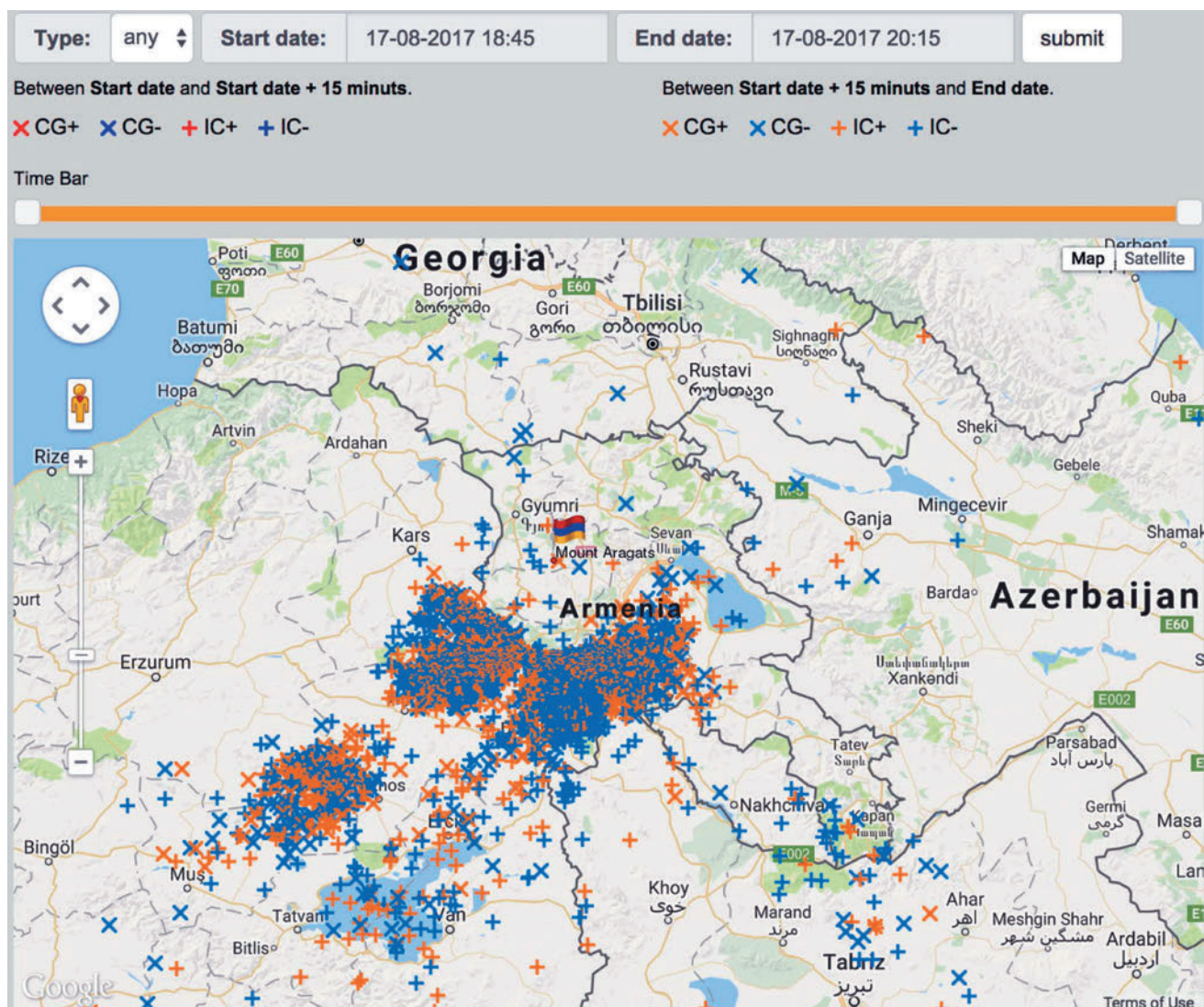


FIG. 1. Pattern of the storm in Armenia mapped by lightning flashes showing the approaching storm front; the Aragats station position on the map is flagged.

Thus, several meteorological factors can be responsible for the measured enhancements of the particle flux. One of the goals of this paper is to find out which of these factors is responsible for the long-lasting TGEs. That is why, in addition to the particle flux measurements, we are continuously monitoring a set of meteorological parameters with the Professional Davis Instruments Vantage Pro2 weather station (<http://www.davisnet.com/>). Also, we trace the evolution of the stormy weather on Aragats by mapping the approaching storm front with a sequence of atmospheric flashes registered by the lightning detector of the Boltek company (Boltek's StormTracker Lightning Detection System, powered by the software from Astrogenic systems, <http://www.boltek.com/stormtracker>).

The wideband fast electric field is measured by three circular flat plate antennas attached to fast digital oscilloscopes, which are triggered by the signal from active whip

antennas [13]. The oscilloscopes are also used to monitor signals from particle detectors. In our first papers on TGE measurements [1,2,14,15], we used particle detectors from the MAKET surface array [16], registering the electron content of extensive air showers (EAS). The energy threshold of these detectors was  $\sim 7$  MeV, suitable for the EAS research. In the presented paper, we analyze measurements obtained with particle detectors having a significantly smaller energy threshold of  $\sim 0.3$  MeV and  $\sim 0.7$  MeV that allows us to discover new important features of TGE.

## II. DETAILED ANALYSIS OF THE SUMMER TGE EVENT OCCURRED ON AUGUST 17, 2017

August 2017 was very stormy on Aragats with numerous lightning flashes, and the first snow appeared on mountain

peaks. On August 17, 2017, a storm started as usual in the Armenian highlands in Turkey, southwest from Aragats, and rapidly moved to Armenia’s border, see Fig. 1. The meteorological environments on August 17, 2017 changed abruptly as the storm reached Aragats, see Fig. 2, where we show in the top of the picture the outside temperature and dew point, the rain rate in the bottom, and atmospheric pressure and disturbances of the near surface electric field in the middle. The height of the cloud is estimated by the measured “spread” parameter—the difference between the air temperature and the dew point. The calculation of the height of cloud base is based on the assumption that the air temperature drops 9.84°C per 1000 m of altitude and the dew point drops 1.82°C per 1000 meters’ altitude.

There are several WEB calculators for the estimation of the altitude of a cloud (see, for instance, <http://www.csgnetwork.com/cloudaltcalc.html>). The simplified estimate consists in multiplying the spread measured in °C by 122 m. With this approach, we estimate the height of cloud before the start of the storm to be  $(9.1-6.0) * 122 \sim 400$  m; sharply decreased to  $\sim 130$  m on the start of the storm  $(7.0 - 5.9) * 122$ . Relative humidity also increased from 81% up to 92%, which signaled the decreasing of the height of the cloud base. During the spring storms when clouds were “sitting” on the station, the height of cloud base was 25–50 m and RH 96%–98%.

Atmospheric pressure increased from 694.8 at 18:40 up to 695.9 at 18:58 and back to 684.9 at 20:10,

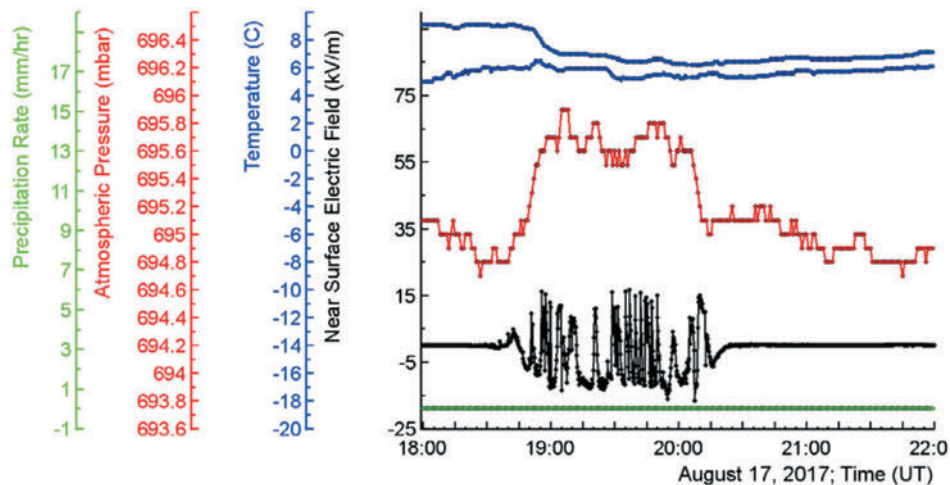


FIG. 2. Meteorological parameters measured on August 17, 2017. On the top of the picture, one-minute time series of the outside temperature and dew point are shown; in the middle—the atmospheric pressure and the disturbances of electric field; in the bottom—the rain rate.

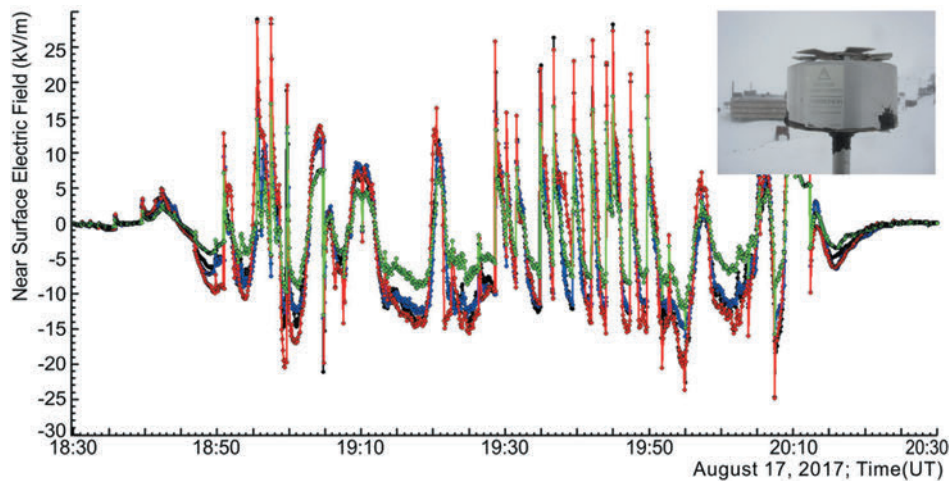


FIG. 3. The lightning activity during a large summer storm on Aragats was coherently detected by the network of the four electric mills EFM-100 of the Boltek company (see inset in the top right corner of the picture).

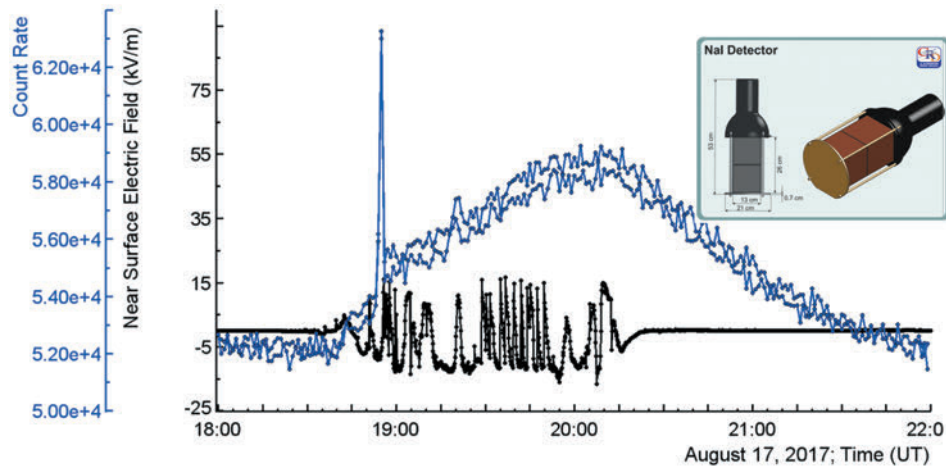


FIG. 4. Thunderstorm ground enhancement (TGE) as measured by the first and second crystals of the NaI network (see inset, energy threshold 0.3 MeV).

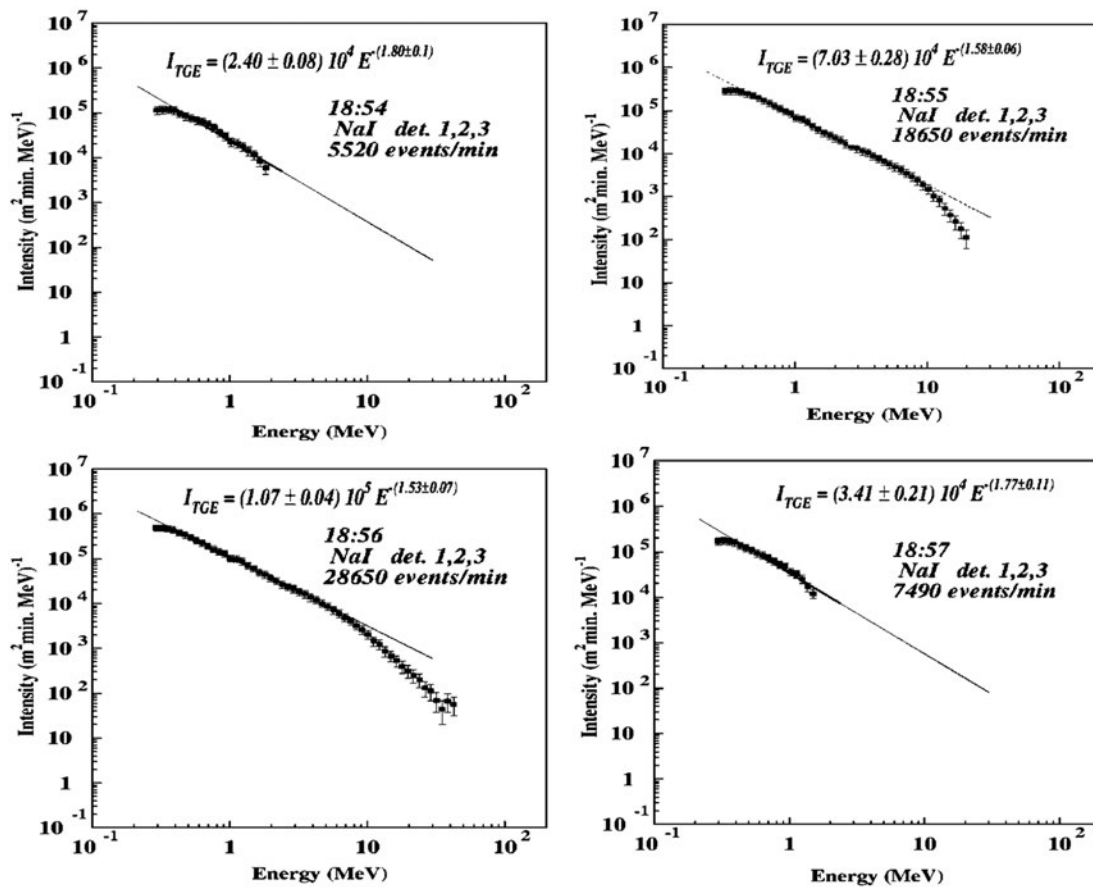


FIG. 5. The differential energy spectra of four subsequent minutes of TGE, recovered from the energy release histograms measured by the N1 and N2 crystals of the NaI network.

precisely coinciding in time with the disturbances of the near-surface electric field (from  $-25$  to  $30$  kV/m) measured by the electric mill located on the roof of the MAKET experimental hall. No rainfall was detected

by the Davis weather station located in the same place.

The storm started on Aragats at 18:36; the near-surface electric field remained disturbed for 1 h 42 min until 20:20,

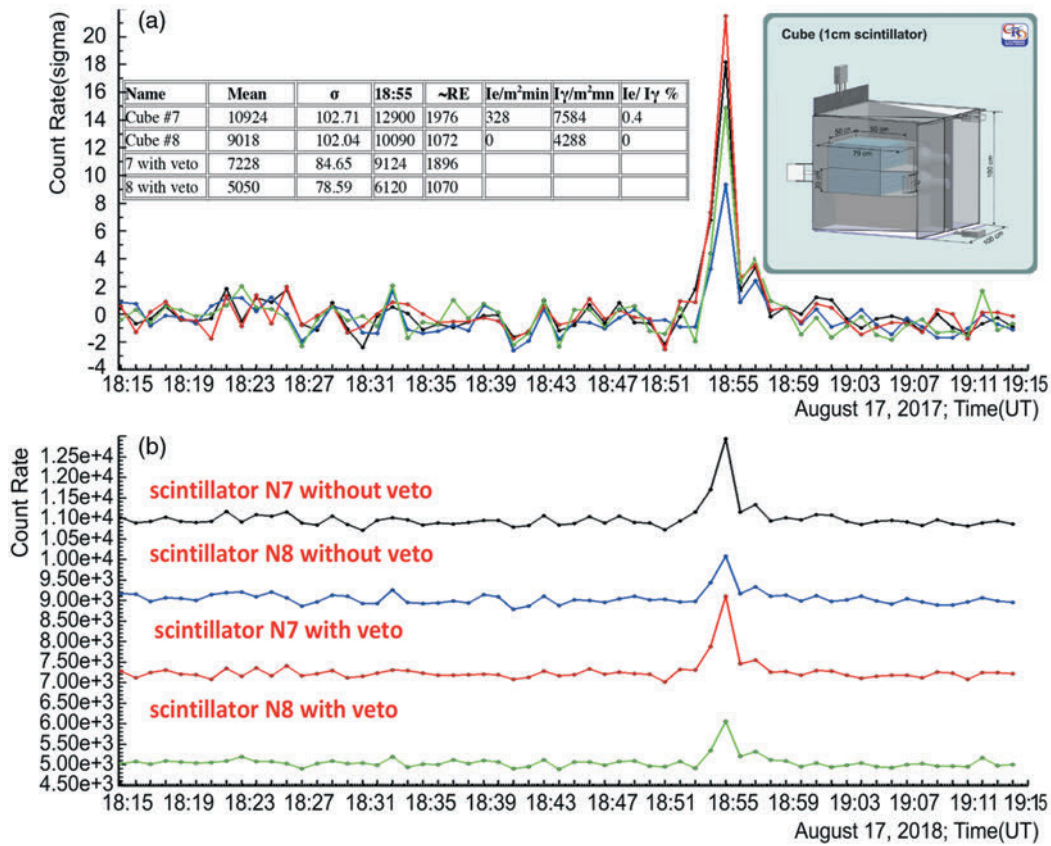


FIG. 6. Recovery of gamma rays and electron fluxes with the CUBE detector. Scintillators N7 and N8 are 20 cm thick 0.25 m<sup>2</sup> stacked plastics. In the Table inset, the recovered fluxes measured by both thick scintillators are shown.

see Fig. 2. The storm was accompanied with numerous lightning flashes (which produced abrupt changes of the electrostatic field of positive and negative polarity) detected by all four electric mills located on the Aragats station, see Fig. 3.

The rise of the particle flux measured by large NaI crystals (12.5 × 25 cm, energy threshold 0.3 MeV, see inset in Fig. 4) started at 18:40; after 13 min there occurred a 2-min long huge burst of particles coming from the cloud. At 18:55–18:56, the flux enhancement was 120%, corresponding to 43 standard deviations from the flux mean value measured before TGE. At 19:00–21:00, the particle flux enhancement was 3%–10%. In Fig. 4, we see that after the short burst, the particle flux continued to rise until the disturbances finished at ~20:20. After the storm calmed down at ~20:20, the flux started to decay and finally declined at ~22:00. Thus, the enhanced flux continued for ~2.5 h and during the last hour—without any detectable disturbance of the electric field.

From Fig. 2, it is obvious that precipitation plays no role in this TGE origination. As there was no rain through the ~4-h duration of the TGE, we cannot connect the enhanced flux with the Radon daughter's decays. The observed enhancement of the atmospheric pressure also cannot explain the TGE: the change of 1 mb can lead only to

an ~0.5% enhancement of the gamma ray flux, and only if the atmospheric pressure is decreasing and not increasing as we see in Fig. 2.

Also, we can notice that the flux enhancement coincides with disturbances of the electric field (a proxy of the intracloud electric field) and with a low location of the cloud base. According to the standard TGE model [17,18], the main negatively charged region with the emerged lower positively charged region (LPCR) formed a dipole which accelerates cosmic ray electrons downwards to the particle detectors located on the Earth's surface. If the electric field is strong enough, a RREA process is unleashed resulting in the large TGE. The explanation of the TGE decay phase that started at 20:20 in the absence of disturbances of the electric field needs additional simulation and experimental efforts and will be discussed in the Conclusions section.

In Fig. 5, we show the energy spectra of the TGE measured during the particle burst and just before and after it. The energy release histograms were measured with the same NaI crystals (N1 and N2); those count rates are posted in the Fig. 4. The differential energy spectra were recovered taking into account the spectrometer's response function for each of NaI crystal (see, for details, the supplement to [12]).

As we can see in Fig. 5, for 2 min only, the particle flux contains particles with energies up to 40 MeV. We identify

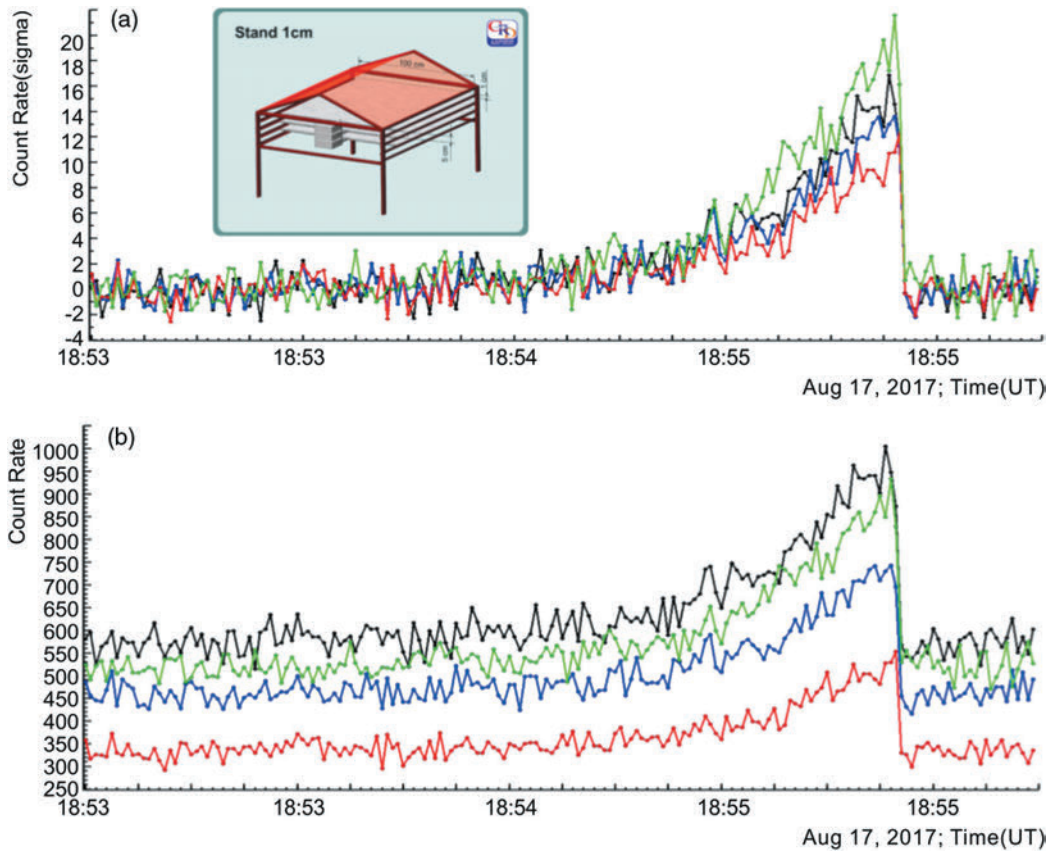


FIG. 7. One-second count rates of the STAND1 detector located nearby the MAKET experimental hall.

the high-energy particle flux with the RB/RRE avalanches released just above the particle detectors site. After the avalanche process stopped (or moved away), the energy spectra resumed to the lower energies, not exceeding few MeV. The cover of the NaI crystals stopped the electrons with energies below  $\sim 3$  MeV; thus, the particle registered by the NaI spectrometers before and after the 2-min burst were gamma rays only.

The RB/RREA cascade after leaving the lower dipole propagates in the air and, depending on the cloud height, the fraction of the electrons reaching the Earth's surface will dramatically change due to a much larger attenuation of electrons (see Fig. 19 of [14]). Usually, the RB/RREA flux as measured on the Earth's surface consists mostly of gamma rays contaminated by a small fraction of electrons. To estimate the electron fraction, we use a CUBE detector (inset in Fig. 6; see, for details, the supplement of [12]).

The CUBE detector consists of two stacked 20 cm thick plastic scintillators of a  $0.25 \text{ m}^2$  area surrounded by the "veto" that consists of six 1 cm thick and  $1 \text{ m}^2$  area plastic scintillators. A CUBE detector registered 1-min count rates of all eight scintillators and counts of the inner thick scintillators under the condition of the absence of an electronic signal from anticoincidence shielding. Because the 1 cm thick scintillators have a nonzero probability to miss the registration of a charged particle as well as to register a neutral particle, we develop a special method to estimate "true" intensities (integral energy spectra) of gamma ray and electron fluxes (see Appendix A of [14]). In Fig. 6(b), we show the count rates of thick scintillators with and without the veto option. In Fig. 6(a), we show the same count rates but in the units of standard deviation (the number of). In the inserted table, we show the mean values of the count rates and variances before a particle burst and

TABLE I. The characteristics of short burst of high-energy particles occurred on August 17, 2017.

Name	Mean	$\sigma$	18:55:33	Sign. peak $N\sigma$	% of drop
STAND1 MAKET Ch. 1	571.4	25.4	1002	17	76
STAND1 MAKET Ch. 2	456.3	22.7	741	14	62
STAND1 MAKET Ch. 3	329.7	18.1	553	12	67
STAND1 MAKET Ch. 4	510.9	22.3	932	21	75

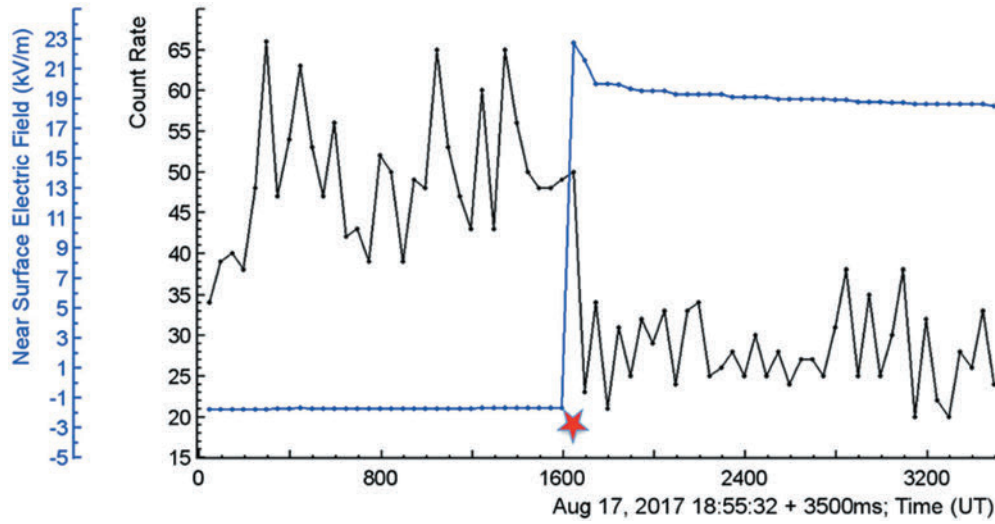


FIG. 8. The 50-ms time series of the STAN1 upper scintillator count rate (located outdoors nearby the MAKET experimental hall) and of the near surface electric field measurements. The asterisk indicates the time of lightning flash registered by the World-Wide Lightning Location Network (WWLLN, detection at 18:55:33.630). The horizontal axes started from 18:55:32; each tick on the axes corresponds to 100 ms.

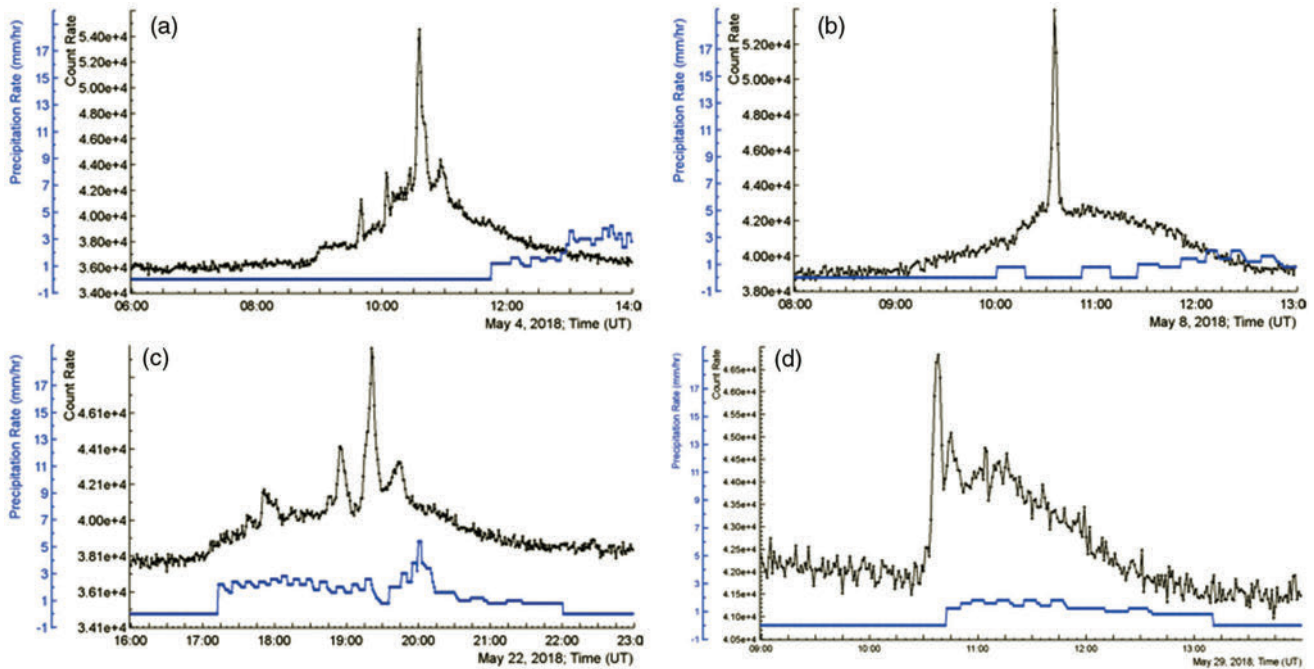


FIG. 9. One-minute time series of the count rates of the 1 cm thick 1 m<sup>2</sup> area plastic scintillator. In the bottom of the frames, we show rain rate in mm per hour.

during the minute of maximal flux, recovered intensities, and electron fractions for both inner 20 cm thick scintillators. The energy thresholds of thick scintillators are estimated to be 5.8 and 6.4 MeV (scintillator N7 is above N8, see Table 1 in [19]). For a lower energy threshold (scintillator N7), the electron contamination is  $\sim 4\%$  and vanishing at higher energies (scintillator N8).

To understand the dynamics of TGE and to investigate the relation of the particle fluxes and lightning flashes, we need to register the time series of the TGEs and electric field disturbances in much more detail. Fast electronics provide the registration of TGEs on time scales of 1 sec and 50 ms, compatible with the fast processes in thunderstorm atmospheres. In Figs. 7 and 8, we demonstrate the

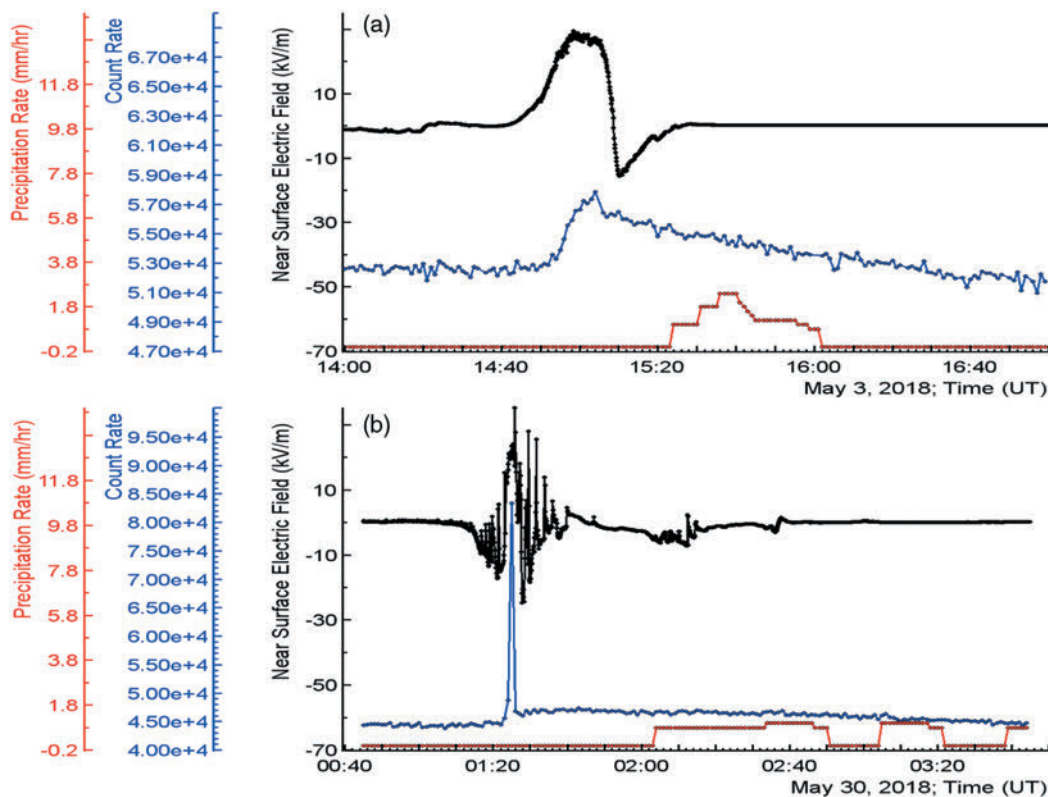


FIG. 10. TGE events registered by the NaI detector. In the top of figures, we show disturbances of the near surface electric field; in the bottom—the rain rate. In the middle—the one-minute count rate of the NaI detector.

possibilities of TGE and lightning analysis at these time scales. The abrupt decay of the TGE is better shown in the one-second time series of the STAND1 detector shown in Fig. 7. The network of the STAND1 detectors comprises three identical units located on Aragats station, each of which consists of three stacked 1 cm thick and 1 m<sup>2</sup> area plastic scintillators and one stand-alone 3 cm thick plastic scintillator of the same type (inset in Fig. 7; see, for details, the supplement of [12]).

In Fig. 7(b), we show the one-second count rates of the stacked and stand-alone scintillators. In Fig. 7(a), we show the same count rates, but plotted in units of the standard deviations from the mean value measured just before the TGE. In Table 1, we demonstrate the numerical values, significances of peaks (in), and count rate drops for each scintillator. The sharp decay of particle flux that occurred at 18:55:33 is enforced by a lightning flash which stopped the RB/RREA process in the cloud [20,13]. In [21], we demonstrate that strong particle fluxes usually precede lightning flashes.

For the in-depth research of the lightning-particle flux relations, we use a fast data acquisition system based on the National Instruments myRIO board, which produced the GPS time stamp of the record and provided registration of the 50 ms time series of detector count rates (see details in [22]).

In Fig. 8, we can see that the rearrangement of the electric field started at 18:55:33.600. The near surface electric field of  $-1.6$  kV/m after 50 ms reached a value of 22 kV/m, i.e., the amplitude was  $\sim 23.6$  kV/m. The abrupt decay of the particle flux started at the same time; the flux decreased from 50 to 23 particles, i.e., by 54% in 50 ms. This flash was registered by the World-Wide Lightning Location Network (WLLN, detection at 18:55:33.630).

### III. LONG LASTING TGES AND RAINFALLS

In Fig. 9, we summarize typical shapes of TGEs observed in May 2018, when an GE especially rich harvest of TGEs was collected. We consider only TGEs accompanied with rainfall to examine its possible influence on the particle flux. The one-minute time series of count rates were measured by a 1 cm thick 1 m<sup>2</sup> area plastic scintillator (energy threshold  $\sim 0.7$  MeV, [19], Fig. 10, Table 1) located outdoor nearby the MAKET experimental hall; the rain rate was measured by the Davis weather station located on the roof of the same building.

Displayed TGEs contain a high-energy part (sharp peaks—gamma rays and electrons with energies up to  $\sim 40$  MeV) lasting a few minutes and a low-energy part (gamma rays below 3 MeV) lasting several hours; see an example of the energy spectra in Fig. 5. In Fig. 9, we can see that TGEs are not connected with rainfall. In Fig. 9(a),

the rain started only at the end of the TGE; in Figs. 9(b), 9(c), and 9(d) strengthening of the rainfall coincides with the decay phase of the TGE. Many other TGEs were not accompanied with rain at all. The TGEs of May 2018 occurred at a highly disturbed near-surface electric field. For the clarity of the displayed information, we do not post the time series of the near surface electric field in Fig. 9 (it is similar to one shown in Fig. 4).

In Fig. 10, we show the count rate enhancement, disturbances of the near-surface electric field, and the rain rate of two TGE events that occurred in the May 2018. The May 3, 2018 event [Fig. 10(a)] is rather small:  $\sim 10\%$  enhancement of the count rate of the NaI detector. Rainfall that started after the TGE reached the maximum did not influence the count rate; the decay of the TGE continued. A large event ( $\sim 100\%$  count rate enhancement) occurred on May 30, 2018 [Fig. 10(b)], again accompanied by a rainfall at the decay phase of TGE. For both TGEs, rain apparently does not influence the count rate. The atmospheric pressure was not strongly disturbed during both events; the fluctuation does not exceed 1 mb. Thus, we can connect the initiation of a TGE only with disturbances of the electric field and not with precipitation or atmospheric pressure variations.

#### IV. CONCLUSIONS

Each year, Aragats facilities register more than 100 TGEs, proving that Mount Aragats is a stable electron accelerator for atmospheric high-energy physics research [23]. TGEs varied significantly in intensity and continuation; nonetheless, we can outline some important features confirming Aragats 10-year observations [1,14,18]:

- (i) TGEs occurred during strong storms approaching Armenia mostly from the Armenian highlands in Turkey, southwest from Aragats, which disturbed the near surface electric field at a particle detector location.
  - (ii) A strong TGE started with a low energy flux (less than 3 MeV), turning to a short (1–10 min) and intense peak containing high-energy particles (up to 40 MeV).
  - (iii) After an abrupt decline of the high-energy part of the TGE, usually forced by a lightning flash, the low-energy flux continued with a prolonged decay. Thus, we detected a sizable flux of gamma rays during the hours of the “fair weather” when the near surface electric field was not disturbed.
  - (iv) The radioactive decay from radon isotopes contained in the rain, as well as the variations of atmospheric pressure (barometric effect) are not the cause of TGEs.
- There are two main hypotheses about the origin of the prolonged gamma ray flux in the absence of sizable disturbances of the near-surface electric field:
- (i) TGEs originated in the thunderstorm atmospheres due to an emerging strong electric field between differently charged layers in the clouds [14,18,24]. Seed electrons from the ambient population of secondary cosmic rays “run away” [4], accelerated, and form electron-gamma ray avalanches reaching and detected at the Earth’s surface. If the cloud with a strong electric dipole inside migrates from the detector site, Compton scattered gamma rays can reach the detector under large zenith angles and be registered for an extended time span.
  - (ii) Small-scale stochastic electric fields randomly emerging in a thundercloud accelerate electrons and enhance the probability of bremsstrahlung radiation and boosts the low energy gamma ray flux.

#### ACKNOWLEDGEMENTS

The detailed analysis of these scenarios will be presented in our next publication. The data for this paper are available via the multivariate visualization software ADEI on the WEB page of the Cosmic Ray Division (CRD) of the Yerevan Physics Institute in Ref. [25]. Author thanks the staff of the Aragats Space Environmental Center for the uninterrupted operation of Aragats research station facilities. Author thanks Hovsepyan Gagik for recovering the energy spectra posted in Fig. 5 and M. Panasuk and V. Bogomolov for useful discussions. Author received support from the Russian Science Foundation grant (Project No. 17-12-01439).

[1] A. Chilingarian, A. Daryan, K. Arakelyan, A. Hovhannisyanyan, B. Mailyan, L. Melkumyan, G. Hovsepyan, S. Chilingaryan, A. Reymers, and L. Vanyan, Ground-based observations of thunderstorm-correlated fluxes of high-energy electrons, gamma rays, and neutrons, *Phys. Rev. D* **82**, 043009 (2010).  
 [2] A. Chilingarian, G. Hovsepyan, and A. Hovhannisyanyan, Particle bursts from thunderclouds: Natural particle accelerators above our heads, *Phys. Rev. D* **83**, 062001 (2011).

[3] A. Chilingarian, G. Hovsepyan, and E. Mantasakanyan, Mount Aragats as a stable electron accelerator for atmospheric high-energy physics research, *Phys. Rev. D* **93**, 052006 (2016).  
 [4] A. V. Gurevich, G. M. Milikh, and R. A. Roussel-Dupre, Runaway electron mechanism of air breakdown and pre-conditioning during a thunderstorm. *Phys. Lett.* **165A**, 463 (1992).

- [5] J. R. Dwyer, A fundamental limit on electric fields in air, *Geophys. Res. Lett.* **30**, 2055 (2003).
- [6] L. P. Babich, E. N. Donskoy, R. I. Il'kaev, I. M. Kutsyk, and R. A. Roussel-Dupre, Fundamental parameters of a relativistic runaway electron avalanche in air, *Plasma Phys. Rep.* **30**, 616 (2004).
- [7] V. V. Alexeenko, N. S. Khaerdinov, A. S. Lidvansky, and V. B. Petkov, Transient variations of secondary cosmic rays due to atmospheric electric field and evidence for pre-lightning particle acceleration, *Phys. Lett. A* **301**, 299 (2002).
- [8] F. Fabr , J. Montany , N. Pineda, J. Montany , N. Pineda, O. Argem , O. A. van der Velde, D. Romero, and S. Soula, Analysis of energetic radiation associated with thunderstorms in the Ebro delta region in Spain, *J. Geophys. Res. Atmos.* **121**, 9879 (2016).
- [9] V. Bogomolov, A. Chilingarian, G. Garipov *et al.*, Study of TGEs and gamma-flashes from thunderstorms in 20–3000 keV energy range with SINP MSU gamma-ray spectrometers, *Proceedings of 6-th TEPA Symposium*, p. 50, Nor Amberd, 2015 (Tigran Mets, Yerevan, 2015); [http://www.iaea.org/inis/collection/NCLCollectionStore/\\_Public/48/037/48037534.pdf](http://www.iaea.org/inis/collection/NCLCollectionStore/_Public/48/037/48037534.pdf).
- [10] A. Chilingarian, G. Hovsepyan, and L. Vanyan, On the origin of the particle fluxes from the thunderclouds: Energy spectra analysis, *Europhys. Lett.* **106**, 59001 (2014).
- [11] D. I. Iudin Lightning initiation as a noise induced kinetic transition, *Radiophys. Quantum Electron.* **60**, 374 (2017).
- [12] A. Chilingarian, G. Hovsepyan, and B. Mailyan, In situ measurements of the runaway breakdown (RB) on Aragats mountain, *Nucl. Instrum. Methods Phys. Res., Sect. A* **874**, 19 (2017).
- [13] A. Chilingarian, Y. Khanikyants, E. Mareev, D. Pokhsranyan, V. A. Rakov, and S. Soghomonyan, Types of lightning discharges that abruptly terminate enhanced fluxes of energetic radiation and particles observed at ground level, *J. Geophys. Res. Atmos.* **122**, 7582 (2017).
- [14] A. Chilingarian, B. Mailyan, and L. Vanyan, Recovering of the energy spectra of electrons and gamma rays coming from the thunderclouds, *Atmos. Res.* **114–115**, 1 (2012).
- [15] A. Chilingarian, G. Hovsepyan, and L. Kozliner, Thunderstorm ground enhancements: Gamma ray differential energy spectra, *Phys. Rev. D* **88**, 073001 (2013).
- [16] A. Chilingarian, G. Gharagyozyan, S. Ghazaryan, G. Hovsepyan, E. Mamidjanyan, L. Melkumyan, V. Romakhin, A. Vardanyan, and S. Sokhoyan, Study of extensive air showers and primary energy spectra by MAKET-ANI detector on mountain Aragats, *Astropart. Phys.* **28**, 58 (2007).
- [17] A. Chilingarian and H. Mkrtchyan, Role of the lower positive charge region (LPCR) in initiation of the thunderstorm ground enhancements (TGEs), *Phys. Rev. D* **86**, 072003 (2012).
- [18] A. Chilingarian, Thunderstorm ground enhancements—Model and relation to lightning flashes, *J. Atmos. Terr. Phys.* **107**, 68 (2014).
- [19] A. Chilingarian, S. Chilingaryan, and G. Hovsepyan, Calibration of particle detectors for secondary cosmic rays using gamma-ray beams from thunderclouds, *Astropart. Phys.* **69**, 37 (2015).
- [20] A. Chilingarian, S. Chilingaryan, and A. Reymers, Atmospheric discharges and particle fluxes, *J. Geophys. Res.* **120**, 5845 (2015).
- [21] A. Chilingarian, S. Chilingaryan, T. Karapetyan, L. Kozliner, Y. Khanikyants, G. Hovsepyan, D. Pokhsranyan, and S. Soghomonyan, On the initiation of lightning in thunderclouds, *Sci. Rep.* **7**, 1371 (2017).
- [22] D. Pokhsranyan, Fast data acquisition system based on NI-myRIO board with GPS time stamping capabilities for atmospheric electricity research, *Proceedings of TEPA 2015* (Nor Amberd, Tigran Mets, 2015), p. 23.
- [23] A. Chilingarian, G. Hovsepyan, and L. Kozliner, Extensive air showers, lightning, and thunderstorm ground enhancements, *Astropart. Phys.* **82**, 21 (2016).
- [24] K. Kudela, J. Chum, M. Koll rik *et al.*, Correlations between secondary cosmic ray rates and strong electric fields at Lomnick y št t, *J. Geophys. Res.* **122**, 70010 (2017).
- [25] <http://adei.crd.yerphi.am/adei>.

## Monitoring of the atmospheric electric field and cosmic-ray flux for the interpretation of results in high-energy astroparticle physics experiments.

Ashot Chilingarian<sup>1,\*</sup>, Johannes Knapp<sup>2</sup>, and Mary Zazyan<sup>1</sup>

<sup>1</sup>A. Alikhanyan National Lab (Yerevan Physics Institute), Yerevan, Armenia.

<sup>2</sup>Deutsches Elektronen-Synchrotron, Zeuthen, Germany.

**Abstract.** Atmospheric electric fields influence experiments using the atmosphere as a detector for very weak fluxes of highest-energy gamma rays and protons/nuclei coming from galactic and extragalactic sources. Multiplication of electrons and gamma rays in strong atmospheric electric fields change particle numbers and energy spectra of the secondary shower particles and consequently influence the reconstructed properties of the primary particles. Here, we present a MC study using the CORSIKA package to explore and quantify these effects.

### 1 Introduction

Atmospheric electricity is always present in the atmosphere, enabling natural acceleration of charged particles. Potential differences in or nearby thunderclouds and between the Earth's surface and clouds accelerate ever-present free charged particles from interactions of gamma rays and cosmic rays with atoms of the atmosphere. The direction of the acceleration depends on the charge of particles and the field strength and orientation. The most prominent effects of strong atmospheric electricity are thunderstorm ground enhancements (TGEs) - huge fluxes of gamma rays, electrons and neutrons which can be detected on Earth's surface. On Mount Aragats in Armenia, the rather stable flux of secondary particles from cosmic-ray air showers are often multiplied many times for a several minutes in the presence of strong electric fields (see [3], [4], [5]), and the energy spectra of secondary particles can be changed significantly. Recently, even long-lasting TGEs of several hours duration have been discovered [8]. Thus, electric fields and processes in the atmosphere can have important consequences on experiments which measure very-high-energy gamma rays and cosmic rays from galactic and extragalactic sources. At high energies, such experiments use large volumes of atmosphere as an "amplifier" that transforms each of the rare primary particles into a particle shower of numerous lower-energy electrons, gamma rays, mesons, protons and neutrons, which is much easier to detect than the primary particles alone. Very-high-energy gamma rays, are detected with so-called atmospheric Cherenkov telescopes (ACTs) with effective areas of  $10^4$ - $10^6$  m<sup>2</sup>. Cosmic rays are detected with gigantic arrays of particle detectors on the Earth's surface, which register the secondary particles of extensive air showers (EAS) on up to  $3 \times 10^9$  m<sup>2</sup>. In all air-shower experiments, the number of secondary particles in a shower is the basis

for the reconstruction of the energy of the primary particle and the longitudinal shower development is the key for the determination of the primary particle type. We discussed that these observables are susceptible to the atmospheric electric fields, and biases can occur not only during thunderstorms, but also several hours after storm ceased, due to the permanent presence of weak electric fields in the post-storm atmosphere. Crucial to the understanding of possible biases of the EAS parameters is the knowledge of the atmospheric electric fields. As was stated in [18], the intensity of EAS are radically changed after propagation in the atmospheric electric fields. To estimate their possible influence, we performed an initial Monte Carlo study with the CORSIKA code which shows that atmospheric electric fields should be considered in EAS physics.

### 2 The electrical atmosphere and particle fluxes

We use a new observable in the atmospheric electricity research, namely, the steady particle fluxes from the clouds to ground. The origin of the fluxes of electrons, gamma rays and neutrons detected on the Earth's surface are Runaway Breakdown (RB) processes [12], nowadays mostly referred to as Relativistic Runaway Electron Avalanches (RREA, [19], [10]) and MODification of the energy Spectra of the electrons (MOS, [6]). Simultaneously to the measurements of cosmic-ray particles, also near-surface electrostatic fields and lightning strikes are recorded. The combination of detailed measurements of particle fluxes and spectra at ground and electric fields and lightning flashes, first investigated on Aragats, allows monitoring the formation of charge accumulations in the overhead atmosphere. The electron acceleration towards Earth is due to the electric field between the main negative charge region in the middle of the cloud and the positive charge that is induced by it on the ground. This field is

\*e-mail: chili@aragats.am

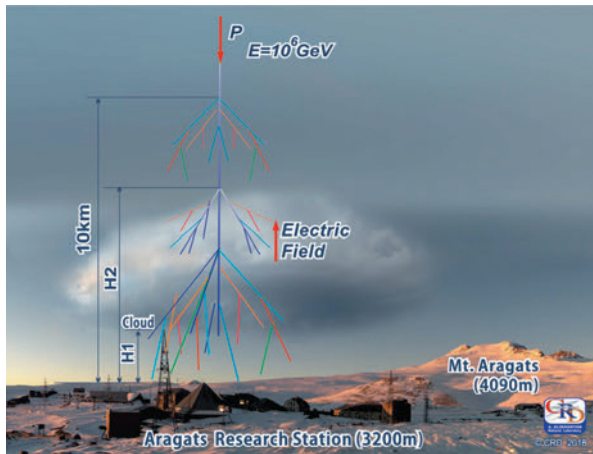


**Figure 1.** EAS development in an atmosphere with electric field.

significantly increased by the electric field between the main negative region and an emerging Lower Positive Charge Region (LPCR) still within the cloud. The maximal intensity (and maximal energy of particles) of TGEs is observed when the strength of the local electric field in the cloud exceeds the “runaway” threshold and RB/RREA avalanches start to develop downwards. Such conditions are met above the LPCR. The lightning leader cannot make its path through the LPCR, and cloud-to-ground flashes are suppressed [15].

The gamma-ray flux attenuates due to lightning flash that brings free electrons from the main negatively charged region to LPCR (inverted intracloud flash) or to the ground (cloud to ground flash). Thus, the charge in the layers, and consequently the electric field decreases and RB/RREA cascades vanish (see Figure 5 of [8]). However, the electric field in the cloud still remain disturbed and low energy gamma-ray flux continue.

In the cartoon (Figure 1) we show the electron-gamma ray avalanche developing in the bottom of the thundercloud above the Aragats high-altitude research station of the Yerevan Physics Institute [2]. The avalanche comes out of the base of the cloud and illuminates various particle detectors measuring count rates of charged and neutral particles and their energies. The distance to the cloud base in spring and autumn is rather short  $H1=25-50$  m; in Summer, it is  $H1=50-500$  m. In our simulation studies of TGEs we assume the strength of electric field in the cloud up to 1.8 kV/m extended over up to  $H2-H1=1$  km. Values of electric field and elongation used in simulation have been measured in balloon flights [14].

In the Figure 2, we show two long-lasting TGEs occurred on August 17 and October 10, 2017. The particle flux remained higher for  $\sim 1.5$  hours after the decline of the thunderstorm. Electric field sensors, so called electric mills, located near the particle detectors do not record any significant disturbances and only by the particle detectors counts, we can deduce that there is still a small electric field in the atmosphere that can affect characteristics of air show-

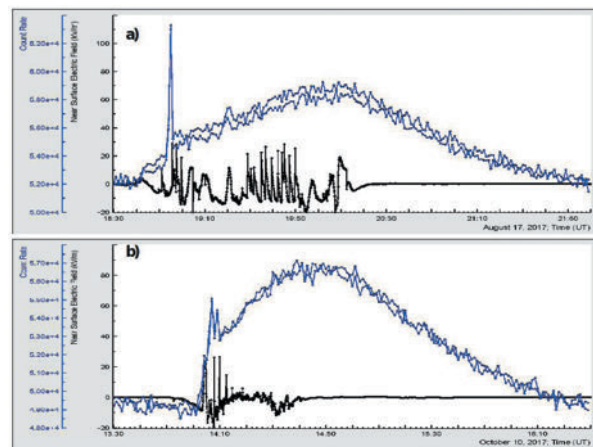


**Figure 2.** Near-surface electric field (black) and count rates (blue) of NaI detectors with energy threshold of 300 keV, for two long-lasting, low-energy TGEs.

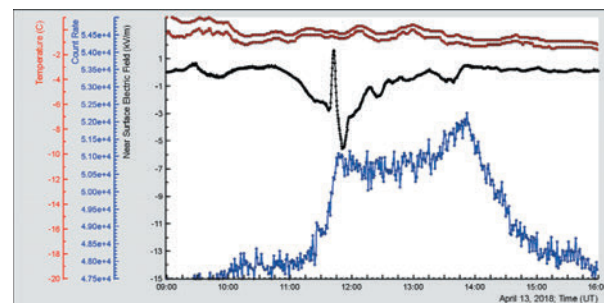


**Figure 3.** Red: outside temperature and dew point; black: near-surface electric field in kV/m; blue: one-minute time series of the count rate in a 1 m<sup>2</sup> plastic scintillator (1 cm thick, energy threshold 0.7 MeV).

ers (number of electrons and gamma rays reaching Earth’s surface). Thus, the monitoring of the near-surface electric field at the detector site is necessary, but it is not a sufficient condition for evaluating the intracloud electric field. A simple NaI crystal based spectrometer that monitors particle flux on one second time scale and stores histogram of energy released each minute will not only provide data for correction of EAS parameters, but will also give valuable data on one of the most complicated and most important topics of atmospheric physics: the atmospheric electricity. By the intensity and energy spectrum of TGE, it is possible to roughly estimate the potential drop in the cloud - [20], [9]. Electric field effects of 1-2 hours’ duration are not the limit for the electrically disturbed atmosphere. In Figure 3 we show enhanced particle fluxes prolonged for  $\sim 6$  hours, thus demonstrating prolonged electrical activity in clouds above detector site. Estimated distances to cloud base do not exceed 50 m. Note that the variations of the near-surface electric field were rather small from -5 to 1 kV/m. In Figure 1, disturbances were -20 kV/m to 10 kV/m. Thus, a small near-surface electric field corresponds to low energy prolonged gamma-ray fluxes.

### 3 Simulation of air showers with electric fields in the atmosphere using the CORSIKA code

To study the influence of atmospheric electric fields on Extensive Air Showers (EAS) parameters, we developed a simple model for the propagation of shower particles in the atmosphere taking into account electric fields. Air showers have been simulated with CORSIKA [13] version 7.56 with QGSJETII [17] and GHEISHA [11] as hadronic interaction models. For electromagnetic interactions, the EGS4 option [16] was used. The electric field option (EFIELD) of CORSIKA was used. An electric field of strength  $E_z \neq 0$  starts at a height H2 above the ground and extends to height H1. Each simulation trial consists of propagation of hundred of vertical proton showers with fixed primary energy of  $10^{15}$  eV. The showers start on the top of atmosphere (first interactions are most probable on heights of 30 km), the secondary particles are propagated and recorded at the altitude of 3200 m (Mt. Aragats station). Shower particles are followed down to 0.3 GeV for hadrons and muons, and to 0.3 MeV for electrons and gamma rays. The simulations show a significant influence of the electric field on the intensity of particles at the ground level. In Table 1, we show the multiplication of the shower particles entering electric fields of different strength and location in the atmosphere. The particles reaching the Earth's surface are registered if their energy exceeds 50 keV. Thus, if the electric field extends down to only 50 m above ground (a common condition for the Spring TOEs on Aragats), the multiplication of electrons and gamma rays is rather significant. In Table 2, the relative changes in particle number are presented. The changes in the number of charged particles of an air shower depend on the strength of the field and on the height of the electric field. Figures 4 and 5 illustrate the effect of electric field on particle intensity at the ground level. Thus, we see that the electric field located

**Table 1.** Average number of shower particles measured on ground per  $10^{15}$  eV vertical proton shower.

	$E_z=0$ kV/cm	$E_z=1.8$ kV/cm at 3250<H<4250m	$E_z=1.8$ kV/cm at 4200<H<5200m	$E_z=1.0$ kV/cm at 4200<H<5200m
$N_e$	$4.03 \cdot 10^5$	$7.25 \cdot 10^5$	$4.34 \cdot 10^5$	$4.08 \cdot 10^5$
$N_\mu$	$11.48 \cdot 10^3$	$11.73 \cdot 10^3$	$12.09 \cdot 10^3$	$11.70 \cdot 10^3$
$N_\gamma$	$1.91 \cdot 10^6$	$2.86 \cdot 10^6$	$2.26 \cdot 10^6$	$1.95 \cdot 10^6$

**Table 2.** Relative changes of shower particles numbers (compared to the  $E_z = 0$  case).

	$E_z=1.8$ kV/cm at 3250<H<4250m	$E_z=1.8$ kV/cm at 4200<H<5200m	$E_z=1.0$ kV/cm at 4200<H<5200m
$\Delta N_e/N_e$	0.80	0.08	0.01
$\Delta N_\mu/N_\mu$	0.02	0.05	0.02
$\Delta N_\gamma/N_\gamma$	0.50	0.18	0.02

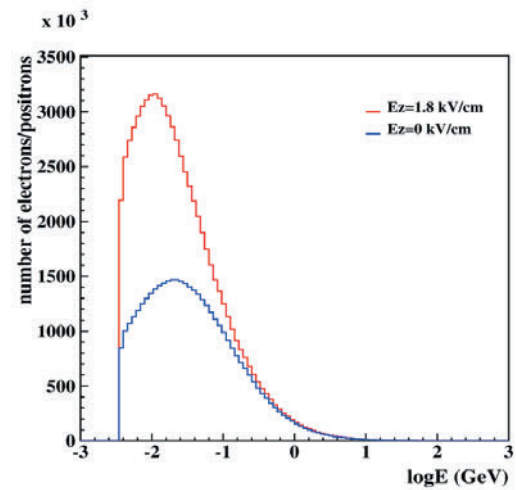


**Figure 4.** Energy distributions for the secondary electrons/positrons.

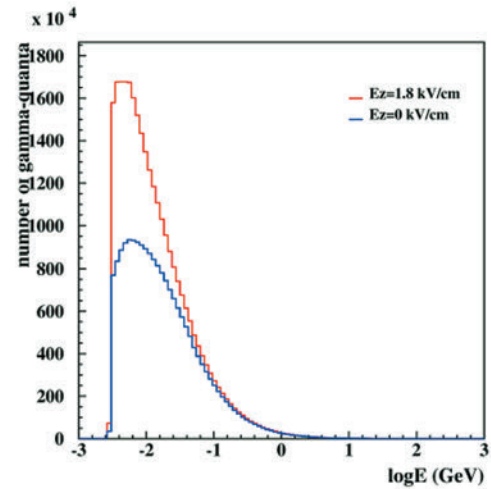


**Figure 5.** Energy distributions of secondary gamma rays in a shower, recorded at the ground level.

in the Earth's atmosphere drastically changes the number of charged and neutral particles of an air shower. This effect is essential for the estimation of EAS primary particle energy. Usually the energy of primary particle is estimated by the number of electrons and muons observed on ground level. For the CASA-MIA detector [21] (energies  $10^{14}$  eV -  $10^{16}$  eV) a combination of measured EAS parameters ( $N_{e^*} + 25N_\mu$ ) has been found [22] to be logarithmically linear with energy (the subscript "e\*" emphasizes that the quantity  $N_e$  does not simply denote the total number of electrons at the ground, but also includes a fraction of the abundant shower photons). For comparison, we use the parametrization:

$$\log E_0[\text{GeV}] = 1.03 * \log(N_e + 25N_\mu) \quad (1)$$

Here,  $N_e$  is the number of electrons and positrons, and the coefficient 1.03 takes also gamma rays contamination into

**Table 3.** Average number of shower particles measured on ground per  $10^{15}$  eV vertical proton shower.

	$E_z=0$ kV/cm	$E_z=1.8$ kV/cm at 3250<H<4250m	$E_z=1.8$ kV/cm at 4200<H<5200m	$E_z=1.0$ kV/cm at 4200<H<5200m
E(GeV)	$10^6$	$1.54 \cdot 10^6$	$1.1 \cdot 10^6$	$1.05 \cdot 10^6$

account. The true and recovered energies according to eq. 1 are presented in Table 3.

With a field strength of  $E_z=1.8$  kV/cm, the errors of the primary particle energy reconstruction are 54% (electric field at 3250 m < H < 4250 m, i.e. the cloud just 50 above ground); and 10% (electric field at 4200 m < H < 5200 m). With a field strength of  $E_z=1.0$  kV/cm, the bias of the primary particle energy reconstruction is 5% (electric field at 4200 m < H < 5200 m).

#### 4 Conclusion

To study the influence of atmospheric electric fields on EAS parameters, we use a simple model of the propagation of shower particles initiated from a primary proton with energy of 1000 TeV. Observing particle fluxes from thunderclouds with electrical fields inside helps to estimate the influence of atmospheric electricity on the size of shower particles. The recent discovery of long-lasting TGEs extends the expected time of atmospheric electric field effects to several hours; thus, the influence of atmospheric electricity on the secondary cosmic-ray particles is potentially a long-lasting phenomenon. MC results prove that atmospheric electric fields should be considered in EAS physics.

#### Acknowledgment

The authors thank the staff of the Aragats Space Environmental Center for the continuous operation of Aragats research station facilities. The data for this paper are available via the multivariate visualization software ADEI on the WEB page of the Cosmic Ray Division (CRD) of the Yerevan Physics Institute, <http://adei.crd.yerphi.am/adei>.

#### References

[1] Babich L.P., Donskoy E.N., Il'kaev R.I., Kutsyk I.M., and Roussel-Dupre R.A., Plasma Phys. Rep. **30**, 616 (2004).

[2] Chilingarian, A., Arakelyan, K., Avakyan, K. et al., Nucl. Instrum. Methods A **543** (2-3) 483 (2005).  
 [3] Chilingarian, A., Daryan A., Arakelyan K. et. Al., Phys. Rev. D, **82**, 043009 (2010).  
 [4] Chilingarian, A., Hovsepyan, G., Hovhannisyanyan, A., Phys. Rev. D: Part. Fields, **83** (6), 062001 (2011).  
 [5] Chilingarian A., Journal of Atmospheric and Solar-Terrestrial Physics, **107**, 68-76 (2014).  
 [6] Chilingarian A., Mailyan B. and Vanyan L., Atmospheric Research **1**, 114-115 (2012).  
 [7] Chilingarian A., Hovsepyan G., and Vanyan L., Europhys. Lett., **106**, 59001 (2014).  
 [8] Chilingarian A., Physical Review D, **98**, 022007 (2018).  
 [9] Cramer E.S., Mailyan B. G., Celestin S., and Dwyer J. R., J. Geophys. Res. Atmos., **122**, 4763-4772 (2017).  
 [10] Dwyer J.R., Geophys. Res. Lett., **30**, 2055 (2003).  
 [11] Fesefeldt H., (1985), The simulation of hadronic showers - physics and applications, Tech. Rep.PITHA-85/02, RWTH Aachen.  
 [12] Gurevich A.V., Milikh G.M. and Rouseel-Dupre R., Physics Letters A, **165**, 463-468 (1992).  
 [13] Heck D., Knapp J., et al., CORSIKA: A Monte Carlo Code to Simulate Extensive Air Showers, Report FZKA 6019 (1998), Forschungszentrum Karlsruhe.  
 [14] Marshall T.C., Stolzenburg M., Krehbiel P.R. et. al., JGR, **114**, D02209 (2009).  
 [15] Nag A. and Rakov V.A., Geophys. Res. Lett., **36**, L05815 (2009).  
 [16] Nelson W., Hirayama H., Rogers W., (1985), The EGS4 Code System, Tech. Rep. 265, SLAC.  
 [17] Ostapchenko S., arXiv:hep-ph/0501093 (2005).  
 [18] P.Schellart, T. N. G.Trinh, S.Buitink, et al., Physical Review Letters, **114**, 165001 (2015).  
 [19] Babich, L.P., et al., IEEE Trans. Plasma Sci., **29** (3), 430-438 (2001).  
 [20] Chilingarian A., Hovsepyan G., Khanikyanc Y., Reymers A. and Soghomonyan S., EPL, **110**, 49001 (2015).  
 [21] A. Borione et al., Nucl. Inst. Meth. Phys. Res. A, **346**, 329 (1994).  
 [22] Glasmacher, M. A. K., et al., in Proc. 26th Int. Cosmic Ray Conf. (Salt Lake City), **3**, 129 (1999).

# Termination of Thunderstorm Ground Enhancements by Lightning Discharges

*A. Chilingarian, Y.Khanikyants and S.Soghomonyan*

*Yerevan Physics Institute, Alikhanyan Brothers 2, Armenia, 0036*

**Abstract.** We present measurements of Thunderstorm Ground Enhancements (TGE) that are abruptly terminated by lightning discharges. The measurements were performed at an altitude of 3200 m above sea level on Mt. Aragats (Armenia). We identified the TGE-terminating lightning types for nearly 50 events detected during 2012-2018. We found that for ~80% of analyzed events the termination of flux enhancement was associated with negative cloud-to-ground (-CG) or normal-polarity intracloud (IC) flashes, and for ~18% - with inverted-polarity IC flashes. Occurrence of the inverted-polarity IC flash provides a direct proof of existence of the lower positive charge region (LPCR) at the bottom of the cloud. Observation of TGE-terminating inverted polarity IC flash confirms the hypothesis that LPCR plays important role in the origination of TGE. Analysis of the observational data allows us to conclude that two downward electron-accelerating fields are responsible for the TGE: field formed by the main negative charge and its mirror image in the ground, and field formed by the main negative charge and the LPCR.

TGE-terminating lightning flashes can produce strong electromagnetic interference (EMI) signals in particle detectors. However, usually these signals are well below the operating threshold of these detectors. Based on the analysis of synchronized measurements of wideband electric field waveforms and signals from particle detectors we found no evidence of particle flux enhancement produced by lightning flash.

## 1. INTRODUCTION

In recent years there has been considerable interest in the Thunderstorm Ground Enhancements (TGEs), i.e., enhanced fluxes of electrons, gamma rays, and neutrons detected by ground-based particle detectors during strong overhead thunderstorms [Brunetti et al., 2000; Alexeenko et al., 2002; Khaerdinov et al., 2005; Torii et al., 2002, 2009, 2011; Tsuchiya et al., 2007, 2009, 2011, 2012, 2013; Kuroda et al 2016; Kelly et al., 2015; Chilingarian et al., 2010, 2011, 2012, 2013, 2015a, 2016, 2017]. The high-energy portion of enhanced fluxes of particles (with energies up to 40 MeV) detected by the ground-based detectors typically last for a few tens of seconds to ~10 min, whereas the low-energy fluxes (with energies less than 3 MeV) can last for several hours [Chilingarian A. (2018)]. Some of the TGEs are abruptly terminated by lightning discharge clearly indicating an association to the electric field of the thundercloud.

In [Chilingarian et al., 2012] a hypothesis was proposed that the downward electron-accelerating electric field responsible for the TGE is formed by the main negative charge in the cloud and the lower positive charge region (LPCR). Chilingarian et al., (2017) identified the types of TGE-terminating lightning flashes for 24 observed events and came to a conclusion that the downward electron-accelerating electric field can be formed by the main negative charge in the cloud and its mirror image in the ground.

This field can be locally enhanced by the LPCR in the cloud and positive corona space charge near the ground.

To get better understanding of electric fields, which are responsible for the TGE, we extend here the work of [Chilingarian et al., 2017] via detailed analysis of ~50 TGEs terminated by lightning discharges. The analyzed events were observed during 2012-2018 by using various radiation and particle detectors.

In [Chilingarian, 2017], for the registration of particle decay we used the count rates of the 3-cm thick plastic scintillator, and the criteria used to identify the TGE termination was ~10% abrupt decrease of the flux coinciding with the lightning flash. The detection efficiency of the 3-cm thick plastic scintillator for the gamma rays is 3-5%, thus we could miss some not very large declines of particle flux. In the present study we use 60-cm thick plastic scintillator, the detection efficiency of which for gamma ray is approaching 80%.

The use of this detector allowed us to observe another type of lightning flashes that terminate the particle flux, namely, the inverted polarity IC, which occur between the main negative charge region and the LPCR. Thus, improvement of sensitivity of particle detector allowed us to discover a new tool for research of not very well understood problem of LPCR emerging in the bottom of the cloud.

The rest of the paper is organized as follows. Section 2 gives a brief overview of the instrumentation and the methodology used for lightning type identification. Examination of the observational data for 50 events is presented in the third section, where we analyze typical examples of TGEs abruptly terminated by lightning flashes of different types. In the Section 4 we summarize the identified lightning types and parameters for 50 analyzed events. In the Section 5 we analyze synchronized measurements of wideband electric field waveforms and the waveforms of particle detectors. Our conclusions are drawn in the final section.

## 2. INSTRUMENTATION AND METHODOLOGY

Data analyzed in this paper were acquired during 2012-2018 at the ASEC located at an altitude of 3200 m above sea level on Mt. Aragats. The fast wideband electric field waveforms produced by lightning flashes were recorded with a circular flat-plate antenna followed by a passive integrator (Fig.1).

The output of the integrator was directly connected with a 60 cm double-shielded coaxial cable to the Picoscope 5244B digitizing oscilloscope. The oscilloscope was triggered by a signal from a commercial MFJ-1022 active whip antenna that covers a frequency range of 300 KHz to 200MHz. The record length was 1 sec including 200 ms pre-trigger time and 800 ms post-trigger time. The sampling frequency was 25 MS/s, corresponding to 40 ns sample interval, and the amplitude resolution was 8 bit. The trigger out of the oscilloscope was relayed to the National Instruments (NI) myRIO board which produced the GPS time stamp of the record.

The near-surface electrostatic field changes were measured by a network of five field mills (Boltek EFM-100), three of which were placed in Aragats station, one in Nor Amberd station at a distance of 12.8 km from Aragats, and another one in Yerevan station at a distance of 39.1 km from Aragats.

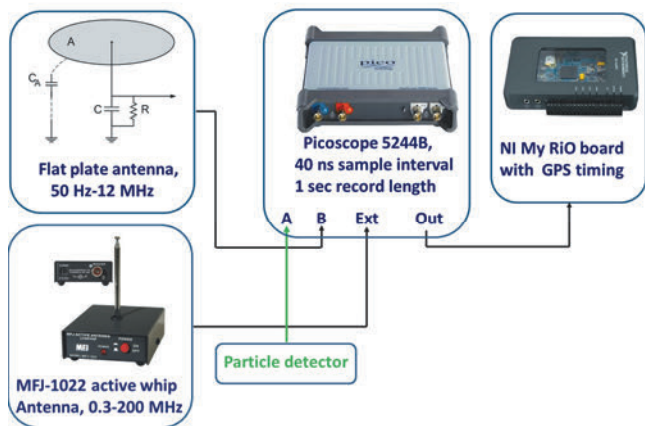


Figure 1. Wideband electric field measurement system

The particle fluxes analyzed in the present study were continuously monitored with 3cm thick and 60cm thick plastic scintillators with sensitive area of 1 m<sup>2</sup> each, and energy threshold ~2-3 MeV and ~5-6 MeV for the 3cm thick and 60cm thick detectors, respectively. The time resolution of particle flux detection was 1s and 2μs for the 3cm thick and 60cm thick scintillator, respectively.

In the present study we use the methodology of lightning type identification described in Chilingarian et al., (2017). A brief overview of the identification methodology is given below. It is based on the analysis of electrostatic field changes produced by lightning and detected by a network of sensors, and the examination of the wideband fast electric field waveforms.

In our analysis we used the well-known vertical tripole model of the normal-polarity thundercloud charge structure. According to this model, there is a main negative charge region in the middle of the thundercloud, a main positive charge region at the top, and a much smaller lower positive charge region (LPCR) near the cloud bottom (Fig.2). Throughout this paper we use the atmospheric electricity sign convention, according to which the downward directed electric field or field change vector is considered to be positive.

We consider four different lightning types illustrated in Figure 2. Negative cloud-to-ground

(-CG) flash occurs between the main negative charge region and the ground. This lightning effectively transfers negative charge from the cloud to the ground. Positive cloud-to-ground (+CG) flash occurs between the main (upper) positive charge region and the ground and transfers a negative charge from the ground to the cloud (or, equivalently, positive charge from the cloud to the ground). Normal-polarity intracloud flash (+IC) occurs in the upper dipole between the main negative and main positive charge regions. Inverted-polarity intracloud flash (-IC) occurs in the lower dipole between the main negative charge region and the LPCR. Negative cloud-to ground flashes CG reduce the negative charge overhead, whereas normal-polarity IC flashes reduce (by equal amounts) both the main negative and main positive charges overhead. At close distances, both of these lightning types produce electrostatic field changes of the same sign [Rakov and Uman, 2003, chapter 3; MacGorman and Rust, 1998, chapter 3]. This sign is positive according to the atmospheric electricity sign convention. Correspondingly, the positive CG and inverted-polarity IC flashes produce negative electric field changes at close distances. The polarity of electric field changes of CGs is independent of distance, while for IC flashes there is a polarity reversal distance.

In order to identify the lightning type, first, we check the polarity of electrostatic field change at the Aragats

station produced by the close lightning flash. If the field change is positive ( $\Delta E > 0$ ), the flash is considered to be either -CG or normal-polarity IC. If the field change is negative ( $\Delta E < 0$ ), the flash is considered to be either +CG or inverted-polarity IC. Next, in order to distinguish between CGs and ICs, we check if the polarity of  $\Delta E$  changes with distance, using our network of field mills. If polarity reversal has been detected, then we identify this lightning as a cloud discharge (normal-polarity or inverted-polarity IC). However, if polarity reversal has not been detected, the lightning-type identification question remains open, and we need to analyse fast electric field waveforms where we search for characteristic return stroke (RS) signatures which are indicative of CGs. In the analysis of fast electric field waveforms, the identification is accomplished by applying waveform criteria to individual electric field pulses. In most cases, RS signatures are readily identifiable in wideband E field record. Certainly, not every lightning event could be reliably classified using this methodology.

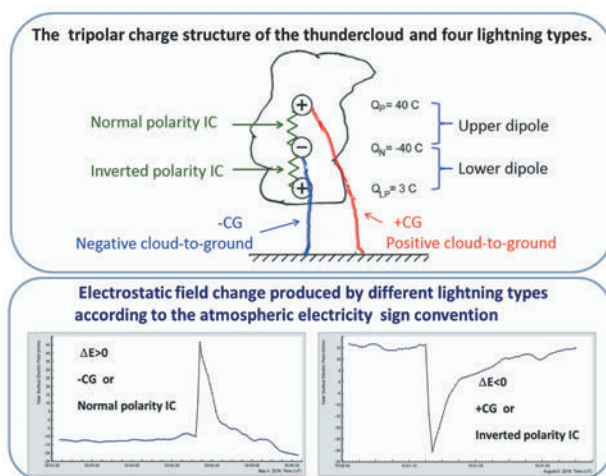


Figure 2. Charge structure of the thundercloud and four main types of lightning (upper panel), and electrostatic field change produced by four lightning types (lower panel).

### 3. ANALYSIS OF TGEs TERMINATED BY LIGHTNING FLASHES

#### 3.1. Negative cloud-to-ground lightning flash

An example of TGE abruptly terminated by two lightning flashes separated by ~5 min is presented in Figure 3. The black curve shows the electrostatic field measured by electric field mill at Aragats, the blue curve shows particle flux measured by 3cm thick scintillation detector (1μs time series). The fast change of the electrostatic field caused by the lightning discharge leads to abrupt termination of the particle flux.

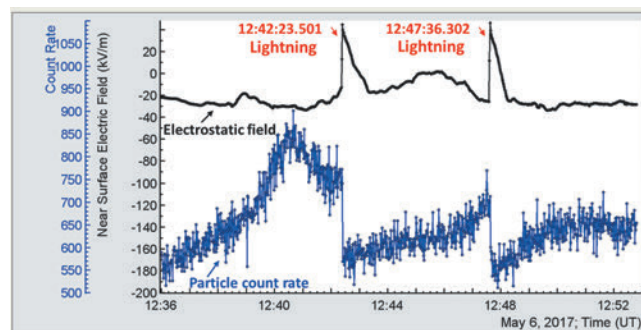


Figure 3. Electrostatic field change and particle flux for TGE terminated by two negative cloud-to-ground (-CG) lightning flashes separated by 5 min (May 6, 2017, 12:42:23.501 and 12:47:36.302 UTC).

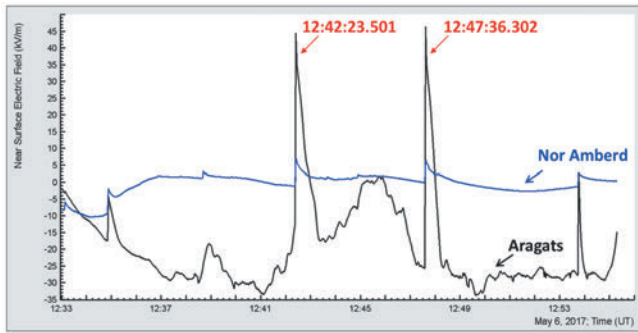


Figure 4. Electrostatic field changes recorded by the field mills in Aragats and Nor Amberd for TGE-terminating lightning flashes shown in Figure 3. Polarity reversal is not observed: field changes measured by the two field mills is positive.

It is worth noting that after abrupt termination by first lightning flash the count rate has an increasing trend during ~5 min, and then it is terminated by second flash, and after second termination shows again an increasing trend. This increase of count rate after abrupt termination can be associated with partial recovery of electric field responsible for the TGE.

Figure 4 shows the electrostatic field changes for these two lightning flashes that were recorded in Aragats and Nor Amberd. It is seen from Figure 4 that both field changes are positive, which suggests that the lightning events were either negative cloud-to-ground (-CG) flashes or normal-polarity intracloud flashes. In order to distinguish between these two lightning types we examined the corresponding fast electric field record. Figure 5 shows fast electric field record for the flash that occurred at 12:47:36.302 (the record for the flash 12:42:23.501 has similar features and is not shown here).

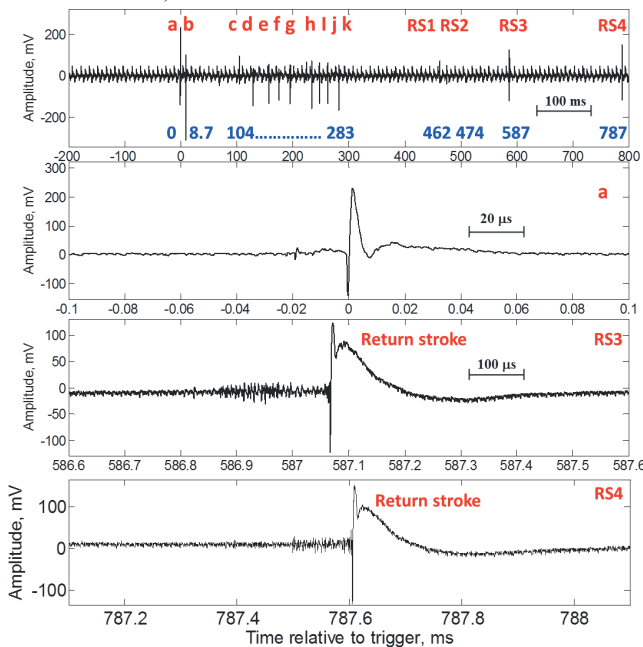


Figure 5. Fast electric field record of negative CG that occurred on May 6, 2017 at 12:47:36.302 UTC. Two lower panels show two strongest return stroke pulses (RS3 and RS4). These wide pulses are typical signatures of CG lightning.

The record in Figure 5 contains four relatively wide pulses (RS1-RS4) of positive polarity at 462 ms, 474 ms, 587 ms, and 787 ms after the trigger. Two strongest pulses RS3 and RS4 are shown on expanded time scale in two lower panels. The risetime of these two pulses is about 3–4  $\mu$ s, and the peak-to-zero fall time is 130–140  $\mu$ s. The positive initial polarity of these wide pulses is the same as the polarity of electrostatic field changes shown in Figure 4.

With a high level of confidence we attribute these wide pulses to return strokes of negative cloud-to-ground (-CG) lightning.

### 3.2 Normal-polarity IC

An example of TGE abruptly terminated by normal-polarity IC flash is shown in Figure 6.

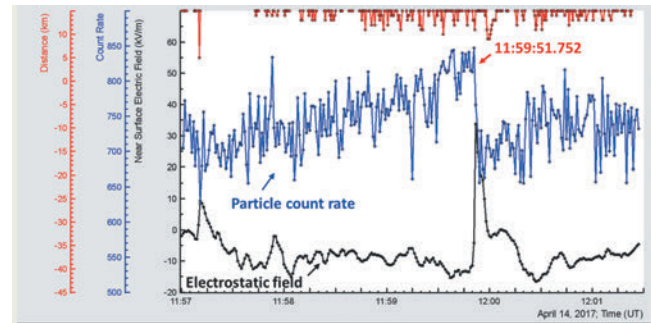


Figure 6. Electrostatic field change and particle flux for TGE terminated by normal-polarity IC flash (April 14, 2017, 11:59:51.752 UTC).

Polarity reversal of electrostatic field change for this flash was not observed, and identification of this lightning is accomplished by examining the corresponding fast electric field record shown in Figure 7. As seen in Figure 7, there are only very short pulses with durations less than 1  $\mu$ s, (shown in panel g), and pulses which have steep leading edge with risetime of less than 0.2  $\mu$ s followed by damped oscillations with a period of 6.2  $\mu$ s (shown in panel a). This oscillatory pulse shape is frequently observed in electric field records of normal-polarity IC flash. We believe that the oscillatory nature of these signals is due to the shock excitation of the detection circuit by a relatively short duration, impulsive radiation event. The shock excitation causes the antenna circuit to ring at its own frequency. These impulsive radiation events produced strong transients in the signals from particle detectors. Analysis of these transients is given in Section 4. Fast electric field record shown in Figure 7 does not contain pulses that could be attributed to return strokes of cloud-to-ground lightning, so we identify this event as normal-polarity IC flash.

Another example of TGE terminated by normal-polarity IC flashes is shown in Figure 8 where two lightning flashes separated by approximately 2 min terminate the particle flux. The corresponding fast electric field record is shown in Figure 9. Here again, the waveform contains short pulses of oscillatory nature, similar to those shown in Figure 7, and there are no wide pulses that could be attributed to return strokes of CG flash. It should be noted that this kind of TGE termination when the particle flux is terminated by two subsequent lightning flashes separated by 2–5 min was observed quite frequently, for about 20 % of 50 analysed events.

It is worth noting that, as a rule, the polarity reversal of electrostatic field change produced by normal-polarity ICs is not detected by our network of field mills. The reason is that for normal-polarity ICs which occur in the upper part of the cloud at higher altitudes, the polarity reversal distance may exceed the distance of 12.8 km between the field mills in Aragats and Nor Amberd, whereas the field mill in Yerevan (39.1 km from Aragats) cannot detect the lightning flash that occurs close to Aragats station because the sensitivity range of the instrument is about 30 km. By contrast, for the inverted-polarity ICs which occur in the lower part of the cloud at lower altitudes, the reversal distance is smaller, and usually, the polarity reversal of

electrostatic field is detected by field mills in Aragats and Nor Amberd. We note that usually, the polarity reversal is expected to occur at a distance of about 10 km for normal ICs and less than 5 km for inverted ICs [e.g., Rakov and Uman, 2003 chapters 3 and 4].

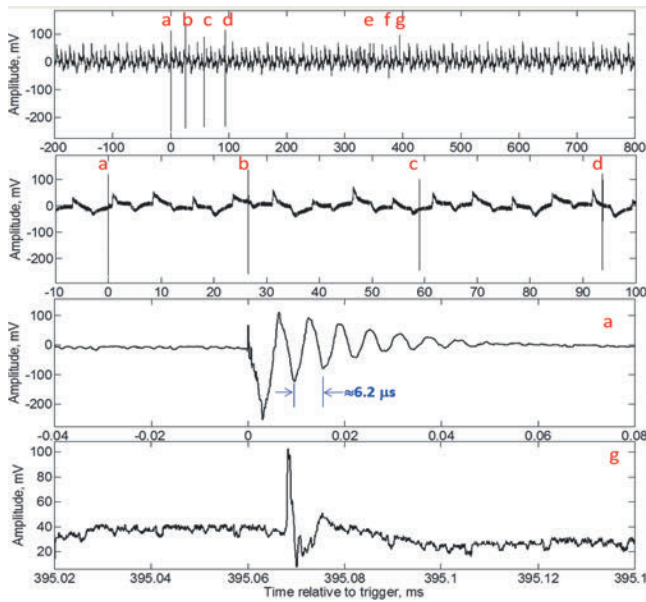


Figure 7. Fast electric field record of normal-polarity IC flash that occurred on April 14, 2017 at 11:59:51.752 UTC. Pulses a, b, c, and d have similar shape shown in panel a. Pulses e, f, and g, have similar shape shown in panel g.

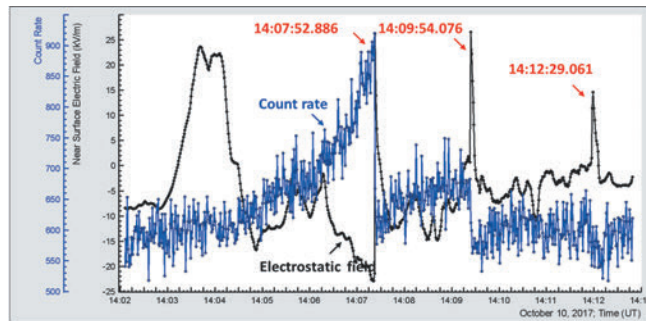


Figure 8. Electrostatic field change and particle flux for TGE terminated by two normal-polarity IC flashes separated by ~2 min (October 10, 2017, 14:07:52.886 and 14:09:54.076 UTC).

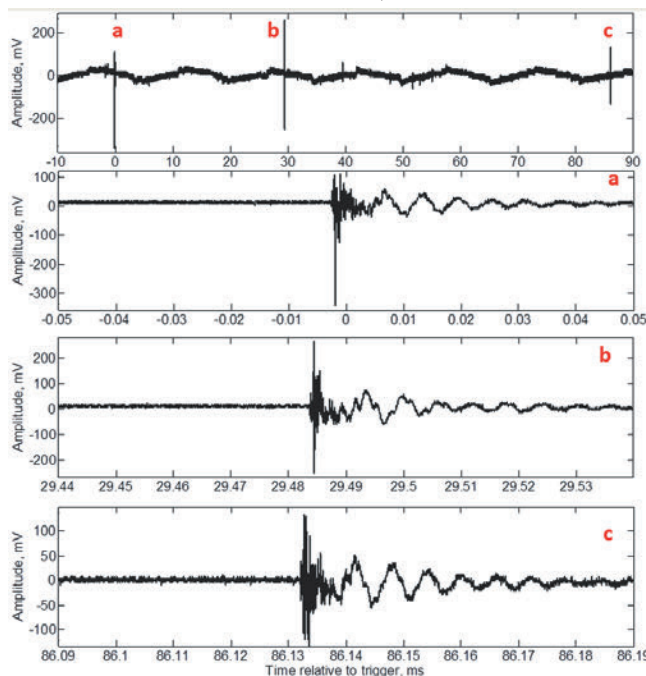


Figure 9. Fast electric field record of normal-polarity IC flash that occurred on October 10, 2017 at 14:07:52.886 UTC.

### 3.3 Inverted-polarity IC

Next we will consider TGEs terminated by inverted-polarity IC flashes.

An example of TGE terminated by inverted-polarity IC flash is shown in Figure 10.

The count rate of particle flux measured by 60 cm scintillator (2 s time series) is abruptly terminated at the time of lightning discharge. The electrostatic field change produced by this lightning is negative, as measured by the field mill in Aragats. However, in Nor Amberd (12.8 km away from Aragats) the polarity of the field change is reversed (Figure 11). As can be seen from Figure 11, the electrostatic field changes detected by two field mills in Aragats and Nor Amberd have opposite polarities, that is, polarity reversal with distance is detected. Therefore, this lightning can be identified as an intracloud flash, because, the polarity reversal with distance occurs only when an elevated dipole is neutralized. The polarity of the larger field change detected in Aragats corresponds to a closer distance and is negative, which is indicative of inverted-polarity IC flash.

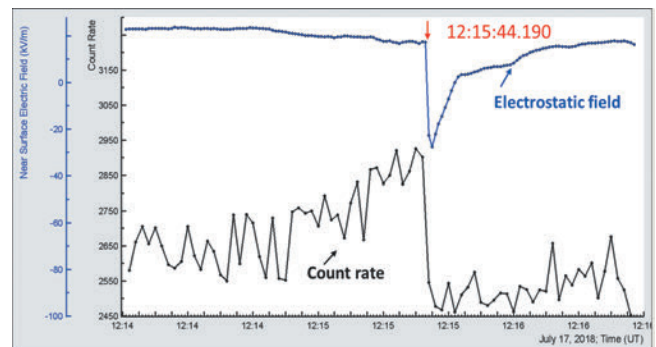


Figure 10. Electrostatic field change and particle flux for TGE terminated by inverted-polarity IC flash (July 17, 2018 1:15:44.190 UTC).

Identification of this event as a cloud flash is further supported by the fast electric field record (see Figure 12) which contains only short bipolar pulses of microsecond and sub-microsecond duration and no signatures characteristic of return strokes.

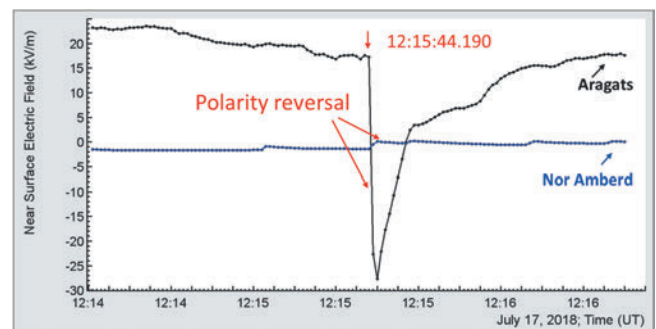


Figure 11. Electrostatic field changes produced by inverted-polarity IC flash that occurred on July 17, 2018 at 12:15:44.190 UTC. The field changes recorded by the field mills located in Aragats and Nor Amberd, have opposite polarities.

An example of multiple termination of TGE by lightning flashes of different types is shown in Figure 13. Polarity reversal of electrostatic field change is detected for flashes N1, N2, and N3 (Figure 14). For flashes N1 and N3, the polarity of the larger field change detected in Aragats corresponds to a closer distance and is negative, which is indicative of inverted-polarity IC flash.

This identification is further supported by examination of fast electric field records, an example which for flash N3 is shown in Figure 15. As seen in the Figure 15 the record contains only short pulses of microsecond and submicrosecond duration.

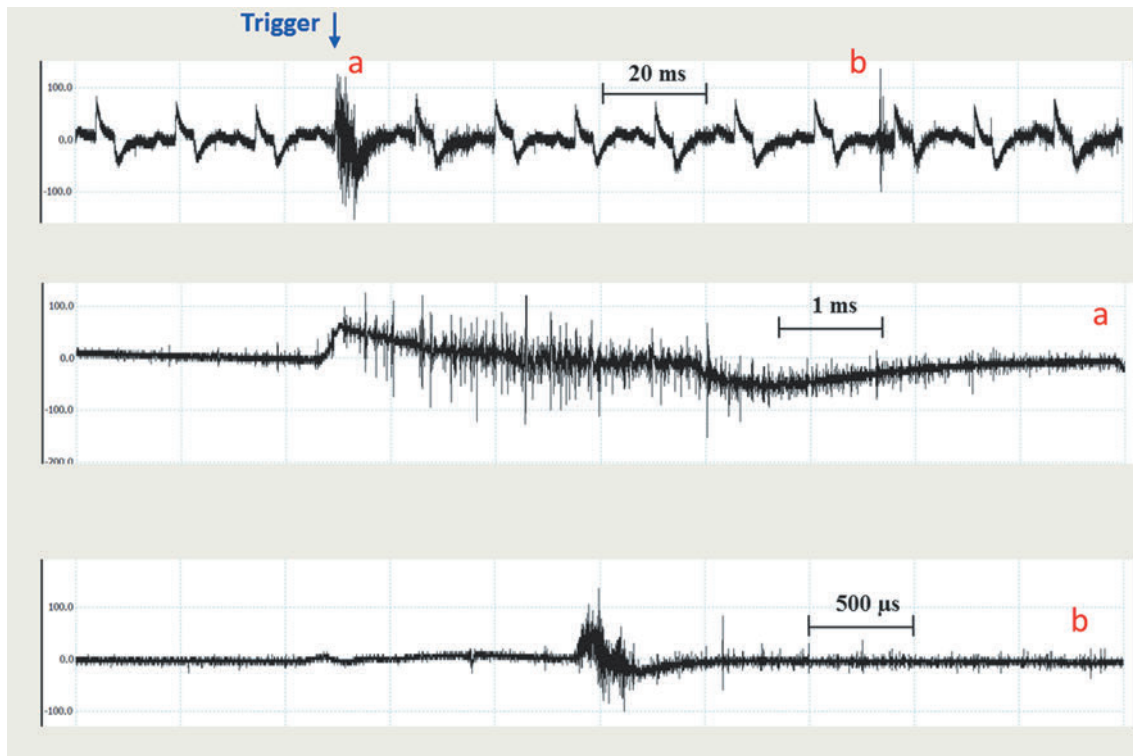


Figure 12. Fast electric field record of inverted-polarity IC flash that occurred on July 17, 2018 at 12:15:44.190 UTC.

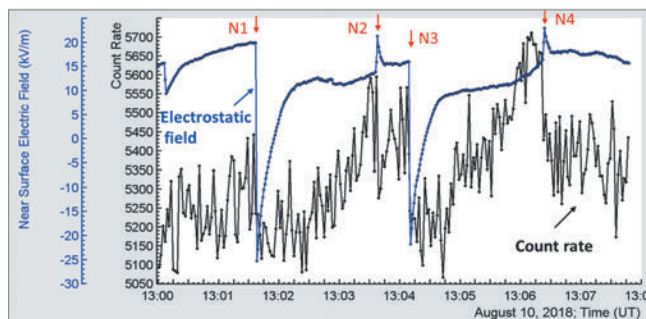


Figure 13. Electrostatic field change and particle flux for TGE terminated by four IC flashes of different polarities: N1 and N3 inverted-polarity; N2 and N4 –normal-polarity (August 10, 2018 UTC).

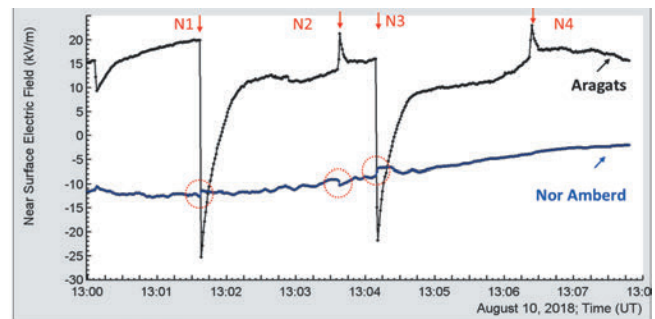


Figure 14. Electrostatic field changes produced by four lightning flashes of August 10, 2018 shown in Figure 13. The field changes recorded by the field mills located in Aragats and Nor Amberd, have opposite polarities for flashes N1, N2, and N3.

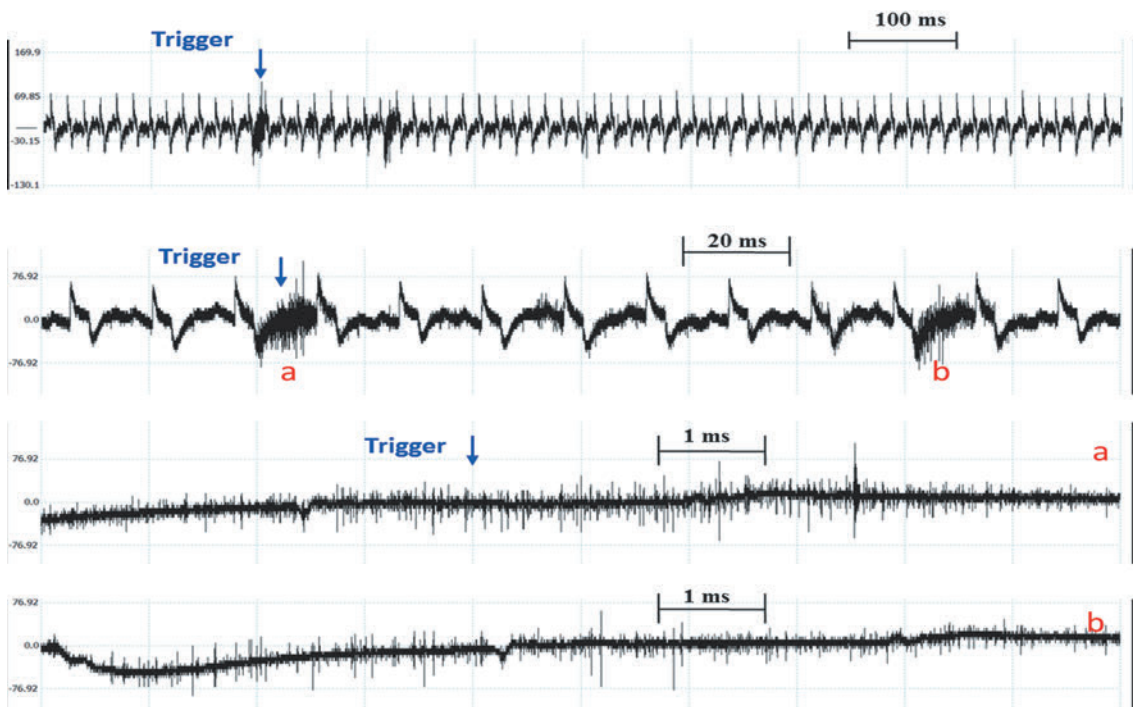


Figure 15. Fast electric field record of inverted-polarity IC flash N3, (August 10, 2018 at 13:04:55.149 UTC) shown in Figures 13 and 14.

For flash N2 the polarity of the larger field change in Aragats is positive, which is indicative of normal-polarity IC flash. For flash N4 the polarity of the field change in Aragats is positive, but there is no discernible field change at Nor Amberd in Figure 14, and, hence, no polarity reversal can be detected for this event. Examination of fast electric field record for flash N4 reveals no pulses that could be attributed to return strokes of cloud-to-ground lightning, so we identify this event as normal-polarity IC flash. Thus, all four TGE-terminating lightning flashes can be identified as cloud flashes: N1 and N3 are inverted-polarity ICs, whereas N2 and N4 are normal-polarity ICs.

#### 4. SUMMARY OF IDENTIFIED LIGHTNING TYPES AND PARAMETERS

Classification of lightning types for 50 analyzed events is summarized in Table 1.

25 of the TGE-terminating lightning events have been identified as normal-polarity IC flashes, 10 events have been identified as negative cloud-to-ground flashes, and for another 5 events which belong to either -CG or normal-polarity IC (both type produce positive field change at close distances) we were unable to distinguish between -CG and normal-polarity IC. These 5 events have been detected during 2012-2014, when the fast wideband electric field measurement system had not been installed, so fast filed records were not available for these events. 9 of the TGE -terminating lightning events have been identified as inverted-polarity IC flashes, and for one event the lightning types was not identified.

Thus, 80 % of TGE-terminating lightning flashes were -CGs and normal-polarity ICs. We note that normal-polarity ICs were observed 2.5 times more frequently than -CGs.

Table 1. Lightning types for 50 TGE termination events

Lightning type	Quantity
Normal-polarity IC	25
Negative cloud-to-ground (-CG)	10
-CG or Normal-polarity IC not distinguished: both types produce $\Delta E > 0$	5
Inverted -polarity IC	9
Not identified	1

It is important to note that about 18 % TGE-terminating lightning flashes were inverted-polarity ICs. The TGE termination by this type of lightning flashes was not observed in previous studies Chilingarian et al., (2017). Observation of these events in the present study has been made possible by using a 60 cm thick plastic scintillator, which has better sensitivity for detecting small drops of enhanced particle flux, as compared to 3 cm thick scintillator. As it is discussed below (Table 2), the TGEs terminated by inverted-polarity ICs have quite small drop of particles flux. We emphasize, that occurrence of the inverted-polarity IC flash provides a direct proof of existence of the LPCR at the bottom of the cloud. Observation of TGE-terminating inverted polarity IC flash supports the hypothesis that LPCR plays important role in the origination of TGE, and that downward electron-accelerating field can be formed by main negative charge region and the LPCR.

In Table 2, we compare the duration of TGE and particle flux drop for 50 analysed events. Last row of the table shows the ratio of number of events detected by the WWLLN network to total number of events. As seen from the Table 2, the TGEs terminated by inverted-polarity ICs

have the smallest drop of particles flux (6 %) as compared to that for the -CGs (29 %) and for normal -polarity ICs (19) %. We believe that electric field change caused by inverted-polarity ICs, and hence, the associated particle flux drop is the smallest because it is limited by the charge of LCPR which is much smaller than main negative and upper positive charge.

Table 2. Parameters for 50 TGE termination events

Parameter	Mean $\pm$ StdDev			
	All events	Events with classified lightning type (N=number of events)		
		Normal polarity IC (N=25)	Negative CG (N=10)	Inverted polarity IC (N=9)
TGE duration, s	186 $\pm$ 142	203 $\pm$ 157	211 $\pm$ 98	88 $\pm$ 40
Particle flux drop, %	19 $\pm$ 17	19 $\pm$ 18	29 $\pm$ 17	6 $\pm$ 5
wwlln/total <sup>1)</sup>	9/50	4/25	5/10	0/9

It can be also seen from the Table 2 that TGEs terminated by inverted-polarity ICs have the shortest duration (88 s) as compared to that for the -CGs (211 s) and normal -polarity ICs (203 s). The reason for that is not understood yet. The highest ratio (50%) of WWLLN/total (last row of Table 2) for the -CG flashes reflects the fact that the detection efficiency of WWLLN for CGs is significantly higher than that for ICs [Rodger et al., 2005].

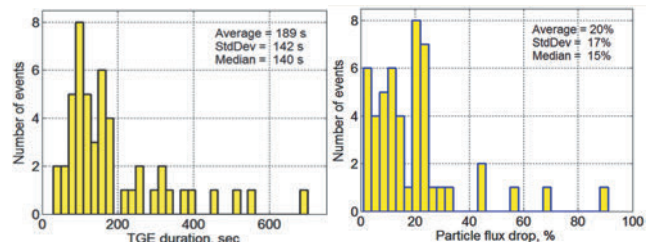


Figure 16. Histograms of TGE duration and particle flux drop for 50 events.

In Figure 16 we show histograms of TGE duration and particle flux drop for 50 analyzed events. The average values of TGE duration and particle flux drop are 189 s and 20 %, respectively.

#### 5. TRANSIENTS IN PARTICLE DETECTOR WAVEFORMS PRODUCED BY TGE-TERMINATING LIGHTNING FLASHES

Data considered in this section relate to one of controversial debate questions in high-energy lightning physics: “Does the lightning discharge produce relativistic particles and energetic radiation like gamma rays with energies of several Mev or even tens of Mev ?”.

One point of view is that lightning discharge did not involve any high-energy processes that might produce MeV particles and energetic radiation [Chilingarian et al, 2015, Chilingarian 2017]. This point of view is supported by multiyear observations of enhanced fluxes of particles and energetic radiation on Aragats during strong thunderstorms, which did not reveal any flux enhancement produced by lightning discharge. However, some groups have measured X rays or gamma rays produced by lightning discharge (e.g., Moore et al., 2001 Dwyer et al., 2003, 2005, Mallick et al., 2012). The main difficulty in the detection of energetic radiation and particles produced by lightning is that close lightning discharges produce strong

transients in various electrical circuits, including power supply lines, signal/data/communication cables, etc.

In order to check does the TGE-terminating lightning discharge produce any particle flux enhancement we performed synchronized measurements of wideband electric field waveforms and the signals of particle detectors. We performed pulse shape analysis in the waveforms of 43 events of TGE termination by lightning flashes for which synchronized measurements were available. Three scintillator detectors in two experimental halls, SKL and MAKET were used for synchronized measurements, namely, NaI detector, one cm thick and three cm thick plastic scintillator counters. The energy threshold of NaI detector, one cm thick and three cm thick plastic scintillator counters to energetic radiation was 300 keV, 0.7-0.8 MeV and 2-3 MeV, respectively.

More information about these detectors can be found in Chilingarian et al, (2015b).

In the SKL hall, the output of NaI detector and the signal from the fast electric field measurement system were connected to two channels of digital oscilloscope (shown in Figure 1 of Section 2). In the MAKET hall, the outputs 1 cm thick and 3 cm thick plastic scintillator counters were connected to two channels of another digital oscilloscope which was triggered by an whip antenna identical to that used for the triggering of first oscilloscope in SKL hall. We observed that all these lightning flashes produced strong electromagnetic interference (EMI) signals in particle detectors. Typical example of synchronized measurements of the TGE-terminating lightning flash is shown in Figures 17-20.

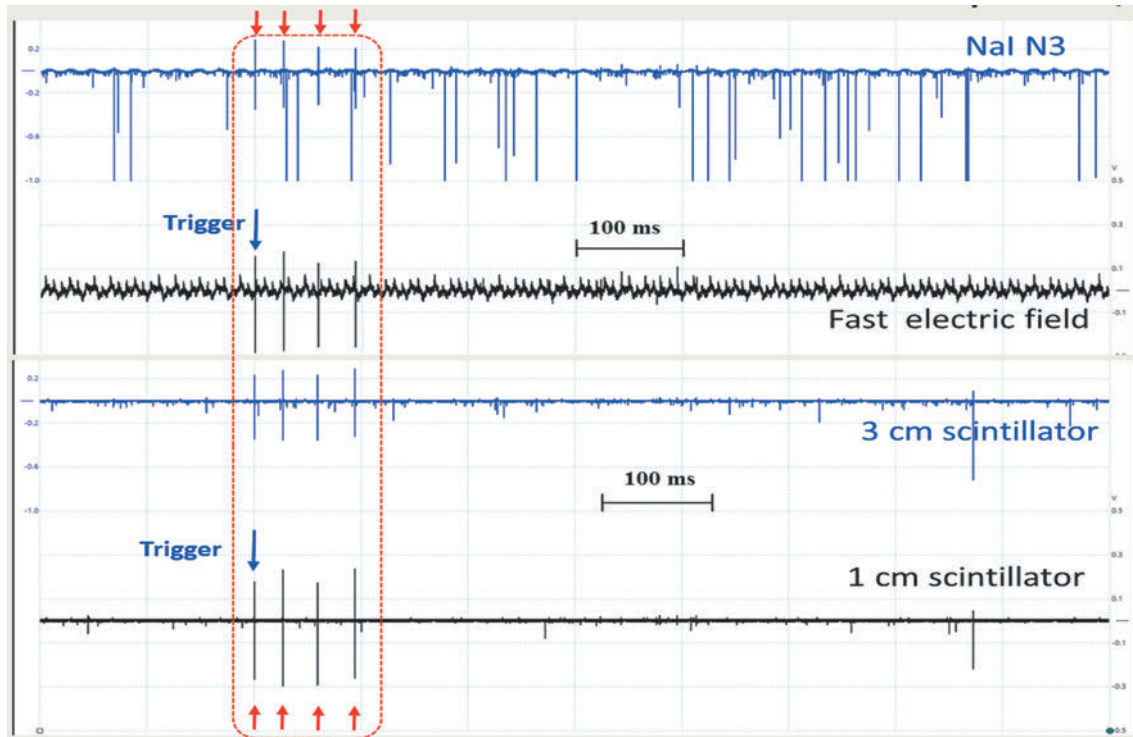


Figure 17. Fast electric field produced by the TGE-terminating normal-polarity IC flash that occurred at 11:59:51.752, April 14, 2017 (shown in Figure 6 and 7), and waveforms of three particle detectors. Four pulses in all three detectors waveforms coincide with the pulses in fast electric field record.

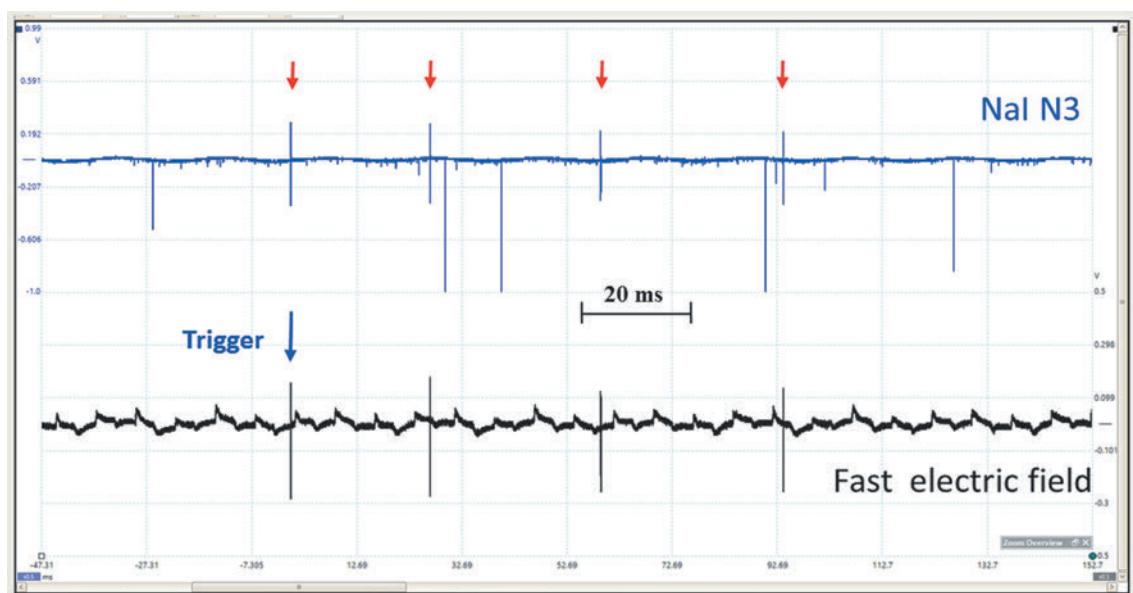


Figure 18. A 100-ms fragment of fast electric field produced by the TGE-terminating normal-polarity IC flash that occurred at 11:59:51.752, April 14, 2017 and waveforms of NaI detector. Four pulses in NaI detector waveform coincide with the pulses in fast electric field record.

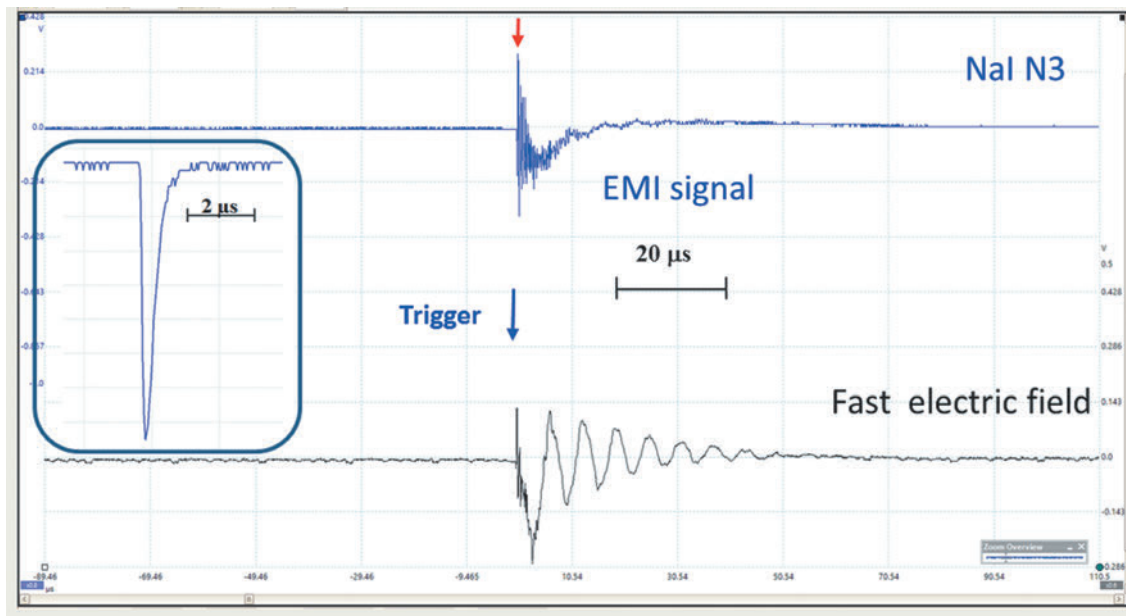


Figure 19. A 200- $\mu$ s fragment of fast electric field produced by the TGE-terminating normal-polarity IC flash that occurred at 11:59:51.752, April 14, 2017 and waveform of NaI detector. The bipolar pulse with oscillatory behavior in the detector output is electromagnetic interference (EMI) signal caused by lightning. For comparison, the true particle detection pulse of negative polarity is shown in the inset.

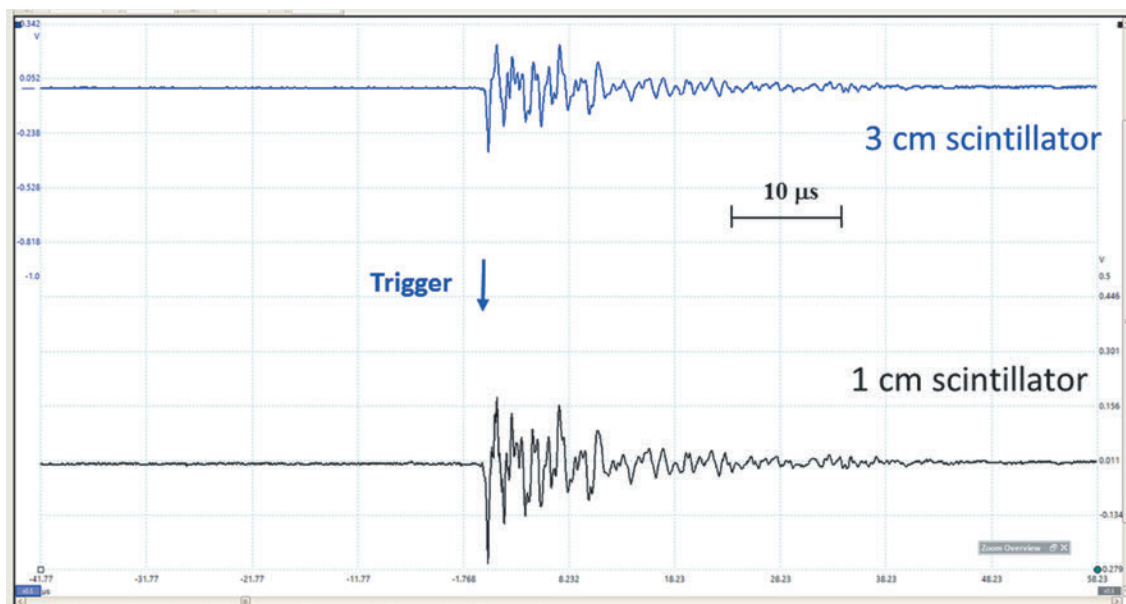


Figure 20. A 100- $\mu$ s fragment of fast electric field produced by the TGE-terminating normal-polarity IC flash that occurred at 11:59:51.752, April 14, 2017 and waveform of 1 cm and 3 cm scintillator. Bipolar pulses with oscillatory behavior output are EMI signal) caused by lightning (similar to that for NaI detector shown in Figure 19).

As seen in Figures 17 and 18, four pulses in all three detectors waveforms coincide with the pulses in fast electric field record. Pulse shape analysis of these four signals in the outputs of particle detectors shows that they are EMI signals produced by lightning. Figure 19 shows one of these pulses (all four pulses have similar shape) on expanded time scale. The EMI signal is clearly distinguished from the genuine signal of particle detection by the examination of the pulse shape: the EMI signal is bipolar and has typical oscillatory behavior whereas the unipolar signal of particle detection has a negative polarity.

The pulse shape analysis of synchronized measurements of wideband electric field waveforms and the signals of particle detectors for 43 TGE-terminating lightning flashes for which synchronized measurements were available does not reveal any particle flux enhancement during 1 s record (including 0.2 s pre-trigger and 0.8 s post-trigger time) triggered by lightning flash.

## 6. CONCLUSIONS

Main results of the present study are summarized below.

- Occurrence of the inverted-polarity IC flash provides a direct proof of existence of the LPCR at the bottom of the cloud.
- TGEs terminated by inverted-polarity ICs have the smallest drop (6 %) of particles flux as compared to that for -CGs (29 %) and for normal -polarity ICs (19) % . We believe that the electric field change caused by inverted-polarity ICs , and hence the associated flux drop is the smallest, because it is limited by the charge of LCPR which is much smaller than main negative and upper positive charge.
- 80 % of TGE-terminating lightning flashes were -CGs and normal-polarity ICs, and ~ 8 % were inverted-polarity ICs. The normal-polarity ICs were observed 2.5 times more frequently than -CGs.

- Two downward electron-accelerating fields can be responsible for the TGE:
  - a)  $E_1$  - formed by the main negative charge and its mirror image in the ground
  - b)  $E_2$  - formed by the main negative charge and the LPCR
- The main negative charge region is involved in both two downward electron-accelerating fields  $E_1$  and  $E_2$  responsible for TGE. These fields are reduced by - CG, normal-polarity ICs, and inverted-polarity ICs. Therefore, these 3 lightning types can terminate the TGE.
- The TGE-terminating lightning flashes produce strong EMI signals in some of particle detector. For the majority of particle detectors these signals were below their detection threshold. We believe that strong EMI signals indicate that TGEs are terminated by nearby lightning flashes.
- Based on our data of lightning flashes the nearest of which occurred at a distance of 2 km from the detector site, we found no evidence of any particle flux enhancement produced by lightning flash. Certainly, we cannot exclude anything, which goes below the sensitivity of our measurements.
- Our observations confirm that the detection efficiency of WWLLN for CGs is significantly higher than that for ICs.

#### REFERENCES

- [1] Alexeenko, V. V., N. S. Khaerdinov, A. S. Lidvansky, and V. B. Petkov (2002), Transient variations of secondary cosmic rays due to atmospheric electric field and evidence for pre-lightning particle acceleration, *Phys. Lett. A*, 301, 299–306.
- [2] Brunetti M., S. Cecchini, M. Galli, G. Giovannini, and A. Pagliarini, (2000), Gamma-ray bursts of atmospheric origin in the MeV energy range *Geophys. Res. Lett.* 27, 1599
- [3] Chilingarian A. (2017) Do Relativistic Elementary Particles Originate in the Lightning Discharges? *Bulletin of the Russian Academy of Sciences: Physics*, 2017, Vol. 81, No. 2, pp. 238–240.
- [4] Chilingarian, A., A. Daryan, K. Arakelyan, A. Hovhannisyanyan, B. Mailyan, L. Melkumyan, G. Hovsepyan, S. Chilingaryan, A. Reymers, and L. Vanyan (2010), Ground-based observations of thunderstorm-correlated fluxes of high-energy electrons, gamma rays, and neutrons, *Phys. Rev. D*, 82, 043009.
- [5] Chilingarian, A., G. Hovsepyan, and A. Hovhannisyanyan (2011), Particle bursts from thunderclouds: Natural particle accelerators above our heads, *Phys. Rev. D: Part. Fields*, 83(6), 062001.
- [6] Chilingarian A. and R. Mkrtchyan, (2012). Role of the Lower Positive Charge Region (LPCR) in initiation of the Thunderstorm Ground Enhancements (TGEs), *Phys. Rev. D* 86, 072003
- [7] Chilingarian A. et al. (2013), Thunderstorm ground enhancements: Gamma ray differential energy spectra, *Phys. Rev. D*, Vol. 88, 073001
- [8] Chilingarian, A., G. Hovsepyan, G. Khanikyan, A. Reymers, and S. Soghomonyan (2015a), Lightning origination and thunderstorm ground enhancements terminated by the lightning flash, *EPL (Europhysics Letters)*, 110(4), 49,001, doi:10.1209/0295-5075/110/49001.
- [9] Chilingarian A. S. Chilingaryan, and G. Hovsepyan, (2015b) Calibration of particle detectors for secondary cosmic rays using gamma-ray beams from thunderclouds., *Astroparticle Physics* 69, 37–43
- [10] Chilingarian, A., G. Hovsepyan, and E. Mnatsakanyan (2016), Mount Aragats as a stable electron accelerator for atmospheric high-energy physics research, *Phys. Rev. D*, 93, 052006.
- [11] Chilingarian, A., Y. Khanikyants, E. Mareev, D. Pokhsranyan, V. A. Rakov, and S. Soghomonyan (2017), Types of lightning discharges that abruptly terminate enhanced fluxes of energetic radiation and particles observed at ground level, *J. Geophys. Res. Atmos.*, 122, 7582–7599, doi: 10.1002/2017JD026744.
- [12] Chilingarian A. (2018), Long lasting low energy thunderstorm ground enhancements and possible Rn-222 daughter isotopes contamination, *PHYSICAL REVIEW D* 98, 022007
- [13] Dwyer, J. R., et al. (2003), Energetic radiation produced during rocket triggered lightning, *Science*, 299, 694–697.
- [14] Dwyer J. R. et al. (2005), X-ray bursts associated with leader steps in cloud-to-ground lightning *Geophys. Res. Lett.* VOL. 32, L01803, doi:10.1029/2004GL021782, 2005
- [15] Kelley, N. A., D. M. Smith, J. R. Dwyer, M. Splitt, S. Lazarus, F. Martinez-McKinney, B. Hazelton, B. Grefenstette, A. Lowell, and H. K. Rassoul (2015), Relativistic electron avalanches as a thunderstorm discharge competing with lightning, *Nature Communications*, 6, 7845, doi:10.1038/ncomms8845.
- [16] Khaerdinov N.S., A.S. Lidvansky T, V.B. Petkov (2005), Cosmic rays and the electric field of thunderclouds: Evidence for acceleration of particles (runaway electrons) *Atmospheric Research* 76 (2005) 346–354
- [17] Kuroda, Y., S. Oguri, Y. Kato, R. Nakata, Y. Inoue, C. Ito, and M. Minowa (2016), Observation of gamma ray bursts at ground level under the thunderclouds, *Physics Letters B*, 758, 286–291, doi:10.1016/j.physletb.2016.05.029.
- [18] Mallick S., V. A. Rakov, and J. R. Dwyer (2012), A study of X-ray emissions from thunderstorms with emphasis on subsequent strokes in natural lightning, *J. Geophys. Res.*, VOL. 117, D16107, doi:10.1029/2012JD017555, 2012
- [19] Moore, C. B., K. B. Eack, G. D. Aulich, and W. Rison (2001), Energetic radiation associated with lightning stepped-leaders, *Geophys. Res. Lett.*, 28, 2141–2144.
- [20] Rodger, C. J., J. B. Brundell, and R. L. Dowden (2005), Location accuracy of VLF World-Wide Lightning Location (WWLL) network: Postalgorithm upgrade, *Ann. Geophys.*, 23, 277–290.
- [21] Torii, T., M. Takeishi, and T. Hosono (2002), Observation of gamma-ray dose increase associated with winter thunderstorm and lightning activity, *Journal of Geophysical Research: Atmospheres*, 107(D17), ACL 2–1–ACL 2–13, doi:10.1029/2001jd000938.

- [22] Torii, T., T. Sugita, S. Tanabe, Y. Kimura, M. Kamogawa, K. Yajima, and H. Yasuda (2009), Gradual increase of energetic radiation associated with thunderstorm activity at the top of mt. fuji, *Geophysical Research Letters*, 36(13), doi:10.1029/2008gl037105.
- [23] Torii, T., T. Sugita, M. Kamogawa, Y. Watanabe, and K. Kusunoki (2011), Migrating source of energetic radiation generated by thunderstorm activity, *Geophysical Research Letters*, 38(24), n/a–n/a, doi:10.1029/2011gl049731.
- [24] Tsuchiya, H., T. Enoto, S. Yamada, T. Yuasa, M. Kawaharada, T. Kitaguchi, M. Kokubun, H. Kato, M. Okano, S. Nakamura, and et al. (2007), Detection of high-energy gamma rays from winter thunderclouds, *Physical Review Letters*, 99(16), doi:10.1103/physrevlett.99.165002.
- [25] Tsuchiya, H., T. Enoto, T. Torii, K. Nakazawa, T. Yuasa, S. Torii, T. Fukuyama, T. Yamaguchi, H. Kato, M. Okano, and et al. (2009), Observation of an energetic radiation burst from mountain-top thunderclouds, *Physical Review Letters*, 102(25), doi: 10.1103/physrevlett.102.255003.
- [26] Tsuchiya, H., T. Enoto, S. Yamada, T. Yuasa, K. Nakazawa, T. Kitaguchi, M. Kawaharada, M. Kokubun, H. Kato, M. Okano, and et al. (2011), Long-duration gamma ray emissions from 2007 and 2008 winter thunderstorms, *Journal of Geophysical Research*, 116(D9), doi: 10.1029/2010jd015161.
- [27] Tsuchiya, H., K. Hibino, K. Kawata, N. Hotta, N. Tateyama, M. Ohnishi, M. Takita, D. Chen, J. Huang, M. Miyasaka, and et al. (2012), Observation of thundercloud-related gamma rays and neutrons in tibet, *Physical Review D*, 85(9), doi:10.1103/physrevd.85.092006.
- [28] Tsuchiya, H., et al. (2013), Detection of high-energy gamma rays from winter thunderclouds, *Phys. Rev. Lett.*, 111, 015001.
- [29] Rakov, V. A., and M. A. Uman (2003), *Lightning: Physics and Effects*, Cambridge Univ. Press, New York.
- [30] MacGorman, D. R., and W. D. Rust (1998), *The Electrical Nature of Thunderstorms*, 422 pp., Oxford Univ. Press, New York.

## Recovery of Electrical Structure of the Cloud with use of Ground-Based Measurement Results

*E. Svechnikova*<sup>1</sup>, *N. Ilin*<sup>1</sup> and *E. Mareev*<sup>1, 2</sup>

<sup>1</sup>*Institute of Applied Physics, Russian Academy of Sciences, Nizhny Novgorod, Russian Federation*

<sup>2</sup>*Nizhni Novgorod State University, Nizhni Novgorod, Russian Federation*

---

**Abstract:** The electric structure of the clouds associated with thunderstorm ground enhancements (TGEs), observed at the Aragats station, is simulated by means of The Weather Research and Forecasting (WRF) model. Clouds that cause TGE events over the rugged terrain of the high-mountainous region of Aragats Research Station (3200 m above sea level) are considered. The inverse dipole structure is found to be typical of the clouds accompanying TGEs. Graupel and snow particles play a major role in cloud electrification because of rather low density of ice particles in the clouds at the Aragats station. It is shown, that convection effectively leads to the condensation of vapour, which facilitates the charge transfer between colliding solid hydrometeors in the conditions of highland. The key evidence on the reverse point of the charge transfer processes is obtained. It is shown that WRF model is a convenient source of additional useful information about the conditions for the occurrence of high-energy events in the Earth's atmosphere.

---

### 1. INTRODUCTION

The study of high-energy processes occurring in the Earth's atmosphere is a rapidly developing issue of climatology and atmospheric physics. The consideration of the mechanisms of energetic particles fluxes development is directly related to the study of lightning discharge and the electric field structure within the cloud.

The events of low-energy (10 keV - 100 MeV, in comparison with terrestrial gamma-ray flashes) long duration (from minutes to several hours) excess over the background value of the electrons and gamma quanta flux recorded on the Earth surface are called the thunderstorm ground enhancements (TGEs) ([1], [2], [3]). The location of the Aragats observation station at a relatively high altitude, as well as the peculiarities of the region's climate and orography, lead to a usually large number of TGE events per year, which results in a large amount of data obtained at the station during ten years of observations.

Electric field and energetic particle flux measurement results is of crucial importance for the consideration of two major issues: mechanism of energetic processes in thunderstorms and structure of electric field in the cloud. These two problems are highly interwoven, as far as all the proposed mechanisms of energetic particles acceleration are field-dependent, and count rate measurement results could be used for electric field structure estimation. The proposed approach enables to recover the cloud particles spatial distribution without making any suggestions about mechanisms of particle flux generation.

The configuration of the electric field, on the one hand, defines the circumstances of lightning discharges development; on the other hand, it affects the acceleration and multiplication of energetic particles, which could be detected on the ground level. This fact is a good reason to study the electric cloud structure and a source of information to deal with the issue simultaneously.

A rather complicated charge structure of a cloud, sometimes recognised by balloon sounding [4], is usually described by highly simplified three-layered model, where the charge of the lower positive charge region (LPCR) is much smaller than absolute values of charges of two main

charge layers (middle negative and higher positive). Simultaneous electric field and count rate measurements, carried out at the Aragats station, testify a correlation between the LPCR charge value and the intensity of particle flux increase. A mature lower positive charge region could accelerate energetic particles towards the ground, being the reason of energetic particles avalanche multiplication in the lower part of the cloud, which leads to the count rate increase.

### 2. CLOUD STRUCTURE RECOVERY TECHNIQUE

In order to recover the cloud structure the ground-based measurement results should be compared with evidence from additional source. As such can be used balloon sounding, radar reflectivity measurements or interferometry data. None of the above exists for the events under consideration, which leaves computer simulation the only source of information. Methods of computer modelling and forecast, rapidly developing in the last two decades, have achieved high reliability and have become one of the main means of atmospheric research. Cloud structure recovery could be performed by applying the Weather Research and Forecast (WRF) Model ([5]), which is a widely used and approved by the scientific community simulation toolkit (examples of WRF-obtained results for cloud dynamics could be found at [6] and [7]).

The Weather Research and Forecasting Model is an atmospheric modelling system designed for both meteorological research and numerical weather prediction. WRF is suitable for a large number of applications from small scale problems to global modelling. It is an accessible research tool involving multiple parameterizations of physical processes, which serves as a basic module for the development of new parameterizations and algorithms. The physics options of the WRF model fall into several categories: parameterizations of microphysical processes, clouds, planetary boundary layer, land surface, and radiation.

To simulate the state of the atmosphere using the WRF-ARW model the strategy of two nested domains was used, with the center at the observation point (Aragats research station of ASEC, 40.4715, 44.1815). The external domain

with dimensions of 2700 x 1800 km (cell size is 3 km) completely covers the Black and Caspian seas, the Caucasus, the Minor Asian, Armenian and Iranian highlands. The internal domain with dimensions of 90 x 90 km (cell size is 1 km) reproduces in detail the Aragats mountain. Initial and boundary conditions are obtained from NCEP GDAS/FNL 0.25 Degree Global Tropospheric Analyses and Forecast Grids [8]. Microphysical parameterization is a description of generation and extinction of cloud particles (or hydrometeors) of each type (or fraction). All the widely used microphysical parameterizations for the WRF Model are bulk, which means that particle size distribution for each fraction is defined by one function in all the size range. Presented results were obtained with use of microphysical parameterization designed by Thompson [9]. Application of other parameterization, which takes into account processes involving ice particles, leads to similar results (for instance, NSSL 2-moment scheme [10] - advanced fast-developing parameterization, the most promising for research applications). The applied parameterization of microphysical processes includes 5 types of hydrometeors (rain and cloud droplets - in what follows are marked RAIN and CLOUD, snowflakes - SNOW, ice particles - ICE, and ice grains - GRAUPEL) [9]. Typical sizes of cloud particles are: CLOUD - less than 50  $\mu\text{m}$ , RAIN - more than 500  $\mu\text{m}$ , ICE particles - 0.001  $\mu\text{m}$  - 1000  $\mu\text{m}$ , SNOW particles - less than 10 mm.

Cloud electric structure and electrification processes were modeled under the following assumptions:

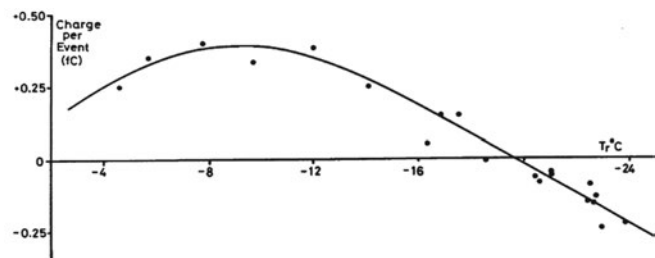
- Electric field is caused by charged hydrometeors only
- Only solid cloud particles could carry electric charge
- Charge density for each kind of particles does not significantly change on time scale of tens of minutes
- Charge density for a mass unit is uniform for each type of hydrometeors

Consideration of electrification processes was carried out with use of additional suppositions of the priority of non-induction charging mechanisms.

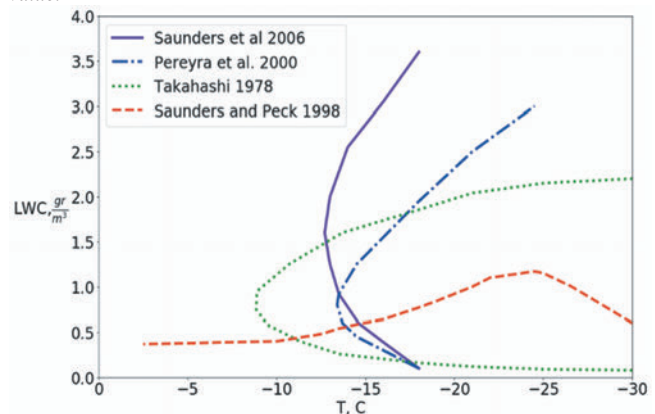
The collisions of hydrometeors of different types is considered in [11], [12]. Interaction of ice and graupel particles plays the major role in thundercloud electrification. A collision of a graupel particle and ice crystal leads to charge transfer, at that the sign of the charge obtained by the graupel particle is dependent on the temperature in a way which for some applications could be described by fig. 1a, [11]. Change of charge transfer direction inside the cloud leads to forming of three-layered charge structure. For the conditions of the Aragats Station temperature value of -17 °C corresponds to the height of approximately 2.5 km above the station. However, in a wider range of parameter values reverse point dependence on liquid water content should be also taken into account: fig. 1b presents several experimentally derived dependencies, which correspond to different setup characteristics. Applicability of each curve to each certain real atmospheric state should be studied separately.

In order to estimate the charge spatial distribution the following sequence of actions was performed:

- For each hydrometeor type spatial distribution of the mass density during all the event was recovered.
- Electric field, generated at the ground level by each type of solid hydrometeors was simulated under the assumption of uniform charge density per unit mass. Solid hydrometeors are graupel, snow and ice particles. For all the events under consideration ice particles density is three or more orders smaller than snow particles density. Consequently, the same relation took place for their charge densities. Therefore, electric field created by ice particles at the ground level is negligibly small. Correlation of measured electric field peaks with the transfer of graupel- and snow-clusters above the station proves the insignificance of charges of all the other hydrometeor types.
- For graupel and snow particles, charge density values are chosen so that resulting electric field at the ground level best matches the measurement results. Mass centres of graupel and snow particle clusters for the majority of the events are spaced horizontally. Due to that fact it is possible to determine the correspondence between electric field peaks of different polarity and two types of hydrometeors.
- Hydrometeors spatial distribution, derived from wrf-simulation, along with obtained on the previous step charge density coefficients makes the estimation of electric cloud structure. For all the cases considered, the electroneutrality of the obtained structure is shown.



(a) The charge transferred to a riming graupel pellet by a separating ice crystal following a collision, at constant cloud water content. Typical temperature of the change of charge transfer direction is about -17 °C: intersection of the curve and the temperature axis defines the reverse point value.



(b) Curves of charge transfer sign alteration in dependence on temperature and liquid water content, from laboratory studies (solid line - [12], dash-dotted - [13], dotted - [14], dashed - [15]).

Figure 1. The direction of charge transfer dependences on temperature and liquid water content. Curves indicate the condition of the charge transfer sign alteration.

Example of empirical and simulated ground-level electric field evolution during the TGE event is presented below (fig.2, fig.3).

The first electric field peak (positive) coincides in time with transfer of the graupel particle cluster above the station, which leads to the conclusion, that graupel particles are charged positively. Similarly, the negative field peak occurred at the same time moment as the maximum snow particles density above the station, consequently, snow-cluster is negatively charged. Sum of electric fields caused by graupel and snow particles at the ground level is shown in the fig.3 and describes the measurement results (fig.2) reasonably well. Negative cloud-to-ground discharges, being the reason of small-time-scale electric field disturbances, do not alter electric field in time scale more than a minute, which proves the self-consistency of constant charge density assumption. Moreover, accepted assumptions allow us to describe the rapid change in the surface electric field strength accompanied by the change of sign without introducing lightning discharges into consideration. The field value rapid change at approximately 11:50 coincides in time with the moving of the graupel-cluster away from the station: the remaining snow-cluster provides the negative electric field observed at the ground surface after 12:00

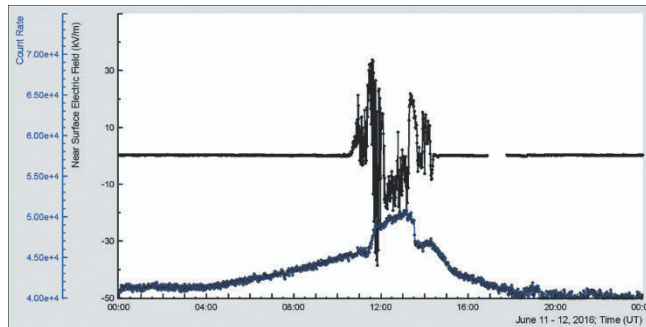


Figure 2. Electric field and energetic particle flux ground-based measurement results obtained by Electric Field Monitor Boltek EFM-100 and NaI-detectors correspondingly at the Aragats Research Station.

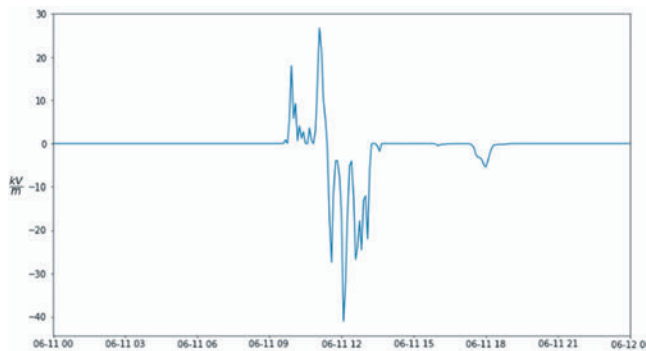


Figure 3. Simulated ground-level electric field time dependence.

The described procedure of charge density recovery leads to the conclusion, that inverse dipole cloud structure (lower positive and middle negative layers) could be a good description of clous particles distribution for several intense TGE events. Inverse dipole structure could be also characterised as conventional three-layered structure, where lower region has two parts: smaller one, localised at about 2 km and corresponding to LPCR, and the more dispersed one, which provides a positive impact into ground-level electric field value on a time scale of an hour or more. The entire charge structure is electrically neutral and causes the electric field evolution pattern similar to observed one.

Figures 4 and 5 demonstrates the recovered cloud structures.

### 3. ELECTRIFICATION PROCESSES

The fact of particular interest is that the inverse dipole structure is shown to be formed in a wide range of altitudes, which signifies the absence of reverse point in corresponding range of temperatures. This evidence could be used for comparison of simulation results with all the proposed reverse point dependencies. Absence of the mature higher positive charge region means that temperature and liquid water content values inside the cloud describe the points lying only on one side of the curve of the charge transfer direction change. Consequently, the choice of reverse point curve (on temperature-LWC plane) is defined by the condition of noncrossing the curve (at least for the temperature values above  $-20^{\circ}\text{C}$ ), which describes the simulation results.

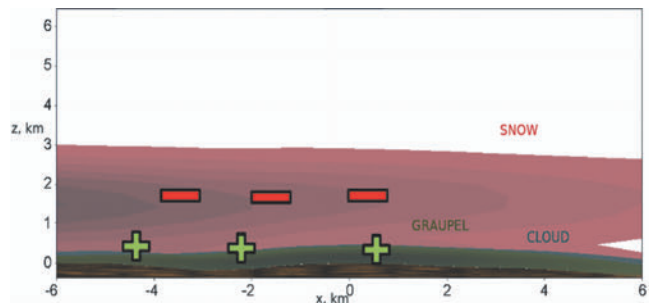


Figure 4. Cloud structure at 07:00 of 2016-10-29 obtained with use of WRF Model. Graupel particles (GRAUP, marked in green) and snow particles (SNOW, marked in red) play the major role in the formation of electric structure of the cloud.

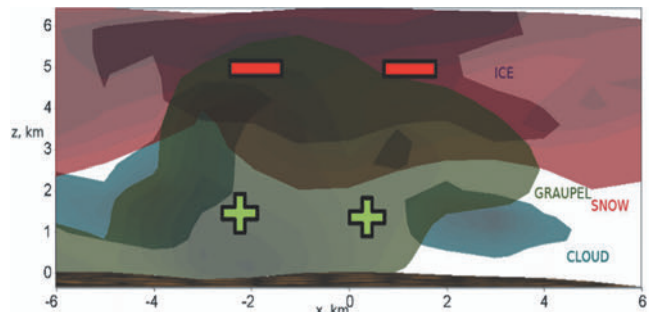


Figure 5. Cloud structure at 11:00 of 2016-06-11 obtained with use of WRF Model. Graupel particles (GRAUP, marked in green) and snow particles (SNOW, marked in red) play the major role in the formation of electric structure of the cloud.

All the proposed models except Saunders and Peck 1998 lead to the reverse point value approximately  $-20^{\circ}$ - $25^{\circ}\text{C}$  (defined as the intersection of the experimental curves with the modeling result), which corresponds to the 3-4 km altitude value, which is in the upper part of the cloud. Consequently, only a thin higher positive charge layer is formed above the altitude corresponding to reverse point value.

Modeling results show a remarkable correlation of the cloud particles (little droplets) and ascending air currents spatial distribution:

Figures 7a and 7b have a certain similarity, which leads to the conclusion, that cloud particles are formed from the vapor by condensation when the air is raised. Existence of significant concentrations of cloud- and rain-particles could intensify the electrification, which accompanies graupel- and snow- particles collisions. Influence of liquid water on the charge transfer processes is described in details in [16], [14].

#### 4. CONCLUSIONS

A cloud electric structure estimation is obtained by comparison of electric field ground-based measurement results with the results of the state of the atmosphere numerical modeling.

Two dozen TGE events analysis has lead to the following conclusions:

- Cloud structure and ground-surface electric field time evolution could be successfully simulated with use of the WRF Model.
- For all the analyzed intense TGE events cloud has a lower layer with the significant positive charge.

- Interaction of graupel and snow particles plays a decisive role for the electrification processes above the Aragats station, instead of graupel-ice. Graupel-snow interaction could have a reverse point, dependent on temperature and liquid water content, by the same way, as for graupel-ice interaction.
- Revers point value is achieved by temperature at altitude about 3-4 km, which leads to formation of the cloud with pronounced lower positive and middle negative layers, instead of ordinary three-layered structure. The impact of the higher positive layer into the ground-level electric field is shown to be insignificant for description of electric field evolution.

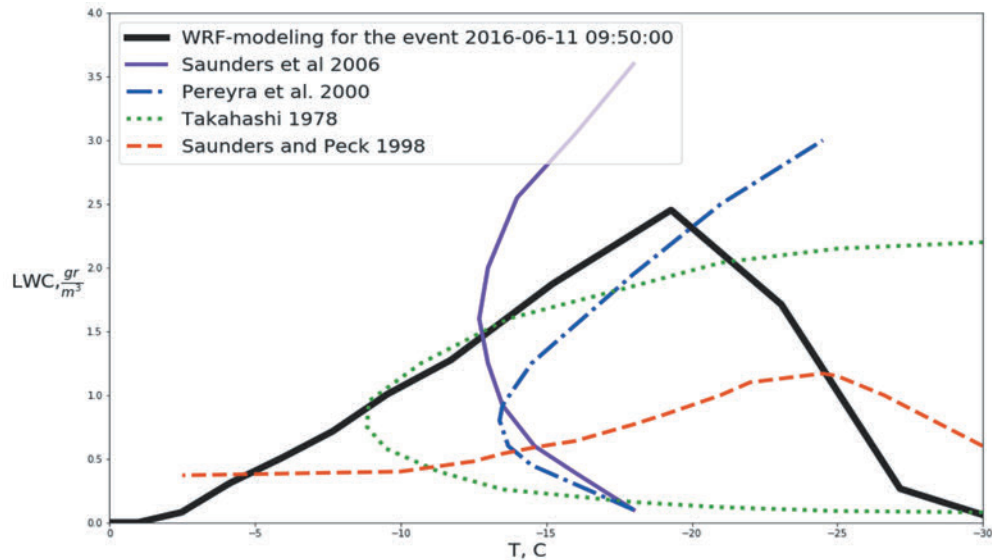
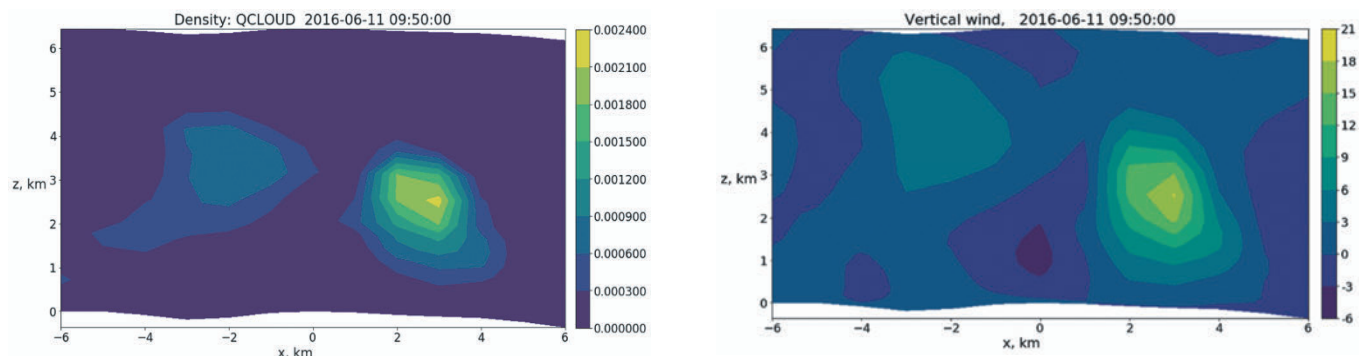


Figure 6. The direction of charge transfer dependences on temperature and liquid water content, according to WRF simulation for the event of 2016-06-11 09:50, in comparison with the results obtained in laboratory studies by other researchers. Curves indicate the condition of the charge transfer sign alteration.



(a) Distribution of cloud particles density at 2016-06-11 09:50, modeled by means of WRF.

(b) Distribution vertical wind speed at 2016-06-11 09:50, the scale is graduated in  $m/s$ , modeled by means of WRF.

Figure 7. Clusters of little water droplets are located in the regions of the strong ascending currents of air.

#### REFERENCES

[1] A. Chilingarian, Thunderstorm Ground Enhancements (TGEs) - New High-Energy Phenomenon Originated in the Terrestrial Atmosphere, Journal of Physics: Conference Series 409, 012019, 2013

[2] A. Chilingarian, T. Karapetan, L. Melkumyan, Statistical analysis of the Thunderstorm Ground Enhancements (TGEs) detected on Mt. Aragats. J. Adv. Space Res., 52, 1178, 319, 2013

[3] A. Chilingarian, MAilyan B., Vanyan L., Observation of Thunderstorm Ground Enhancements with intense fluxes of high-energy electrons, Astron. Phys., 48, 1, 2013

[4] T.C. Marshall Et.al., Rocket and balloon observations of electric field in two thunderstorms, J. Geophys. Res., 100, 20,815-20,828, 1995

[5] <https://www.mmm.ucar.edu/weather-research-and-forecasting-model>

[6] Daniel T. Dawson II, Edward R. Mansell, Matthew R. Kumjian, Does Wind Shear Cause Hydrometeor Size Sorting?, J. Atmos. Sci., 72, 340-348, 2014

[7] Pengguo Zhao, Yan Yin, Hui Xiao, The effects of aerosol on development of thunderstorm electrification: A numerical study. Athm. Res, 153, 376-39, 2015

- [8] <https://doi.org/10.5065/D65Q4T4Z>, Research Data Archive at the National Center for Atmospheric Research, Computational and Information Systems Laboratory.
- [9] G. Thompson et.al, Explicit Forecasts of Winter Precipitation Using an Improved Bulk Microphysics Scheme. Part II: Implementation of a New Snow Parameterization. *Mon. Wea. Rev.*, 136, 5095-5115, 2008.
- [10] Mansell, E. R., C. L. Ziegler, and E. C. Brun- ing, Simulated electrification of a small thunderstorm with two-moment bulk microphysics *J. Atmos. Sci.*, 67, 171–194, 2010
- [11] Clive Saunders, Charge Separation Mechanisms in Clouds, *Space Sci Rev*, 137, 335–353, 2008
- [12] C. Saunders, H. Bax-Norman, C. Emersic, E. E. Avila, and N. E. Castellano, Laboratory studies of the effect of cloud conditions on graupel/crystal charge transfer in thunderstorm electrification. *Quart. J. Roy. Meteor. Soc.*, 132, 2653–2673, 2006
- [13] R.G. Pereyra, E.E. Avila, N.E. Castellano, C.P.R. Saunders, A laboratory study of graupel charging, *J. Geophys. Res.*, 105, 20,803-20,812, 2000
- [14] T. Takahashi, Riming Electrification as a Charge Generation Mechanism in Thunderstorms. *Journal of the Atmospheric Sciences*, Vol. 35, No. 8, 1978
- [15] C.P.R. Saunders, S.L. Peck, Laboratory studies of the influence of the rime accretion rate on charge transfer during crystal/graupel collisions, *J. Geophys. Res.*, 103, 13949-13956, 1998
- [16] T. Takahashi, Electrification of condensing and evaporating liquid drops. *Journal of the Atmospheric Sciences*, Vol.30, No.2, 1973

## Modelling of the Electron Acceleration and Multiplication in the Electric Fields Emerging in Terrestrial Atmosphere

*A. Chilingarian, M. Zazyan, G. Karapetyan*

*A. Alikhanyan National Lab (Yerevan Physics Institute), Yerevan 0036, Armenia*

**Abstract:** Thunderstorm ground enhancements, fluxes of electrons, gamma rays, and neutrons originated in the thunderstorm atmospheres are controlled by the strength of the atmospheric electric fields. If the strength is above a threshold value, that is inversely proportional to the air density, a Relativistic Runaway Electron Avalanche (RREA) is unleashed, in which large-scale multiplication of the particles took place. The second process, Modification of the electron energy spectra (MOS) operates on much less scales however is effective for almost all strengths of atmospheric electric fields. In the series of simulations with the CORSIKA code we show that MOS process can be responsible for long lasting TGEs recently discovered on Aragats.

### 1. INTRODUCTION

The emerging field of High Energy Atmospheric Physics (HEAP, Dwyer et al., 2012), studies events producing high energy particles in the terrestrial atmosphere, such as thunderstorm ground enhancements (TGEs, Chilingarian et al., 2010,2011), terrestrial gamma-ray flashes (TGFs, Fishman et al., 1994) and gamma-ray glows (McCarthy and Parks (1985); Kelly et al., 2015). It is widely accepted that all 3 processes are driven by electric fields, ionization, scattering and bremsstrahlung (Dwyer, 2003, Chilingarian, Mailyan and Vanyan, 2012, Saria et al., 2018). One of underlying processes, namely Runaway Breakdown (RB, Gurevich et al., 1992), now mostly refereed as Relativistic Runaway Electron Avalanche (RREA, Babich et al., 2001, Dwyer, 2003) is a “threshold” process controlled by the strength of the electric field to be above definite threshold value dependent on the density of the air. RB/RREA is responsible for the expansion of electron-gamma ray avalanches in the atmosphere and, consequently, for the large-scale multiplication of the particles detected on the earth surface or observed in atmosphere by facilities on balloons and aircraft. The second process, Modification of the electron energy spectra (MOS, Dorman and Dorman, 2005, Chilingarian, Mailyan and Vanyan, 2012) operates on much less scales however is effective for almost all strengths of atmospheric electric fields.

Monte Carlo simulations for such a complicated domain as HEAP is not a precise tool. We do not know the distribution of the electric charges in the atmosphere unique for each observed event, and, therefore, strength and elongation of the emerging electric fields. Nonetheless, these simulations give us understanding of the operation of RB/RREA and MOS processes and expected behavior of the energy spectra, as it is measured by the particle detectors located on the earth’s surface.

What we always have in the heart of our modelling activities is that simulation should be paired with experimentation; and each should profit from other. After our recently observation of Long Lasting TGEs (LL TGEs, Chilingarian et al., 2018) – a hours extending flux of gamma rays observed at Aragats, we started a cycle of simulations to get answer if the MOS process can provide such a long duration of gamma ray flux, or remote Extensive Cloud Showers (ECSs) can contribute to this flux, or we should consider another origin of gamma rays,

say, a stochastic electron acceleration by a set of randomly distributed charges in the atmosphere, or Radon progenies gamma ray radiation. Thus, our simulations are always pairing with observations and with hypothesis testing.

### 2. MODELLING OF THE RB/RREA AND MOS PROCESSES IN THE ATMOSPHERE

In 2012, we perform GEANT4 simulations of the particle propagation in the atmosphere with an electric field of 1.8 kV/cm spread uniformly from 5000m till 3600m a.s.l. above Aragats research station located on 3200m a.s.l. (Chilingarian, Mailyan and Vanyan, 2012). As seed particles were used secondary Cosmic Ray (CR) electrons in the energy range of 1–300 MeV. We also test fields below this threshold for RB/RREA to illustrate the possibility to registered TGEs not ultimately related to the avalanched process in the atmosphere, i.e. - by the MOS process. Due to finite sizes of our spectrometers, the maximal energy of observed electrons did not exceed 40-50 MeV. By examining the ratio of electron to gamma ray flux for the largest TGE event of 19 September 2009, we estimate the height above particle detectors where electrons and gamma rays of the avalanche leave the region of strong electric field (see Appendix C of Chilingarian, Mailyan and Vanyan, 2012). Using obtained estimate of ~50 m, the number of electrons with energies above 1 MeV at the exit from the cloud was estimated to be  $\sim 2 \cdot 10^7$  /m<sup>2</sup>/min; if we assume that the radiation region in the atmosphere has a radius of 1 km the total number of electrons crossing this region in a minute is  $\sim 6 \cdot 10^{13}$ .

For a new series of simulations, we use the CORSIKA package (details of used options of CORSIKA code one can find in Chilingarian, Knapp and Zazyan, 2019) to achieve a model independent inference and to get clues in the recent observations of the long-lasting TGEs and “winter” TGEs that were not accompanied with thunderstorms and large disturbances of the near-surface electric field. From the consideration of the ~500 TGE events observed in the last decade, we conclude that far not all TGEs are due to RB/RREA process. To investigate the “small fields” effect, we use in simulations rather low values of the atmospheric electric fields strengths starting from 0.1kV/cm. Overall scheme of the simulations is presented in Fig. 1.

Each simulation set consists of  $10^8$  showers originated from vertically traversing CR electrons with energies in the interval 1–300MeV. The power law shape of the differential energy spectrum of electrons with spectral

index  $\gamma = -1.21$  was used in simulations. Avalanche particles were followed till the Earth's surface ( $H_{\text{obs}} = 3200\text{m a.s.l.}$ ) or till their energy become less than  $E_{\text{cut}}=0.05\text{MeV}$ . Electric field  $Ez>0$  was introduced in a kilometer length above the "cloud base"  $H$ , that was changed from 50 to 1000 m. modeled under the following assumptions:

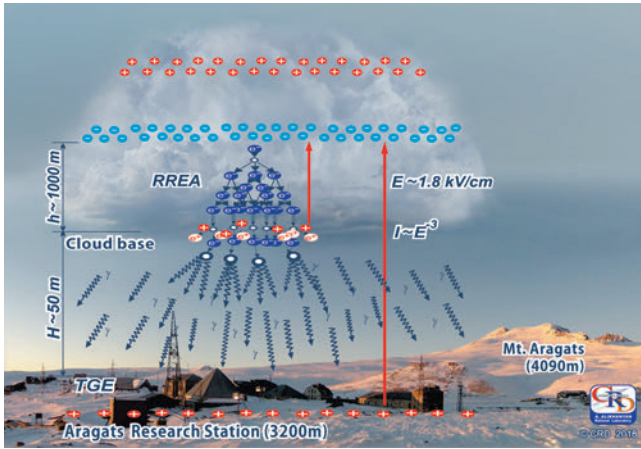


Figure 1. The scheme of the electron acceleration modelling in the atmosphere.

As we can see in the Figure 1 two fields are supporting the electron acceleration downwards: the field between main negative layer and its mirror on the earth and field between the same negative layer and small positively charged layer in the bottom of the cloud. Sure, it is highly simplified structure, however, the most intense TGEs happened when both fields are in play and their superposition exceeds the avalanche initiating threshold. In simulation, we make no difference between these fields, assuming existence of constant field a kilometer length with fixed preselected strength. Both such a field elongation and strength were routinely measured in balloon flights (Marshall et al., 1995, 2005).

In Figure 2, we show the energy spectra of secondary gamma rays reaching earth's surface after crossing 1 km long electric field from 0.1 to 2 kV/cm above Aragats research station.

In Table 1, we enumerate the gamma ray flux enhancement. After reaching RB/RREA threshold, the number of particle exponentially rose in the electron – gamma ray avalanches. However, even for the small electric fields we have significant enhancement that can be reliably registered by the spectrometers and counters located on Aragats.

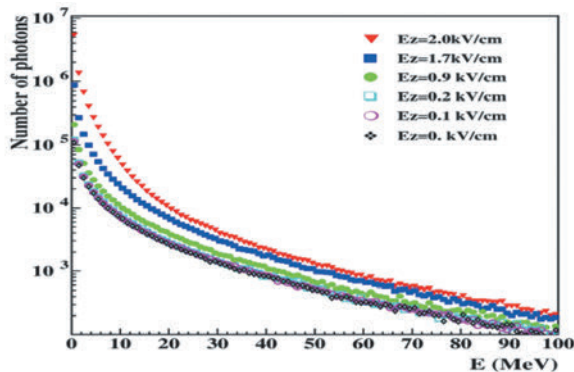


Figure 2. Energy spectra of secondary photons reaching earth's surface after traversing electric field of 1km located 50m above Aragats research station (3200m a.s.l.).

Table 1. Number of secondary photons reaching earth's surface after traversing electric field of 1km located 50 m above Aragats research station (3200m a.s.l.).

$Ez$ (kV/cm)	$N(Ez)$	$(N(Ez)-N(0))/N(0)$ (%)
0.	370647	0
0.1	387271	4.5
0.2	405065	9.3
0.3	425962	14.9
0.9	626225	69.0
1.7	1879136	407.0
2.0	9052389	2342.3

In Table 2 we post the particle flux enhancement (comparing with fair weather values) in different energy intervals. We see that most of enhancement for sizable electric fields occurred at low energies.

Table 2 Enhancement  $(N(Ez)-N(0))/N(0)$  (%) of secondary photons in different energy intervals.

$Ez$ (kV/cm)	0.3 - 2 MeV	50 - 60 MeV	70 - 80 MeV
0.1	5.6	5.7	3.7
0.2	11.3	7.4	3.7
0.3	17.7	11.8	4.7
0.9	82.9	37.1	32.1
1.7	547.4	109.7	94.1
2.0	3412.3	157.3	133.9

The enhancement of gamma ray flux for different energy intervals are shown in Figure 3.

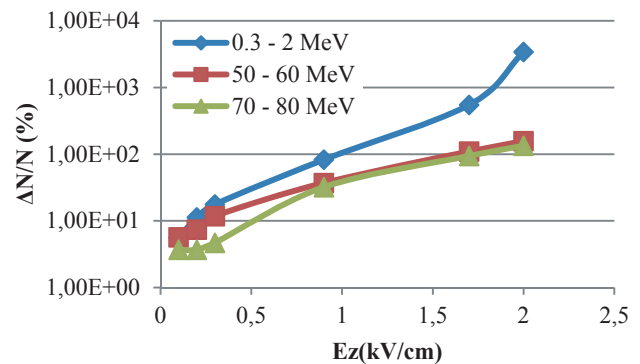


Figure 3. Enhancement  $(N(Ez)-N(0))/N(0)$  (%) of secondary photons in different energy intervals.

In Table 3, we show the gamma ray flux after crossing 1 km long electric field located at different distances above earth's surface.

Table 3. Number of gamma rays at observation level and for different heights of electric field above it.

$Ez$ (kV/cm)	$H=50\text{m}$	$H=200\text{m}$	$H=500\text{m}$
0.	370647	304168	211015
0.8	581764	466073	313161
1.7	1879136	1397688	859752

In Table 4-6, we show the same information as in Table 3 but separately for different energy intervals and heights of electric field above earth's surface.

**Table 4. Number of gamma rays reaching earth's surface from H=50m**

Ez (kV/cm)	0.3 - 2 MeV	50 – 60 MeV	70 – 80 MeV
0.	112754	4022	2042
0.8	189429	5337	2610
1.7	729999	8434	3965

**Table 5. Number of gamma rays reaching earth's surface from H=200m**

Ez (kV/cm)	0.3 - 2 MeV	50 – 60 MeV	70 – 80 MeV
0.	90213	3564	1756
0.8	146062	4482	2192
1.7	536886	7085	3252

**Table 6. Number of gamma rays reaching earth's surface from H=500m**

Ez (kV/cm)	0.3 - 2 MeV	50 – 60 MeV	70 – 80 MeV
0.	60344	2347	1184
0.8	93111	3254	1489
1.7	307121	5305	2375

In Table 7 and Figure 4 we demonstrate the influence of electric field height on the number of additional gamma rays reaching the earth's surface. We can see that from 50m to 200m the number of additional gamma rays decreases ~1.2 times, and from 50 to 1000m – more than 3 times. In the spring season (April-June at Aragats), the cloud base height do not exceed 200 m. and usually is ~ 50 m.

**Table 7. Number of gamma rays reaching earth's surface from different heights.**

	H=0m	H=50m	H=200m	H=500m	H=1000m
N <sub>γ</sub>	1106968	581764	466073	313161	185241

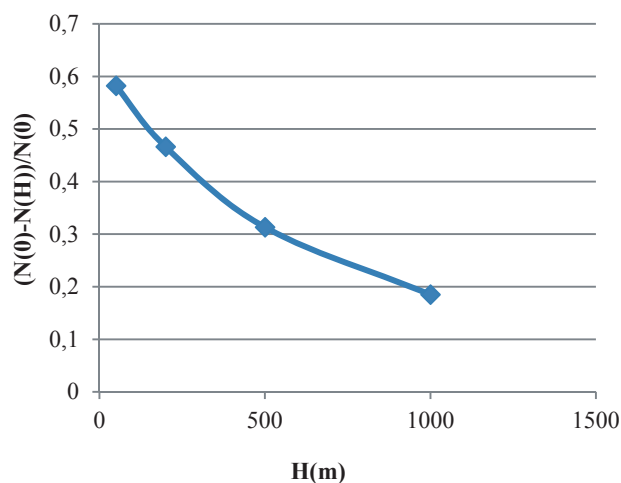


**Figure 4. Ratio of gamma rays reaching earth's surface after escaping from electric field at different heights, Ez=0.8kV/cm with elongation of 1 km.**

### 3. DEPENDENCE OF MOS PROCESS ON THE ELECTRON ENERGY

We perform another trial of simulation to find out which energies of electron entering electric field make major contribution to the gamma ray flux observed on the earth's surface. The parameters of simulation were as follows:

Each simulation set consists of 2 trials of  $10^8$  electrons each, distributed according the power law with index  $\gamma = -1.21$  with energies in the interval 1÷100MeV (a) and, 1÷300MeV (b). Secondary particles energy cut was  $E=0.05\text{MeV}$ . Observation level  $H_{\text{obs}} = 3200\text{m}$  above sea level. The electric field was located between 3250m  $< H < 4250\text{m}$ .

Results of simulations are presented in Figures 5-6 and Tables 8-9.

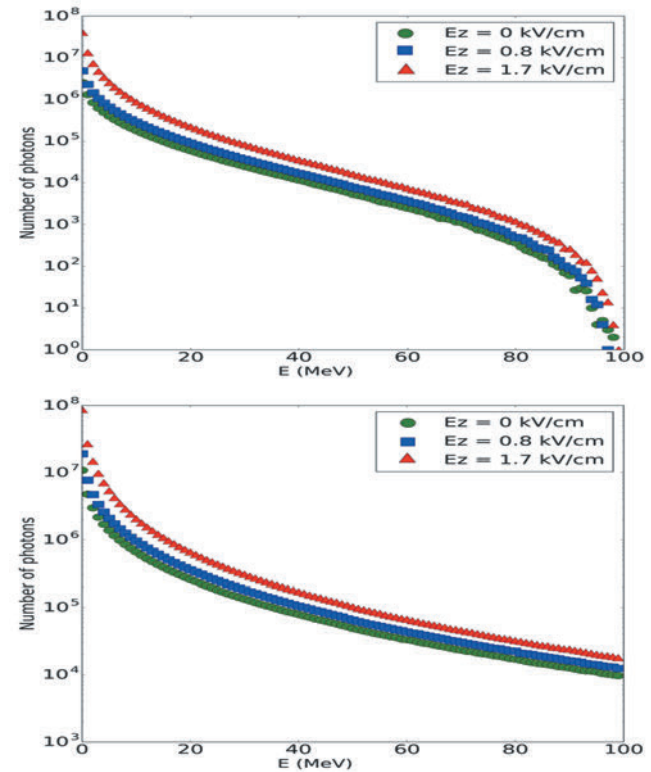


**Figure 5. Secondary photon spectra for two cases of initial electrons energy intervals (1÷100MeV (a) and, 1÷300MeV (b) and different electric fields.**

**Table 8. Number of secondary photons in different energy intervals for the case of the energy of initial electrons up to 100 MeV (a).**

Ez (kV/cm)	0.3 - 2 MeV	50 – 60 MeV	70 – 80 MeV
0	3019282	39615	7031
0.8	5458312	58407	10355
1.7	36234358	120930	22292

**Table 9. Number of secondary photons in different energy intervals for the case of the energies of initial electrons up to 300 MeV(b).**

Ez (kV/cm)	0.3 - 2 MeV	50 – 60 MeV	70 – 80 MeV
0	11625191	460104	225106
0.8	19334083	620002	296145
1.7	74755429	1087393	494531

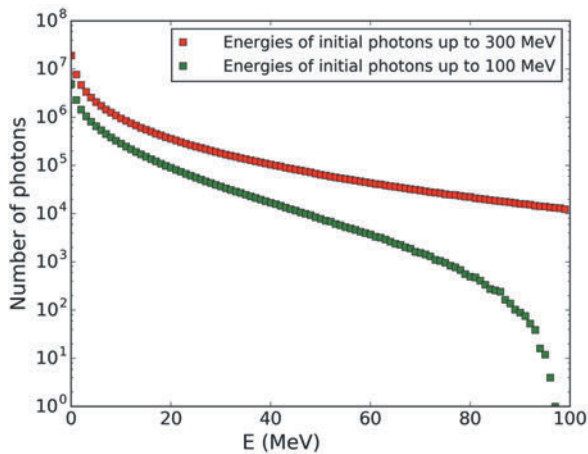


Figure 6. Secondary photons spectra for primary electrons for two cases of initial electrons energy intervals

From Tables 8 and 9 and from Fig. 5 it is apparent that the main contribution to the MOS gamma rays comes mostly from the high-energy electrons. This is expected due to very strong dependence of the bremsstrahlung cross section on electron energy.

#### 4. EFFECT OF NEAR EARTH ELECTRIC FIELD ON THE INTENSITY OF THE ANNIHILATION PEAK AT 511 KEV

During a few aircraft campaigns gamma-ray glows have been observed in the energy range (50 keV to 10 MeV). In 2 flight ( a short pulses (200 ms -1 s) of enhanced fluxes of 511 keV emissions have been reported, indicating an enhanced flux of positrons annihilating (Dwyer *et al.*, 2015 and Kochkin *et al.*, 2018). To estimate how much the 511 keV peak was enhanced due to atmospheric electric field we performed CORSIKA simulation with CR electrons in the energy range of 1–300 MeV as seed particles. Electric field  $E_z > 0$  was introduced in a kilometer above observation level. Results of simulations for  $E_z=1\text{kV/cm}$  and  $E_z=0$  are presented in Figure 6.

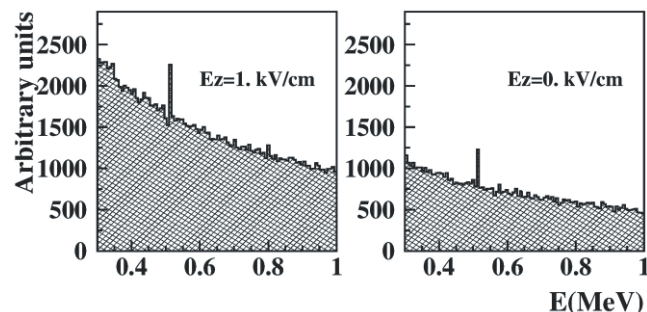


Figure 6. Annihilation peak for two cases of CORSIKA simulation.

The annihilation peak height above background is 1.5 times larger for the case of  $E_z=1\text{kV/cm}$  comparing with no-field case.

#### CONCLUSIONS

We use the CORSIKA code to get clues in the recent observations of the long-lasting TGEs and “winter” TGEs that were not accompanied with thunderstorms and large disturbances of the near-surface electric field. From the consideration of the ~500 TGE events in the last decade, we conclude that far not all TGEs are due to RB/RREA process. To investigate the “small fields” effect, we use in simulations rather low values of the atmospheric electric fields strengths starting from 0.1 kV/cm. We show that the modification of the cosmic ray electron energy spectra

(MOS process) lead to additional bremsstrahlung radiation reaching the earth and sustaining significant additional gamma ray flux. Small disturbances of the near-surface electric field can be induced by larger disturbances of atmospheric electric field; thus, the MOS process can continuously enlarge the flux of bremsstrahlung gamma rays in the energy domain 0.3-3 MeV ever for the minimal fields started from 0.1 kV/cm. The main contribution to the MOS gamma rays comes mostly from the high-energy electrons from ambient population of secondary electrons (100 – 300 MeV).

#### REFERENCES

- [1] Babich, L.P., Donskoy, E.N., Kutsyk, I.M., Kudryavtsev, A.Y., Roussel-Dupre, R.A., Sharmraev, B.N., and Symbalysty, E.M.: Comparison of relativistic runaway electron avalanche rates obtained from Monte Carlo simulations and kinetic equation solution, IEEE transactions on plasma science, 29, 430–438, 2001.
- [2] Chilingarian, A., Daryan, A., Arakelyan, K., Hovhannisyanyan, A., Mailyan, B., Melkumyan, L., Hovsepyan, G., Chilingaryan, S., Reymers, A., and Vanyan, L.: Ground-based observations of thunderstorm-correlated fluxes of high-energy electrons, gamma rays, and neutrons, Physical Review D, 82, 043009, 2010.
- [3] Chilingarian A.A., Hovsepyan G., and Hovhannisyanyan A.: Particle bursts from thunderclouds: Natural particle accelerators above our heads, Physical review D, 83, 062001, 2011.
- [4] Chilingarian A., Mailyan B., and Vanyan L.: Recovering of the energy spectra of electrons and gamma rays coming from the thunderclouds, Atmospheric Research, 114, 1–16, 2012.
- [5] Chilingarian, A., Hovsepyan, G., Soghomonyan, S., Zazyan, M., and Zelenyy, M.: Structures of the intracloud electric field supporting origin of long-lasting thunderstorm ground enhancements, Physical review 98, 082001, 2018.
- [6] Chilingarian, A., Knapp, J., Zazyan, M.: Monitoring of the atmospheric electric field and cosmic-ray flux for the interpretation of results in high-energy astroparticle physics experiments, The European Physical Journal Conferences 197(2-3):03001, DOI: 10.1051/epjconf/201919703001, 2019.
- [7] Dwyer, J. R., D. M. Smith, B. J. Hazelton, et al., Positron clouds within thunderstorms, J. Plasma Phys., 81, 475810405 2015, doi:10.1017/S0022377815000549.
- [8] Dorman, L.I., Dorman, I.V., 2005. Possible influence of cosmic rays on climate through thunderstorm clouds. Adv. Space Res. 35, 476–483.
- [9] Dwyer, J.R.: A fundamental limit on electric fields in air, Geophysical Research Letters, 30, 2055, 2003.
- [10] Dwyer, J.R., Smith, D.M., and Cummer, S.A.: High-Energy Atmospheric Physics: Terrestrial Gamma-Ray Flashes and Related Phenomena, Space Science Review, 173, 133–196, 2012.
- [11] Fishman, G.J., Bhat, P.N., Mallozzi, R., Horack, J.M., Koshut, T., Kouveliotou, C., Pendleton, G.N., Meegan, C.A., Wilson, R.B., Paciesas, W.S., Goodman, S.J., and Christian, H.J.: Discovery of Intense Gamma-Ray Flashes of Atmospheric Origin, Science, 264, 1313–1316, 1994.

- [12] Gurevich, A., Milikh, G., and Roussel-Dupre, R.: Runaway electron mechanism of air breakdown and preconditioning during a thunderstorm, *Physics Letters A*, 165, 463–468, 1992.
- [13] Kelley, N.A., Smith, D.M., Dwyer, J.R., Splitt, M., Lazarus, S., Martinez-McKinney, F., Hazelton, B., Grefenstette, B., Lowell, A., and Rassoul, H.K.: Relativistic electron avalanches as a thunderstorm discharge competing with lightning, *Nature communications*, 6, 2015.
- [14] Kochkin, P. O., D. Sarria, C. Skeie, et al., In-Flight Observation of Positron Annihilation by ILDAS, *J. Geophys. Res.*, 123, 2018, doi: 10.1029/2018JD028337.
- [15] Marshall, T. C., McCarthy, M. P. & Rust, W. D. Electric field magnitudes and lightning initiation in thunderstorms. *J. Geophys. Res.* 100, 7097–7103, 1995.
- [16] Marshall, T. C., Stolzenburg, M., Maggio, C. R. et al., Observed electric fields associated with lightning initiation. *Geophys. Res. Lett.* L03813, 2005.
- [17] McCarthy, M. and Parks, G.: Further observations of X-rays inside thunderstorms, *Geophysical Research Letters*, 12, 393–396, 1985.
- [18] Sarria, D., Rutjes, C., Diniz, et al., Evaluation of Monte Carlo tools for high-energy atmospheric physics II: relativistic runaway electron avalanches, *Geoscientific Model Development*, *Geosci. Model Dev.*, 11, 4515–4535, 2018

## Mapping Observation Project of High-Energy Phenomena during Winter Thunderstorms in Japan

**Y. Wada,<sup>1,2</sup> T. Enoto,<sup>3</sup> Y. Furuta,<sup>4</sup> K. Nakazawa,<sup>5</sup> T. Yuasa,<sup>6</sup> T. Matsumoto,<sup>1</sup> D. Umemoto,<sup>7</sup> K. Makishima,<sup>2,1,8</sup> H. Tsuchiya,<sup>9</sup> and the GROWTH collaboration**

<sup>1</sup>Department of Physics, Graduate School of Science,  
 The University of Tokyo, 7-3-1 Hongo, Bunkyo-ku, Tokyo 113-0033, Japan

<sup>2</sup>High Energy Astrophysics Laboratory, Nishina Center for Accelerator-Based Science,  
 RIKEN, 2-1 Hirosawa, Wako, Saitama 351-0198, Japan

<sup>3</sup>The Hakubi Center for Advanced Research and Department of Astronomy,  
 Kyoto University, Kitashirakawa Oiwake-cho, Sakyo-ku, Kyoto 606-8502, Japan

<sup>4</sup>Collaborative Laboratories for Advanced Decommissioning Science, Japan Atomic Energy Agency,  
 2-4 Shirane Shirakata, Tokai-mura, Naka-gun, Ibaraki 319-1195, Japan

<sup>5</sup>Kobayashi-Maskawa Institute for the Origin of Particles and the Universe,  
 Nagoya University, Furo-cho, Chikusa-ku, Nagoya, Aichi 464-8601, Japan

<sup>6</sup>Block 4B, Boon Tiong Road, Singapore 165004, Singapore

<sup>7</sup>Discrete Event Simulation Research Team, Center for Computational Science,  
 RIKEN, 7-1-26 Minatojima-minami-machi, Chuo-ku, Kobe, Hyogo, 650-0047 Japan

<sup>8</sup>Kavli Institute for the Physics and Mathematics of the Universe,  
 The University of Tokyo, 5-1-5 Kashiwa-no-ha, Kashiwa, Chiba 277-8683, Japan

<sup>9</sup>Nuclear Science and Engineering Center, Japan Atomic Energy Agency,  
 2-4 Shirane Shirakata, Tokai-mura, Naka-gun, Ibaraki 319-1195, Japan

The Gamma-Ray Observation of Winter Thunderclouds (GROWTH) collaboration has been performing observation campaigns of high-energy radiation in coastal areas of Japan Sea. Winter thunderstorms in Japan have unique characteristics such as frequent positive-polarity discharges, large discharge current, and low cloud bases. These features allow us to observe both long-duration gamma-ray bursts and lightning-triggered short-duration bursts at sea level. In 2015, we started a mapping observation project using multiple detectors at several new observation sites. We have developed brand-new portable gamma-ray detectors and deployed in the Kanazawa and Komatsu areas as well as the existing site at Kashiwazaki. During three winter seasons from 2015, we have detected 27 long-duration bursts and 8 short-duration bursts. The improved observation network in Kashiwazaki enables us to discover that the short-duration bursts are attributed to atmospheric photonuclear reactions triggered by a downward terrestrial gamma-ray flash. Collaborating with electric-field and radio-band measurements, we have also revealed a relation between abrupt termination of a long-duration burst and a lightning discharge. We demonstrate that the mapping observation project has been providing us clues to understand high-energy atmospheric phenomena associated with thunderstorm activities.

### INTRODUCTION

Recent discoveries of high-energy phenomena associated with thunderstorm activities have been proving that thunderclouds and lightning discharges can be powerful electron accelerators. From space, terrestrial gamma-ray flashes (TGFs) were first discovered by Compton Gamma-Ray Observatory[1], then have been observed by gamma-ray astronomy satellites such as RHESSI[2], AGILE[3] and Fermi[4]. They last for a few hundred microseconds to several milliseconds, and their photon energy extends beyond 20 MeV. In addition, similar lightning-associated events at ground-level have been also detected by mountain top experiments[5-8] and by rocket-triggered lightning experiments[9, 10]. They are referred to as "downward terrestrial gamma-ray flashes". In contrast, long-lasting radiation enhancements from thunderclouds have been also detected by airborne [11-14], mountain-top[15-21], and sea-level measurements[22-26]. They are called long bursts[23], gamma-ray glows[13], and thunderstorm ground enhancements especially when detected by on-ground experiments[20]. They have second- to minute-order duration which is much longer than TGFs, and their photon energy can also reach a few tens of MeV[25]. The long-

lasting emissions often precede and sometimes terminate with lightning discharges[11-13, 24, 27-30].

These atmospheric high-energy phenomena are thought to be bremsstrahlung of electrons accelerated in strong electric fields of lightning and thunderclouds. Based on Wilson's runaway electron hypothesis [31], Greig et al.[32] proposed relativistic runaway electron avalanches (RREA). When thunderstorms have strong electric fields (e.g. more than 284 kV/m at standard temperature and pressure, derived by a simulation of Dwyer[33].), energetic seed electrons, whose energy is more than a few hundreds of keV, are accelerated and exponentially multiplied. RREA is thought to be the most plausible model for these high-energy phenomena associated with thunderstorm activities. In addition, the relativistic feedback model was introduced by Dwyer[34] to explain the brightness of TGFs.

Winter thunderstorms in Japan are ideal targets for observations of atmospheric high-energy phenomena. Long bursts in Japanese winter thunderstorms were first discovered by radiation monitoring stations in nuclear power plants [22], and have been observed by sea-level measurements [22-26]. Winter thunderstorms have unique features comparing to summer ones such as high-current discharges, a large proportion of positive-polarity discharges and upward leaders, and lower cloud bases [35, 36]. In usual, long bursts

in summer thunderstorms can be hardly detected at sea-level because their charged region is located typically above 3 km altitude, which is too high for gamma-rays of MeVs to penetrate toward the ground. On the other hand, lower cloud bases of winter thunderstorms, typically less than 1 km, allow gamma rays to reach the sea level.

In order to investigate high-energy phenomena in winter thunderstorms, we started the GROWTH (Gamma-Ray Observation of Winter Thunderclouds) experiment in 2006. Radiation monitors were deployed at Kashiwazaki-Kariwa Nuclear Power Plant in Niigata Prefecture, Japan. Coastal areas of Japan Sea, including the Kashiwazaki site, often encounter active thunderstorms during every winter season. We have observed two types of energetic phenomena. Long bursts, as referred above, are minute-order bremsstrahlung emissions from thunderclouds, apparently not associated with lightning [24, 25, 28]. Tsuchiya et al. [24] revealed that long bursts originate from bremsstrahlung of electrons accelerated beyond 10 MeV in winter thunderclouds. In contrast, we have also detected short-duration radiation bursts called "short bursts" [37] coinciding with lightning discharges. Short bursts have a duration of a few hundred milliseconds, which is shorter than long bursts, but longer than TGFs. Typical count-rate histories and energy spectra of the two phenomena are presented in Figure 1.

As observational results of long bursts are accumulated, several important questions to be answered are raised:

- How long bursts emerge, develop, and terminate?
- How thunderclouds keep highly electrified region responsible for electron acceleration?
- How large energy thunderclouds release by emitting high-energy photons?

In addition, what causes short bursts was completely missing, which is addressed later (see section "Interpretation of short bursts"). To answer these questions, we started a mapping observation project with multiple observation sites. The project was launched in 2015 with 2 portable detectors, and is expanding the number of detectors in coastal areas of Japan Sea. The project aims to detect long bursts and short bursts with multiple detectors, and to measure spatial ux distribution, spectra, and temporal ux variations. In the present paper, we introduce our detectors dedicated to the project, and high-lights of observational results in 2015-2017 winter seasons.

## INSTRUMENTATION

### Development of portable detector

The mapping observation project requires a portable detector system dedicated to outdoor observation of gamma-rays. We have been deploying detectors mainly in urban areas because it is easy to obtain power sources. In this case, detectors should be compact for limited installation spaces on rooftops. In addition, to deploy more than 10 detectors, the detector system should be portable, easy to handle, easy to assemble, and suitable for mass production. Therefore, we employed a simple configuration consisting of a main scintillation crystal coupled with photomultipliers (PMTs), data acquisition (DAQ) system, and telecommunication system.

Scintillation crystals are utilized as the main detection component. To detect gamma rays of more than 10 MeV, we employ inorganic scintillators such as Be<sub>4</sub>Ge<sub>3</sub>O<sub>12</sub> (BGO), sodium iodide (NaI), and cesium iodide (CsI) crystals. For example, BGO crystals with 2.5 cm thickness can interact with ~50% of 10 MeV gamma rays. Light yields from these scintillation crystals are read by PMTs. Although we utilize various crystals and PMTs for mass production, our popular configurations are 25x8x2.5 cm<sup>3</sup> BGO crystals coupled with Hama-matsu R1924 PMTs, and 30x5x5 cm<sup>3</sup> CsI crystals with Hamamatsu R6231 PMTs.

Telecommunications are performed via mobile phone network. A mobile router is employed to connect the DAQ system to the cellular network such as the Long Term Evolution network in Japan. The DAQ system continually sends telemetries of operation status, temperature of the system, electricity consumption, and so on. Due to a limited amount of data transfer, all data cannot be sent in real time. Instead, we can download required data (e.g. during thunderstorms) on demand.

These components are packed in a waterproof box BCAR453520T (Takachi Electronics Enclosure), whose size is 45 cm (width) x 35 cm (length) x 20 cm (height). The inside and outside of the detector are presented in Figure 2. Electricity is supplied via a waterproof cable. A typical weight of the whole system is ~15 kg, depending on scintillation crystals. The system is fixed to concrete blocks or building facilities in order to prevent it from being away due to severe winter thunderstorms.

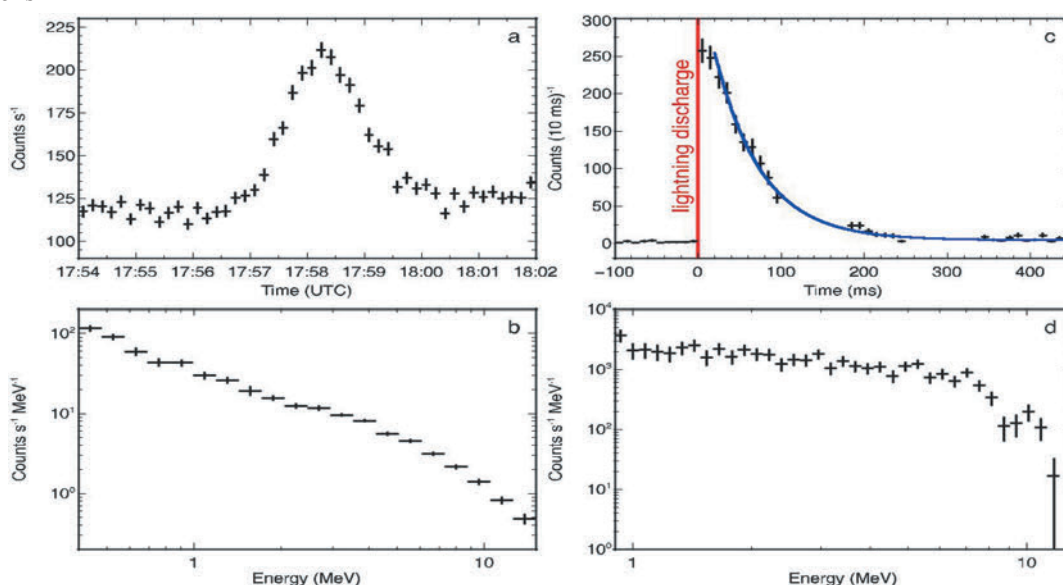


**Figure 1:** Typical time series of count rates and spectra of long bursts (a and b) and short bursts (c and d). (a) A 10-sec-binned count-rate history of a long burst in 0.7-15.0 MeV, observed in Komatsu on 8th December 2016. (b) An energy spectrum of the long burst shown in panel a, extracted from 17:56:30-17:57:30 (UTC). Detector responses remain unremoved. (c) A count-rate history of a short burst in 0.35-20.0 MeV, observed in Kashiwazaki on 6th February 2017. The origin of the X axis and the red-dashed line show the timing of a lightning discharge at 08:34:06. The best-fit exponential function to the count-rate history are overlaid with the blue-dashed line. (d) An energy spectrum of the short burst in panel b, extracted from 40-100 ms.

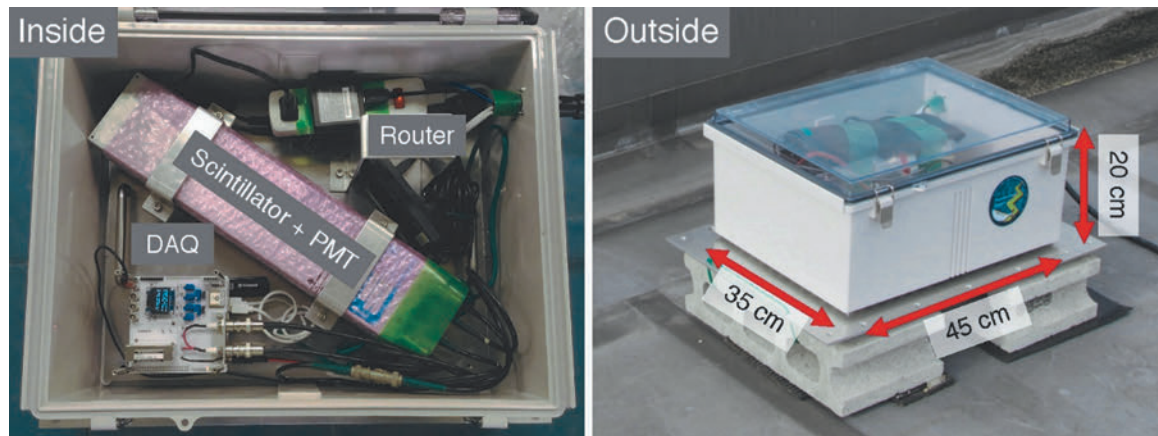


Figure 2: The inside (left) and outside (right) of the detector.

### Data acquisition system

It is necessary to develop a compact DAQ system for portable detectors. In our configuration, scintillation crystals and DAQ system can be made small. However, the size of main scintillation crystals, which affects the sensitivity to gamma rays, cannot be smaller than necessary. Therefore, we focused on developing a compact new DAQ system dedicated to the mapping observation project. The DAQ system consists of three components: GROWTH FPGA/ADC board, GROWTH daughter board, and Raspberry Pi. The photographs and block diagram of the DAQ system is presented in Figure 3.

The GROWTH FPGA/ADC board has been developed in cooperation with Shimafuji Electronics Co., Ltd. It is a general-purpose analog-to-digital converting board with an embedded programming gate array (FPGA). It has 4-channel analog inputs with 5 V to 5 V coverage. The input signals are at first buffered by differential amplifiers, then sampled by 12-bit ADC chips (Analog Devices AD9231). The ADC chip can be operated with up to 65 MHz. We employ the 50 MHz sampling rate for the experiment. The converted signals are processed by FPGA (XILINX Artix-7 XC7A35T-2FTG256C). We employed a self-trigger system. Once the input signal gets over the threshold, FPGA extracts maximum and minimum values and arrival time of the sampled data during a gate time. The extracted information from sampled waveform is sent via a USB-driving chip (FTDI FT232HL) to Raspberry Pi 3 by the Universal Asynchronous Receiver/Transmitter (UART) interface. The gate time and trigger thresholds are also modifiable via Raspberry Pi. In addition, a slow ADC chip (Microchip Technology MPC3208) connected to temperature and current sensors, and a slow digital-to-analog converter (DAC) chip (Microchip Technology MPC4822) are onboard. These slow ADC and DAC are controlled by Raspberry Pi via Serial Peripheral Interface. The GROWTH FPGA/ADC board is also connected with Raspberry Pi via 2x20-pin GPIO (general purpose input/output), besides the UART interface. The FPGA/ADC board is powered by DC12 V input.

Since the GROWTH FPGA/ADC board is a general-purpose ADC board, it has no amplifier circuits dedicated to e.g. PMT and silicon photomultiplier readouts. Instead, the board can be connected to a daughter board designed for a certain purpose via a 2x20-pin connector. As described in the next paragraph, daughter boards are expected to have charge amplifiers, waveform-shaping amplifiers, high-voltage suppliers, temperature sensors, and so on. Also, a global positioning system (GPS) receiver on daughter boards can be

connected to the ADC/FPGA board. If the receiver obtains GPS signals properly, accurate absolute timing (better than 1  $\mu$ s) is assigned to the digitized waveform by FPGA. Otherwise the absolute timing is assigned by internal clock of Raspberry Pi with an accuracy of  $\sim 1$   $\mu$ s. We also developed the GROWTH daughter board to read PMT outputs. The daughter board has 4-channel charge amplifiers and shaping amplifiers. These two amplifiers have time constants of 10  $\mu$ s and 2  $\mu$ s, respectively. The amplified signals are sent to the FPGA/ADC board via the 2x20-pin connector, then sampled by the ADC chips. A GPS receiver (Global Top FGPM-MOPA6H) is onboard and connected to FPGA. A GPS antenna can be connected to the daughter board via SMA terminal. The daughter board has also a module-type high-voltage suppliers for PMTs (Matsusada Precision OPTON-1.5PA/NA-12) which can supply 0-1500 V. The high-voltage supplier accepts reference voltage to control output voltage. In our case, we utilize the slow DAC on the FPGA/ADC board to generate the reference voltage, thus the output voltage can be controlled by Raspberry Pi. PMTs can be connected to the high-voltage suppliers via SHV connectors. In addition, the daughter board has a small display (OLED SSD1306) and an environmental sensor to measure temperature, humidity, and atmospheric pressure. They are connected to Raspberry Pi through the FPGA/ADC board and controlled by the Inter-Integrated Circuit interface. The size of the assembled DAQ system is 9.5 cm (width) x 9.5 cm (length) x 10.3 cm (height) including the daughter board and HV suppliers. Total electricity consumption including Raspberry Pi is 7 W.

### Deployment

Since the launch of the mapping observation project in 2015, we are expanding the number of detectors. In 2017-2018 winter season, we had 16 observation sites in Kanazawa, Komatsu, Toyama, Suzu, and Kashiwazaki with 16 detectors in total. Figure 4 presents observation sites in the 2017-2018 season. All the observation sites are located in coastal areas of Japan Sea. Suzu and Toyama sites are at Universities. Kanazawa and Komatsu sites consist of a university, local high schools, and a science museum. The Kashiwazaki site is in Kashiwazaki-Kariwa Nuclear Power Plant, where we have been performing the GROWTH experiments since 2006, and updated with 4 detectors in 2016.

### Calibration

We perform timing and energy calibration for obtained data. Timing of each photon event is assigned by GPS signals. Successfully-received GPS signals are compared to

give absolute timing better than 1 s. The energy calibration is performed by using persistent background radiation such as the 1.46 MeV line of  $^{40}\text{K}$  and the 2.61 MeV line of  $^{208}\text{Tl}$ . In addition, lines from  $^{214}\text{Bi}$  are also utilized to estimate the accuracy of the energy calibration. Figure 5 presents background spectra obtained by a detector at Kanazawa University in March 2018. During raining, count rates below 3 MeV because  $^{214}\text{Bi}$ , which is a daughter product of  $^{222}\text{Rn}$ , resides in rain drops, then falls onto the ground. In this case,

the 0.609 MeV line of  $^{214}\text{Bi}$  is suitable to investigate the calibration accuracy. When the energy is calibrated by a linear function derived from 1.46 MeV and 2.61 MeV background lines, the accuracy of the energy calibration is less than 2% at 0.609 MeV. Since BGO scintillation crystals have a temperature dependence on light yields, these calibration procedures are performed for every 30 minutes. Whereas, the procedures for NaI and CsI crystals are performed daily due to the low temperature dependences.

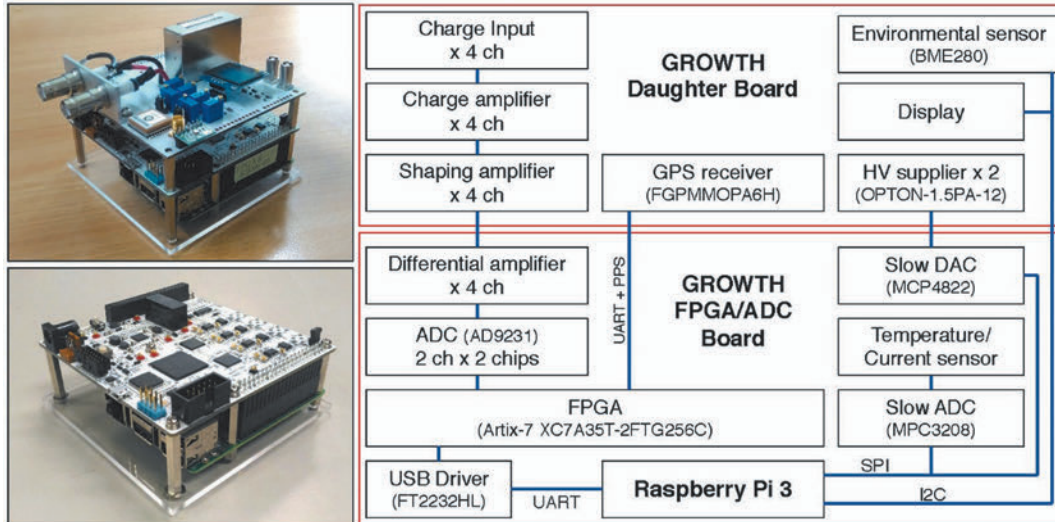


Figure 3: Photographs of the DAQ system with (left top) and without (left bottom) the GROWTH daughter board, and a block diagram (right).

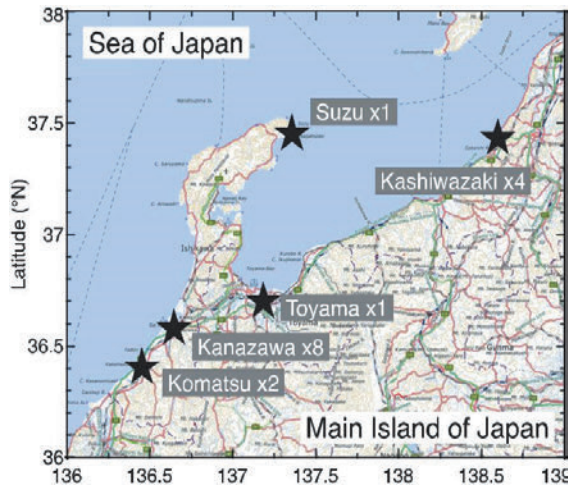


Figure 4: The observation sites in the 2016-2017 winter season.

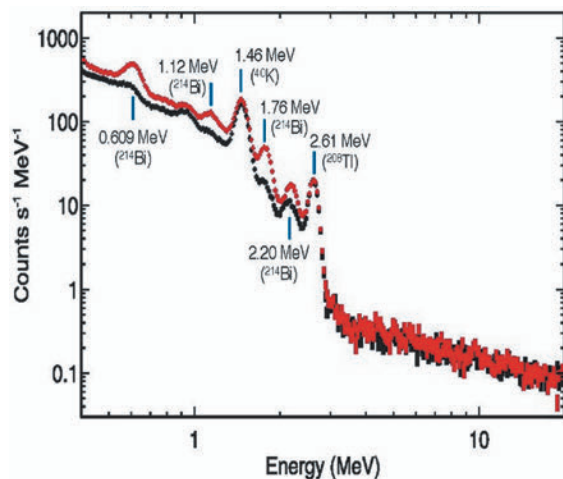


Figure 5: Averaged background spectra in 5th March 2018 (black; sunny) and 6th March 2018 (red; rainy) obtained at Kanazawa University. the spectra are accumulated for 30 minutes.

## RESULTS

### Number of detected events

The number of detected events since 2006 is presented in Figure 6. During 2006-2014, we operated only the Kashiwazaki site with 2 detectors. In average, 0.8 short bursts and 1.6 long bursts were observed for one winter season. Since 2015, we started the mapping observation campaigns. After the launch, the detection rate becomes 9.0 per year for long bursts, and 2.3 per year for short bursts. Among the 41 long bursts, we observe 5 events which abruptly terminated with lightning discharges.

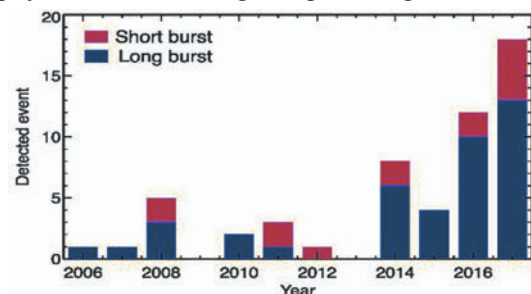


Figure 6: High-energy event detections from 2006-2007 to 2017-2018 winter seasons. Blue and magenta bars show long bursts and short bursts, respectively.

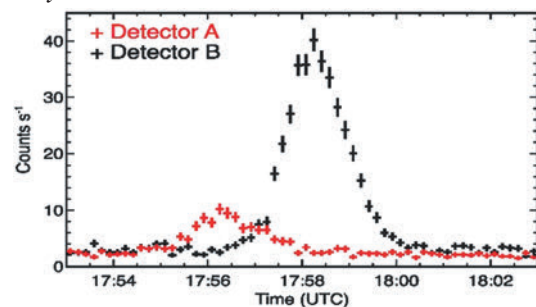


Figure 7: Count-rate histories of a long burst observed in the Komatsu sites with 10-sec bins. The energy range is 3.0-15.0 MeV. Red and black data points present count rates in detectors A and B, respectively.

### Tracking of long bursts

One of the main purposes of the mapping observation project is to reveal life cycles of long bursts. We introduce a successful example to track an identical long burst by two radiation monitors. In the Komatsu site, two radiation monitors were deployed at the roof of a high school and a science museum with 1.3 km separation. The monitors detected a long burst during heavy thunderstorms on 8th December 2016. Count-rate histories of the long burst are shown in Figure 7. We fitted the count-rate histories with a Gaussian function, and obtained count-rate peak time at detectors A and B as 17:56:25.6 ± 2.5 and 17:58:19.5 ± 0.8 (UTC), respectively. Temporal separation of the peak time at two detectors is 114:02:6 sec.

To investigate the wind flow at that moment, we utilized data of XRAIN (eXtended RADar Information Network). XRAIN is an X/C-band radar network operated by Japanese Ministry of Infrastructures, Land and Transportations. It can observe radar-echo and precipitation maps with a 1-minute interval. Precipitation maps with a 5-minute interval are shown in Figure 8. A high-precipitation area, namely thunderclouds, passed above the detectors from north-west to southeast during 17:55-18:00, consistent with the detection time of the long burst. In addition, it is indicated that detector A located upwind was required to detect the long burst prior to detector B. This is also consistent with the detection order of the long burst. By comparing pairs of precipitation maps with the 5-minute interval, we obtained the wind flowing at a speed of  $10.9 \pm 1.2 \text{ m s}^{-1}$  with a direction of  $296^\circ$ .

The expanded map in Komatsu is shown in Figure 9. The two observation sites has a 1.36 km separation. We assumed that the long burst moved with the wind flow. With the wind direction of  $296^\circ$  separation, the distance between the closest points from the detectors to the center of the long burst is 1.20 km. The wind needed  $110^{+14}_{-11}$  sec to pass the distance of 1.20 km. This is consistent with the temporal separation of the peak time at the detectors, 114:02:6 sec. Therefore, it

is clear that an identical long burst moved with the ambient wind flow, then irradiated the two detectors with a time lag.

In this case, the center of the long burst passed by detector B closer than detector A because the peak count rate of detector B was higher than that of detector A. On the other hand, the observation with two detectors cannot determine the exact position of the long burst center. Observations with 3 or more detectors will give us not only the burst center, but also structures of irradiated areas, total gamma-ray fluxes, and so on. In addition, time variations of long burst will be also revealed with the mapping observation project by tracking an identical long burst. In conclusion, our pilot observation in the 2016-2017 winter season demonstrated a successful tracking of a long burst with multiple detectors, and suggested scientific importance of the mapping observation.

### Interpretation of short bursts

In this section, we briefly summarize the interpretation of short bursts published as Enoto et al.[38]. The short burst event detected in the Kashiwazaki site enabled us to demonstrate atmospheric photonuclear reactions triggered by a lightning discharge. On 6th February 2017, four detectors deployed in the Kashiwazaki site simultaneously detected a short burst coinciding with a lightning discharge reported by Japanese Lightning Detection Network. It lasted for ~200 ms and decayed with a time constant of 50-60 ms. The spectra of the short burst present a continuum and sharp cutoff at 10 MeV, which is different from bremsstrahlung (see Figure 1). At the beginning of the short burst, fast (less than a few milliseconds) and large energy deposit into scintillation crystals (more than hundreds of MeVs) were suggested by paralyzed output signals. After the short burst, two of the four detectors recorded an afterglow in the 0.4-0.6 MeV range lasting for 1 minute. The spectra apparently present the 0.511 MeV line of electron-positron annihilations. Since the annihilation emission was not accompanied by significant numbers of photons with energies more than 1 MeV, this is not of the pair-production origin.

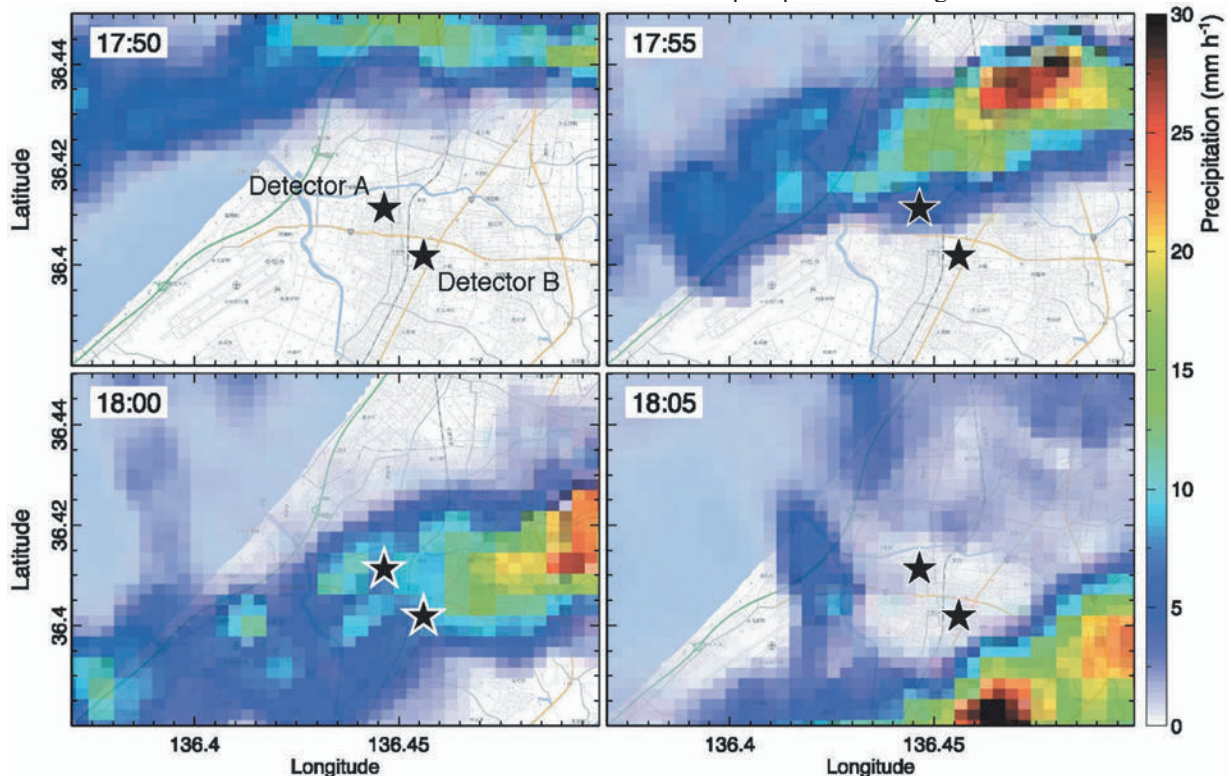


Figure 8: Five-minute interval precipitation maps in Komatsu obtained by XRAIN. Black star markers present the observation sites.



Figure 9: An aerial photograph in Komatsu. red star markers and a magenta arrow present observation sites and wind direction, respectively. The cyan-dashed lines present possible areas of the long-burst center when the long burst reaches the closest position to each detector.

These are interpreted as photonuclear reactions triggered by a lightning discharge. First of all, the lightning discharge provoked the fast and large energy deposit at the beginning of the short burst, namely a downward TGF. Due to high-energy photons of more than 10 MeV (ref), the downward TGF triggered atmospheric photonuclear reactions such as  $^{14}\text{N} + \gamma \rightarrow ^{13}\text{N} + n$  and  $^{16}\text{O} + \gamma \rightarrow ^{15}\text{O} + n$ , producing fast neutrons. These neutrons gradually lost their kinetic energy via elastic scattering in the atmosphere with time scale of  $\sim 50$  ms, and finally reacted with ambient  $^{14}\text{N}$ . Most of the neutrons were thought to exhibit charged-particle reaction  $^{14}\text{N} + n \rightarrow ^{14}\text{C} + p$ , producing quasi-stable carbon isotope  $^{14}\text{C}$ . The rest reacted with  $^{14}\text{N}$  via neutron captures  $^{14}\text{N} + n \rightarrow ^{15}\text{N} + \gamma$ . After the neutron captures,  $^{15}\text{N}$  immediately emitted deexcitation gamma rays consisting of multiple line emission. The short burst was caused by the deexcitation gamma rays. The energy spectra are explained as superposition of such de-excitation gamma rays with moderate energy resolution of BGO scintillation crystals. The time scale of the short burst is consistent with that of neutron thermalization in the atmosphere.

The annihilation afterglow originates from the by-products of photonuclear reactions  $^{13}\text{N}$  and  $^{15}\text{O}$ . These isotopes emit positrons via beta-plus decay with decay constants of 10 and 2 minutes, respectively. The region where the photonuclear reactions were provoked is considered to be filled with  $^{13}\text{N}$  and  $^{15}\text{O}$ . Since the region can flow with the ambient wind, the detector recorded the annihilation emission only when the region was above it. Therefore, the duration of the annihilation emission is shorter than decay constant of the isotopes.

By photonuclear reactions, various isotopes such as  $^{13}\text{N}$ ,  $^{15}\text{O}$ ,  $^{13}\text{C}$ ,  $^{15}\text{O}$ , and  $^{14}\text{C}$  are produced. Our result thus demonstrates a new channel for isotope production inside the Earth's atmosphere. Especially,  $^{14}\text{C}$  is the important isotope for dating method of archeology. Therefore, how many the  $^{14}\text{C}$  isotopes are produced by lightning is of great importance. In addition, what type of lightning can trigger TGFs and photonuclear reactions still remains as an open question. Our further observation will answer the questions, as well as give indications on questions for ordinal TGFs observed from space.

### Termination of long bursts

In this section, the observation reported in Wada et al.[39] is presented. We performed an observation campaign at the Suzu site with high-energy radiation and atmospheric electric field (AEF) monitors. This observation site was also monitored by a low-frequency lightning mapping network (LF network). The LF network consists of 5 stations installed along Toyama Bay, which has a plate antenna sensitive to the 0.8-500 kHz radio frequency band.

On 11th February 2017, the gamma-ray monitors recorded a long burst lasting for 1 minute as the AEF monitor detected a negatively-charged thundercloud approaching. The energy spectrum of the long burst extends up to 20 MeV, and is well reproduced by a power-law function with an exponential cutoff. When it was reaching its maximum flux, the long burst was abruptly terminated. At that moment, the AEF monitor detected a pulse indicating a lightning discharge.

The lightning discharge was also detected by the LF network. The LF network recorded continuous wave-form lasting for 300 ms. Most pulses of the waveform are small-amplitude emissions such as stepped leaders, thus originate from a leader development. The lightning discharge was initiated 15 km west from the gamma-ray detectors, then developed for 300 ms with 70 km expansion. Several ones of the lightning pulses were located within 1 km from the radiation detectors. Since timing of the pulses close to the observation site is consistent to the moment when the long burst was terminated, we conclude that the long burst was terminated by the leader development.

This is the first simultaneous detection of the long burst termination with gamma-ray, AEF, and LF mapping observation. It proves that the combination of these methods gives us the clues to understand the mechanism of long bursts. As the collaboration continues for observation in Japanese winter thunderstorms, it will provide us new sites into the phenomena.

### CONCLUSION

We launched the mapping observation project for high-energy phenomena in Japanese winter thunderstorms in 2015. The portable gamma-ray detectors with the new DAQ system dedicated to the project were developed, and up to 16 detectors were deployed and operated in coastal areas of Japan Sea during 2015-2018 winter seasons. During the three-year observations, we detected 27 long bursts and 8 short bursts. The number of detected events increases as more detectors are deployed.

Owing to the mapping observation, we succeeded in observing the identical long burst moving with ambient wind flow by using 2 gamma-ray detectors. Also, the observation in the Kashiwazaki site with 4 detectors enabled us to interpret the short burst as atmospheric photonuclear reactions triggered by the TGF at ground level. In addition, the collaborative campaign in Suzu with the AEF and LF measurements allowed us to investigate the relation between lightning and long bursts, and the charge structure responsible for electron acceleration. We demonstrated that the mapping observation project continues to give us fruitful scientific results. Further observations not only with gamma-ray but also radio-band and electric field measurements will enable us to resolve the questions in high-energy atmospheric physics.

- 
- [1] G. J. Fishman, P. N. Bhat, R. Mallozzi, J. M. Horack, Koshut, C. Kouveliotou, G. N. Pendleton, C. A. Meegan, R. B. Wilson, W. S. Paciesas, and et al., *Science* **264**, 1313 (1994).
- [2] D. M. Smith, *Science* **307**, 1085 (2005).
- [3] M. Marisaldi, A. Argan, A. Ursi, T. Gjesteland, Fuschino, C. Labanti, M. Galli, M. Tavani, C. Pittori, Verrecchia, and et al., *Geophysical Research Letters* **42**, 9481 (2015).
- [4] M. S. Briggs, V. Connaughton, C. Wilson-Hodge, R. D. Preece, G. J. Fishman, R. M. Kippen, P. N. Bhat, W. S. Paciesas, V. L. Chaplin, C. A. Meegan, and et al., *Geo-physical Research Letters* **38**, n/a (2011)
- [5] C. B. Moore, K. B. Eack, G. D. Aulich, and W. Rison, *Geophysical Research Letters* **28**, 2141 (2001).
- [6] R. Colalillo (Pierre Auger), *The Pierre Auger Observa-tory: Contributions to the 35th International Cosmic Ray Conference (ICRC 2017)*, ICRC2017 Proceedings, 138 (2017), [PoSICRC2017, 314(2018)].
- [7] R. Abbasi, M. Abe, T. Abu-Zayyad, M. Allen, R. Anderson, R. Azuma, E. Barcikowski, J. Belz, D. Bergman, Blake, and et al., *Physics Letters A* **381**, 2565 (2017).
- [8] R. U. Abbasi, T. Abu-Zayyad, M. Allen, E. Barcikowski, W. Belz, D. R. Bergman, S. A. Blake, M. Byrne, Cady, B. Cheon, and et al., *Journal of Geophysical Research: Atmospheres* **123**, 6864 (2018).
- [9] J. R. Dwyer, *Science* **299**, 694 (2003).
- [10] B. M. Hare, M. A. Uman, J. R. Dwyer, D. M. Jordan, M. I. Biggerstaff, J. A. Caicedo, F. L. Carvalho, A. Wilkes, D. A. Kotovsky, W. R. Gamerota, and et al., *Journal of Geophysical Research: Atmospheres* **121**, 6511 (2016).
- [11] M. McCarthy and G. K. Parks, *Geophysical Research Letters* **12**, 393 (1985).
- [12] K. B. Eack, W. H. Beasley, W. D. Rust, T. C. Marshall, and M. Stolzenburg, *Journal of Geophysical Research: Atmospheres* **101**, 29637 (1996).
- [13] N. A. Kelley, D. M. Smith, J. R. Dwyer, M. Splitt, Lazarus, F. Martinez-McKinney, B. Hazelton, Grefenstette, A. Lowell, and H. K. Rassoul, *Nature Communications* **6**, 7845 (2015).
- [14] P. Kochkin, A. P. J. van Deursen, M. Marisaldi, A. Ursi, I. de Boer, M. Bardet, C. Allasia, J.-F. Boissin, Flourens, and N. stgaard, *Journal of Geophysical Research: Atmospheres* (2017), 10.1002/2017jd027405.
- [15] M. Brunetti, S. Cecchini, M. Galli, G. Giovannini and Pagliarin, *Geophysical Research Letters* **27**, 1599 (2000).
- [16] T. Torii, T. Sugita, S. Tanabe, Y. Kimura, M. Kamogawa, K. Yajima, and H. Yasuda, *Geophysical Research Letters* **36** (2009), 10.1029/2008gl037105.
- [17] H. Tsuchiya, T. Enoto, T. Torii, K. Nakazawa, T. Yuasa, Torii, T. Fukuyama, T. Yamaguchi, H. Kato, Okano, and et al., *Physical Review Letters* **102** (2009), 10.1103/physrevlett.102.255003.
- [18] H. Tsuchiya, K. Hibino, K. Kawata, N. Hotta, Tateyama, M. Ohnishi, M. Takita, D. Chen, J. Huang, Miyasaka, and et al., *Physical Review D* **85** (2012), 10.1103/physrevd.85.092006.
- [19] A. Chilingarian, A. Daryan, K. Arakelyan, A. Hovhannisyan, B. Mailyan, L. Melkumyan, G. Hovsepyan, Chilingaryan, A. Reymers, and L. Vanyan, *Physical Review D* **82** (2010), 10.1103/physrevd.82.043009.
- [20] A. Chilingarian, G. Hovsepyan, and A. Hovhannisyan, *Physical Review D* **83** (2011), 10.1103/physrevd.83.062001.
- [21] A. Chilingarian, G. Hovsepyan, and E. Mnatsakanyan, *Physical Review D* **93** (2016), 10.1103/physrevd.93.052006.
- [22] T. Torii, M. Takeishi, and T. Hosono, *Journal of Geophysical Research: Atmospheres* **107**, ACL 2 (2002).
- [23] T. Torii, T. Sugita, M. Kamogawa, Y. Watanabe, and K. Kusunoki, *Geophysical Research Letters* **38**, n/a (2011).
- [24] H. Tsuchiya, T. Enoto, S. Yamada, T. Yuasa, M. Kawaharada, T. Kitaguchi, M. Kokubun, H. Kato M. Okano, S. Nakamura, and et al., *Physical Review Letters* **99** (2007), 10.1103/physrevlett.99.165002.
- [25] H. Tsuchiya, T. Enoto, S. Yamada, T. Yuasa, K. Nakazawa, T. Kitaguchi, M. Kawaharada, M. Kokubun, H. Kato, M. Okano, and et al., *Journal of Geophysical Research* **116** (2011), 10.1029/2010jd015161.
- [26] Y. Kuroda, S. Oguri, Y. Kato, R. Nakata, Y. Inoue, C. Ito, and M. Minowa, *Physics Letters B* **758**, 286 (2016).
- [27] V. Alexeenko, N. Khaerdinov, A. Lidvansky, and V. Petkov, *Physics Letters A* **301**, 299 (2002).
- [28] H. Tsuchiya, T. Enoto, K. Iwata, S. Yamada, T. Yuasa, T. Kitaguchi, M. Kawaharada, K. Nakazawa, M. Kokubun, H. Kato, and et al., *Physical Review Letters* **111** (2013), 10.1103/physrevlett.111.015001.
- [29] A. Chilingarian, G. Hovsepyan, G. Khanikyanc, A. Reymers, and S. Sghomonyan, *EPL (Europhysics Letters)* **110**, 49001 (2015).
- [30] A. Chilingarian, Y. Khanikyants, E. Mareev, D. Pokhsraryana, V. A. Rakov, and S. Sghomonyan, *Journal of Geophysical Research: Atmospheres* **122**, 7582 (2017).
- [31] C. T. R. Wilson, *Mathematical Proceedings of the Cambridge Philosophical Society* **22**, 534 (1925).
- [32] A. Gurevich, G. Milikh, and R. Roussel-Dupre, *Physics Letters A* **165**, 463 (1992).
- [33] J. R. Dwyer, *Geophysical Research Letters* **31**, n/a (2004).
- [34] J. R. Dwyer, *Journal of Geophysical Research: Space Physics* **117**, n/a (2012).
- [35] Y. Goto and K. Narita, *Res. Lett. Atmos. Electr.* **12**, 57 (1992).
- [36] V. A. Rakov and M. A. Uman, *Lightning: Physics and Effects* (Cambridge University Press, 2003).
- [37] D. Umamoto, H. Tsuchiya, T. Enoto, S. Yamada, T. Yuasa, M. Kawaharada, T. Kitaguchi, K. Nakazawa, M. Kokubun, H. Kato, and et al., *Physical Review E* **93** (2016), 10.1103/physreve.93.021201.
- [38] T. Enoto, Y. Wada, Y. Furuta, K. Nakazawa, T. Yuasa, K. Okuda, K. Makishima, M. Sato, Y. Sato, T. Nakano, and et al., *Nature* **551**, 481 (2017).
- [39] Y. Wada, G. S. Bowers, T. Enoto, M. Kamogawa, Y. Nakamura, T. Morimoto, D. M. Smith, Y. Furuta, K. Nakazawa, T. Yuasa, and et al., *Geophysical Research Letters* **45**, 5700 (2018).

## ACKNOWLEDGEMENT

We deeply thank M. Kamogawa, G. S. Bowers and D. M. Smith for the collaborative observation in Suzu, T. Morimoto and Y. Nakamura for LF observation, M. Sato and Y. Sato for interpretation of the short burst event, S. Otsuka, H. Kato, and T. Takagaki for detector development. Detector deployment was supported by D. Yone-toku, T. Sawano, K. Watarai, K. Yoneguchi, K. Kimura, K. Kitano, K. Kono, K. Aoki, staffs of Kanazawa Uni-versity Noto School, and the radiation safety group of Kashiwazaki Kariwa Nuclear Power Plant, Tokyo Elec-tric Power

Company Holdings. This work is supported by JSPS/MEXT KAKENHI grants 15K05115,15H03653, 16H06006, 18J13355, by Hakubi project and SPIRITS 2017 of Kyoto University, and by the joint research pro-gram of the Institute for Cosmic Ray Research (ICRR), the University of Tokyo. The background images in Fig-ure 4, 8 and 9 were provided by the Geospatial Information Authority of Japan. The XRAIN data obtained by Japan Ministry of Land, Infrastructure, Transport and Tourism was retrieved from Data Integration and Analy-sis System (DIAS) operated by the University of Tokyo.

## Recent Results from the Pierre Auger Observatory on Lightning Related Events

R. Colalillo<sup>1</sup>, for the Pierre Auger Collaboration<sup>2</sup>

<sup>1</sup>INFN, Sezione di Napoli, Italy

<sup>2</sup>Observatorio Pierre Auger, Av. San Martin Norte 304, 5613 Malargüe, Argentina

**Abstract.** The Pierre Auger Observatory, the biggest hybrid detector in the world designed to observe cosmic rays at the highest energies, has turned out to be a valid instrument for studying transient phenomena related to atmospheric electricity. The fluorescence detector, which observed the first elves in 2005, operates as a 10 Mfps camera and represents an unprecedented opportunity to study the evolution of these phenomena with the best time resolution available. Since 2013, a dedicated trigger was added to allow detection and storage of elves events; the readout window was extended from 100 $\mu$ s to 300 $\mu$ s (2014-6), to 900 $\mu$ s (2017-8) in order to study more closely the light emission above the lightning source. Peculiar events related to lightning activity were also observed by the surface detector. They present a big footprint at the ground with a radius which goes from 2 to 8 km. The typical traces of these events are two orders of magnitude longer than cosmic-muon traces, and each event has at least one station with signal dominated by high-frequency noise. Studies are in progress to understand the origin of these anomalous events.

### 1. INTRODUCTION

In the last years, the ground-based observatories, designed to detect radiation from outer space, are highlighting their potential for observing phenomena related to atmospheric electricity. In particular, the Pierre Auger Observatory [1], located in the Mendoza province of Argentina, can detect ELVES (Emissions of Light from Very low frequency Electromagnetic pulse Sources) using its Fluorescence Detector (FD) and peculiar lightning related events with the Surface Detector (SD). The FD consists of 24 telescopes organized on four sites, which are arranged on the perimeter of the surface array. Each telescope has a FOV of 30° x 30° in azimuth and elevation and a 14% duty cycle, taking data only during clear and moonless nights. The telescope is composed of a UV transmitting filter and a mirror of 13 m<sup>2</sup> which collects the fluorescence light and sends it to a matrix of 440 photomultiplier tubes (PMT). The signals are digitized every 100 ns. This time resolution is the best ever reached compared to that of other experiments devoted to elves detection. The standard signal trace is 100 $\mu$ s long including a 28 $\mu$ s pedestal. The SD consists of 1660 water-Cherenkov Detectors (WCDs) arranged in a triangular grid with nearest neighbors separated by 1.5 km. The Cherenkov light produced by the passage of a charged particle travelling at a speed higher than that of light in water is collected by three PMTs. Each PMT has two readout channels, the High Gain (HG) channel that is taken from the anode, and the low gain channel from the last dynode. There is an amplification factor of about 32 between the two channels. Signals are digitized every 25 ns, and the trace lasts 19.2  $\mu$ s. The Pierre Auger Observatory also has a suite of devices for the atmospheric monitoring being the atmosphere used as a large calorimeter. Moreover, in the last years, instruments to monitor lightning were added. On the site, five Boltek Storm-Trackers are able to detect lightning strikes within a radius of 1000 km and an E-field mill measures the strength of electric fields in the atmosphere [2].

### 2. ELVES CHARACTERISTICS AND THEIR DETECTION

Elves are a type of Transient Luminous Events (TLEs), which are secondary phenomena occurring in the upper atmosphere in association with underlying thunderstorm lightning. An electromagnetic pulse (EMP), caused by lightning strikes whose direct light is not visible from the

Auger Observatory due to the Earth' limb, accelerates free electrons at the base of the ionosphere (80-90 km). Electrons collide and excite nitrogen molecules. The UV emission coming from the de-excitation of these molecules creates the elves footprint on the camera of the FD telescopes. This process is the same that happens when secondary particles of an UHECR shower collide inelastically in the closer troposphere. Typical UHECR signals at the FD aperture are tens to thousands of photons/m<sup>2</sup>/100 ns, and typical distances of observed UHECR showers range from 3 to 30 km. In contrast, the observed elves are usually 200-1000 km away, and in the signal observed at the FD, the higher intrinsic brightness of elves due to the energy scale of lightning compensates for the further distance between FD and elves. In figure 1, the footprints on the FD camera of an UHECR shower, on the left, and of an elves, on the right, are shown. In the central picture, the optical signature of an elves at the base of the ionosphere is shown. It is a ring that extends up to 600 km with its central hole expanding to radii greater than 200 km, and its duration is less than 1 ms.

Recently, elves have been studied by linear arrays of horizontal and vertical photometers with a time resolution of about 40  $\mu$ s, or by multianode PMTs, installed on satellites, with time resolutions between 50 and 100  $\mu$ s. The unprecedented time resolution of the FD telescopes will help to investigate the variations in the light emission due to the internal structure of the EMP. Moreover, the elves observational footprint of the Pierre Auger Observatory covers 3x10<sup>6</sup> km<sup>2</sup> sampling above lands, coasts and oceans. It also includes the Córdoba region, famous for the most energetic and destructive convective thunderstorm systems in the world, where the RELAMPAGO (Remote Sensing of Electrification, Lightning, and Mesoscale/Microscale Processes with Adaptive Ground Observations) campaign [3] started in November 2018. The Auger and RELAMPAGO measurements will be extensively compared.

The first elves was observed by the Auger FD on May 18, 2005 [4]. The FD trigger consists of two hardware triggers, the first one being a pixel threshold trigger (T1) and the second one based on a track shape identification (T2). The third level, which is a software trigger, was designed to distinguish between close lightning and real cosmic-ray events and is based on the pixel multiplicity. As we can see in figure 1, elves signature has a high pixel multiplicity as "lightning event". Therefore, the third level trigger also

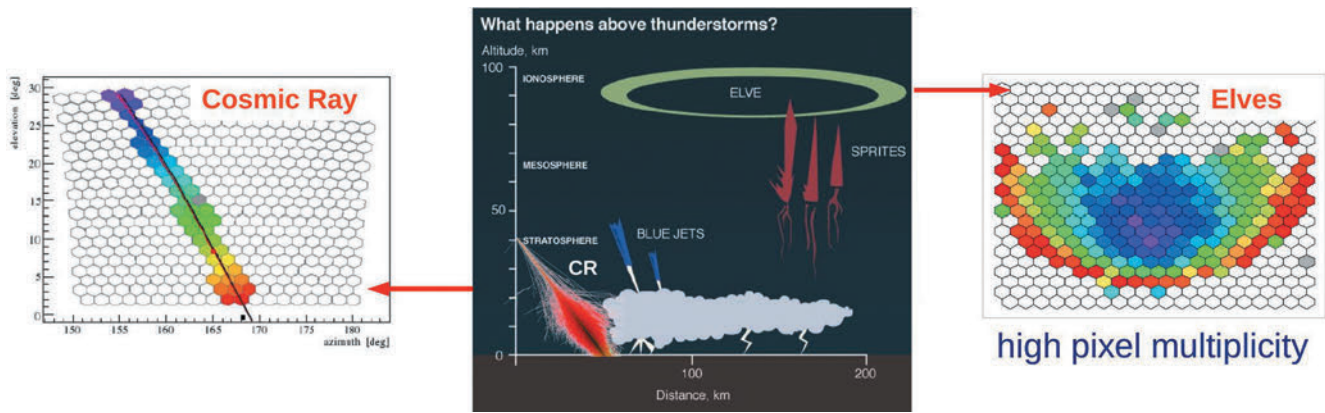


Figure 1. The central figure shows the representation of TLEs in the upper atmosphere and of cosmic rays and electrical-discharge phenomena in the troposphere. In the left and right pictures, the footprints on the FD camera of an UHECR shower and of an elves are respectively shown.

prevents the elves detection. After the first serendipitously observation, a detailed scan was performed on a sample of events which did not pass the whole trigger selection but satisfied the T2 trigger, searching for other elves candidates. From 2007 to 2011, 58 T2 elves events were found. They were used to define a new trigger optimized for elves detection. It finds the first pixel, and afterwards searches for adjacent triggered pixels on the same column and row of the first pixel. The pulse start times of these pixels are required to have a monotonic growth. A radially expanding light front is expected. The first triggered pixel is related to the first light emission that occurs in a point at the base of the ionosphere, which is halfway between the FD and the lightning source. This point is far from the center of the elves ring corresponding to the vertical above the lightning source. The internal part of the elves signature is very important: the size of the central gap, for example, is related to the maximum electron speed reachable in the lightning stroke. Similar information is very useful to understand better and improve models of elves production and evolution. With the standard readout window, which lasts 72  $\mu\text{s}$  and is optimized for cosmic-ray detection, it is not possible to see the light closer to the vertical above the lightning. For this reason, the readout was first extended up to 300  $\mu\text{s}$ , and in this condition, it was possible to observe the beginning of the central gap. In 2017, the super extended readout was implemented arriving at an acquisition time of 900  $\mu\text{s}$ . Since 2013, when the dedicated trigger for elves was added, thousands of elves have been detected, one-third of which were observed by two or more FD telescopes. Studies are underway to further improve the trigger increasing the elves detection efficiency and preserving a high signal/background ratio and the reconstruction of events.

The location of the lightning which produced elves is reconstructed with a simple geometrical model starting from the position of the first triggered pixel. The reconstructed

locations were compared to that ones of lightning collected by the WWLLN (World Wide Lightning Location Network). Moreover, for a sample of 800 elves, their trigger times were compared with those registered by WWLLN. More than 40% of elves have a WWLLN correlation within 5 ms.

Another important thing that we want to know is the surface density of light emission at the base of the ionosphere to estimate the elves energy. The number of photons detected by the FD camera has to be corrected taking into account the distance of the camera from the ionosphere and the ionosphere surface that each pixel can observe. In fact, the asymmetry of the signal detected by each pixel increases down the camera as a result of a wider observation area for pixels pointing at low elevation angles. Moreover, the atmospheric effect has to be considered because a different amount of atmosphere between the emission surface and the FD mirror strongly affect the amplitude of the traces. On the left of figure 2, the photon density as a function of the distance from the lightning source after the geometrical and atmospheric correction is shown.

Beyond the single elves observed, characterized by a single peak in the detected trace as shown in figure 2, double or multiple elves, characterized by two or more peaks, were collected. We expect that cloud-to-ground (CG) lightning strikes radiate only one EMP towards the ionosphere producing a single elves; while an intra-cloud (IC) discharge can radiate an EMP directly towards the ionosphere and another one towards the ground. The latter bounces off the ground and reaches the ionosphere with a time delay related to the height of the lightning strike. Also, more complex phenomena could explain these different signatures. The increase of the statistics, the 100 ns resolution of the Auger FD, and the improvements in the reconstruction will help to verify these hypotheses and allow a better understanding of one of the most energetic atmospheric phenomena known up to now.

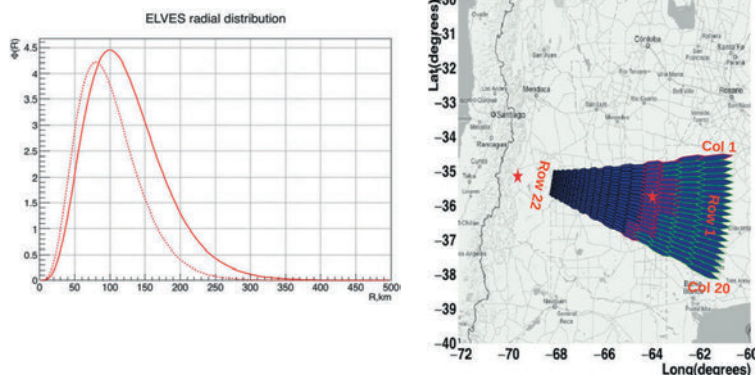


Figure 2. Left: photon density as a function of the distance from the lightning source after the geometrical and atmospheric correction. Right: Camera of an FD telescope projected onto the base of the ionosphere. The pixels higher in the camera see the base of the ionosphere 300 km away, while the lower pixels are projected almost 1000 km away.

### 3. THE LIGHTNING RELATED EVENTS OBSERVED WITH THE SD

Peculiar events were also detected by the surface detector of the Pierre Auger Observatory [5]. They are characterized by a large disk footprint at the ground shown in figure 3 (a). The largest ones triggered at least 20 stations, more than the stations triggered by the most energetic cosmic-ray showers. Among these stations, there is at least one station, called “lightning station” and shown in figure 3 (b), with a signal dominated by high-frequency noise. This suggests that these events happen during thunderstorms. We verified this hypothesis searching for a correlation between our events and the lightning strikes collected by WWLLN. We found a very good correlation in time and space

considering that the global location accuracy for the WWLLN network assuming five-station involvement ranges over 1.9 to 19 km. Another hallmark of these events is the so-called “long-signal stations” shown in figure 3 (c), that have a signal which lasts more than 10  $\mu\text{s}$ , two orders of magnitude longer than the duration of the signal produced by a cosmic muon. A final point to consider is the lack of signal in the central part of the footprint of the largest events, which are more than half of the present statistics. The origin of this hole in the center is not clear right now. It could be a physical origin or could be related to the Auger trigger that is optimized for the detection of cosmic rays with a very different signature.

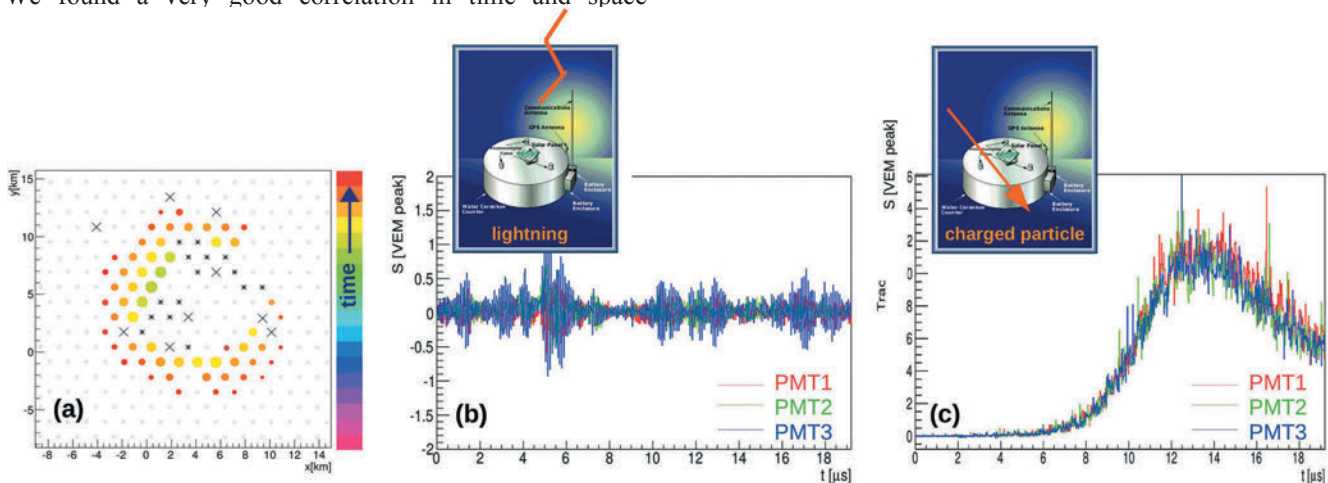


Figure 3. The typical footprint of a lightning related event is shown in panel (a). The colored circles represent the long-signal stations. The marker size is related to the intensity of the signal, the color to the arrival time. The asterisks represent the lightning stations, and the crosses the muon stations, which are not correlated in time with the long-signal stations. In panel (b), the characteristic signal of a lightning station is shown. Finally, there is a long signal shown in panel (c). The three colors represent the signals collected by the three PMTs of a station.

The search of these events was performed on the data collected by the SD since January 2004 up to May 2017, which passed the third level of the SD trigger necessary to define a standard event. The requests done to select an event are the presence of at least one lightning station and at least 10 long-signal stations. A station is tagged in this way if the signal of at least two PMTs passes the long-signal condition. Starting from a sample of about  $10^7$  events, we selected about  $2 \times 10^5$  events passed the first condition and finally 28 events with at least ten long-signal stations. Among these events, there are 16 “large” events with more than 20 triggered stations and whose footprints have a radius which spans from 4 to 8 km. One of these events, called SD-ring for the lack of the signal at the center of the footprint, is shown on the left of figure 4.

register the same signal if it is produced by a charged particle, which crosses the station. We calculated the ratio between the signals of the two PMTs at a time bin-by-bin for each station and then an average ratio, and for each PMT, we calculated the ratio between the HG signal and the LG one multiplied by the amplification factor. The distributions of these ratios are peaked at 1 as expected for both cases. The long signals are not usually fully contained in the standard acquisition window. It is necessary to find a function, which describes the signal to recover the missing part. Various functions were tested on a small sample of signals fully contained in the acquisition window. The best one resulted to be an asymmetric Gaussian, which perfectly describes the leading and falling edge of the signal. A chi-square minimization is performed to fit each long signal. A fit is accepted if:

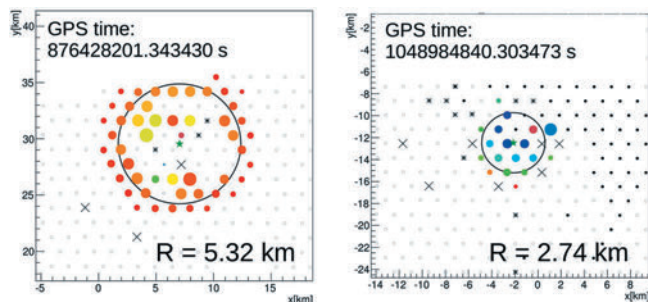


Figure 4. Footprint at the ground for a “large” (left) and “small” (right) event.

At the discovery of the SD-rings, we checked that these events have a physical origin, and are not an artifact due to electromagnetic noise. We expect that the three PMTs in each station and the two readout channels of each PMT

- the Gaussian peak lies between 2.5  $\mu\text{s}$  and 16.7  $\mu\text{s}$  of the acquisition window to see at least a small part of the leading and falling edge;
- the percentage difference between the sum of the content of the trace bins and the integral of the fitting function in our time window is less than 5%;
- the duration of the total fitting function is less than 100  $\mu\text{s}$ .

The station is tagged as “good station” if the fitting procedure was successful for at least two PMTs. The signal detected by each PMT is given by the total integral of the fitting function. The signal per station is the mean of the “good” signals.

The first step requested for the characterization of the global event is the calculation of the center of the footprint

and its radius. We performed an unweighted chi-square minimization on the station coordinates to find them, and in addition to the large events described above, we found “small” events, whose radius is about 2-3 km and which present a compact footprint. One of these events is shown on the right of figure 4. On the sample of “good events”, that are the events with at least eight “good stations”; we studied the evolution of the signal to move away from the center of the footprint. The signal expands radially at the speed of light and is larger in the inner part of the disk decreasing as the distance from the center increases. The signal of each station can be transformed into deposited energy. We found that the energy per long-signal station spans from  $10^4$  MeV to  $10^6$  MeV, while the total energy deposited at the ground by an SD-ring varies between  $10^{17}$  eV and  $10^{18}$  eV. This energy is about two orders of magnitude higher than the energy deposited at the ground by a cosmic-ray shower initiated by a proton with energy  $10^{19}$  eV.

Finally, we studied the time evolution of the front of our events. We performed a three-dimensional fit with four free parameters assuming a spherical propagation front. The first three parameters are the three coordinates of the source of the event, while the last one,  $t_{off}$ , takes into account the offset between the starting time of the ideal event and the GPS time of the real event. We obtained that the altitude of the source never exceeds 1 km. We also compared our measured arrival times, defined as the time corresponding to the 10% of the peak value of the fitted function, with the arrival times at the ground obtained by a simple geometrical Toy MC always based on a spherical propagation front. We calculated the arrival times for several altitudes of the source, from 0 to 10 km. Subtracting  $t_{off}$  obtained with the three-dimensional fit from the measured arrival times, we found they match the simulated times corresponding to an altitude of 0 km as expected. Another result that supports the evidence of a source very close to the ground is the value of the propagation velocity at the ground that should be higher than the speed of light for a high source and equal to this quantity for a source at the ground. Fitting with a straight line the measured arrival time as a function of the distance from the center of the footprint, we found a velocity very close to the speed of light as expected. All the described results, obtained on large events, were verified with a raw reconstruction on the small events. These events do not pass all the quality cuts requested for a reliable reconstruction because many long-lasting signals do not have the peak in the acquisition window, but we found again that the signal starts from the inner part of the footprint, where it is bigger, and decreasing, moves toward the outer part at the speed of light. Moreover, the source resulted again in being close to the ground.

#### 4. CONCLUSION

Elves have been studied by many experiments in the last years, and their origin is well known. The Pierre Auger Observatory, with a time resolution of 100 ns, the best ever reached, and the super-extended readout, represents a unique opportunity right now to investigate the variations in the light emission due to the internal structure of the EMP, which originates the elves.

Other peculiar events related to the atmospheric electricity were detected by the SD. Their footprints at the ground were characterized, and the altitude of their sources resulted in being very close to the ground, but the present knowledge did not allow us to uniquely identify the atmospheric electricity phenomenon that can accelerate particles up to the

energies necessary to produce the signal observed in our WCDs. Further studies are underway to increase the statistics of these events and compare them with predictions of different theoretical models and with the environmental conditions under which they occurred.

#### 5. ACKNOWLEDGMENTS

The authors wish to thank the World Wide Lightning Location Network (wwlln.net), a collaboration among over 50 universities and institutions, for providing the lightning location data used in this paper.

#### REFERENCES

- [1] Pierre Auger Coll., Nucl. Instrum. Meth. A **798**, 172–213 (2015).
- [2] J. Rautenberg, for the Pierre Auger Coll., 34th Int. Cosmic Ray Conf., The Hague (2015).
- [3] [https://www.eol.ucar.edu/field\\_projects/relampago](https://www.eol.ucar.edu/field_projects/relampago)
- [4] R. Mussa et al., EPJ Plus **127**, 94 (2012).
- [5] R. Colalillo, for the Pierre Auger Coll., 35th Int. Cosmic Ray Conf., Busan, Korea (2017).

# An Automatic Algorithm for the Recovering of TGE Differential Energy Spectra

G. Hovsepyan

A. Alikhanyan National Lab (Yerevan Physics Institute), Yerevan 0036, Armenia

**Abstract.** The paper describes an algorithm for processing the histograms of energy releases in the large NaI (TI) crystals comprising a network operating on Aragats high-altitude research station in Armenia. Hundreds of thunderstorm ground enhancements (TGEs) registered on Aragats during the last decade can be approximated with three types of analytic dependences: power law, exponential, and mixed. The latter group, as a rule, consists of two power laws with different indices connected at a transition (turnover) point (“knee”). We present techniques for approximation these spectra with a five-parametric function.

## 1. INTRODUCTION

Hundreds of time series of particle count rates and histograms of energy releases in NaI crystals and thick plastic scintillators are entering online in the database of the ASEC collaboration [1]. In MySQL database data collected on the time span, more than 10 years is stored as standard XML files. The data from NaI (TI) network [2,3] comprises of energy release histograms ( logarithmic ADC codes [2]).

The daily information contains 10080 histograms, each of which is supplied with the UTC date, the exposure time, and the data on energy release distribution over the ADC codes (127 channels). The sum of events in all histogram channels equals to the detector one-minute time-series count rates. The database maintaining software allows downloading any quantity of histograms in XML or CSV formats. Figure 1 shows the first 13 channels of the histogram in CSV format.

```
22:22:00,3281,3007,2806,2880,2861,2920,2776,2647,2438,2402,2180,2115,2058,
22:23:00,3290,3036,3056,2991,2947,2721,2805,2636,2395,2338,2137,2135,2091,
22:24:00,3365,2994,2935,3024,3027,2876,2808,2624,2536,2269,2206,2134,2005,
22:25:00,3309,2874,2820,2844,2835,2832,2876,2655,2430,2352,2401,2163,1984,
22:26:00,3186,2966,2780,2872,2909,2902,2778,2635,2458,2335,2164,2131,1989,
22:27:00,3280,2968,2925,2863,2929,2873,2747,2559,2538,2308,2112,2188,2037,
22:28:00,3212,3022,2846,2857,2923,2838,2675,2629,2590,2280,2321,2163,1989,
22:29:00,3213,2967,2950,2896,2890,2915,2762,2616,2499,2445,2218,2119,1959,
22:30:00,3263,3008,3004,2962,2933,2850,2700,2589,2436,2431,2194,2016,2048,
22:31:00,3284,3062,3164,3095,2951,2932,2657,2635,2467,2352,2198,2146,1998,
22:32:00,3230,2919,2968,2863,2915,2911,2718,2548,2441,2333,2166,2139,2026,
22:33:00,3231,3111,3033,2931,2897,2898,2794,2606,2472,2287,2168,2037,2058,
22:34:00,3231,2927,2868,2896,2893,2885,2822,2668,2476,2343,2182,2103,2110,
22:35:00,3322,3142,3071,2948,2952,2887,2695,2592,2515,2318,2263,2125,1996,
22:36:00,3216,3121,3091,3068,2991,2826,2621,2684,2488,2308,2241,2127,2064,
22:37:00,3324,3043,3086,2977,2971,2880,2788,2586,2564,2388,2185,2171,2000,
22:38:00,3173,3072,2940,2969,2957,2889,2798,2636,2550,2333,2197,2113,2069,
22:39:00,3212,2949,2843,2840,2993,2771,2699,2644,2447,2327,2235,2118,1988,
22:40:00,3237,2972,2825,2887,2955,2948,2762,2713,2506,2369,2172,2154,2009,
22:41:00,3175,2913,2835,2879,2836,2921,2795,2675,2543,2296,2286,2093,1974,
22:42:00,3263,2979,2739,2908,2848,2962,2824,2599,2586,2317,2228,2060,1950,
22:43:00,3267,3058,2953,2836,2820,2810,2761,2681,2519,2367,2218,2095,2004,
22:44:00,3163,2925,2905,2865,2846,2874,2770,2657,2475,2299,2182,2146,1995,
22:45:00,3314,3046,2880,2801,2865,2776,2739,2602,2551,2304,2208,2102,2027,
22:46:00,3223,3012,2947,2793,2828,2899,2707,2684,2597,2361,2245,2076,1946,
22:47:00,3409,3048,2851,2867,2944,2872,2734,2617,2505,2318,2224,2080,1931,
```

Figure 1. A sample of energy release data in csv format

## 2. RECOVERING OF THE ENERGY SPECTRA

A program for the automatic data processing and energy spectra recovering was written in the C++ in a block-architectural form. Figure 2 shows the block diagram of the program.

The downloaded file with ADC codes initially is examined to determine the intervals of the times for calculating the background (no TGE) and the TGE + background. Then, for each detector was determined value of the  $K_0$  code, the mode of energy losses of muons in the NaI crystal. The  $K_0$  code is used as a calibration point for combining data from NaI network (7 spectrometers); each of them can have slightly different  $K_0$  value. The overall energy scale is determined by a detector with minimal energy threshold. Further, for each selected minute of TGE, from each bin of the histogram of ADC codes, the background is subtracted  $\{x_i\} = \{a_i\} - \{b_i\}$ , where  $a_i$  is the number of events in the  $i$ -th bin of the ADC codes during TGE event, and  $b_i$  is the number of background events in the same bin.

The TGE energy spectrum is recovered from the calculated  $\{x_i\}$  values by solving the inverse problem with previously calculated transition matrix  $A_{k,i}$ . Each element of  $A_{k,i}$  matrix represents the probability of a gamma photon with energy  $E_k$  to generate the energy release corresponding to the  $i$ -th bin. Probability matrix  $A_{k,i}$  is calculated by Monte Carlo method, taking into account the response of the detector [4, 5].

The intensities of the reconstructed spectra are recorded in the text format for Figure generation. The design of the picture of recovered spectra is performed using the ROOT software package [6]. For obtaining all requested energy spectra a special bash script is used. Recovered TGE spectra, as a rule, can be approximated by three types of dependencies: exponential, power, and double power with a change in the slope of the spectrum (with a spectral “knee”). In fig. 3 we show examples of approximations of the recovered TGE spectra.

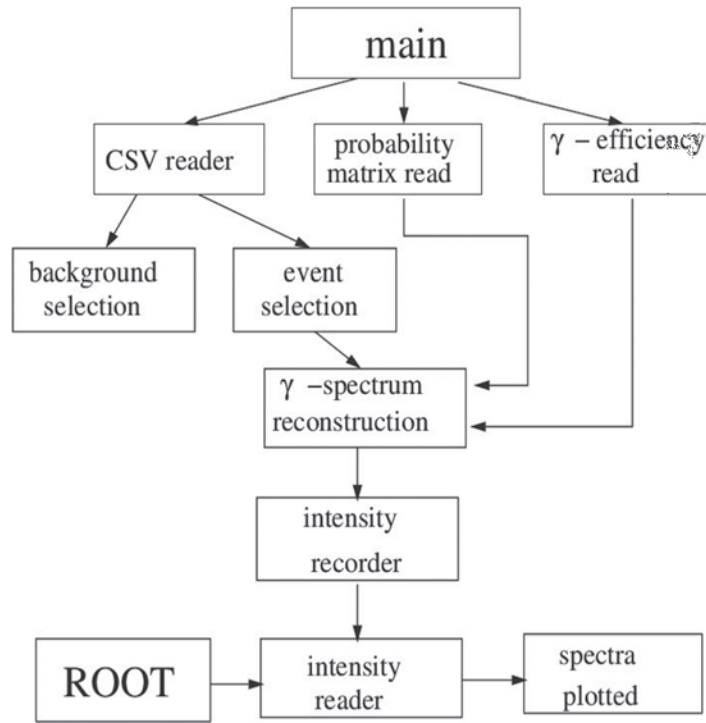


Figure 2. Outline of the algorithm of the program of data processing of spectrometers NaI (Tl).

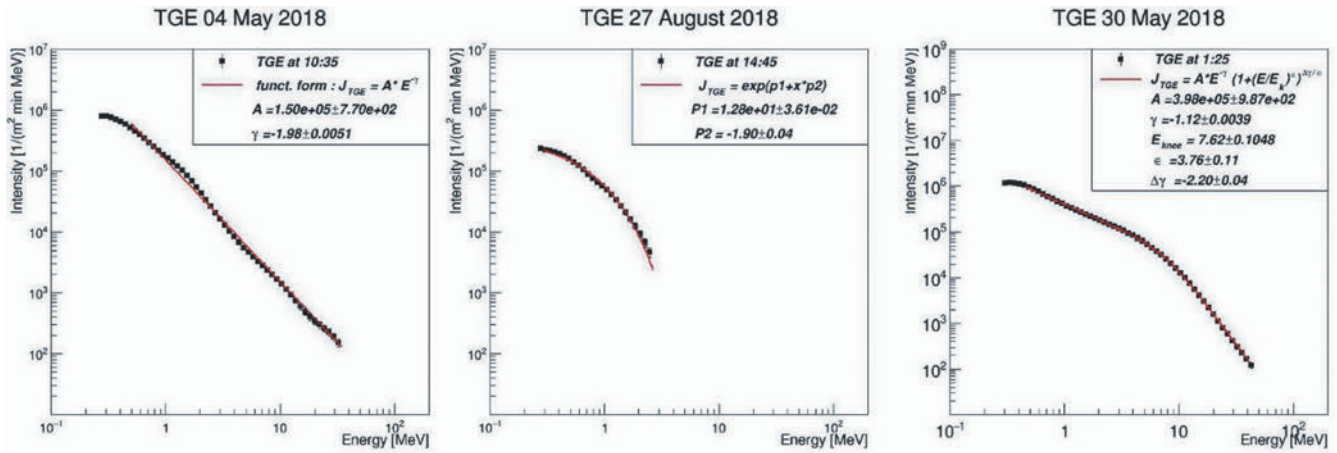


Figure 3. Main types of analytic dependencies used for fitting TGE spectra

For fitting of exponential and power-law dependencies, we use simple instruments from the ROOT package. The approximation of energy spectra with turnover (knee) is done with 2 two separate power law functions, or one five-parameter function [7]:

$$J(E) = AE^{-\gamma} \left( 1 + \left( \frac{E}{E_{knee}} \right)^\epsilon \right)^{-\frac{\Delta\gamma}{\epsilon}}$$

2 power law fit individual parts of the spectrum are approximated independently and then a turnover (position of spectral “knee”) energy should be selected. The position of the “knee” is determined from the condition of equality of intensities for two power functions before and after the “knee”. Parameters of the approximation: -  $\gamma$ ,  $E_{knee}$ ,  $\epsilon$  and  $\Delta\gamma$ , i.e., the power law index, the “knee” position, sharpness of the “knee” and the difference in the spectral slopes before and after the “knee” are determined in the optimization procedure.

Figure 4 shows a five-parameter fit for different value of the sharpness parameter  $\epsilon$  with fixed other parameters. The values of the parameters are shown in the figure.

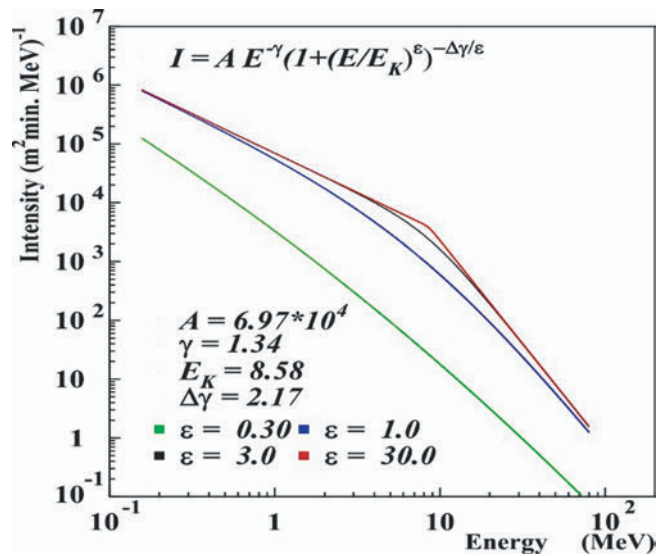


Figure 4. Five-parameter function shape for the different values of the sharpness parameter  $\epsilon$ .

When  $\Delta\gamma = 0$ , the approximation function turns to a simple power function  $A * E^{-\gamma}$  for any value of  $E_{knee}$  and  $\epsilon$ .

The multiplier of the approximation function depends strongly on the parameter  $\varepsilon$  - the sharpness of the “knee”. At  $\varepsilon < 0$ , the multiplier is inverse proportional to  $E_{\text{knee}}$ : the slope of the spectrum before the “knee” is  $\gamma$  and after the knee - ( $\gamma + \Delta\gamma$ ). For  $0 \lesssim \varepsilon \lesssim 1.0$ , the power law multiplier becomes less than 1. When  $\varepsilon > 30$ , starting from some E, the multiplier sharply tends to zero, i.e. the spectrum abruptly ends.

Thus, it is preferable to choose the region  $3 \lesssim \varepsilon \lesssim 30$  for fitting spectra.

#### CONCLUSIONS

A program for the fast assessing the energy releases histograms from the network of NaI (Tl) detectors located on the high mountain station Aragats was created. The software allows for the 3 types of approximation obtain differential energy spectra in graphical form in the ROOT environment. Running a bash script for the selected time interval of the background and investigated TGE event, we obtain the energy spectra for each minute of the TGE.

#### REFERENCES

- [1] S. Chilingaryan, A. Chilingarian, V. Danielyan, W. Eppler The Aragats data acquisition system for highly distributed particle detecting networks Journal Of Physics: Conference Series 119 (2008) 082001
- [2] K. Avakyan, K. Arakelyan, A. Chilingarian, et al. NaI Detector Network at Aragats, Journal Of Physics: Conference Series 409 (2013) 012218
- [3] A. Chilingarian, G. Hovsepyan, L. Kozliner, Thunderstorm ground enhancements: Gamma ray differential energy spectra, Physical Review D 88, 073001 (2013)
- [4] K. Arakelyan, A. Daryan, G. Hovsepyan, L.Kozliner, A. Reimers Design and response function of NaI detectors of Aragats complex installation. Nuclear Instruments and Methods in Physics Research A, 763 (2014) 308-313.
- [5] Chilingarian, G. Hovsepyan, L. Kozliner Measurements of the Energy Spectra of TGE Gamma Ray Flux on Aragats Mountain. 6-th International TEPA Symposium, Oct.3-7,2016, Nor Amberd, Armenia, 70-75 pp. ROOT. <https://root.cern.ch/>
- [6] S. Ter-Antonyan, L. Haroyan, hep-ex/0003006, 2000

## Recovering the Information on Atmospheric Discharges from Interferometric Data

A. Kiselyov<sup>1</sup>, M. Dolgonosov<sup>1,2</sup>, S. Soghomonyan<sup>3</sup>, V. Karedin<sup>1</sup>

<sup>1</sup>Space Research Institute of RAS, Moscow, Russia

<sup>2</sup>Higher School of Economics, Moscow, Russia

<sup>3</sup>Yerevan Physics Institute, Yerevan, Armenia

**Abstract.** One of the more useful methods of recovering spatial information of signal sources is interferometry. Broadband VHF signal is recorded on multiple antennas, which is cross-correlated to find arrival delays and direction to the signal source. The hardware part of the interferometer consisted of the receivers at Mt Aragats, Armenia and Tarusa, Russia. Each site consisted of 3 disk-type antennas separated by about 10 m, which were connected to an oscilloscope for the signal digitization. The processing algorithm was implemented in software along with some data processing and visualizing aids. In the course of the work the quantitative accuracy metrics of the algorithm were obtained both for the simulated and experimental data, including a comparison of spatial maps obtained using the interferometer with WLLN and meteorological data.

### 1. INTRODUCTION

The observation of the electromagnetic radiation in radio band of lightning discharges can give valuable information about impulsive current events in the cloud. In particular, VHF radiation is produced by small-scale discharge activity and can be used to reconstruct the details of lightning flash formation.

Historically, the first lightning mapping systems were TOA (Time of Arrival) type, when the pulse arrival is measured on several spatially dispersed antennas [1, 2, 3]. Such systems have simpler and cheaper receiving hardware setup, but have several serious drawbacks: limited temporal resolution (up to 30 ns, New Mexico Lightning Mapping Array [4]), inability to detect continuously radiating sources, lower sensitivity, large minimum distance between antennas (tens of kilometres). The alternative approach is to employ interferometry. The signal waveform is then coherently recorded with a high discretization rate, correlated to find phase-time difference [5, 6, 7, 8]. The advantages of such technique are: better temporal resolution, smaller setup (tens of meters), possibility to observe both impulsive and continuous sources. The narrowband interferometers are also susceptible to phase ambiguity. The use of multiple baseline lengths can partly alleviate this problem, but manual ambiguity resolution may be still required. On the other hand, broadband

interferometers are free from the fringe ambiguity altogether.

In our work, the latter method was used to map lightning activity at two locations. The processing technique mostly follows the one described in [9, 10].

### 2. EXPERIMENTAL SETUP

The signal was received by interferometers in two sites, on Mt. Aragats, Armenia and near Tarusa, Russia. Each receiving system consisted of 3 main antennas and a trigger antenna, connected to a digital oscilloscope. The schemes of each site are shown on Figure 1.

The setup on Aragats featured three aluminium disc-type antennas forming a right triangle with 13 m sides on the same height. Each antenna had 30 cm diameter and effective filtering frequency of 100 MHz. Additionally, the signal was filtered with KR Electronics 2804-SMA bandpass filter with frequency range 24-82 MHz at 2 dBc, centered at 53 MHz. Analog-digital conversion was performed by Picoscope 6403D digital oscilloscope with 6.4 ns sampling period (156.25 MS/s).

In Tarusa, the antennas were placed closer, forming a triangle with sides from about 3 to 8 m, forming a sloped plane with respect to the horizon. The diameter of antennas was slightly more, 35.5 cm. However, no bandpass filtering was used here. ADC was performed by the same type oscilloscope.

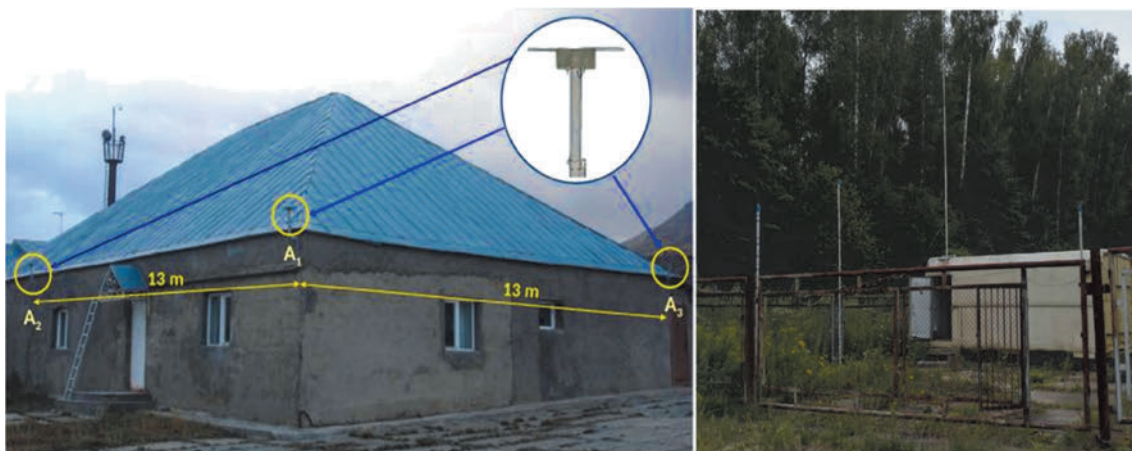


Figure 1: Schemes of the interferometer setup on Mt Aragats and in Tarusa.

### 3. DATA PROCESSING ALGORITHM

Signal processing and source geometry determination was made in software. The general scheme is the following: lag determination using cross-correlation for each window, merging of separate windows into pulse events, source coordinate determination using lag values.

The first step is preprocessing. It consists of removing saturation points and optional bandpass FFT filtering useful for the data from Tarusa.

Then the signal is divided into overlapping windows. Typical window size is 256 samples with 75% overlap. These parameters are selected based on the expected delay and signal width values and temporal resolution considerations. For each channel pair windows are cross-correlated using the equivalent presentation via the Fourier transform

$$R_g(\tau; W(f) = 1) = \int f(t)g(t + \tau)dt$$

$$\left. \begin{array}{l} f(t) \xrightarrow{\mathcal{F}} F(f) \\ g(t) \xrightarrow{\mathcal{F}} G(f) \end{array} \right\} F(f) G^*(f) W(f) \xrightarrow{\mathcal{F}^{-1}} R_g(\tau), \quad (1)$$

where  $f(t), g(t)$  are windows from two different channels,  $W(f)$  is correlation weighting function. The absolute maximum of the correlation function is taken as the lag value of this window pair. But finding the maximum as is may be inaccurate because of the low number of points corresponding to the valid delay range and, therefore, severe aliasing. There are two techniques to enhance the accuracy: up sampling (adding zero high-frequency harmonics to  $F(f)$ ) and parabolic fitting near correlation function. The second method is more performant, but heavy up sampling (e.g. 32 times) is still quite fast and gives similar results. In the following, the windows with physically unfeasible lags due to antenna geometry are ignored.

The usage of overlapping windows allows us to enhance the accuracy of both event lag and time estimation, but requires an additional step of merging of "good" windows into pulse events. The merging criterion is the near values of the absolute signal maximum in a series of adjacent windows with a length of not shorter than 2. The event time corresponds to the middle of the intersection between corresponding window time ranges, the event lag is the mean of corresponding window lags.

The event coordinates are calculated under an assumption of a point source far compared to interferometer size and, therefore, at wave front. Using the lags corresponding to two antenna pairs gives us two solutions on the sky, above and under the antenna plain, with the solution above the horizon selected.

It is possible to get the coordinates in three ways by permutations of channel pairs.

The accuracy of the acquired solutions is estimated mainly using closure phase:

$$\tau_{123} = \tau_{12} + \tau_{23} - \tau_{13} \quad (2)$$

where  $\tau_{ij}$  are the signal delays for each antenna pair. For far point-like sources  $\tau_{123} = \Delta t \lesssim 1$ , where  $\Delta t$  is the sampling period. The angular difference is the difference between source coordinates obtained for 3 possible channel pair configurations, which ideally should be very small.

Secondary accuracy criteria used are maximum correlation function value and event multiplicity, number of windows which form the event.

### 4. RESULTS AND DISCUSSION

As an example, analysis results of an event registered at Aragats on September 27, 2018 are presented. In Figures 2 and 3 the sky map are presented, with the  $\tau_{123}$  scale on the latter. It is important to note that cosine projection is used. It has an advantage of showing location uncertainty constant for all elevations. The results show good correlation between the direction of the return stroke at  $\approx 290^\circ$  as measured by the interferometer and WWLLN data at  $312^\circ$ .

Still, the observations showed several problems with the existing setup. One of the most serious problems is the correlation errors when several signals with varying duration and coordinates are overlapping (e.g. step leader versus almost continuum of background discharges). Unfortunately, these events cannot be separated using aforementioned means, as they might be overlapping both in temporal and in frequency space. The second important problem was small but noticeable ( $\approx 10\%$ ) part of pulses registered only by two out of three channels of the interferometer. Figure 4 shows a pulse present in channels A, B and absent in C. This is probably to an interaction of antennas on Aragats with metallic roof. Also the sensitivity of the equipment turned out to be too small: for the record shown, the maximum peak-to-peak value is  $190 \text{ mV} = 19$  discretization steps, much less than full oscilloscope 8-bit range. Consequently, the majority of the registered events have the amplitude of 1-2 steps with the noise of around 1 step. It can cause cross-correlation to "lock" into noise, producing a lot of bogus events. Figure 5 gives an example of such situation.

### 5. CONCLUSION

In this work the observations of lightning discharges using three-antenna broadband interferometers were described, as well as encountered challenges. Good correlation between WWLLN data and interferometric observations proves the operability of the equipment and processing software.

#### ACKNOWLEDGEMENTS

This work was supported by the RSF grant 17-12-01439.

#### REFERENCES

- [1] D. Proctor, "VHF radio pictures of cloud flashes", JGR, 86(C5), 4041-4071, 1981
- [2] L. Maier et al., "LDAR system performance and analysis", Proceedings of the International Conference on Cloud Physics, 1995
- [3] W. Rison et al., "A GPS-based three-dimensional lightning mapping system", GRL, 26(23), 3573-3576, 1991
- [4] R. Thomas et al., "Accuracy of the Lightning Mapping Array", JGR, 109(D14), 2004
- [5] J. W. Warwick, C. O. Hayenga, J. W. Brosnahan, "Interferometric directions of lightning sources at 34 MHz", JGR: Oceans, 84(C5), 2457-2468, 1979

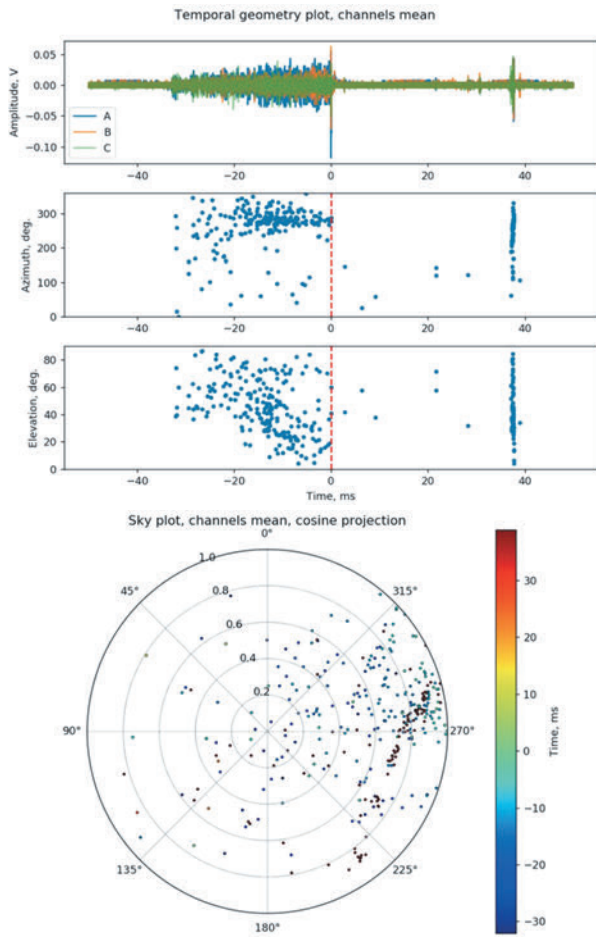


Figure 2. Sky map for the recording on September 27, 2018 at Aragats

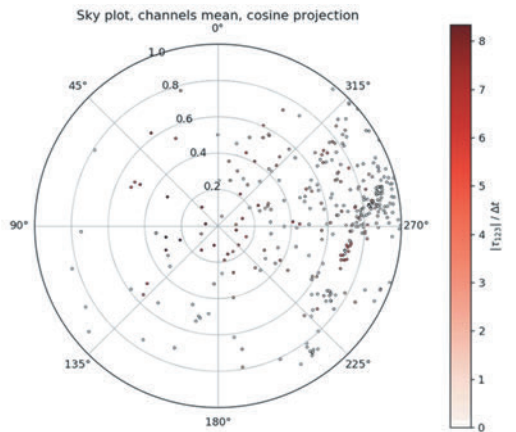


Figure 3. Sky map with accuracy color scale.

- [6] C. Hayenga, J. Warwick, "Two-dimensional interferometric positions of VHF lightning sources", JGR, 86(C5), 7451-7462, 1981
- [7] Z. Kawasaki, R. Mardiana, T. Ushio, "Broadband and narrowband RF interferometers for lightning observations, GRL, 27(19), 3189-3192, 2000
- [8] S. Qui et al., "An improved method for broadband interferometric lightning location using wavelet transform", JGR, 114(D18211), 2009
- [9] M. Stock, "Broadband interferometry of lightning", PhD thesis, New Mexico Institute of Mining and Technology, 2014
- [10] M. Stock et al., "Continuous broadband digital interferometry of lightning using a generalized cross-correlation algorithm", JGR: Atmospheres, 119, 3134-3165, 2014

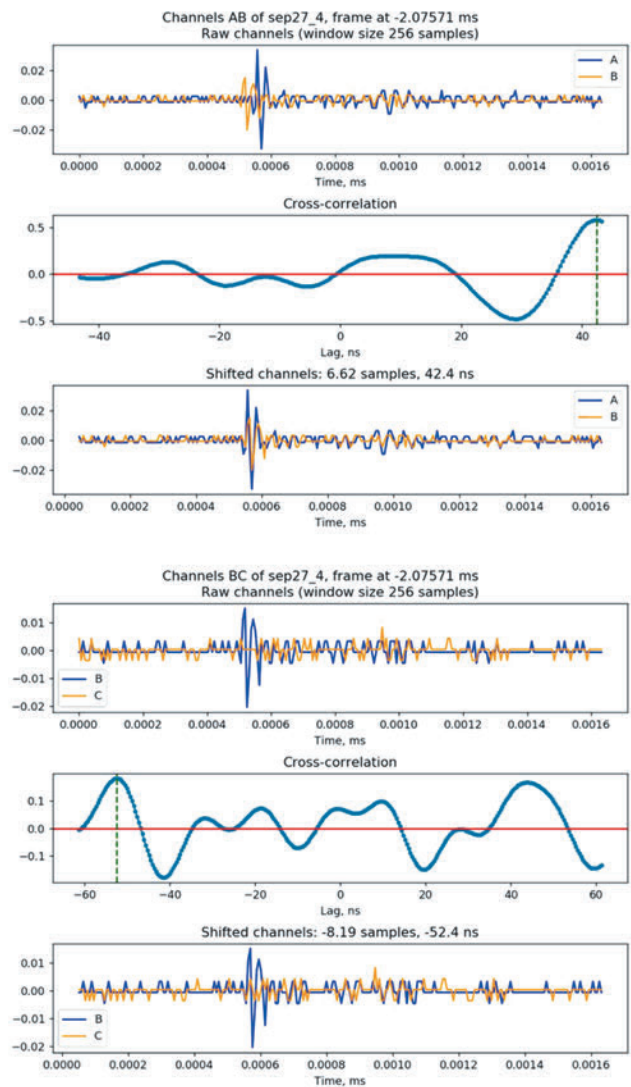


Figure 4. An example of cross-correlation for incomplete pulse for AB and BC channel pairs.

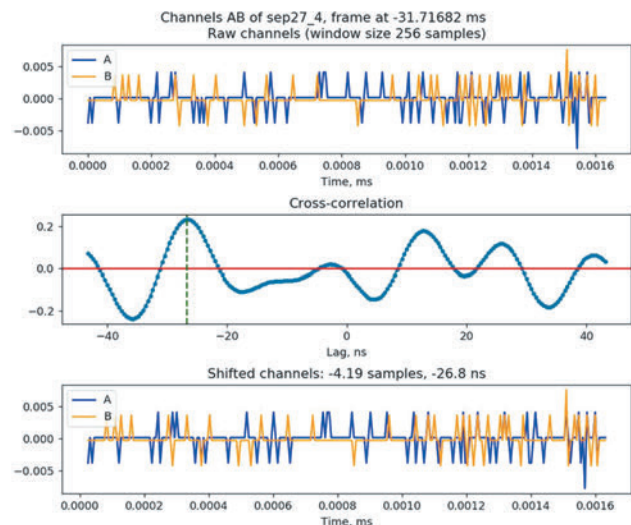


Figure 5. An example of noise "lock".

## Monte Carlo Simulation of the Relativistic Feedback Discharge Model (RFDM)

*E. Stadnichuk<sup>1,2</sup>, M. Zelenyy<sup>1,2,3</sup>, M. Dolgonosov<sup>3,4</sup>, A. Nozik<sup>1,2</sup>*

<sup>1</sup>*Moscow Institute of Physics and Technology (MIPT),*

<sup>2</sup>*Institute for Nuclear Research (INR RAS),*

<sup>3</sup>*Space Research Institute (IKI),*

<sup>4</sup>*Higher School of Economics (HSE)*

**Abstract.** In recent years, gamma radiation escaping from the thunderclouds attracted a lot of attention of the scientific community. Experimental observations of terrestrial gamma ray flashes (TGF) and thundercloud gamma-ray enhancement (TGE) establishes a basis for new scientific direction, namely, high-energy atmospheric physics (HEAP). The core theory underlying HEAP is Gurevich runaway breakdown model. While it describes in general mechanism of relativistic runaway electron avalanches (RREAs), it has difficulties in explaining observed by orbiting gamma ray observatories intense TGF bursts. This drawback was admittedly fixed by Dwyer's relativistic feedback discharge model (RFDM). RFDM predicts relativistic feedback sustaining RREA in strong electric fields and providing enough seed electrons for explaining TGF observations. In this article, we present a simulation of Dwyer's mechanism in realistic atmospheric electric fields. Simulations presented in this paper are questioning the realization of the feedback mechanism resulting in modification of the RREA dynamics in electric fields experimentally observed in thunderclouds at altitudes below 10 km.

### 1. INTRODUCTION

Gurevich et. al. (1992) has made a notable contribution in the understanding of electron avalanche physics in the atmosphere. Energetic electrons that gain from the atmospheric electric field more energy than lost for ionization, runaway and initiate electron gamma-ray relativistic avalanches (Gurevich et. al. 1999, 2001). Relativistic runaway electron avalanches (RREAs) constitutes the most intense source of natural radiation and are routinely measured by orbiting gamma ray observatories and particle detectors located on the earth's surface. However, despite decades of investigations and observations, the theory of the atmospheric discharge is far from being complete. Nowadays it is well known how lightning is developed in the thundercloud. However, the mechanism of lightning initiation is unknown yet. Either various revealing effects appearing in thunderstorms were not precisely described. Terrestrial gamma-ray flashes (TGFs) are enormous bursts of gamma-ray radiation detected by orbiting gamma ray observatories. This phenomenon did not get yet full explanation, particularly the causal relation of TGFs and lightning flashes (Østgaard et. al. 2013).

The flux of cosmic ray electrons (seed particles for RREA) is not intensive enough to explain initiation of the TGFs. Dwyer et. al. (2003) proposed a mechanism of positron feedback, which increases the runaway electron flux in strong electric fields. Dwyer studied RREA dynamics in the cell with electric field value 1000 kV/m and with length 200 m. A cell is a cylinder of air with an electric field. Dwyer's feedback mechanism is described briefly as follows. A runaway electron propagating through such a cell radiates bremsstrahlung. If the bremsstrahlung photon has enough energy, then it can produce an electron-positron pair. The positron charge is opposite to the electron charge. That is why positron reverses in the electric field and then propagates in the direction opposite to the runaway electron motion direction. Such positrons produce ionized electrons almost at the beginning of primary runaway electron track. Then ionization electrons

can reverse in the electric field and propagate through cell creating secondary electron avalanche. The runaway theory with Dwyer feedback mechanism is considered as one of the most promising theory for describing processes of TGF initiation.

On the other hand, on the Aragats research station and on other ground-based stations another thundercloud phenomenon is observed, so-called, thundercloud ground enhancement (TGEs, Chilingarian et. al. 2010, 2011, 2012). Intense fluxes of gamma rays, electrons, and rarely also neutrons were observed routinely during thunderstorms. Sometimes the duration of intense gamma radiation continuous for hours (Chilingarian, 2018). Thus, in TGE events gamma radiation duration is much more than the time of a single RRE avalanche. The avalanches comprising TGE events are developed just above the particle detectors on the heights 25-200 m, thus it is much more easy to measure energy spectra and intensities of TGE particles, than ones detected by satellites fast moving on distances 400-600 km from particle sources in thunderstorm atmospheres.

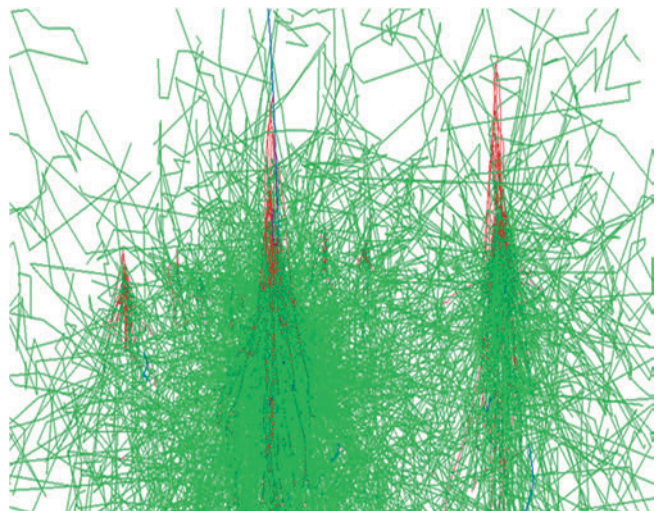


**Figure 1.** Dwyer model in Geant 4 simulation. Red tracks – electrons. Blue tracks – positrons. Green tracks – gamma-rays.

Experimentally observed thundercloud electric field is less than 200 kV/m (Mazin et. al. 1989, Marshall et. al. 1995). To the best of knowledge, there are no results in the literature regarding how positron feedback works under such conditions. The aim of the present work is to reveal whether Dwyer model operates in cells with uniform electric field less than 200 kV/m and air density between 0.3 and 0.8 kg/m<sup>3</sup> and to calculate positron feedback coefficients for different electric fields. We want also to check if RFDM model is applicable for TGE physics; i.e. can feed back mechanism be applicable for the cloud heights 4-5 km.

## 2. METHODOLOGY

Dwyer's model (Dwyer, 2003) was investigated by finding total feedback coefficient in conditions typical for thunderclouds. According to Dwyer, electron flux in clouds increases by positrons. These particles are generated by electrons' bremsstrahlung. Electric field makes positrons reverse and move to the beginning of the cell, area with uniform electric field with average size about hundreds of meters. Then positrons produce new electrons that become new part of the initial electron flux. Feedback coefficient is number of such electrons divided by number of primary ones.

Calculation of feedback coefficient was done by Monte-Carlo simulation in C++ library developed for high-energy physics – GEANT4 (Allison et. al. 2016). As physics list *G4EmStandartPhysics\_option4* was chosen, which includes all electromagnetic interactions with sufficient accuracy. There were several steps in the calculation. In the first simulation, runaway electrons were sent in cell. For all generated positrons their position, motion direction and energy in the moment of birth were calculated. Figure 2 shows number of positrons generated depending on cell electric field. Figure 3 shows positron angle spectrum. In the next simulations, new positrons with the same parameters were launched and all generated electrons' properties were received. Not all of these electrons are available to generate new avalanche. So, on the next step valid electrons were chosen.

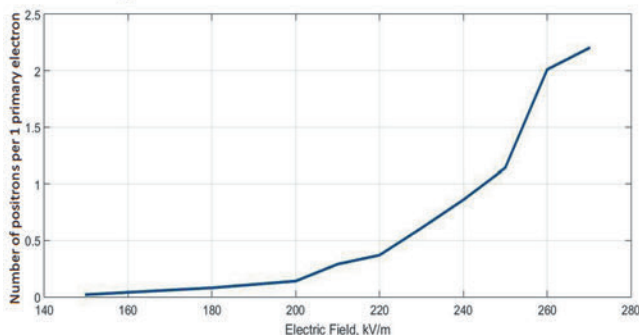


**Figure 2.** Number of generated positrons by primary electrons depending on cell electric field with cell length 400 m and 0.526 kg/m<sup>3</sup> air density. Typical for thunderclouds electric field is up to 200 kV/m, consequently in natural conditions number of produced electrons is less than number of electrons.

Choosing electrons, which are able to produce secondary avalanche, is a particular task. Three criteria were used. First, electron must runaway to propagate through thundercloud. So, its energy should be at least above 0.1 MeV. Then, electron must be produced within cell. Those runaway electrons that were produced in the end of the cell in this work were considered to be part of the primary electron avalanche. Secondary electron avalanches

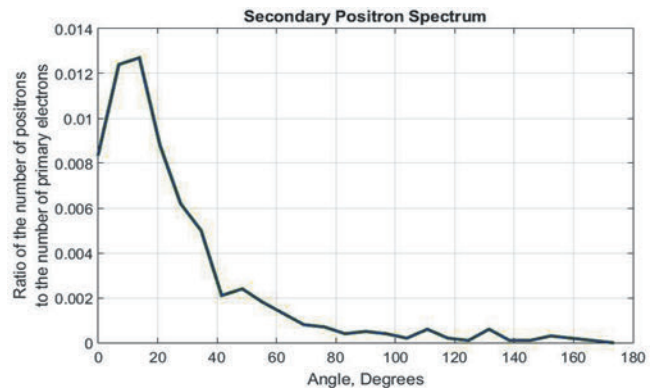


**Figure 3.** Generated positrons angle diagram. Angle is reckoned from primary electrons motion direction. The graph shows that positrons mostly move forward relatively to electric field direction. Consequently, not all of the positrons are able to reverse and move to the top of the cell.

were counted only in the first half of the cell. Finally, electron should be able to reverse in the electric field and continue to be accelerated after reversal. Within the third criteria another calculation was conducted using programming language Python. Electron was considered as a solid ball moving in uniform field. This ball faces air friction according to widely known Bethe-Bloch formula. Bremsstrahlung energy losses were not taken into account due to their smallness compared with ionization losses. Figure 4 shows minimum reversal angle between electron motion direction in moment of its birth and electric field depending on electron energy.

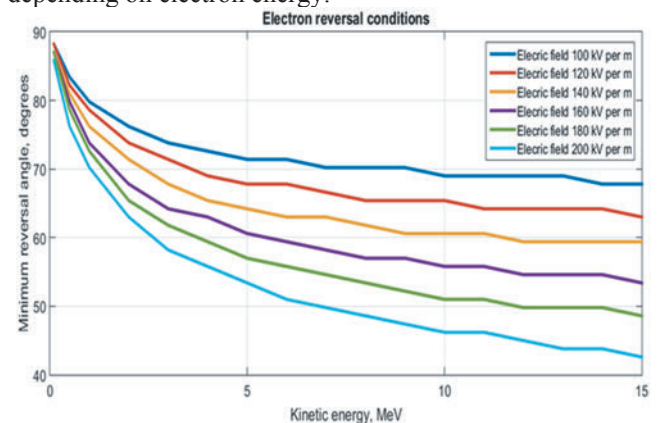


**Figure 4.** Minimum reversal angle between electron motion direction in moment of its birth and electric field depending on electron energy. All of electrons situated above the curve are able to generate secondary electron avalanche in the cell. According to this graph, less than 50% of electrons produced by positrons will generate secondary electron flux.

Number of generated positrons in the first simulation per primary electron multiply number of secondary avalanches per positron in the second simulation gives total feedback coefficient in Dwyer's model.

## 3. RESULTS

The model was examined in experimentally observed thundercloud conditions. The positron gain coefficient was calculated for cells with 0.5 kg/m<sup>3</sup> density and electric field value varying from 100 to 200 kV/m.

Figure 5 shows how Dwyer gain coefficient depends on electric field in the cell with length 400 m. According to this graph, the positron gain coefficient is less than 0.01 in such conditions. That means, that one hundred relativistic electron avalanches produces less than one electron avalanches by Dwyer mechanism in thunderclouds. For cells with electric fields less than 100 kV/m the gain

coefficient is even less than  $10^{-6}$ . In addition, feedback coefficient was calculated for other cells. Figures 6 and 7 show positron and gamma gain for 200 m. Figures 8 and 9 show feedback coefficients for 600 m long cell. Density everywhere was considered uniform and equal to  $0.5 \text{ kg/m}^3$ . These graphs shows, that in studied cells total feedback coefficient is less than 1.

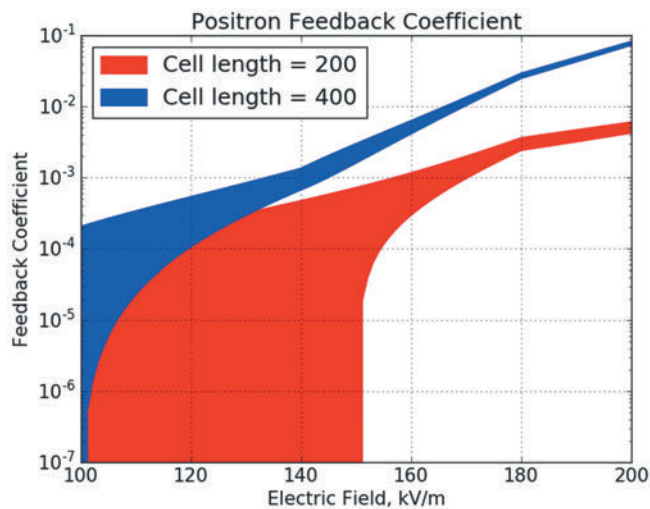


Figure 5. Positron feedback coefficient dependent on cell electric field with air density  $0.526 \text{ kg/m}^3$ .

According to Dwyer (2003), there is another feedback mechanism occurring in thunderclouds. Electron avalanche bremsstrahlung can additionally reverse by scattering and then produce new electron avalanches at the beginning of the cell. The gamma-ray coefficient was additionally calculated in the present work. The calculation was conducted similarly to the positron gain coefficient calculation. Figure 6 shows the gamma-ray coefficient for the same cell with different length. The plot reveals, that the gamma-ray coefficient is also much less than 1, but for 600 m cell with 200 kV/m electric field feedback works.

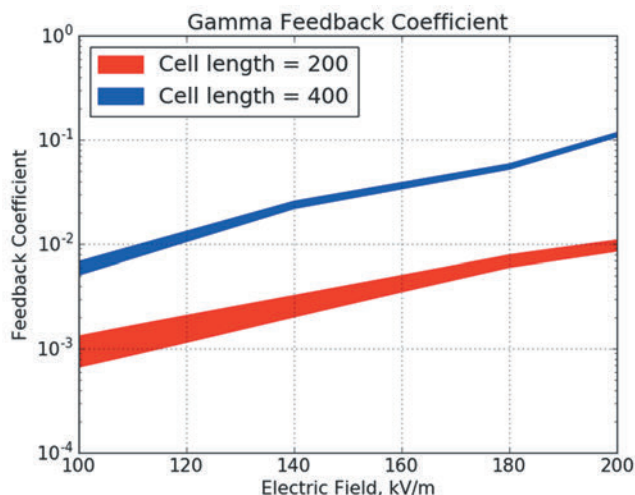


Figure 6. Gamma feedback coefficient from electric field in different cells with air density  $0.526 \text{ kg/m}^3$ .

Additionally feedback coefficient was calculated in cell with 1 km length. In such cells density should not be considered uniform, consequently, in this calculation density gradient was taken into account. Air density was chosen suitable for Aragats experiment conditions (Chilingarian et al. 2018). Cell started on 4200 meters altitude and ended on 3200 meters altitude. The electric

field was uniform with value  $180 \text{ kV/m}$ . The counting shows, that positron gain coefficient is around 0.084 and gamma feedback coefficient is around 0.2. Even in such sizable cells, total feedback coefficient is less than 1.

#### 4. DISCUSSION AND CONCLUSIONS

Several questions in atmospheric discharge physics still have no answer. For instance, though the experimentally measured atmospheric electric field does not exceed  $200 \text{ kV/m}$ , the air breakdown requires the electric field value an order of magnitude larger. Consequently, there should exist different from conventional discharge mechanism or air in the cloud should be ionized much more to create conventional breakdown conditions. A possible option is that clouds are ionized to a necessary degree by the EAS electrons. But it appears that EAS flux is not intensive enough to provide necessary ionization for the lightning initiation. Also, EASs do not provide enough seed electrons for RREA to sustain intense TGFs observed by orbiting gamma ray observatories. To overcome this drawback, Dwyer (2003) proposed a mechanism that dramatically increases the number of seed electrons. Dwyer's model creates infinite gain for relativistic electron avalanches in cells with the electric field about  $1 \text{ MV/m}$ . Dwyer extrapolated his results to realistic thundercloud conditions in the following way. The electric field measured in thunderclouds is less than  $1 \text{ MV/m}$ , but on the other hand, the air density is lower than in laboratory conditions, which results in larger mean free path for particles. Consequently, the feedback mechanism (RFDM) should work similarly in clouds.

However, in our paper was shown that RFDM does not work in thunderclouds located on altitudes up to  $10 \text{ km}$ , i.e. are not applicable for the description of the TGE initiation.

The results of the paper are supported by experimental observations on Aragats station (Chilingarian, 2017, Chilingarian et al., 2017). During strongest TGEs Aragats detectors observed individual RREA cascades initiated by electrons from the ambient population of cosmic ray particles with the array of 16 scintillators with  $1 \text{ m}^2$  area each. Trigger condition was to measure at list 1 particles in 8 scintillators. The time resolution of electronics was  $1 \text{ usec}$ . Thus, in principle, it was possible to measure  $\sim$  million individual showers if RFDM if self-sustainable RREA (RFDM) works. However, the measured one-second count rate of triggers do not exceed 5 particles. Thus, the particle flux was discrete, started when CR electron enters the strong field region, runaway and make an avalanche. And so on. That means that Dwyer feedback at the peak of strong TGE events does not create self-sustainable RREA.

#### ACKNOWLEDGEMENT

The work was performed within the framework of an international project of Russia and Armenia and was supported by the Russian Science Foundation under grant No. 17-12-01439 and Program P28.

#### LITERATURE:

- Allison J., Amako K., Apostolakis J., et al., Recent developments in GEANT4 et al., NIM A, 835, 186 2016.
- Chilingarian A., A. Daryan, K. Arakelyan, A. Hovhannisyanyan, B. Mailyan, L. Melkumyan, G. Hovsepyan; Ground-based observations of thunderstorm-

- correlated fluxes of high-energy electrons, gamma rays, and neutrons, *Phys Rev D*. 82.043009, 2010.
- Chilingarian A., Hovsepyan G., and Hovhannisyan A., Particle bursts from thunderclouds: Natural particle accelerators above our heads, *Physical review D* 83, 062001 2011.
- Chilingarian A., Hovsepyan G., Mailyan B., In situ measurements of the Runaway Breakdown (RB) on Aragats mountain, *Nuclear Inst. and Methods in Physics Research*, A 874,19–27, 2017.
- Chilingarian A., Comments on the models based on the concept of runaway electrons for explaining high-energy phenomena in the terrestrial atmosphere, *Izvestiya Rossiiskoi Akademii Nauk, Seriya Fizicheskaya*, 2017, Vol. 81, No. 2, pp. 254–257, © Allerton Press, Inc., 2017.
- A. Chilingarian, B. Mailyan & L. Vanyan (2012). Recovering of the energy spectra of electrons and gamma rays coming from the thunderclouds. doi:10.1016/j.atmosres.2012.05.008. *Atmospheric Research* 114–115 (2012) 1–16.
- A.Chilingarian, G. Hovsepyan, S. Soghomonyan, M. Zazyan, and M. Zelenyy, Structures of the intracloud electric field supporting origin of long-lasting thunderstorm ground enhancements, *Physical review* 98, 082001, 2018.
- Dwyer, J., Liu, N., & Rassoul, H. (2013). Properties of the thundercloud discharges responsible for terrestrial gamma-ray flashes. *Geophysical Research Letters*, 40, 4067-4073.
- Dwyer, J. (2003). A fundamental limit on electric fields in air. *Geophysical Research Letters*, 30(20), 1-4.
- Dwyer, J., & Babich, L. (2011). Low-energy electron production by relativistic runaway electron avalanches in air. *Journal of Geophysical Research*, 116, 1-14.
- Gurevich, A., Milikh, G. & Roussel-Dupre, R. (1992). Runaway electron mechanism of air breakdown and preconditioning during a thunderstorm. *Physics Letters A*, 165, 463-468.
- Gurevich, A., Carlson, H., Medvedev, Yu. & Zubin, K. (2001). Kinetic theory of runaway breakdown in inhomogeneous thundercloud electric field. *Physics Letters A*, 282, 180-185.
- Gurevich, A., Zubin, K. & Raussol-Durpe, R. (1999). Lightning initiation by simultaneous effect of runaway breakdown and cosmic ray showers. *Physics Letters A*, 254, 79-87.
- I.P. Mazin, A.K. Khrgian, I.M. Imyanitov, *Clouds and cloudy atmosphere* (1989)
- T.C. Marshall, M.P. McCarthy, W.D. Rust, *Journal of Geophysical Research: Atmospheres* 100 , 7097 (1995)
- Østgaard, N., Gjesteland, T., Carlson, B. E. et. al. (2013). Simultaneous observations of optical lightning and terrestrial gamma ray flash from space. *Geophysical Research Letters*, 40, 10, 2423-2426.

## Electrification of the Lower Dipole: Scenarios of TGE Initiation

A. Chilingarian

A. Alikhanyan National Lab (Yerevan Physics Institute), Yerevan 0036, Armenia

**Abstract:** The problem of thundercloud electrification is one of the most difficult ones in atmospheric physics. The structure of electric fields in the atmosphere still escapes from the detailed in situ measurements. Few balloon flights although providing us with overall knowledge on possible structures and strengths of the atmospheric electric fields, cannot reveal the dynamics of the intracloud electric field governed by intense runaway electron fluxes and atmospheric discharges. To get insight into the theory of the fast-changing charge structure of the thundercloud we use new key evidence – the fluxes of particles from thundercloud registered on the earth’s surface, the so-called Thunderstorm Ground Enhancements – TGEs. TGEs originate from electron acceleration and multiplication processes in the strong electric fields in the atmosphere, and the intensity and energy spectra of electrons and gamma rays as observed at the Earth’s surface are directly connected with the charge structure of the cloud.

### 1. INTRODUCTION

The atmospheric electric fields and atmospheric discharges in last decades were intensively investigated using radars, 3D lightning mapping arrays, worldwide lightning location networks, observations of wideband electric field waveforms, and by VHF interferometer systems, all synchronous with measurements of near-surface electric field disturbances.

The localization of charged layers in the thundercloud can be rather sophisticated, however, the tripole structure is assumed to be a basic configuration. The three charge layer arrangement with 2 main charged regions (positive above negative) and - relatively weak lower positively charged region (LPCR) is referred to as the classic tripole.

The lower dipole plays a significant role in the initiation of the thunderstorm ground enhancements (TGEs) and lightning flashes on Aragats as well as on the Tibetan plateau. In [1,2] it was established that larger than usual LPCR prevents negative cloud-to-ground lightning flashes (-CG) to occurred, and only in the late stage of the storm -CG discharges could be triggered frequently. Nag and Rakov examined various scenarios of atmospheric discharges depending on the maturity of LPCR [3]. In [4] it was stated that negative CG usually started as an inverted-polarity intracloud discharge which partly neutralized the lower positive charge so that a hole in the positive charge region was formed and eventually led to a negative CG. In turn, the intense TGE can provide enough ionization to facilitate intracloud discharge and usually discharges occurred just after the maximum of particle flux [5]. Thus, lightning flashes and TGEs are interconnected phenomena and should be studied comprehensively. H.Tsuchiya in [6] suggested that warm winds moved from the sea originate winter thunderstorms in Japan with short-lived tripole structures appeared in a thundercloud and accelerated CR electrons toward the bottom positive layer. Chilingarian and Mkrtchyan in [7] mentioned that only after the creation of the lower dipole in the thundercloud electrons can be accelerated and particle flux can be directed downward. In this paper the correlations between thundercloud electrification (near-surface electrical field and type of lightning discharge) and measured particle fluxes were studied, thus invoking in the atmospheric electricity research a new type of key evidence—temporal evolution of the TGEs, presenting and classifying simultaneous measurements of the particle fluxes, disturbances in the near-

surface electrical field, and lightning flashes of different types. In [8], it was mentioned that downward electron-accelerating electric field can be formed by the main negative charge in the cloud and its mirror image in the ground. This field is influenced by other charges in the cloud (and their images) and can be locally enhanced by the LPCR in the cloud and positive corona space charge near the ground. Various scenarios of electron acceleration in thundercloud electric fields were discussed in [9]. They mentioned that electron acceleration could take place between the LPCR and a negative charge layer above the LPCR and between negatively charged cloud base its mirror positive image charge in the ground, without any LPCR structure. Thus, there are different scenarios of TGE initiation and corresponding lightning type occurrence. However, they are dependent on each other and should be analyzed together for scrutinizing the structure and evolution of the lower dipole.

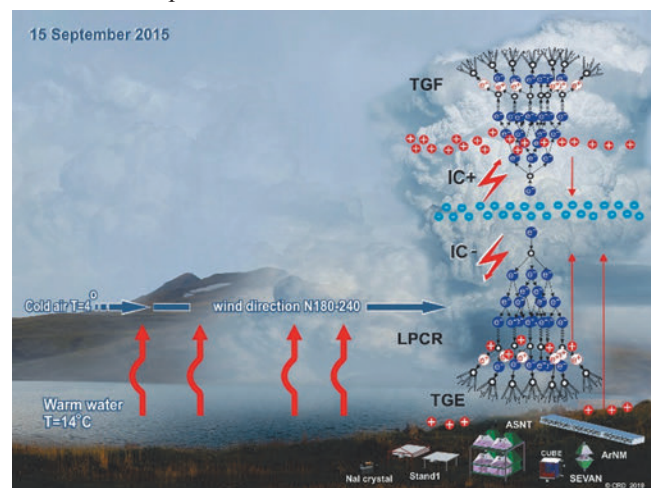


Figure 1. The lake-effect: cloud origination due to an updraft of the moisture brought by wind from the warm lake surface.

In our recent papers [10, 11] we outlined and classified a subsample of TGEs abruptly terminated by the lightning flash. We found that nearly (~75%) of TGEs abruptly terminated by lightning flashes were associated with -CG flashes and normal-polarity intracloud flashes, signaling that charge of the main negative region is rather large and the lightning leader preferably makes its path to the upper positively charged region. Another ~25% of TGEs abruptly terminated by lightning flashes were associated with

inverted-polarity intracloud flashes (IC) flashes and hybrid flashes (inverted-polarity ICs followed by -CGs).

Hundreds of TGEs were observed at the Aragats research station in Armenia during the last 10 years [12]. Numerous particle detectors and field meters are located in three experimental halls as well as outdoors; the facilities are operated all year round providing continuous registration of the time series of charged and neutral particle fluxes on different time scales and energy thresholds. In 2017 Aragats facilities registered more than 100 TGEs [12], most of them originate in cumulonimbus clouds due to charge separation triggered by the moisture updraft of orographic and lake effects, see Fig.1.

In the right side of Fig. 1, we present electron- gamma ray avalanches developed in the lower dipole (TGE) and upper dipole of the thundercloud (so-called terrestrial gamma flashes, TGFs, [13]).

Red arrows denote 3 electric fields: downward directed field in the upper dipole of the cloud formed by the main negative (MN) and upper positive charge, upward directed field in the lower dipole formed by MN and the LPCR, and upward directed field formed by MN and its mirror (MIRR) image in the ground. Throughout this letter, we use the atmospheric electricity sign convention, according to which the downward directed electric field or field change vector is considered to be positive. Thus, the negative field measured by the EFM-100 electric field mill corresponds to dominant negative charge overhead (upward directed electric field).

Following possible scenarios of electron acceleration in the atmospheric electric fields can be considered:

1. MN-MIRR only (no LPCR). The near-surface field is negative. If the field in the cloud is very strong, the RREA can be unleashed and TGE will be large and energies up to 50 MeV will be observed (RREA is a threshold process, which occurred only if electric field above Aragats is larger than 1.7 kV/cm and it prolongs 0.5 – 1 km). If the cloud base is high enough, the electric field between LPCR and its mirror on the earth's surface can decelerate electrons and negative muons, and in turn, accelerate positive muons and positrons. However, for all sizable TGEs this distance is rather short (see Table 1) and we do not foresee any strong effect from this field.
2. MN-LPCR (influence of MN-MIRR is minimal), rather rare process, occurred when LPCR is very large and close to detectors, fully screening MN (or if the charge of MN is not very large). The near-surface field is positive. If larger than usual LPCR is developed, and if electric field between MN and LPCR is larger than 1.7 kV/cm and it extends to 0.5 – 1 km; TGE will be very intense.
3. A mixture of 1 and 2 with different weights. In this case, each of 1 and 2 scenarios alone cannot sustain the electric field above the threshold, but their sum - can. The near-surface electric field is mostly negative, sometimes it can rise and for a short time reach positive values.
4. Sometimes, upon unexplored circumstances yet, the storm had a deep mid-level positive charge and upper negative charge above the positive [14]. Thus, the charge in the bottom of cloud becomes very large, and the strong field between the lower positive and upper negative charges of the cloud

accelerates electrons downward. Such a configuration, named inverse dipole, potentially can initiate extremely intensive TGE. Numerous inverted polarity intracloud discharges abruptly terminated TGE flux [15] evidenced inverted storms at Aragats. Numerical simulations with the Weather Research and Forecasting (WRF-model) [16], also reproduce the inverse dipole configuration above Aragats for several TGE events.

If the electric field is not strong enough to cause runaway effect, only MOS (modification of the electron energy spectra, [17, 18]) process can accelerate electrons; the intensity of TGE will be moderate. The lightning activity also is governed by the electric field and, in turn, lightning flashes reduce the negative charge above the earth's surface, thus decreasing the electric field in the lower dipole below the RREA threshold. RREA declines and high energy particles are eliminated from the TGE flux. However, a smaller field is still in place and MOS process continues to give additional energy to electrons and, in turn, gamma ray flux still is above "background" level, Long Lasting TGE continued [19,20].

Thus, the scenarios of the origination of the downward electron-accelerating electric field are numerous and the corresponding TGEs may vary in intensity and energy spectra, as well as in the fraction of particles reaching the earth's surface. In the letter, we will present and discuss observed TGEs and corresponding structures of the atmospheric electric field.

## 2. ANALYSIS OF THE TGES OCCURRED DURING MOSTLY NEGATIVE OR MOSTLY POSITIVE NEAR SURFACE ELECTRIC FIELD

Copious TGEs of 1 and 3 scenarios and much fewer of 2 and 4 scenarios were detected at Aragats during the last decade. In Fig. 2 we collect TGEs of 2 and 4 class occurred at positive near-surface electric field. The events occurred during much more frequently observed negative near-surface electric field (1 and 3 classes) are shown in Fig. 3.

In the figures, we show the 1-s time series of the particle flux enhancement (TGE) measured by 3-cm thick and 1 m<sup>2</sup> sensitive area plastic scintillator of the STAND1 network located outdoors nearby MAKET experimental hall. The near-surface electrostatic field (1-s time series) shown in the figures were measured by the EFM-100 electric field mill of BOLTEK company.

The initiation of TGEs observed during negative near-surface electric field can be classified as scenarios 1 and 3, where the LPCR is rather small or didn't yet developed at all.

For the TGEs observed during positive near-surface electric field (scenarios 2 and 4) we assume that larger than usual LPCR is formed in the lower part of the cloud above the particle detectors.

Sure, there could be also intermediate situations, when LPCR is forming just during TGE, see for instance Figure 3c, where large outburst of electrostatic field to the positive domain coincides with a maximum of particle flux. We assume that the first scenario is changed to the second one as LPCR get maturity. An example of a very rare 4-th scenario is depicted in Fig. 2.d. On May 30, 2018, all Aragats detectors registered extremely large TGE [20]; the particle flux from thundercloud exceeds the gamma ray background more than twice. Thus, the intracloud electric field was very large and electron acceleration excessive.

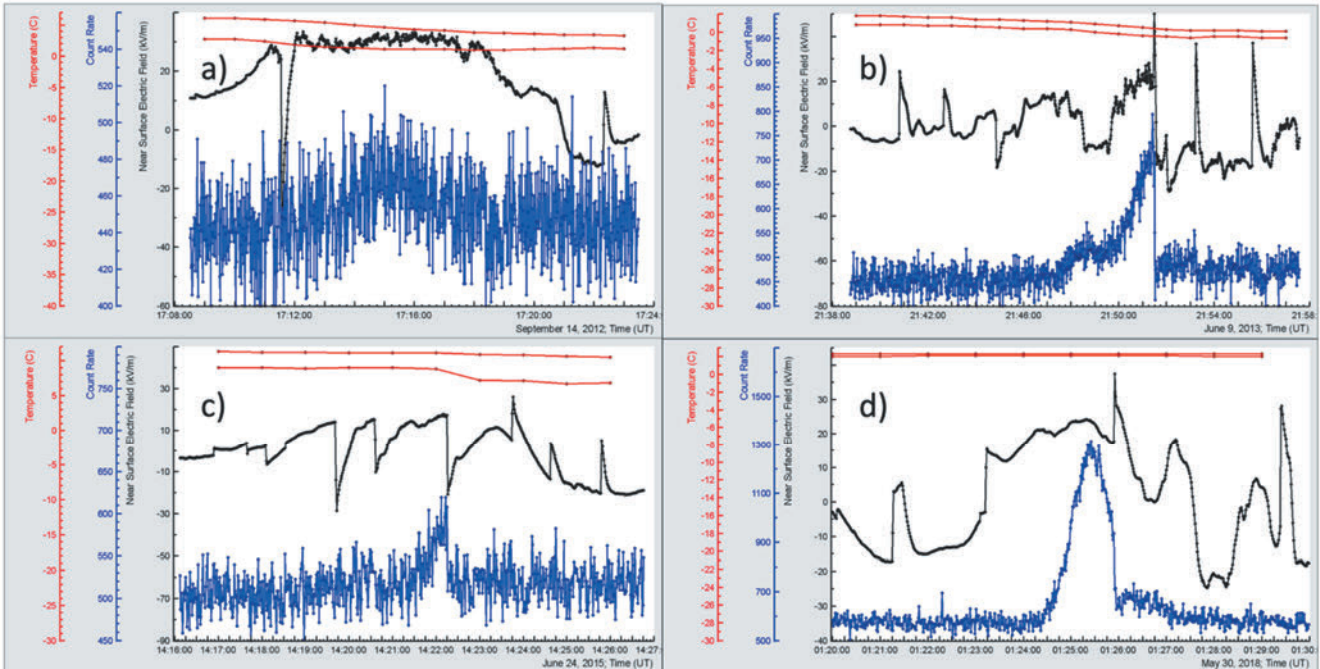


**Figure 2.** TGEs observed during the positive near-surface field. The lower dipole is formed by the main negative layer and larger than usual LPCR (electric field is measured by the EFM-100 device from Boltek company); one-second count rates are measured by the 3-cm thick scintillator of MAKET STAND1; outside temperature and dew point are measured by the Davis automatic weather station.

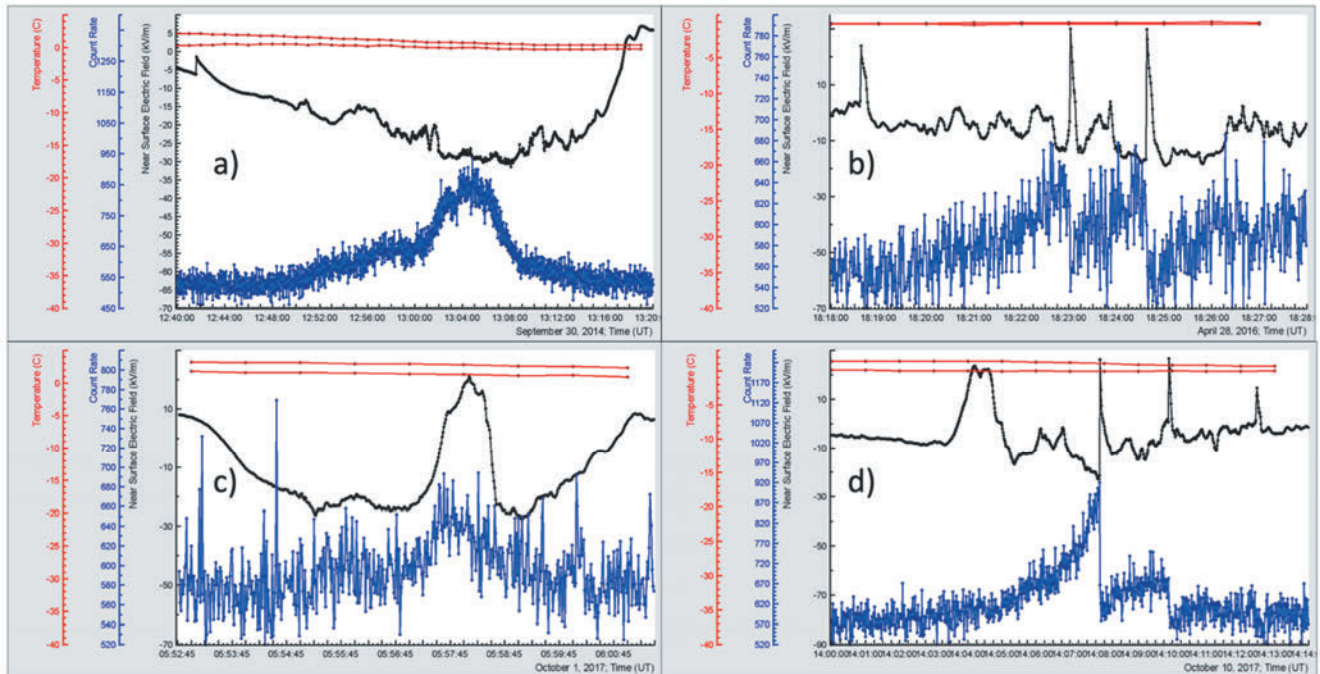


**Figure 3.** TGEs observed during the negative near-surface field. A lower dipole is formed mostly by the main negative layer and its mirror on the earth's surface (electric field is measured by the EFM-100 device from Boltek company); one-second count rates are measured by the 3-cm thick scintillator of MAKET STAND1 detector; outside temperature and dew point are measured by the Davis automatic weather station.

Another proof of our classification scheme is the lightning occurrence. As we see in Fig.2a and 2c before TGE only inverted IC flashes are observed. It is another evidence of the large LPCR [15].

In the third column of Table we put the duration of TGE, the time between 2 same background values of count rate; in the fourth column – the significance in percent and in the number of standard deviation from the mean value measured just before the TGE; in the fifth column – estimate of cloud base height made by meteorological measurements – the outside temperature and dew point [21]. In the sixth – the near-surface electric field corresponding to the maximal value of particle flux. TGEs of the first type are significantly shorter than ones of the second type. It is expected because

the size of the main negative charged region is much larger than LPCR and can sustain the electrical field conditions necessary for electron multiplication and acceleration longer time. The significance of TGEs is approximately of the same range for both classes; however, from 4 largest TGEs, 2 are of the first class, in spite of rareness of it. Distance to cloud base is larger for the first class. However, it depends basically on the season and we cannot claim that our samples of 4 events are representative. We select events randomly mostly for illustration and not for rigorous statistical analysis. And in the seventh column, we post the electric field strength corresponding to the maximal flux, that proves our selection with exception of event 3c discussed above.

Table 1. Summary of TGE characteristics

Fig.N	Date	TGE Start Time	Duration minutes	Significance %/N of $\sigma$	Distance to cloud base m	Field TGE Max Kv/m
2a	14/9-12	17:13	6	12/3	400	30
2b	9/6-13	21:48	5	75/14	100	20
2c	24/6-15	14:21	1	22/6	250	10
2d	30/5-18	01:15	3	120/30	25	20
3a	30/9-14	12:50	20	70/11	50	-25
3b	28/4-16	10:16:02	4	20/5	25	-17
<b>3c</b>	<b>1/10-17</b>	<b>05:56</b>	<b>3</b>	<b>16/4</b>	<b>200</b>	<b>-24(20)</b>
3d	10/10-1718	14:04	8	56/12	150	-23

## CONCLUSIONS

We demonstrate a big variety of atmospheric electric field configurations leading to emerging of the electron acceleration downward in the earth's direction. We explain the mechanisms of dipole origination and show how the emerged electrical structures in the atmosphere lead to the enhanced fluxes of electrons and gamma ray.

For scenarios 2 and 4 we should consider also the "inverse" (downward directed) electric field between the bottom of the cloud and earth's surface. In the modeling the propagation of CR particles in the atmospheric electric field more attention should be paid to muons due to "muon charge ratio" problem [22] (abundance of positively charged muons upon negative muons due to mostly positive galactic cosmic ray flux).

## ACKNOWLEDGEMENT

Author thanks Soghomonyan Suren for useful discussions on the atmospheric electric fields

## REFERENCES

[1] Qie, X. S., Zhang Y., Yuan T., et al., A review of atmospheric electricity research in China. *Adv. Atmos. Sci.*, 32(2), 169–191, doi: 10.1007/s00376-014-0003-z (2015).

[2] Qie, X. S., T. L. Zhang, C. P. Chen, et al., The lower positive charge center and its effect on lightning discharges on the Tibetan Plateau. *Geophys. Res. Lett.*, 32, L05814, doi: 10.1029/2004GL022162 (2005).

[3] Nag, A., and Rakov, V., Some inferences on the role of lower positive charge region in facilitating different types of lightning, *Geophys. Res. Lett.*, 36, L05815, doi:10.1029/2008GL036783 (2009).

[4] Liu, D. X., X. S. Qie, L. X. Pan, and L. Peng, Some characteristics of lightning activity and radiation source distribution in a squall line over north China. *Atmospheric Research*, 132–133, 423–433 (2013).

[5] Chilingarian A., Chilingaryan S., Karapetyan T., et al., On the initiation of lightning in thunderclouds, *Sci. Rep.* 7 (2017) 1371., <http://dx.doi.org/10.1038/s41598-017-01288-0>.

[6] Tsuchiya, H., et al., Long-duration  $\gamma$  ray emissions from 2007 and 2008 winter thunderstorms, *J. Geophys. Res.*, 116, D09113 doi:10.1029/2010JD015161 (2011).

[7] Chilingarian, A. and Mkrtychyan, H., Role of the Lower Positive Charge Region (LPCR) in initiation of the Thunderstorm Ground Enhancements (TGEs), *Physical Review D* 86, 072003 (2012).

[8] Chilingarian, A., Khanikyants Y., Mareev E., et al., Types of lightning discharges that abruptly terminate enhanced fluxes of energetic radiation and particles observed at ground level, *J. Geophys. Res. Atmos.*, 122, doi: 10.1002/2017JD026744 (2017).

[9] Wada, Y., Bowers, G., Enoto, T., et al., Termination of electron acceleration in thundercloud by intracloud/intercloud discharge. *Geophysical Research Letters*, 45, 5700–5707 (2018).

[10] Chilingarian A., Hovsepian G., Khanikyants Y., et al., Lightning origination and thunderstorm ground enhancements terminated by the lightning flash, *EPL* 110, 49001 (2015). Chilingarian, Hovsepian G., Soghomonyan S., et al., Structures of the intracloud electric field supporting origin of long-lasting thunderstorm ground enhancements, *Physical review* 98, 082001(2018).

[11] Chilingarian A., Hovsepian G., and Mntasakanyan E., Mount Aragats as a stable electron accelerator for atmospheric High-energy physics research, *Phys. Rev. D* 93, 052006 (2016).

[12] Chilingarian A., Mkrtychyan H., G.Karapetyan G., et al., Catalog of 2017 Thunderstorm Ground Enhancement (TGE) events observed on Aragats, *ScienceReports*, Nature, in press.

[13] Fishman G. J., Bhat P. N., Mallozzi v, et al. Discovery of intense gamma ray flashes of atmospheric origin, *Science* 264, 1313 (1994).

[14] Rust W.D, MacGorman D.R., Bruning E.C., et al., Inverted-polarity electrical structures in thunderstorms in the Severe Thunderstorm Electrification and Precipitation Study (STEPS), *Atmospheric Research* 76, 247–271 (2005).

[15] Chilingarian A., Khanikyants Y., and Soghomonyan S., Termination of Thunderstorm Ground Enhancements by lightning discharges, *Proceeding of TEPA-2018 conference*, Nor-Amberd, Armenia, 2018.

[16] Svechnikova E.K., Ilin N.V., and Mareev E.A., Recovery of electrical structure of the cloud with use of ground-based measurement results, *Proceeding of TEPA-2018 conference*, Nor-Amberd, Armenia, 2018.

[17] Chilingarian A., Mailyan B., and Vanyan L., Recovering of the energy spectra of electrons and gamma rays coming from the thunderclouds, *Atmos. Res.* 114–115, 1 (2012).

[18] Chilingarian A., Zazyan M., Karapetyan G., Modelling of the electron acceleration and multiplication in the electric fields emerging in terrestrial atmosphere, *Proceeding of TEPA-2018 conference*, Nor-Amberd, Armenia, 2018.

[19] Chilingarian, Hovsepian G., Soghomonyan S., et al., Structures of the intracloud electric field supporting origin of long-lasting thunderstorm ground enhancements, *Physical review* 98, 082001(2018).

[20] Chilingarian A., Long lasting low energy thunderstorm ground enhancements and possible Rn-222 daughter isotopes contamination, *Physical review D* 98, 022007 (2018).

[21] Chilingarian A., Hovsepian G., Mailyan B., In situ measurements of the Runaway Breakdown (RB) on Aragats mountain, *Nuclear Inst. and Methods in Physics Research*, A 874,19–27 (2017).

[22] Muraki Y, Axford W.I., Matsubara Y., et al., Effects of atmospheric electric fields on cosmic rays, *Physical Review D* 69, 123010 (2004)

## Influence of the Barometric Effect on the Surface Particle Detectors Count Rates

T. Karapetyan, B. Sargsyan

A. Alikhanyan National Lab (Yerevan Physics Institute), Yerevan 0036, Armenia

**Abstract:** Facilities of the Aragats Space Environment Center (ASEC) observe charged and neutral fluxes of secondary cosmic rays by the variety of particle detectors located on the slopes of Mt. Aragats at altitude 3200 m. During 2008-2018 by ASEC particle detectors were registered more than 500 so called Thunderstorm Ground Enhancements (TGEs), fluxes of electrons and gamma rays well the background level correlated with thunderstorms. For taking into account a possible influence of the barometric effect on the enhanced fluxes and for correcting TGE significance, the barometric coefficients for ASEC detectors were calculated. In this work, we present barometric coefficients, calculated for STAND1cm, STAND3cm and SEVAN detectors as well as a comparison of pressure corrected and uncorrected data for some of registered TGE events.

### 1. INTRODUCTION

Particle detectors of the Aragats Space Environmental Center (ASEC) (Chilingarian et al., 2003, 2005) are located on the slopes of the mountain Aragats and in CRD headquarters in Yerevan, Armenia; geographic coordinates: 40\_300N, 44\_100E, altitudes: 3200 m, 2000 m and 1000 m a.s.l. Various ASEC detectors, measuring fluxes of secondary cosmic rays, are sensitive to different energetic populations of primary cosmic rays. A network of particle detectors located at middle to low latitudes known as SEVAN (Space Environment Viewing and Analysis Network, Chilingarian & Reymers, 2008, Chilingarian et al., 2009, Chilingarian et al. 2018) was developed in the framework of the International Heliophysical Year (IHY-2007) and now operates and continues to extend within International Space Weather Initiative (ISWI). SEVAN detectors measure time series of charged and neutral secondary particles born in cascades originating in the terrestrial atmosphere.

With SEVAN network, we realize an integrated approach for research of the solar-terrestrial connections, space weather and high-energy atmospheric physics issues. Our approach consists from monitoring of the solar and atmospheric modulation effects posed on the counts rates of particle detectors registering charged and neutral cosmic ray (CR) fluxes along with electric and geomagnetic fields and meteorological parameters. Variety of measured geophysical parameters allows disentangling influence of all drivers separately and finding nontrivial relations between solar and atmospheric physics. SEVAN modules and other particle detectors operated at high altitudes in last decade discovered so-called thunderstorm ground enhancements (TGEs, Chilingarian et al., 2010, 2011, 2012) huge fluxes of electrons, gamma rays and neutrons of thunderstorm origin.

To exclude the influence of meteorological effects on the count rate enhancements and to correctly calculate significances of observed events, the barometric coefficients were calculated and count rates of ASEC detectors were corrected. We present barometric coefficients, calculated for STAND1cm, STAND3cm and SEVAN detectors as well as a comparison of pressure corrected and uncorrected data for some of registered TGE and solar modulation events.

### 2. INSTRUMENTATION

Basic module of the SEVAN network (Fig.1) is assembled from plastic scintillator slabs of 50x50x5cm<sup>3</sup> size. Between two identical assemblies of 100x100x5cm<sup>3</sup>

scintillators (four standard slabs) two 100x100x4.5cm<sup>3</sup> lead absorbers and thick 50x50x25cm<sup>3</sup> scintillator stack (5 standard slabs) are located. Scintillator lights capture cones and Photomultipliers (PMTs) are located on the top, bottom and in the intermediate layers of the detector. Incoming neutral particles undergo nuclear reactions in the thick 25 cm plastic scintillator produce charged particles and by this way are registering. In the upper 5cm thick scintillator charged particles are registered very effectively; however, for the nuclear interactions of neutral particles there is not enough matter. When a neutral particle traverses the top thin (5cm) scintillator, usually no signal is produced. The absence of the signal in the upper scintillators, coinciding with the signal in the middle scintillator, indicates neutral particle traversal (gamma ray or neutron). The coincidence of signals from the top and bottom scintillators indicates of traversal of high-energy muons. Microcontroller-based Data Acquisition (DAQ) electronics provides registration and storage of all logical combinations of the detector signals for further off-line analysis and for online alerts issuing (S. Chilingaryan et al 2009). If we denote by “1” the signal from a scintillator and by “0” the absence of a signal, then the following combinations of the detector output are possible: 111 and 101—traversal of high energy muon; 010—traversal of a neutral particle; 100—traversal of a low energy charged particle stopped in the scintillator or in the first lead absorber. 110—traversal of a high energy charged particle stopped in the second lead absorber. 001—registration of inclined charged particles.

For investigation of high-energy phenomena in the thunderstorm atmosphere new type of particle detectors were developed in Aragats which consists of 1cm and 3-cm thick molded plastic scintillators arranged in stacks (named STAND1cm and STAND3cm) see Figure 2 and 3. The STAND1cm detector (3200m a.s.l) (Chilingarian et al. 2013a) Figure 2, exclusively designed for the TGE research comprise of three-layers assembly of 1 cm thick and 1m<sup>2</sup> sensitive area molded plastic scintillators one above the other and 3cm thick scintillator located aside. Outdoor location, 1 cm thickness and three-layer design allow to measure flux of TGE electrons with 3 different energy thresholds starting from 0.8 MeV and to recover integral spectrum of TGE electrons (Chilingarian et al. 2017). Proper tuning of the detector provides 98-99% signal detection efficiency simultaneously suppressing electronic noise down to 1-2%. The DAQ electronics allows measuring and storing all coincidences of the detector channel operation.

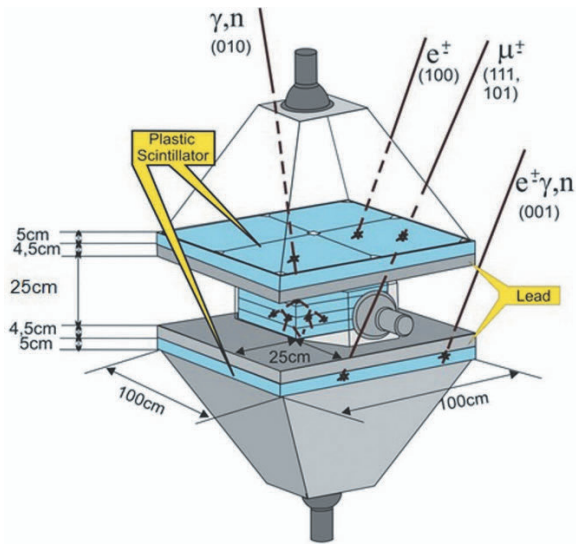


Figure 1. Schematic view of SEVAN module.

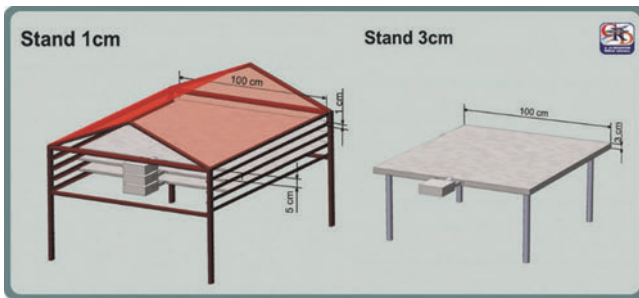


Figure 2. Schematic view of STAND1cm detector.

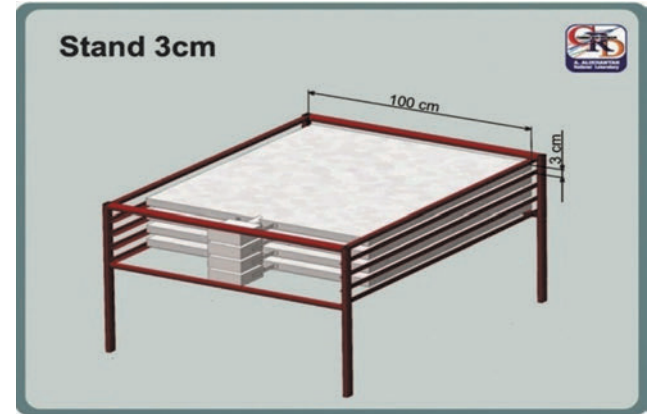


Figure 3. Schematic view of STAND3cm detector.

### 3. REGRESSION METHOD USED FOR CALCULATION OF THE BAROMETRIC COEFFICIENT

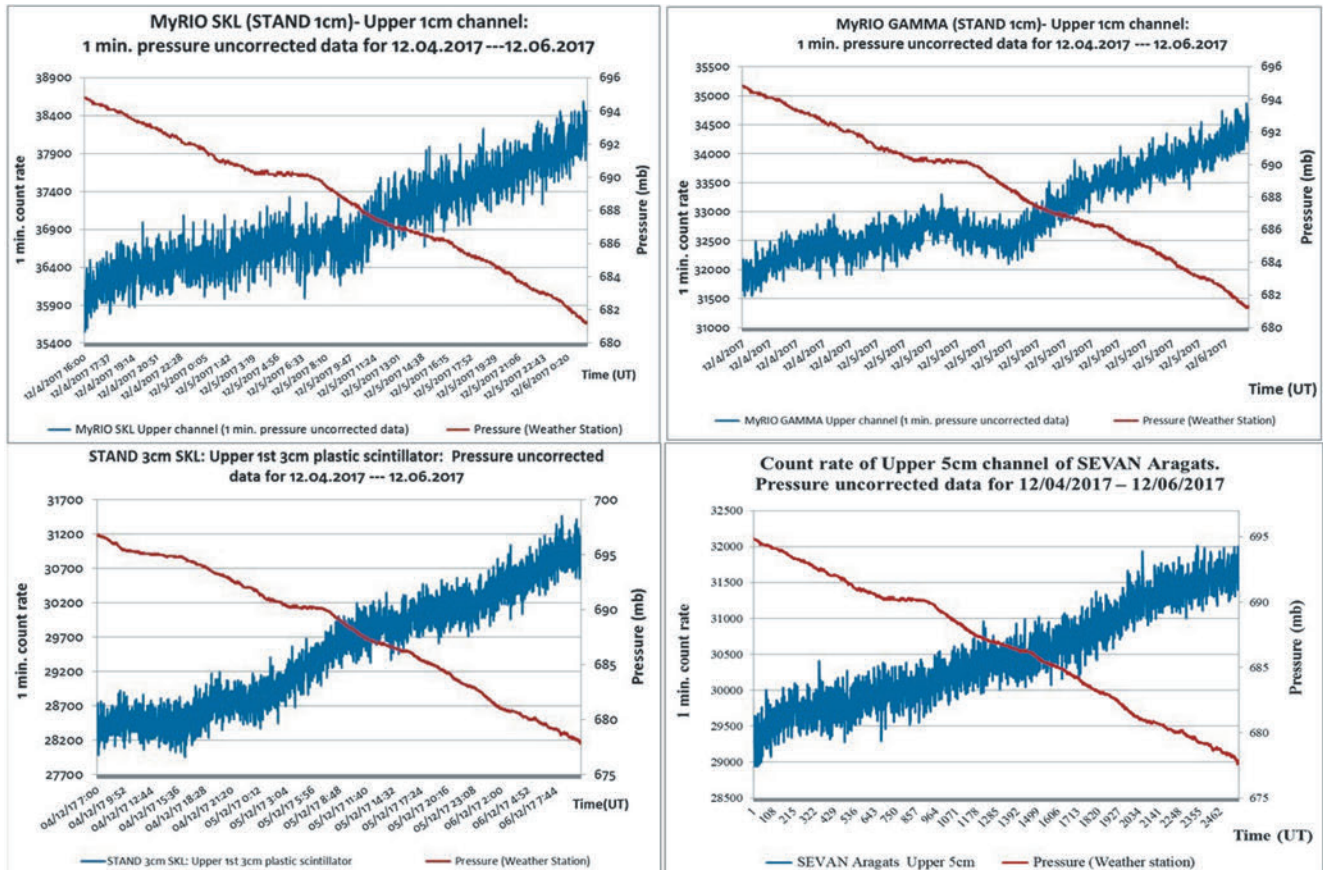


Figure 4. Variation of count rates recorded in Upper channels of STAND1cm SKL, STAND1cm GAMMA, STAND3cm SKL, SEVAN detectors and atmospheric pressure registered in Aragats from 04.12.2018 to 06.12.2018

Experimentally, the intensity  $I$  of any secondary cosmic ray component varies with a small change in the atmospheric pressure  $P$  as (Dorman, 1974, Chilingarian et.al., 2009):

$$dI = -\beta dP \quad (1)$$

where  $\beta$  is the absorption coefficient for the secondary component under consideration. For

$\beta = \text{constant}$ , the equation (1) gives

$$I = I_0 e^{-\beta(P-P_0)} \quad (2)$$

where  $P$  is pressure and  $P_0$  is reference pressure, usually the average pressure at station.  $I$  and  $I_0$  are counting rates at these pressures.

Empirically value of the barometric coefficient can be found by means of liner correlation between intensity of cosmic rays  $I_i$  and data of atmospheric pressure  $P_i$ .

$$\beta = r \cdot \sigma_I / \sigma_P \quad (3)$$

where  $r$  correlation coefficient. Data for calculation of barometric coefficient is selected at time when there were no disturbances of the Interplanetary Magnetic Field (IMF) and magnetosphere; and in addition there were significant changes in the atmospheric pressure about 14mb.

In Figure 4 is shown examples of increase of count rates in upper channels of STAND1cm SKL, STAND1cm GAMMA, STAND3cm SKL and SEVAN detectors that are caused by decrease of atmospheric pressure.

For mentioned period of time the barometric coefficients of the count rates recorded in ASEC detectors have been calculated and in Figure 5 is shown example of calculation of the barometric coefficients of the upper channels of STAND1cm SKL, STAND1cm GAMMA, STAND3cm SKL and SEVAN detectors.

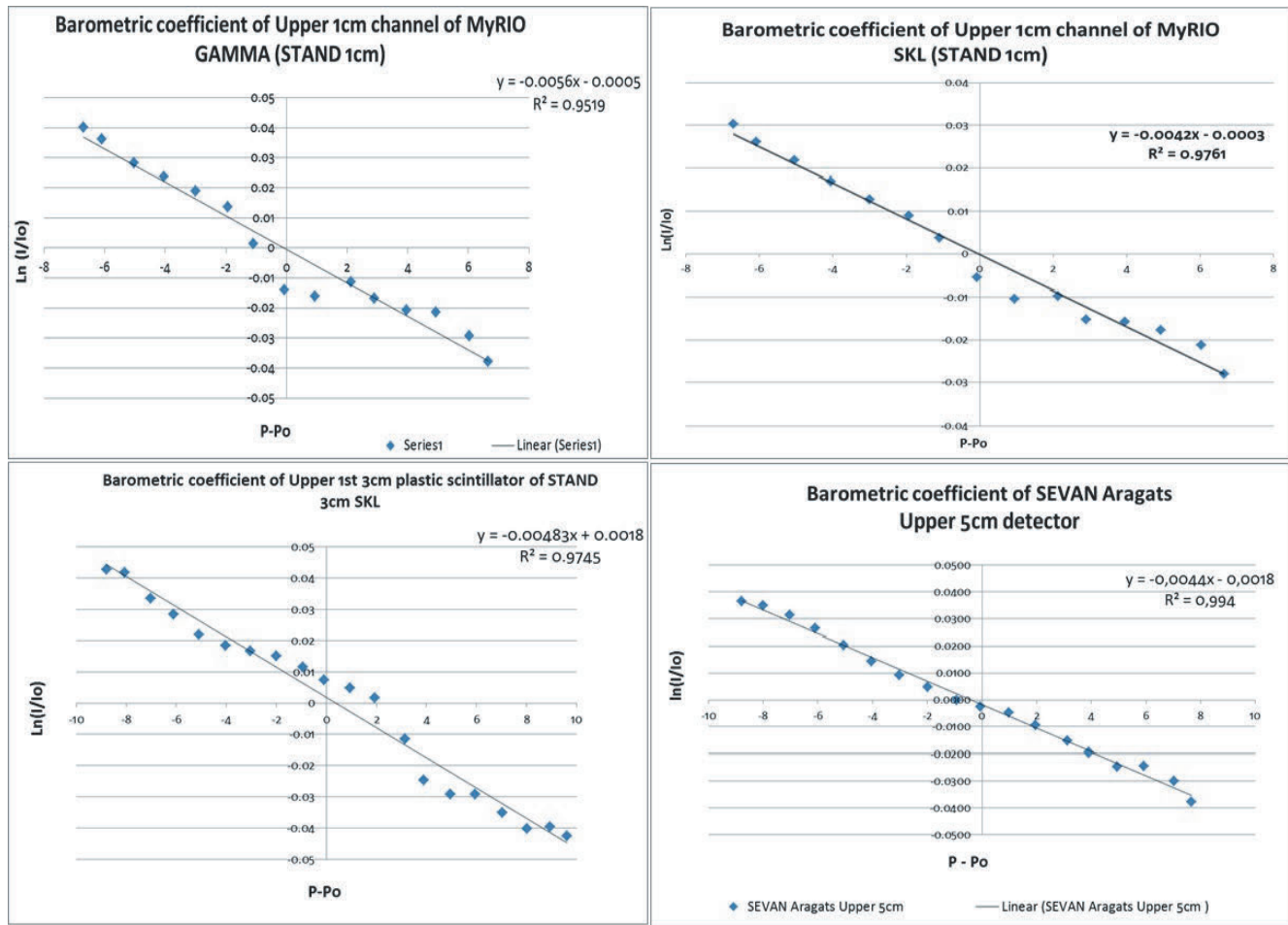


Figure 5. Calculation of barometric coefficients of the upper channels of STAND1cm SKL, STAND1cm GAMMA, STAND3cm SKL and SEVAN detectors.

In the columns of Table 1 accordingly are posted the name of detector (1 column); altitude (2 column); cutoff rigidity; barometric coefficient; correlation coefficient; count rate; relative error; ‘‘Poisson’’ estimate of relative error (standard deviation divided by an average count rate). The values posted in the last two columns should be very close to each other if the particle arrival can be described by the Poisson process.

Calculated barometric coefficients were used for pressure correction of the count rates registered by ASEC particle detectors and in Figure 6 is shown example of comparison of pressure corrected and uncorrected data. The increase of count rate is caused only by decrease of atmospheric pressure, after pressure correction the count rates are returning to the background value.

In Table 2 we compare new calculated barometric coefficients with barometric coefficients calculated on the beginning of the 24<sup>th</sup> solar activity cycle in 2008 (Chilingarian and Karapetyan 2011). New calculated barometric coefficients on the start of the next 25<sup>th</sup> solar activity cycle, are in good agreement with old ones. The barometric coefficients calculated for 3 layers of SEVAN detector and lower energy particles (coincidence 100) coincide within error bars for 2008 and 2019 years. The barometric coefficients related to high energy muons and neutrons (last 2 columns) differs more, but are compatible: neutrons are much more influenced by the atmospheric pressure than high-energy muons. The stability of barometric coefficients proves the quality of multiyear observations of the solar-terrestrial connections with SEVAN network.

Table 1. Barometric coefficients, count rates and relative errors of ASEC monitors.

Detector	Alt. (m.)	Rc (GV)	Barometric Coeff. %/mb (Dec-2017)	Correlation Coefficient	1 min. count rate [mean]	Relative error	$\frac{1}{\sqrt{N}}$
STAND1cm GAMMA (MyRIO GAMMA) Upper 1cm ch.	3200	7.1	-0.557 ± 0.035	0.976	33128	0.006	0.006
STAND1cm GAMMA (MyRIO GAMMA) Middle 1cm ch.	3200	7.1	-0.627 ± 0.035	0.980	23436	0.007	0.007
STAND1cm GAMMA (MyRIO GAMMA) Lower 1cm ch.	3200	7.1	-0.671 ± 0.071	0.935	13500	0.009	0.009
STAND1cm GAMMA (MyRIO GAMMA) 4th aside 3cm ch.	3200	7.1	-0.492 ± 0.026	0.987	34960	0.006	0.005
STAND1cm SKL (MyRIO SKL) Upper 1cm ch.	3200	7.1	-0.419±0.018	0.988	37078	0.005	0.005
STAND1cm SKL (MyRIO SKL) 4th aside 3cm ch.	3200	7.1	-0.399±0.012	0.994	31247	0.006	0.006
STAND3cm SKL 1st 3cm ch.	3200	7.1	-0.483 ± 0.018	0.987	30270	0.006	0.006
STAND3cm SKL 2nd 3cm ch.	3200	7.1	-0.477 ± 0.014	0.992	28758	0.006	0.006
STAND3cm SKL 3rd 3cm ch.	3200	7.1	-0.432 ± 0.021	0.980	25590	0.006	0.006
STAND3cm SKL: Coincidence 1000	3200	7.1	-0.624 ± 0.032	0.977	8657	0.012	0.011
STAND3cm SKL: Coincidence 1100	3200	7.1	-0.489 ± 0.014	0.993	3729	0.016	0.016
SEVAN Upper 5cm detector	3200	7.1	-0.438±0.009	0.997	29083	0.006	0.006
SEVAN Middle 20cm detector	3200	7.1	-0.436±0.009	0.997	7826	0.011	0.011
SEVAN Lower 5cm detector	3200	7.1	-0.348±0.01	0.993	17596	0.010	0.007
SEVAN Coincidence 100 Low energy charged particles	3200	7.1	-0.488±0.009	0.997	20109	0.007	0.007
SEVAN Coincidence 010 Neutrons and gammas	3200	7.1	-0.628±0.019	0.986	2323	0.020	0.020
SEVAN Coincidence (101+111) High energy muons	3200	7.1	-0.293±0.011	0.978	7653	0.011	0.011

Table 2. Comparison of 2 sets of barometric coefficients calculated at the beginnings of 24<sup>th</sup> and 25<sup>th</sup> solar activity cycles

Detector	Alt. (m.)	Rc (GV)	Barometric Coeff. %/mb (Dec-2017)	Barometric Coeff. %/mb (2008)
SEVAN Upper 5cm detector	3200	7.1	-0.438±0.009	-0.466 ± 0.018
SEVAN Middle 20cm detector	3200	7.1	-0.436±0.009	-0.406 ± 0.012
SEVAN Lower 5cm detector	3200	7.1	-0.348±0.01	-0.361 ± 0.016
SEVAN Coincidence 100 Low energy charged particles	3200	7.1	-0.488±0.009	-0.5 ± 0.018
SEVAN Coincidence 010 Neutrons and gammas	3200	7.1	-0.628±0.019	-0.511 ± 0.018
SEVAN Coincidence (101+111) High energy muons	3200	7.1	-0.293±0.011	-0.351 ± 0.038

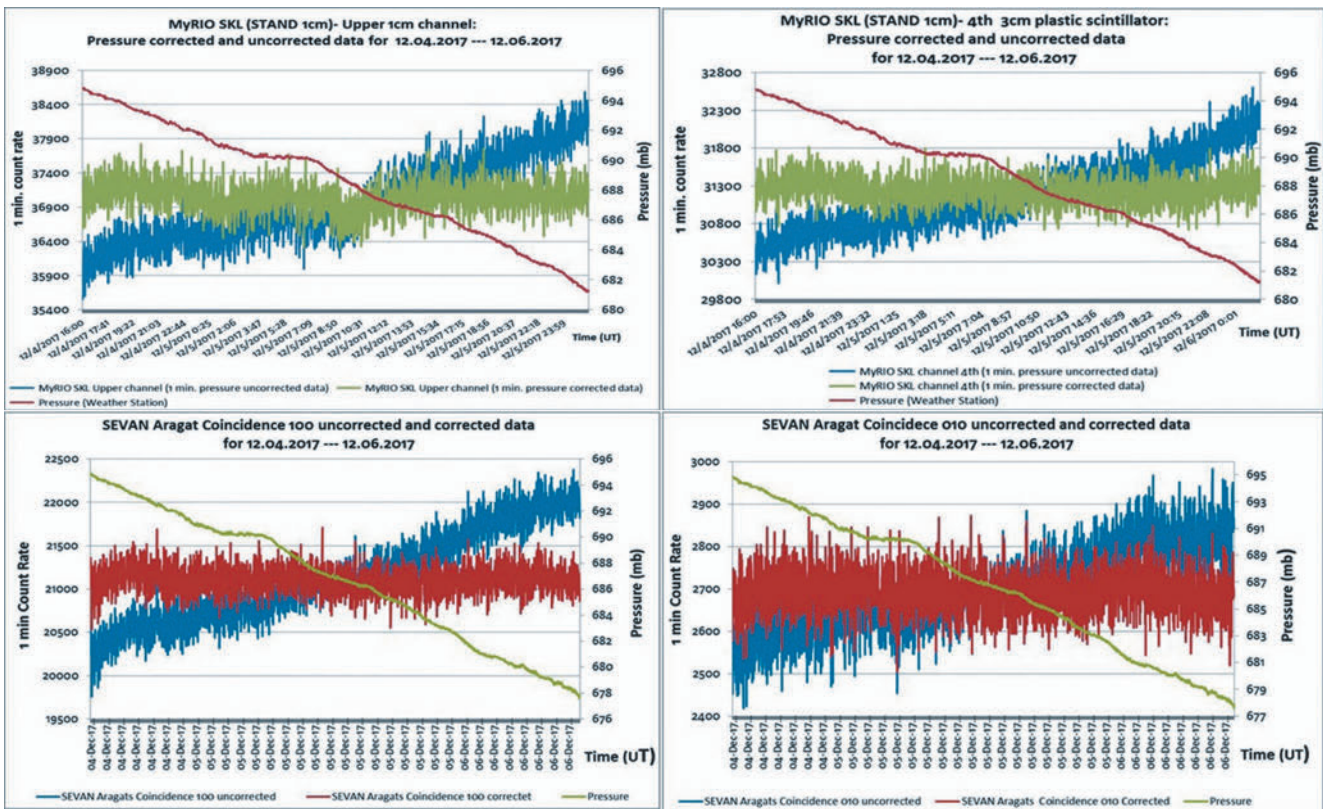


Figure 6. Pressure corrected and uncorrected data for 12.04.2017 to 12.06.2017. Upper channels of SKL and GAMMA STAND1cm detectors and coincidences of 100 and 010 of SEVAN detector.

#### 4. CORRECTION OF TGE EVENTS FOR ATMOSPHERIC PRESSURE

On 08.05.2018 at Aragats a TGE was registered by SEVAN and STAND3cm detectors (see Figs 7 and 8). The enhancement started at 10:30(UT) and reaches its maximum at 10:34 UT in STAND3cm detector and at 10:35 UT in SEVAN detector: The values of maximum of TGE registered in different detectors are posted in Table 3.

We make a correction of particle detector count rates using barometric coefficients from Table 1. As it is seen in Table 3, corrected count rates and peak significances do not notably differ from the uncorrected one. Thus, the enhancement of secondary charged and neutral particle fluxes during thunderstorm activity at Aragats on 08.05.2018 are not influenced by variations of atmospheric pressure and these fluctuations can be neglected when presenting TGEs.

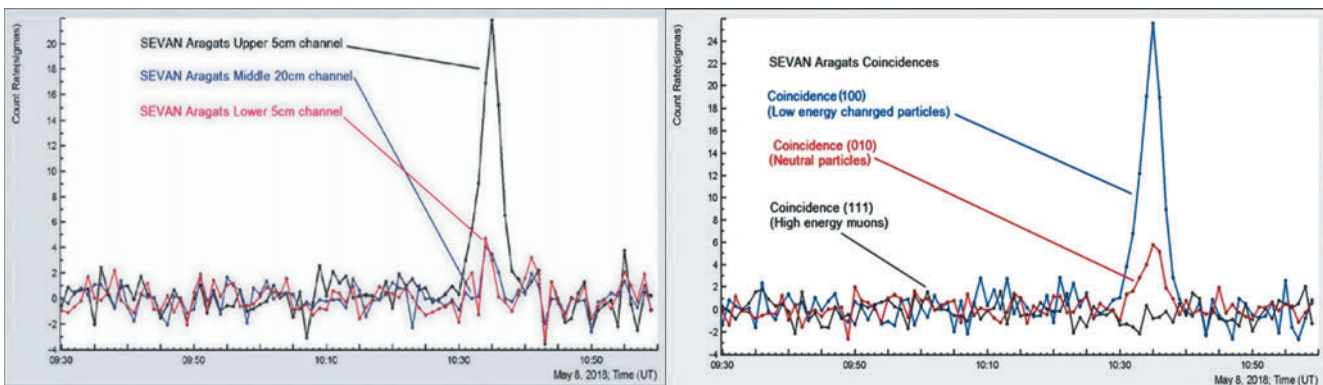


Figure 7. TGE registered in SEVAN Aragats detector on 08.05.2018.

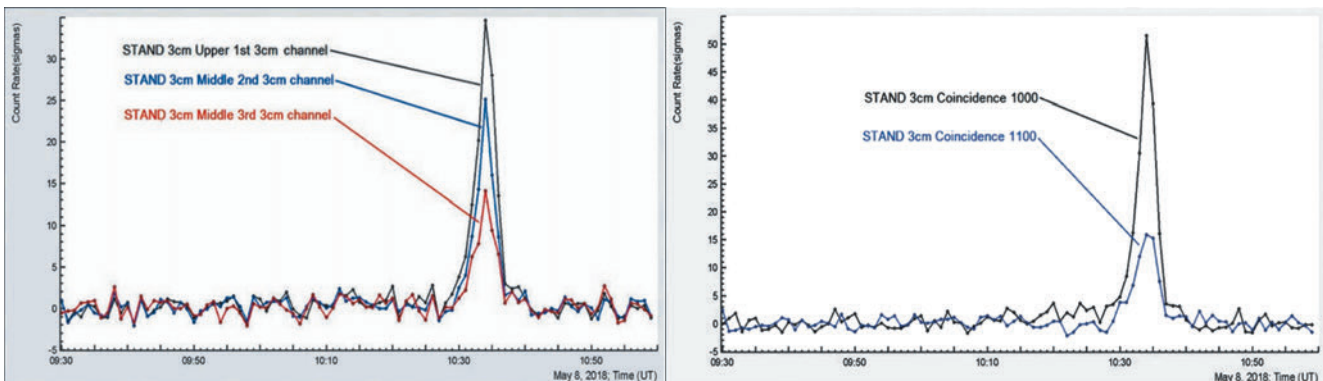


Figure 8. TGE registered in STAND3cm detector on 08.05.2018.

Table 3. Characteristics of TGE registered on 08.05.2018 at Aragats.

Detector	Time of max.	Number of sigmas ( $\sigma$ ) at the time of maximum pressure uncorr. data	Number of sigmas ( $\sigma$ ) at the time of maximum pressure corr. data	1 min. count rate at the time of maximum, pressure uncorr. data	1 min. count rate at the time of maximum, pressure corr. data	Difference of pressure corrected and uncorrected data	Difference of pressure corrected and uncorrected data by ( $\sigma$ )
SEVAN Upper 5cm detector	10:35	21.81	21.06	32124	32054	70	0.75
SEVAN Middle 20cm detector	10:34	4.01	3.95	8098	8084	14	0.06
SEVAN Lower 5cm detector	10:34	4.68	4.57	17821	17796	25	0.11
SEVAN Coincidence 100 Low energy charged particles	10:35	25.54	25.27	23019	22963	56	0.27
SEVAN Coincidence 010 Neutrons and gammas	10:35	5.66	5.65	2451	2443	8	0.01
STAND3cm, Upper 1 <sup>st</sup> 3cm channel	10:34	33.97	34.31	34572	34505	67	-0.34
STAND3cm, Middle 2 <sup>nd</sup> 3cm channel	10:34	25.12	25.14	32821	32758	63	-0.02
STAND3cm, Middle 3 <sup>rd</sup> 3cm channel	10:34	14.09	13.86	26481	26435	46	0.23
STAND3cm, Coincidence 1000	10:34	49.89	50.24	11756	11727	29	-0.35
STAND3cm, Coincidence 1100	10:34	15.85	15.89	5358	5348	10	-0.04

#### CORRECTION OF TGE EVENTS FOR ATMOSPHERIC PRESSURE

After rather weak, but the strongest since 18 February 2018 solar flare, a geomagnetic storm was unleashed on January 31 reaching Kp value 5 (G1 minor storm according to NOAA scales). During the storm a particle flux alert was distributed by Aragats Space Environmental Center (ASEC). ASEC alerts are mostly issued on thunderstorm ground enhancement events (TGEs), the abrupt enhancements of electron and gamma ray fluxes well above cosmic ray (CR) background. TGEs are connected with atmospheric electric fields emerging during thunderstorm. However, in the beginning of February, there were never any thunderstorms on Aragats and electric field was very calm corresponding to fair weather values. And it was for the first time in 10 years that ASEC issued an alert in February. In Figure 9 we show one-minute time series of all 4 scintillators of STAND3cm

detector. All four 3 cm thick and 1 m<sup>2</sup> area plastic scintillators measure flux enhancement above 1.5 standard deviation of the mean (background) flux.

There was no enhancement in the detectors registering neutral particles and no enhancement in detector with energy threshold above 5 MeV. Thus, the Aragats detectors registered additional charged flux (electrons and muons) correlated with geomagnetic storm. We can speculate that there were oscillation of geomagnetic rigidity and for a minute additional flux of galactic CR penetrate atmosphere above Aragats. It should be mentioned that solar activity and interactions of the magnetized solar plasma with magnetosphere surely can induce particle flux enhancements on the earth's surface, however the last such an event was registered on Aragats in January 2005. Thus, the alert on 1st February is the first manifestation in 14 years of the solar origin of particle flux enhancement.

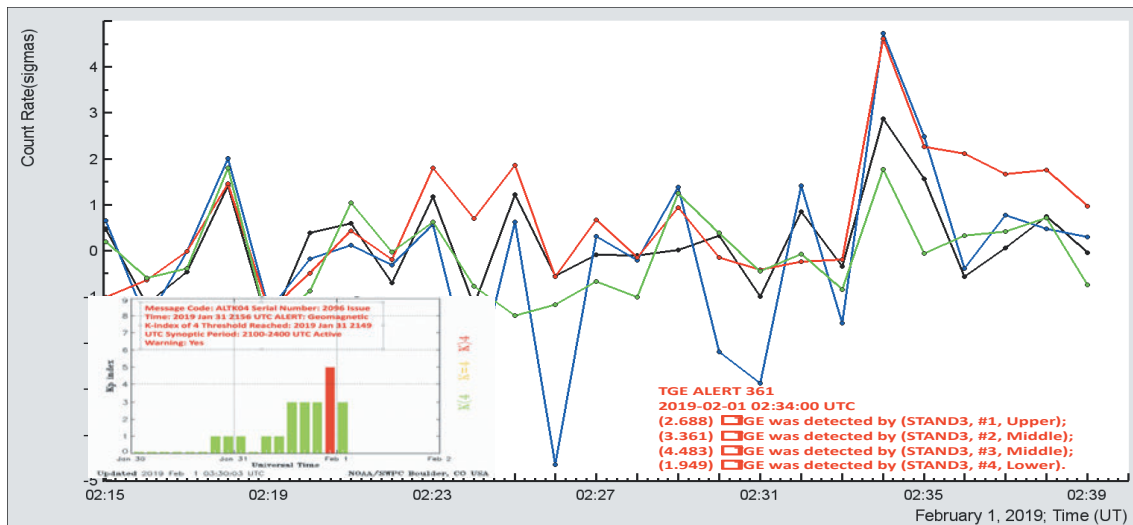


Figure 9. The flux enhancement measured by the STAND3cm detector on Aragats. In the insets alerts issued by NOAA on geomagnetic storm, and by ASEC on particle flux abrupt enhancement are located.

### CONCLUSIONS

- Barometric coefficients of STAND1cm network, STAND3cm and SEVAN detectors located at Aragats high altitude station (3200m a.s.l) were calculated.
- The pressure correction of the data was done using new calculated barometric coefficients.
- Comparison of pressure corrected and uncorrected TGE and geomagnetic effect data show that the influence of the barometric effect on the event count rates and significances is of few fractions of percent.
- New barometric coefficients will be used for pressure correction of the data for long lasting and short variations of particle fluxes.
- New calculated barometric coefficients on the start of the next 25th solar activity cycle are in good agreement with old ones. The barometric coefficients calculated for 3 layers of SEVAN detector and lower energy particles (coincidence 100) coincide within error bars for 2008 and 2019 years. The barometric coefficients related to high energy muons and neutrons (last 2 columns) differs more, but are compatible: neutrons are much more influenced by the atmospheric pressure than high-energy muons. The stability of barometric coefficients proves the quality of multiyear observations of the solar-terrestrial connections with SEVAN network.

### REFERENCES

[1] Chilingarian, K. Avakyan, V. Babayan, et al. Aragats space-environmental centre: status and SEP forecasting possibilities J. P Hys. G: Nucl. Part. Phys. 29, 939–951, 2003.

[2] Chilingarian, A., Arakelyan, K., Avakyan, K., et al., Correlated measurements of secondary cosmic ray fluxes by the Aragats Space-Environmental Center monitors, Nucl. Instrum. Methods Phys. Res. Sect. A 543 (2–3) p.483–496, 2005.

[3] Chilingarian A. and Reymers A., Investigations of the response of hybrid particle detectors for the Space Environmental Viewing and Analysis Network (SEVAN), Ann. Geophys, 26, (249-257), 2008.

[4] Chilingarian A., Hovsepyan G., Arakelyan K., et al., Space Environmental Viewing and Analysis Network (SEVAN), earth, Moon and Planets: Vol.104, Issue 1, 195, 2009.

[5] A. Chilingarian, V. Babayan, T. Karapetyan, B. Mailyan, B Sargsyan and M. Zazyan, Worldwide network of particle detectors SEVAN: 10 years of operation, Advances in Space Research, doi: https://doi.org/10.1016/j.asr.2018.02.030, 2018.

[6] A. Chilingarian, A. Daryan, K. Arakelyan, et al. Ground-based observations of thunderstorm-correlated fluxes of high-energy electrons, gamma rays, and neutrons, Phys.Rev. D., 82, p. 043009, 2010.

[7] Chilingarian, G. Hovsepyan, and A. Hovhannisyan, Particle bursts from thunderclouds: Natural particle accelerators above our heads, Physical review D 83, p. 062001, 2011.

[8] Chilingarian A., Bostanjyan N., Karapetyan T., Vanyan L., Remarks on recent results on neutron production during thunderstorms, Physical Review D, 86, 093017/1-093017/7, 2012.

[9] S. Chilingaryan, A. Chilingarian, V. Danielyan, W. Eppler, Advanced data acquisition system for SEVAN, Advances In Space Research 43, 717–720, 2009.

[10] A. Chilingarian, G. Hovsepyan, L. Kozliner, Thunderstorm ground enhancements: Gamma ray differential energy spectra, Physical Review D 88, 073001, 2013a.

[11] A. Chilingarian, S. Chilingaryan, T. Karapetyan, L. Kozliner, Y. Khanikyants, G. Hovsepyan, D. Pokhsranyan, S. Soghomonyan, On the initiation of lightning in thunderclouds, SCIENTIFIC REPORTS, 7: 1371, 1-10, 2017.

[12] A. Chilingarian, L. Vanyan, B. Mailyan, Observation of Thunderstorm Ground Enhancements with intense fluxes of high-energy electrons Astroparticle Physics 48, 1-7, 2013b.

[13] Dorman, L.I. Cosmic Rays, Variations and Space Exploration. Amsterdam, North-Holland, 1974.

[14] A. Chilingarian, T. Karapetyan, Calculation of the barometric coefficients at the start of the 24<sup>th</sup> solar activity cycle for particle detectors of Aragats Space Environmental Center, Advances in Space Research 47, 1140–1146, 2011.

## Thunderstorm Electric Field Structural Features and Lightning Initiation Problem

I. Iudin<sup>1</sup>, V. Rakov<sup>2</sup>, A. Syssoev<sup>1</sup>, and A. Bulatov<sup>1</sup>

<sup>1</sup>Institute of Applied Physics of Russian Academy of Sciences, Nizhny Novgorod, Russia

<sup>2</sup>University of Florida, Gainesville, USA

**Abstract.** Formation of elevated-conductivity regions that have a spatial scale of the order of decimeters and a lifetime of about 1 ms inside thunderclouds can lead to the enhancement of the electric field needed for lightning initiation. We show that the elevated-conductivity regions are generated due to the presence of stochastic small-scale electric field of charged hydrometeors. Fluctuations of this field can exceed, from time to time, the critical breakdown level, which can be sufficient to ensure the survival of free electrons under the conditions when the average small-scale electric field is significantly lower than the air breakdown field. The rate of above-critical electric field enhancements and hence the occurrence of elevated-conductivity regions is determined by two main factors: hydrometeor concentration and the variance of their charge magnitude distribution. Formation of elevated-conductivity regions occurs on a relatively long time interval due to the interaction of electron and ion components. Specifically, the rapid attachment of electrons is balanced by their liberation in negative ion destruction processes. Further, the drift of ions in a stochastic electric field leads to enlargement of elevated-conductivity regions. The growth of conductivity is limited to spatial-temporal clusters occupying a very small portion of the overall space-time domain, so that the average conductivity of the medium does not change significantly. The presence of elevated-conductivity regions in a dielectric medium (thundercloud) lowers its effective electric breakdown field, because of the concentration of large-scale quasi-static field across the gaps between the decimetre-scale elevated-conductivity regions, which are essentially equipotential in a quasi-static electric field.

### 1. INTRODUCTION

The cloud environment breakdown field  $E_b$  is determined by the balance between the processes of birth and disappearance of free electrons. In the absence of heterogeneity, the equilibrium condition is determined as a threshold of exponential growth of the solution of the following equation for the free electrons number density  $n_e$

$$\frac{\partial n_e}{\partial t} = (v_i - v_a)n_e, \quad (1)$$

where  $v_i$  is the ionization frequency and  $v_a$  is the frequency of electron attachment to oxygen in air, and both are functions of the applied field. It is obvious that the equilibrium condition simply reduces to the equality of the frequencies  $v_i$  and  $v_a$  [70]:

$$v_i(E_b) = v_a(E_b). \quad (2)$$

The electron attachment to the oxygen, which is the electronegative component of the air, plays a major role in the losses of free electrons during discharge development in the atmosphere. In the atmospheric air under normal conditions attachment frequency makes  $v_a \simeq 10^8 \text{ s}^{-1}$  [1]. In attachment process the electrons form negative oxygen ions, which have very low mobility and impede the development of the discharge. Electric strength of air has a value of  $E_b \simeq 2.6 \sim 3.2 \text{ MV/m}$  under normal conditions at sea level and decreases with height in proportion to the atmospheric pressure. Below this threshold field, the frequency of electron attachment in air is much greater than the ionization frequency,  $v_i \ll v_a$ .

It is well known that the amplitude of the electric field measured in a thundercloud, is an order of magnitude less than the threshold value  $E_b$ , which is necessary for the conventional electrical breakdown of air [71]:

$E_a \ll E_b$ . This discrepancy gave rise to an endless story that revolves around the competition between the following two mechanisms. The first one is conventional dielectric breakdown due to the local enhancement of the electric field in the vicinity of thundercloud water or ice particles, called hydrometeors [51, 67, 28]. Firstly Loeb [51] suggested that positive streamers could be initiated on polarized raindrops in high electric field regions and could develop into branching systems capable of funneling and concentrating the diffuse negative space charge of the thundercloud, leading to the initiation of a negative stepped leader. Later on, however, Phelps and Griffiths [67] reasonably argued that the electrical conductivity of positive streamer tails falls off rapidly in time due to electron attachment and recombination processes implying that Loeb's funneling mechanism cannot occur. To improve Loeb's idea Griffiths and Phelps [28], based on experimental investigations of positive corona streamer propagation, suggested a numerical model to calculate the electric field enhancement in a thundercloud due to the propagation of a growing system of positive corona streamers, such as might be initiated by a hydrometeor. They showed that the positive charge carried in the head of the positive streamer system increases in magnitude, and the negative charge is deposited in the trail, and thus an electric dipole that tends to enhance the original field is created. Griffiths and Phelps [28] found that a series of three to seven such systems traversing the same volume could lead to local enhancement of the ambient electric field up to 1.5 MV/m over a distance of a few meters, which is sufficient to insure dielectric breakdown and possibly launch the stepped leader. However, the electric fields required for this modified funneling mechanism to produce significant electric field intensification appear to be

at least a factor of two larger than the strongest observed thundercloud electric fields [61, 66].

The second is runaway breakdown, due to extended acceleration of high-energy electrons by the incloud electric field proposed by [29]. This mechanism relies on the fact that the deceleration force of an electron in the medium is inversely proportional to its energy. Therefore, in the presence of an external electric field that exceeds some threshold value, an energetic seed electron can be constantly accelerated and gain an energy sufficient for the ionization of neutral molecules. As a result, the so-called secondary electrons appear in the medium. Part of them have a high energy and can also become runaway electrons. The resulting avalanche of runaway electrons and a large number of slow secondary electrons can change drastically the conductivity of the medium and lead to an electric breakdown [30]. The source of seed electrons are cosmic rays or terrestrial sources of ionizing radiation, whose energy determines in many respects the shape of the formed pulse of the current and the broadband electromagnetic emission of the electron avalanche.

However, detailed interpretation of the lightning initiation within the runaway-electron breakdown theory encounters certain difficulties [38]. Some of them are discussed in [1], where on the example of three recorded bipolar electric-field pulses from compact intracloud discharges it was shown that for their generation, the runaway-electron breakdown should have extreme parameters. For example, the breakdown-initiating particle of cosmic rays should have an energy of about  $10^{21}$  eV, which decreases abruptly the probability of such a breakdown. Indeed, according to [1], a particle of the corresponding energy enters a cloud with an area of 100 km<sup>2</sup> once per 67 years. Moreover, the breakdown itself should develop in an intracloud electric field that exceeds many times the critical value in a considerable range of altitudes, but this was never observed in the actual thunderclouds. It should be also noted that the estimates presented in [15] concerning the increase in conductivity of the intracloud medium due to the generation of secondary electrons bring into a question on the very mechanism of the runaway-electron breakdown.

Dwyer [14] suggested that runaway mechanism may not be viable due to the lateral spreading of a runaway avalanche and corresponding dilution of the resulting plasma, claiming it to be not clear how these diffuse discharges can lead to the generation of a lightning leader. At the same time Dwyer proposed a promising mechanism, in which continued runaway avalanches in the same volume, sustained by feedback processes, could result in a zone of locally intense electric field near the propagating discharge boundary. It is suggested that this locally intense electric field could attain values in excess of 1 MV/m at sea level pressure and thus support "conventional" breakdown processes.

Three years later Petersen [66] proposed a hybrid mechanism whereby runaway breakdown and hydro-

meteor-initiated positive streamer systems serve to locally intensify the electric field. Following this local field intensification, it is hypothesized that formation of the initial lightning leader channel is analogous to the formation of a space leader in a laboratory negative stepped leader. Petersen [66] closed the circle of searches for the mechanism of lightning initiation: the scientific community engaged in thunderstorm electricity returned to the idea of traditional breakdown, which is developing in the form of a positive streamer system from hydrometeor surface.

Hereupon Liu et al. [50] carried out more accurate investigation of the conventional breakdown processes and reported streamer formation from a model hydrometeor in an electric field value of half of the conventional breakdown threshold for air. Theirs was the first theoretical study to show streamers are able to form from isolated model hydrometeors in electric fields close to the measured thundercloud field. In the short run, Sadighi et al. [73] presented modeling results for streamer formation in electric fields as low as one third of the breakdown threshold  $E_{cb}$ . According to [73], initiation of stable streamers from thundercloud hydrometeors in a  $0.3 \cdot E_{cb}$  electric field is possible in subbreakdown conditions at thundercloud altitudes, only if enhanced ambient ionization levels (e.g., the ionization created by corona discharges around the same or other nearby hydrometeors) are present ahead of the streamer. Babich et al. [2] recently demonstrated that the relatively small particles (with  $\sim 0.5 - 1.5$  mm) with a net charge on the order of 100 to 400 pC are able to initiate a streamer. The recent findings of [69] also support the idea that positive streamers are responsible for the lightning initiating. At last, in [13] conditions for avalanche to streamer transition are documented using a model of two spherical hydrometeor particles placed in a uniform ambient field.

Despite disagreements and the lack of a generally accepted mechanism for lightning initiating, the community engaged in atmospheric electricity has a well-established understanding of the evolution of a lightning stroke. The commonly accepted picture of the lightning stroke evolution involves the following stages: (i) buildup of in-cloud electric fields on large spatial scales via microphysical and dynamic processes; (ii) local enhancement of the electric field to produce streamers and to support their extension; (iii) propagation of sufficient electric current through and beyond the approximately 10 meters scale region to form the hot, completely ionized lightning channel, or leader. In this paper, we are concerned only with step (ii); that is, with the creation of conditions for streamers propagating in thunderclouds. We associate the stage (ii) with the generation of elevated-conductivity regions that have a spatial scale of the order of decimeters and a lifetime of about a millisecond. We show that the elevated-conductivity regions are created due to the presence of stochastic

electric field of charged hydrometeors. The stochastic electric field fluctuations increase significantly due to the clusterization of hydrometeors in a thundercloud turbulent flow and can even exceed sometimes the critical level. Having appropriate rate the above-critical bursts of the local electric field can ensure the survival of free electrons under conditions when the root-mean-square (RMS) level of the small-scale stochastic field is significantly lower than the air electric breakdown field. The above-critical electric field bursts rate and hence the formation of elevated-conductivity regions are driven by two main factors: hydrometeor concentration and the variance of their charge magnitude distribution.

This paper is organized as follows. Section 2 is devoted to the lightning initiation preliminary stage when elevated-conductivity regions are generated. Subsection 2.1 based on Appendix Appendix A presents the fine-scale fluctuations of the collective electric field produced by charged hydrometeors. We show that on thundercloud development mature stage the electric field fluctuations can significantly exceed the average field and can even reach breakdown values on the extent of approximately the size of large hydrometeors. Areas where the fine-scale electric field exceeds breakdown value we named ionization centers. Formulation of the basic equations of the ionization centers joint operation is given in Subsection 2.2 in the frame of hydrodynamic description. Another important manifestation of the fine-scale electric field fluctuations is the electrons and ions stochastic drift. In Subsection 2.4 we use the analogy with the advective mixing to estimate the characteristic scale of electrons and ions stochastic drift flow from the ionization centers. In Subsection 2.5 we focus on the consideration of the free electrons generation process within the mean field approximation. Subsection 2.6 outlines the statistical properties and the modeling of the ionization centers correlation effects. We explain how percolation theory can describe the origins of the appearance of the highly conductive regions that we name elevated-conductivity areas. Subsection 3.1 suggests that elevated-conductivity regions can produce streamer discharges easier than hydrometeors due to higher polarization charge and field enhancement at their tips. Subsection 3.2 presents illustrative simulation results. The different modifications and variants of percolation models which are mostly used in the paper are briefly reviewed in Appendix Appendix B. Finally, we briefly summarize our results in Section 3.

## 2. FORMATION OF ELEVATED-CONDUCTIVITY REGIONS INSIDE THUNDERCLOUDS

### 2.1 Electric Field of Charged Hydrometeores and Its Fluctuations

Thundercloud electric field can be represented by a sum of two components. The first one is quasi-regular component that appears due to the large-scale convective dynamics, and its values at different altitudes in a thundercloud can be characterized by the amplitude  $E_a/N$

reduced by the concentration of air molecules  $N$  (for normal conditions  $N \approx 2,7 \cdot 10^{25} \text{ m}^{-3}$ ). The maximum measured values of the reduced electric field amplitude reach the magnitude  $E_a/N \approx 9 \text{ Td} = 9 \cdot 10^{-21} \text{ V}\cdot\text{m}^2$ , an order of magnitude less than the electric strength of air. Second, the stochastic component of the electric field is represented by small-scale fluctuations of the collective field of charged hydrometeors. The volume charge density of hydrometeors  $\rho(\mathbf{r}, t)$  can be considered as spatial white noise, whose intensity is yielded by the product of hydrometeors concentration with their charge variance. In Appendix A it is shown that observed fine-scale electric field fluctuations provide the following two key points. First, fluctuations of electric field amplitude  $E_r$  demonstrate a power law distribution and spatially decrease very slowly with a critical exponent equal to  $-1/2$ . Second, on the thundercloud development mature stage the electric field fluctuations can significantly exceed the average field  $\langle \mathbf{E}(\mathbf{r}, t) \rangle = \mathbf{E}_a$  and can even reach breakdown values  $E_b$  on the extent of approximately the size of large hydrometeors  $r_0 \approx 3 \text{ mm}$ . For instance, in a storm cell with a diameter  $L \approx 1 \text{ km}$  for typical values of the average charge  $Q \approx 10^{-11} \text{ C}$  and the hydrometeors density  $N_h \approx 10^4 \text{ m}^{-3}$  [5, 6, 7] we get  $\delta E(r \approx r_0) \gtrsim 1 \text{ MV/m}$ . The level of the fine-scale electric field RMS fluctuations is about one third of breakdown field. That is quite enough for discharge processes collectively referred to as corona come into operation. Three basic types of discharge can occur in the vicinity of hydrometeors in the presence of a strong electric field: surface disruption discharge that occurs when the electrostatic repulsive force on a drop exceeds the surface tension; burst pulse discharges which are intermittent; and continuous streamers which are capable of propagation. The space-time regions, where the fine-scale electric field amplitude  $E(\mathbf{r}, t)$  exceeds the critical value  $E_b$  ensuring the free electrons generation, will be called below as *ionization center*. The characteristic spatial scale of ionization centers coincides with the correlation length  $r_0$  of the potential relief  $\varphi(\mathbf{r}, t)$  and their lifetime  $\tau_0$  is restricted by the electron attachment process  $\tau_0 \gtrsim \nu_a^{-1}$ . Inhomogeneity of the fields causes a sharp discontinuity in the frequency of ionization  $\nu_i(\mathbf{r}, t) = \nu_i(E(\mathbf{r}, t))$ . The total electric field  $\mathbf{E}(\mathbf{r}, t) = -\nabla\varphi(\mathbf{r}, t)$  satisfies the Poisson equation

$$\nabla^2\varphi = -\frac{e}{\epsilon_0}(n_p - n_e - n_n) - \frac{\rho(\mathbf{r}, t)}{\epsilon_0}, \quad (3)$$

where  $n_e$ ,  $n_p$  and  $n_n$  are the electron, positive ion and negative ion number densities, respectively;  $\rho(\mathbf{r}, t)$  is the charge density due to charged hydrometeors that fill the thundercloud and  $\epsilon_0$  is the permittivity of free space.

### 2.2 Production and Dynamics of Electrons and Ions

Another important manifestation of the fine-scale electric field fluctuations (A7) is the stochasticity of the drift velocities of electrons and ions. In a weakly ionized gas electrons and ions mainly collide with neutral molecules, and these collisions are mostly elastic. In atmospheric air under normal conditions, the mean free

path of electrons and ions is of the order of  $10^{-7}$  m. This is considerably less than the typical linear size of small hydrometeors that makes  $5 \cdot 10^{-6}$  m and determines the finest electric field fluctuations. Electron or ion velocity chaotization is going on considerably faster than the changes of the electric field that is external with respect to the moving particle. Therefore, on spatial scales exceeding the mean free path of electrons and ions and on time intervals that exceed the inverse collisions frequency the electrons and ions move with the drift velocities  $\mathbf{V}_e$ ,  $\mathbf{V}_n$ ,  $\mathbf{V}_p$  that are determined by the local electric field:  $\mathbf{V}_e(\mathbf{r}, t) = -\mu_e \cdot \mathbf{E}(\mathbf{r}, t)$ ;  $\mathbf{V}_n(\mathbf{r}, t) = -\mu_n \cdot \mathbf{E}(\mathbf{r}, t)$ ;  $\mathbf{V}_p(\mathbf{r}, t) = \mu_p \cdot \mathbf{E}(\mathbf{r}, t)$ , where  $\mu_e$ ,  $\mu_p$ ,  $\mu_n$  are the absolute values of electron, positive ion and negative ion mobilities, respectively. Along with this the drift velocity fluctuations simply track those of the fine-scale electric field. From the above reasoning it is clear that flux densities  $\mathbf{J}_e$ ,  $\mathbf{J}_p$ ,  $\mathbf{J}_n$  of electrons, positive and negative ions respectively can be represented in the following form:

$$\begin{aligned} \mathbf{J}_e(\mathbf{r}, t) &= \mu_e n_e \nabla \cdot \Phi - D_e \nabla \cdot n_e = n_e \mathbf{V}_e(\mathbf{r}, t) - D_e \nabla \cdot n_e, \\ \mathbf{J}_n(\mathbf{r}, t) &= \mu_n n_n \nabla \cdot \Phi - D_n \nabla \cdot n_n = n_n \mathbf{V}_n(\mathbf{r}, t) - D_n \nabla \cdot n_n, \\ \mathbf{J}_p(\mathbf{r}, t) &= -\mu_p n_p \nabla \cdot \Phi - D_p \nabla \cdot n_p = n_p \mathbf{V}_p(\mathbf{r}, t) - D_p \nabla \cdot n_p, \end{aligned} \quad (4)$$

where  $D_e$ ,  $D_p$  and  $D_n$  are the electron and ion diffusion coefficients. In the atmosphere under normal conditions  $D_e \simeq 0.1 \text{ m}^2 \text{ s}^{-1}$  and  $D_p \simeq D_n \simeq 2 \cdot 10^{-4} \text{ m}^2 \text{ s}^{-1}$  [17].

To describe the production and dynamics of electrons and ions in a thundercloud with charged hydrometeors taking into account the Poissons equation (3) and flux density equations (4) should be coupled with the following system of the drift-diffusion equations:

$$\begin{aligned} \frac{\partial n_e}{\partial t} + \nabla \cdot \mathbf{J}_e &= (v_i(\mathbf{r}, t) - v_a) n_e + v_d n_n - \beta_{ep} n_e n_p + \Omega, \\ \frac{\partial n_p}{\partial t} + \nabla \cdot \mathbf{J}_p &= v_i(\mathbf{r}, t) n_e - \beta_{ep} n_e n_p - \beta_{np} n_n n_p + \Omega, \\ \frac{\partial n_n}{\partial t} + \nabla \cdot \mathbf{J}_n &= -v_d n_n + v_a n_e - \beta_{np} n_n n_p, \end{aligned} \quad (5)$$

where  $v_i(\mathbf{r}, t) = v_i(\mathbf{E}(\mathbf{r}, t))$  is the ionization frequency irregularities caused by the fine-scale electric field;  $v_a$  is the electron attachment frequency;  $v_d$  is the electron detachment frequency:  $v_d \lll v_a$ ;  $\Omega$  is the number of pairs of electrons and positive ions that appear per unit volume and per unit time in collisions of neutrals or by their ionization by photons and cosmic particles. In the atmosphere under normal conditions  $\Omega \simeq 10^7 \text{ m}^{-3} \text{ s}^{-1}$  [70].  $\beta_{ep}$  is the coefficient of electron-ion recombination;  $\beta_{np}$  is the coefficient of ion-ion recombination. The coefficients of electron-ion recombination  $\beta_{ep}$  and ion-ion recombination  $\beta_{np}$  are comparable with each other and make approximately  $10^{-13} \text{ m}^3/\text{s}$ . Therefore the recombination, in particular, the electron-ion recombination becomes significant when  $\beta_{ep} n_p \simeq v_a$ , and the positive ions number density runs up to  $n_p \simeq 10^{20} \text{ m}^{-3}$ . When the density of positive ions drops to  $n_p \lesssim 10^{19} \text{ m}^{-3}$  attachment begins to prevail over recombination.

### 2.3 Loss of Ions to Hydrometeors

The elevated-conductivity regions contain multiple hydrometeors that serve as immobilizers of charge carriers. To estimate this effect let us calculate the frequency of collisions  $v_h$  of negative ions moving in a "gas" of hydrometeors:  $v_h = N_h \Sigma u$ , where  $N_h$  is the number density of hydrometeors,  $\Sigma$  is the effective collision cross-

section and  $u$  is the flow velocity. Even if we take higher values of the parameters:  $N_h \approx 10^6$ ;  $\Sigma \approx 10^{-8} \text{ m}^2$ ;  $u \approx 100 \text{ m/s}$ , we get  $v_h \approx 1 \text{ s}^{-1}$ . It means that the losses of ions to hydrometeors are relatively (in comparison with recombination) small. Corona discharge on hydrometeors is quite another matter. Moving hydrometeors at times become closer to each other and polarized in local field that fluctuates and can reach above-critical amplitudes. Yes, in this way hydrometeors should be a source of corona. Moreover, they should be a source of multielectrode corona discharges and we consider these corona flashes as centers of ionization in our initiation mechanism. In main part of our manuscript we estimate the required rate of these ionization centers.

For cumulonimbus clouds the water content can reach several  $\text{g/m}^3$ . It means that for hydrometeors that have typical radius equal to 1mm the concentration makes about  $N_h \approx 10^3 \text{ m}^{-3}$ . For radius equal to 0.1mm the concentration makes about  $N_h \approx 10^6 \text{ m}^{-3}$ . Accordingly, the typical distance between the particles is equal to  $N_h^{-1/3} = 10 \text{ cm}$  in the first case and 1 cm in the second. It is important to note that the density  $N_h$  characterizes the number density of all hydrometeors, both positive and negative:  $N_h = N_h^+ + N_h^-$ . Along with that the average charge density is much less than the product of the absolute value of the characteristic charge of hydrometeors on their concentration  $Q \cdot |N_h^+ - N_h^-| \lll Q \cdot (N_h^+ + N_h^-)$ .

### 2.4 Enlargement of Elevated-Conductivity Regions via Stochastic Drift of Ions

As follows from the expressions (4) for flux densities the output of electrons and ions from the generation area is carried out through the following two mechanisms: because of diffusion flow and flux due to the drift in a stochastic field, whose average magnitude coincides with the amplitude of the ambient (external) electric field in the considered cloud area  $\mathbf{E}_a = \langle \mathbf{E}(\mathbf{r}, t) \rangle$ . During the time period  $\tau_e^* \gtrsim v_a^{-1}$  when a spot of electron concentration returns to the background level, the diffusion length of electron density spreading makes  $l_e \approx \sqrt{D_e/v_a}$ . For the typical values of electron diffusion coefficient  $D_e \approx 0,1 \text{ m}^2 \text{ s}^{-1}$  [17] and the electron spot lifetime  $\tau_e^* \gtrsim 10^{-8} \text{ s}$  we receive  $l_e \approx 0,03 \text{ mm}$  and hence, the shape of the spot density does not considerably change due to the diffusion:  $l_e \ll r_0$ . While diffusion coefficient of ions is relatively small, their lifetime substantially exceeds that of electrons and we get  $l_n \approx \sqrt{D_n \cdot \tau_i^*} \simeq 1 \text{ mm}$  that does not exceed the size of ionization center.

But the situation significantly changes when we turn to the electrons and ions density spreading by means of stochastic drift. Using the electron flux density expression in (4) the equation for the concentration of electrons can be rewritten in the advective form of scalar impurities  $n_e(\mathbf{r}, t)$  mixing by turbulent flow  $\mathbf{V}_e(\mathbf{r}, t)$  [77, 43] with taking account of the impurities absorption and re-production:

$$\frac{\partial n_e}{\partial t} + \mathbf{V}_e(\mathbf{r}, t) \cdot \nabla n_e = (v_i(\mathbf{r}, t) - v_a(\mathbf{r}, t) - \mu_e \nabla^2 \Phi(\mathbf{r}, t)) \cdot n_e + D_e \nabla^2 n_e. \quad (6)$$

The word *turbulent* is highlighted (or logically emphasized) due to the fact that in the present case, the physical reason for the particles transfer is not the velocity of atmospheric turbulence but the stochastic electric field of charged hydrometeors  $\mathbf{E}(\mathbf{r}, t)$ . This predetermines the specific features of the stochastic advection of charged particles in a random potential. First, the considered velocity field depends on the charge and mobility of the drifting particles. For positive ions, for example, the drift velocity amplitude  $\mathbf{V}_p(\mathbf{r}, t) = \mu_p \mathbf{E}(\mathbf{r}, t)$  will be smaller by two orders of magnitude and will have an opposite direction relative to the field of electron velocities:

$$\mathbf{V}_p(\mathbf{r}, t) = -\frac{\mu_p}{\mu_e} \cdot \mathbf{V}_e(\mathbf{r}, t). \quad (7)$$

Secondly, the charged *impurity* is not passive, as its advective transfer changes the distribution of volume charge density, and hence the electric field  $\mathbf{E}(\mathbf{r}, t)$  distribution. And finally, if for ordinary turbulent advection the characteristic time of speed changes of an arbitrary impurity particle coincides with the velocity field correlation time, for stochastic drift these time intervals considerably differ. Indeed, due to the wide range of sizes and charges of hydrometeors the electric field fluctuations exhibit multi-scale characteristics, spanning from the size of small fractions of hydrometeors to the typical distances between large particles. In other words, the electric field *turbulence* inertial range extends from the micron scale to the scale of the order of the stochastic field  $\mathbf{E}(\mathbf{r}, t)$  correlation length  $r_0$ . The correlation length  $r_0$  plays the role of the integral scale of the *turbulence*. For the conventional turbulent advection, the ratio of the integral scale of the turbulence to the velocity mean squared fluctuations determines the velocity field correlation time. For the stochastic drift this ratio characterizes the time  $\tau_e$  of speed changes of an arbitrary *impurity* particle:

$$\tau_e \approx \frac{r_0}{\langle (\mathbf{V}_e(\mathbf{r}, t) - \mathbf{V}_{ea})^2 \rangle^{\frac{1}{2}}}, \quad (8)$$

where  $\mathbf{V}_{ea} = -\mu_e \mathbf{E}_a$  is a turbulent flow average speed. The real correlation time  $\tau_0$  of the stochastic field  $\mathbf{E}(\mathbf{r}, t)$  can substantially differ from  $\tau_e$ .

However, taking into account the comments made, one can use the analogy with the advective mixing to estimate the characteristic scale of electrons and ions turbulent flow from the generation region. According to the hypothesis of Taylor [79], the motion of individual particles in a turbulent flow is diffusive in nature and is determined by the ratio

$$\langle r^2(t) \rangle \approx \mathcal{D}_e \cdot t, \quad (9)$$

where  $r(t)$  describes the displacement of particles in the reference system moving with the average speed of turbulent flow  $\mathbf{V}_{ea}$  with the effective diffusion coefficient or coefficient of advective mixing  $\mathcal{D}_e$ , which is determined by the correlation time  $\tau_e$  and the turbulent flow velocity mean squared fluctuations  $\langle (\mathbf{V}_e(\mathbf{r}, t) - \mathbf{V}_{ea})^2 \rangle$ :

$$\mathcal{D}_e \approx \langle (\mathbf{V}_e(\mathbf{r}, t) - \mathbf{V}_{ea})^2 \rangle \cdot \tau_e. \quad (10)$$

It is obvious in our case that the turbulent velocity mean square fluctuation is represented by the middle square of the electron drift speed in a stochastic field  $\mathbf{E}(\mathbf{r}, t) - \mathbf{E}_a$ . Using Eq. (8) together with Eq. (10) for the effective diffusion coefficient we obtain

$$\mathcal{D}_e \approx \langle (\mathbf{V}_e(\mathbf{r}, t) - \mathbf{V}_{ea})^2 \rangle^{\frac{1}{2}} \cdot r_0. \quad (11)$$

For the typical values of the electrons RMS velocity  $\langle (\mathbf{V}_e(\mathbf{r}, t))^2 \rangle^{\frac{1}{2}} \approx 10^5$  m/s and the correlation radius  $r_0 \approx 1$  cm we get  $\mathcal{D}_e \approx 10^3$  m<sup>2</sup>s<sup>-1</sup>, i.e.  $\mathcal{D}_e \gg D_e$ . Accordingly, over the lifetime of the electrons the number density spot  $\tau_e^*$ , the characteristic length of the advective spreading of the spots of the electron density is  $L_e \approx \sqrt{\mathcal{D}_e \cdot \tau_e^*} \approx \sqrt{\mathcal{D}_e / \nu_a} \approx 3$  mm, which is comparable to the ionization zone linear size  $r_0$  and substantially exceeds the electron diffusion length  $l_e$ .

Similar conclusions can be drawn about features of the ions advective transfer from the generation zone by means of stochastic drift. The only difference is that their mobility is two orders of magnitude less than the mobility of electrons (see (7)), and the lifetime of the ions, in contrast, substantially exceeds the lifetime of electrons that go through attachment. So, by analogy with (11), for the effective diffusion coefficient of ions, we obtain

$$\mathcal{D}_n \approx \langle (\mathbf{V}_i(\mathbf{r}, t) - \mathbf{V}_{ia})^2 \rangle^{\frac{1}{2}} \cdot r_0, \quad (12)$$

where  $\mathbf{V}_{ia} = \mu_p \mathbf{E}_a$  for positive and  $\mathbf{V}_{ia} = -\mu_n \mathbf{E}_a$  for negative ions. For the typical values of the mobility  $\mu_p \approx \mu_n \approx 2 \cdot 10^{-4}$  m · V<sup>-1</sup> · s<sup>-1</sup> [17] we get  $\mathcal{D}_n \approx 2$  m<sup>2</sup>s<sup>-1</sup>. So, over the lifetime of the ion concentration spot  $\tau_i^* \approx 5 \cdot 10^{-3}$  s, the characteristic length of the advective spreading of the ion concentration spot is  $L_n \approx \sqrt{\mathcal{D}_n \cdot \tau_i^*} \approx 1$  dm, which is more than an order of magnitude larger than the radius of the advective spreading of the electron density spot  $L_e$  and the ionization center characteristic scale  $r_0$ .

The frequency of electrons diffusion losses  $\nu_{D_e}$  can be estimated as follows [70]

$$\nu_{D_e} \approx \frac{D_e}{r_0^2}. \quad (13)$$

In much the same way it is possible to estimate the electron losses due to stochastic drift using the definition of the advective diffusion coefficient (12):

$$\nu_{\mathcal{D}_e} \approx \frac{\mathcal{D}_e}{r_0^2} \approx \frac{\langle (\mathbf{V}_e(\mathbf{r}, t) - \mathbf{V}_{ea})^2 \rangle^{\frac{1}{2}}}{r_0} \approx \frac{\langle \mathbf{V}_e^2(\mathbf{r}, t) \rangle^{\frac{1}{2}}}{r_0}. \quad (14)$$

On the border of the ionization center the frequency of electron advective losses can be as large as the electron attachment frequency:  $\nu_{\mathcal{D}_e} \lesssim \nu_a$ . It is obvious that  $\nu_{\mathcal{D}_e} \gg \nu_{D_e}$ . Expressions similar to (13) and (14) can be

also obtained for ion losses. For example, for negative ions we have

$$v_{D_n} \simeq \frac{D_n}{r_0^2} \quad (15)$$

and

$$v_{\mathcal{D}_n} \simeq \frac{\mathcal{D}_n}{r_0^2} \simeq \frac{\langle \mathbf{V}_n^2(\mathbf{r}, t) \rangle^{\frac{1}{2}}}{r_0}. \quad (16)$$

Since on average the spot size of ion concentration considerably exceeds the ionization center size  $r_0$ , the actual frequency of advective and diffusive losses of ions is much less than the estimations made above.

### 2.5 Electron Production in the Mean Field Approximation (independent ionization centers)

Before proceeding to the system (3) – (5) for numerical simulation let us try to obtain as much information as possible from the consideration of the free electrons generation process within the mean field approximation. Consider the first of equations (5) assuming that diffusion losses of electrons are negligible compared to advective losses. Then, ignoring the extraneous ionization and detachment processes we get the following equation for the dynamics of free electrons number density  $n_e$

$$\frac{\partial n_e}{\partial t} = (v_i(\mathbf{r}, t) - v_a - v_{\mathcal{D}_e}) \cdot n_e, \quad (17)$$

It is obvious that areas where  $v_i(\mathbf{r}, t) \gtrsim v_a$  coincide with the ionization centers, which we introduced in the section 2.1 and where the condition  $E(\mathbf{r}, t) \gtrsim E_b$  is satisfied. As far as the appearance of ionization centers is exponentially rare, the fluctuating field  $v_i(\mathbf{r}, t)$  could be represented for simplicity by the sum of the identical pulses  $\mathcal{I}(\mathbf{r}, t)$  that occur independently of one another and are located at random points  $(\mathbf{r}_i, t_i)$ :

$$v_i(\mathbf{r}, t) = \sum_i \mathcal{I}(\mathbf{r} - \mathbf{r}_i; t - t_i). \quad (18)$$

and the average number of pulses per unit time and per unit volume is constant and equal to  $\mathfrak{M}$ . Random processes of the type (18) are known as Poisson processes. We assume that the function  $\mathcal{I}(\mathbf{r}, t)$  that describes an individual ionization center is of the form

$$\mathcal{I}(\mathbf{r}, t) = J\psi(\mathbf{r})\theta(t), \quad (19)$$

where quality  $J$  characterizes the ionization intensity,  $\psi(\mathbf{r}) = 1$  at  $r \leq r_0$  and  $\psi(\mathbf{r}) = 0$  at  $r > r_0$ ;  $\theta(t) = 1$  at  $0 < t < \tau_0$  and  $\theta(t) = 0$  when  $t < 0$  and  $t > \tau_0$ , so  $r_0$  and  $\tau_0$  give the characteristic spatial size of the individual ionization centre and its lifetime respectively. The space and time average generation rate of electrons is

$$\langle v_i(\mathbf{r}, t) \rangle = \mathfrak{M} \cdot \int \mathcal{I}(\mathbf{r}, t) d\mathbf{r} dt = J \cdot \frac{\pi^2}{2} r_0^3 \tau_0 \mathfrak{M} = J \cdot \mathfrak{G}, \quad (20)$$

where

$$\mathfrak{G} = \frac{\pi^2}{2} r_0^3 \tau_0 \mathfrak{M}, \quad (21)$$

is the dimensionless concentration of the ionization centers. The expression (21) is just a product of centers appearance rate  $\mathfrak{M}$  per unit volume per unit time with the space-time volume occupied by separate center and, therefore, gives the geometric definition of the dimensionless concentration of the ionization centers that we obtained in (A12) from statistical consideration.

When the parameter  $\mathfrak{G}$  is small  $\mathfrak{G} \ll 1$ , various centers of ionization are independent of each other and the calculation of the threshold of electrons generation could be carried out in the framework of the mean-field approximation [64]. A separate ionization center can be considered as a point system where the production of free electrons obeys the following equation

$$\dot{n}_e = (J - v_a - v_{\mathcal{D}_e}) n_e, \quad (22)$$

In equation (22), as well as above in equation (17), we neglect diffusive losses of electrons in comparison with advective losses and losses due to attachment of electrons. The justice of this restriction will be discussed below. Because the intensity of ionization center satisfies the condition  $J \gtrsim v_a + v_{\mathcal{D}_e}$ , we can estimate the total increase in electron density on each of them during their lifetime in the following way

$$\Delta N = \frac{4\pi}{3} n_0 r_0^3 \{ \exp\{(J - v_a - v_{\mathcal{D}_e})\tau_0\} - 1 \}, \quad (23)$$

where  $n_0$  is the initial density level that is constant in space. The equality of electron concentration growth on the ionization centers and electron concentration decay per unit volume per unit time determines the generation threshold for equation (17). If we neglect the mutual influence of the centers, this equality condition can be represented in the form  $\mathfrak{M}\Delta N = v_a n_0$ , so that the critical concentration of the ionization centers  $\mathfrak{G}_1$  is given by the following expression:

$$\mathfrak{G}_1 = \frac{3\pi}{8} v_a \tau_0 \{ \exp\{(J - v_a - v_{\mathcal{D}_e})\tau_0\} - 1 \}^{-1}. \quad (24)$$

Given the fact that in the considered situation  $J \gtrsim v_a + v_{\mathcal{D}_e}$  and  $v_a \tau_0 \gtrsim 1$ , the expression (24) could be simplified as follows

$$\mathfrak{G}_1 \approx \frac{3\pi}{8} v_a \tau_0 \exp\{-(J - v_a - v_{\mathcal{D}_e})\tau_0\} \approx 5 \cdot 10^{-2}. \quad (25)$$

Then using definition (21) for the critical rate of ionization centers appearance  $\mathfrak{M}_1$  we get

$$\mathfrak{M}_1 = \frac{2\mathfrak{G}_1}{\pi^2 r_0^3 \tau_0} \approx 10^{12} \text{ m}^{-3} \text{ s}^{-1}. \quad (26)$$

It is necessary to state that the generation threshold rate (26) is simply inaccessible in thundercloud situation.

This is so indeed when we consider the free electron generation without regard of negative ions. The

solution is prompted by practice of stationary glow discharges in electronegative gases [70]. It turns out that during a quasi-stationary development of the glow discharge on time interval exceeding the time of spark discharge development, active particles are accumulated that destroy negative ions, liberating the captured electrons. The detachment processes partially compensate the effect of attachment and thereby reduces the electrons losses. Thus, the electrons that appeared in the ionization centers very quickly proceed due to attachment process to a kind of depository, represented by the community of negative ions, which in turn, over times of the order of the inverse frequency of detachment  $v_d$  become free electrons sources.

To date, there is a certain lack of data on the nature and number of active particles, causing the destruction of negative ions in the specific discharge conditions. Existing estimations are obtained by matching the calculations of discharge parameters with discharge measurements. This analysis [70] allows us to estimate the rate constant of detachment  $k_d$ , calculated for one molecule, in accordance with the following definition:

$$\left(\frac{\partial n_e}{\partial t}\right)_d = -\left(\frac{\partial n_n}{\partial t}\right)_d = v_d n_n = k_d N n_n. \quad (27)$$

The value of  $k_d$  is less sensitive to gas pressure than the frequency  $v_d$  and makes  $k_d \approx 10^{-20} \text{ m}^3 \text{ s}^{-1}$ . For normal conditions  $N \approx 2.7 \cdot 10^{25} \text{ m}^{-3}$ , and we obtain  $v_d \approx 2,7 \cdot 10^5 \text{ s}^{-1}$ , which is nearly four hundred times lower than the attachment frequency.

To account for the discussed effects, we consider the following system

$$\begin{aligned} \frac{\partial n_e}{\partial t} &= (v_i(\mathbf{r}, t) - v_a - v_{\mathcal{D}_e})n_e + v_d n_n - \beta_{ep} \bar{n}_p n_e \\ \frac{\partial n_n}{\partial t} &= v_a n_e - v_d n_n - \beta_{np} \bar{n}_p n_n, \end{aligned} \quad (28)$$

where  $n_n$  is the concentration of negative ions;  $v_d$  is the electrons detachment frequency:  $v_d \lll v_a$ ;  $\beta_{ep}$  is the coefficient of electron-ion recombination;  $\beta_{np}$  is the coefficient of ion-ion recombination;  $\bar{n}_p$  is the background level of positive ions concentration; also we temporarily neglect diffusive and advective losses of electrons and ions (we go into details below). The background level of ion concentration in the atmosphere under normal conditions, is only  $10^9 \text{ m}^{-3}$  [70] and is not higher than  $10^{11} \sim 10^{12} \text{ m}^{-3}$  even in the afterglow of streamer discharge in air according to [72]. The coefficients of electron-ion recombination  $\beta_{ep}$  and ion-ion recombination  $\beta_{np}$  are comparable with each other and make approximately  $10^{-13} \text{ m}^3/\text{s}$ .

With a weak background of positive ions the negative ions are destroyed in detachment acts faster than through the recombination process  $v_d \gg \beta_{np} \bar{n}_p$ . Then, according to the second equation in the system (28), an approximate dynamic equilibrium between attachment and detachment processes is established:

$$v_a n_e \approx v_d n_n. \quad (29)$$

The ratio of the electrons and ions concentrations remains approximately constant, although the concentrations themselves may vary considerably. In such conditions with relation (29) taking into account we get:

$$\frac{\partial n_e}{\partial t} = (v_i(\mathbf{r}, t) - v_{\mathcal{D}_e} - \beta_{ep} \bar{n}_p) \cdot n_e. \quad (30)$$

By analogy with the consideration of equation (17) in the frame of the mean field approximation the generation threshold in equation (30) could be carried out:

$$\mathfrak{G}_2 = \frac{3\pi}{8} \beta_{ep} \bar{n}_p \tau_0 \left\{ \exp \left\{ (J - v_{\mathcal{D}_e}) \tau_0 \right\} - 1 \right\}^{-1}. \quad (31)$$

With taking into account relation  $J\tau_0 \gtrsim 1$  the last expression could be simplified

$$\mathfrak{G}_2 \approx \frac{3\pi}{8} \beta_{ep} \bar{n}_p \tau_0 \cdot \exp \left\{ - (J - v_{\mathcal{D}_e}) \tau_0 \right\} \approx \frac{\beta_{ep} \bar{n}_p}{v_a} \cdot \exp \left\{ -v_a \tau_0 \right\} \mathfrak{G}_1 \approx 5 \cdot 10^{-10} \quad (32)$$

Than for the corresponding critical rate of the appearance of ionization centers  $\mathfrak{M}_2$  we get

$$\mathfrak{M}_2 = \frac{2\mathfrak{G}_2}{\pi^2 r_0^3 \tau_0} \approx 10^4 \text{ m}^{-3} \text{ s}^{-1}. \quad (33)$$

The low threshold of the exponential growth of negative ions leads through the detachment process to a significant drop in the generation threshold of free electrons and, consequently, to a significant drop in thundercloud breakdown field.

## 2.6 Mutual Influence of Ionization Centers (cumulative effect)

To this point the assumption has been made that various centers of ionization are independent of each other and the calculation of the generation thresholds (26) and (33) has been carried out in the framework of the mean-field approximation. However, in the expressions (24) and (31) we do not take into account correlation effects. Actually, each ionization center leaves behind a higher (electron and/or negative ion) density stain. If two ionization centers were randomly placed close enough to each other in space and in time, there emerges a supplementary concentration increase in addition to the independent growth of the electron and/or negative ion concentration in the two centers. This addition appears due to the fact that the exponential increase of electrons and/or negative ion at the second center begins not from the concentration average over space at the current time, but from the higher spot of the electron and/or negative ion concentration that has survived from the first centre.

Let us estimate the spatio-temporal volume  $\mathfrak{S}$  occupied by the higher concentration stain left by a single ionization center. The value  $\mathfrak{S}$  is approximately equal to the product of time  $\tau^*$  during which the concentra-

tion stain remains noticeable against the background, over the volume of the spatial region occupied by the stain at this time. When we separately analyze equation (17) we consider the free electron generation without regard to negative ions. In that case the concentration stain remains significant against the background during the time interval, which is, as an order of magnitude, equal to the inverse attachment frequency  $\tau^* \approx \tau_e^* \approx \nu_a^{-1}$ . In turn, the volume occupied by the electron concentration stain by the time  $\tau_e^*$ , is determined by the appropriate diffusion length, i. e. size  $L_e \approx \sqrt{\mathcal{D}_e \tau^*} \lesssim r_0$  [64]. Whereas the spatio-temporal size of electron concentration stains remains approximately the size of the ionization center  $\mathfrak{S} = \frac{\pi^2}{2} L_e^3 \tau_e^* \approx \frac{\pi^2}{2} r_0^3 \tau_0 \simeq 10^{-13} \text{ m}^3 \text{ s}$ , spatio-temporal size of ions density spots is much higher than that of the center of ionization. This happens due to the huge lifetime of the negative ions  $\tau_n^* \gtrsim 1 \text{ ms}$ . Correspondingly when we analyze the system (28) the negative ions lifetime defines the appropriate diffusion length, i. e. size  $L_n \approx \sqrt{\mathcal{D}_n \tau_n^*} \gg r_0$ . Thus for the spatio-temporal volume  $\mathfrak{S}$  occupied by the negative ions density spot we get

$$\mathfrak{S} = \frac{\pi^2}{2} L_n^3 \tau_n^* = \frac{\pi^2}{2} \mathcal{D}_n^{3/2} \tau_n^{5/2} \gg \frac{\pi^2}{2} r_0^3 \tau_0. \quad (34)$$

Substituting values  $\mathcal{D}_n \simeq 1 \text{ m}^2 \text{ s}^{-1}$  and  $\tau_n^* \gtrsim 1 \text{ ms}$  we have  $L_n \approx 1 \text{ dm}$  and  $\mathfrak{S} \simeq 10^{-5} \text{ m}^3 \text{ s}$ . While longitudinal displacement of the spots is determined by the ion drift in the external electric field  $\mathbf{E}_a$  and makes  $\tau_n^* \cdot |\mathbf{V}_{an}| \approx 1 \text{ dm}$ . Figure 1 schematically illustrates a two-dimensional space-time domain that contains ionization centers and the ion density spots produced by them. For a spatial coordinate we use vertical axis  $z$

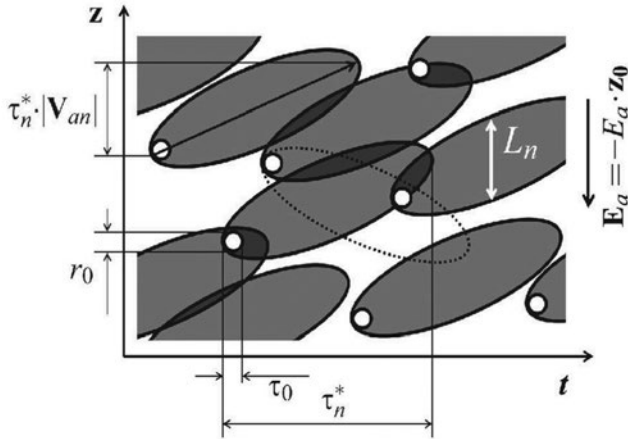


*Figure 1: Two-dimensional schematic representation of the ion density spots. Whereas the small white circles correspond to the ionization centers, the gray ellipses correspond to the spots of ion density. The ellipses are stretched along the direction  $\mathbf{z} = -|\mathbf{V}_{an}| \cdot t$ . An ellipse conducted by a dotted line corresponds to a spot density of positive ions and is stretched along the direction  $\mathbf{z} = -|\mathbf{V}_{ap}| \cdot t$ .*

assuming that the external electric field is directed vertically  $\mathbf{E}_a = -E_a \cdot \mathbf{z}_0$ , where  $\mathbf{z}_0$  is vertical unit vector.

The generation threshold in the framework of the system (3) – (5) is determined by the appearance of connected component in the ensemble of overlapping spots of the residual electron density. It must be emphasized that we are talking about the spots overlapping in the space-time continuum. The dimensionless concentration of spots is determined by the following expression:

$$\mathfrak{V} = \mathfrak{S} \mathfrak{M} = \frac{\pi^2}{2} \mathcal{D}_n^{3/2} \tau_n^{5/2} \mathfrak{M}. \quad (35)$$

The connectedness in the ensemble of overlapping ion density spots is the essential characteristic of the percolation phase transition when the dimensionless concentration of spots  $\mathfrak{V}$  reaches the critical value (see Appendix Appendix B for details):

$$\mathfrak{V}_c \simeq 0.1. \quad (36)$$

Then for the correspondent critical rate of ionization centers appearance  $\mathfrak{M}_3$  we obtain

$$\mathfrak{M}_3 = \frac{\mathfrak{V}_c}{\mathfrak{S}} = \frac{2\mathfrak{V}_c}{\pi^2 L_n^3 \tau_n^*} \approx 10^2 \text{ m}^{-3} \text{ s}^{-1}. \quad (37)$$

We see that the critical rate of ionization centers appearance is significantly reduced with allowance made for the correlation effects. The result obtained reveals the deep relationship of physics to geometry: the generation threshold drop appears due to the emergence of a cluster of overlapping ion density spots. Herewith for the dimensionless concentration of the ionization centers we get

$$\mathfrak{S}_3 = \frac{r_0^3 \tau_0}{L_n^3 \tau_n^*} \mathfrak{V}_c \simeq 5 \cdot 10^{-12}. \quad (38)$$

### 2.7 Occurrence rate of above-critical electric field enhancements

The positive streamers initiation mechanism we discuss in this study advantageously differ from the other ones because it only demands the rate of occurrence of ion production centers per unit time in a unit volume exceeding the critical level  $10^{-1} \text{ m}^{-3} \text{ s}^{-1}$  that is easily achieved in a typical thundercloud. There are a number of publications in which collision rates based on in-situ measurements and modeling are presented. Note that the collision rate is proportional to the product of concentrations of colliding particles (usually millimeter-scale graupel and small ice crystals or snow) and cross-sectional area and fall speed of larger particles (graupel), e.g., Ziegler et al. [84]. Gardiner et al. [22] reported a collision rate of  $25 \text{ m}^{-3} \text{ s}^{-1}$  for large graupel and small ice crystals, observed in a small isolated thunderstorm in Montana. A similar collision rates, up to  $30 \text{ m}^{-3} \text{ s}^{-1}$ , were reported for graupel and snow by Ziegler et al. ([84], Fig. 17), who compared measurements during the early stage of a thunderstorm in New Mexico with predictions of their cloud electrification model. At their maximum rate, the computed mean diameter of snow

reached about 0.3 mm and that of graupel was about 2 mm. Further, Ziegler and MacGorman [85], (p. 841 and Fig. 5) reported a graupel-snow collision rates of 50-250  $\text{m}^{-3}\text{s}^{-1}$  for a tornadic storm.

Ziegler et al. [84], p. 12,848 reported very high observed ice particle concentrations, about 1000 per liter, that were not consistent with their model predictions. Such high ice concentrations are expected to yield very high collision rates, several orders of magnitude higher than their model values of up to 30  $\text{m}^{-3}\text{s}^{-1}$ . Authors of [84] interpreted this difference as being due to their data containing a large fraction of ice particles smaller than a few hundred micrometers in diameter, which apparently do not significantly contribute to charge transfer in collisions. It is not clear if collisions of the smaller ice particles produce corona (most of the laboratory data are for water drops with diameters exceeding 150  $\mu\text{m}$  or so).

Dye et al. [18], who studied the initial stage in two small thunderstorms in New Mexico, reported hydrometeor collision rates exceeding  $10^2 \text{ m}^{-3}\text{s}^{-1}$  (see their Fig. 9) and up to about  $10^3 \text{ m}^{-3}\text{s}^{-1}$  (see their Fig. 8). In the latter case, ice particle concentrations up to several thousand per liter were observed (particles larger than about 50  $\mu\text{m}$  in diameter were detectable). The authors noted potential problems with the measurements and adjusted the collision rates presented in their Fig. 8 (and probably in Fig. 9), which we cited above, in an attempt to account for possible overestimation of particle concentrations.

It is important to emphasize that the above estimates of the occurrence rate  $\mathfrak{M}$  of small-scale supercritical enhancements of thundercloud electric field, were obtained taking into account only pairwise interactions of hydrometeors. The pairwise approach implies a relatively low probability of triple interactions:

$$\frac{4\pi}{3}r_0^3n_h \ll 1, \quad (39)$$

where  $n_h$  is the density numbers of small particles,  $r_0$  is, recall, the radii of big particles. However, the role of the interaction of large hydrometeors with small hydrometeors increases, with the characteristic distance between them  $n_h^{-1/3}$  being of the same order of magnitude as the size of large hydrometeors:  $\frac{4\pi}{3}r_0^3n_h \gtrsim 1$ . In this case, multi-body interactions become more probable compared to the pairwise ones. As a result, the rate of occurrence of small-scale supercritical enhancements of electric field greatly increases. Another important source of rise in the rate of occurrence of electric field small-scale enhancements is represented by fluctuations of hydrometeor number density caused by turbulent mixing discussed in [39].

### 3. DISCUSSION

Despite centuries of scientific efforts, many of the fundamentals of lightning physics remain still enigmatic.

The main difficulty lies in capturing the lightning initiation problem. It appears that the maximum values of the large-scale electric fields likely to be observed in thunderclouds are of insufficient magnitude to explain the lightning production [61]. This fact makes the lightning initiation a question as one of the most intriguing problem of thunderstorm electricity.

The proposed mechanism relates the lightning discharge initiation with the peculiarities of the thundercloud electric field, which can be represented by a sum of two components. The first, quasi-regular component is caused by large-scale convective dynamics, and its values at different altitudes in a thundercloud can be characterized by amplitude  $E_a/N$  reduced by the concentration of air molecules  $N$  (for normal conditions  $N \approx 2,7 \cdot 10^{25} \text{ m}^{-3}$ ). The maximum measured amplitudes reach values of  $E_a/N \approx 9 \text{ Td} = 9 \cdot 10^{-21} \text{ Vm}^2$  that is an order of magnitude less than the electric strength of air. Despite the fact that the ambient field is substantially at sub-threshold  $E_a \ll E_b$  it plays a crucial role in the discharge initiation. First, the field  $E_a$  increases the quasi-electrostatic noise intensity, stimulating the induction mechanisms of hydrometeors charging. Secondly, the field  $E_a$  significantly reduces the recombination losses of the interacting component so long as advective spots of positive ions drift in the opposite direction in comparison with the density spots of electrons and negative ions. The second, stochastic component of the electric field is caused by small-scale fluctuations of the collective field of charged hydrometeors. The fine-scale electric field produced by charged hydrometeors leads to the emergence of centers of ionization and provide a stochastic drift of electrons and ions.

In this paper we argue that the stage (ii) of lightning stroke evolution that involves local enhancement of the electric field to produce streamers and to support their extension is associated with the generation of highly conductive regions. We named the regions as elevated-conductivity areas. These elevated-conductivity areas appear due to the stochastic electric field of charged hydrometeors. Above-critical bursts of the stochastic field provide the survival of the free electrons in conditions when the RMS level of the stochastic field is significantly less than the air electric strength.

The considered appearance of those elevated-conductivity areas has several characteristic features that distinguish it from other mechanisms of lightning initiation. First, due to interaction of electron and ion components the dynamic implementation of this transition is stretched in time interval, which significantly exceeds the development time of ordinary spark discharge. In this case the rapid attachment of electrons is balanced by the processes of their liberation during negative ions destruction. Thereby the account for the detachment effects leads to a significant drop in the free electron generation threshold in the system discussed. Secondly, ions drift in the stochastic electric field plays

a significant role in the transition kinetics. From a formal mathematical point of view, this stochastic drift is indistinguishable from advection of a scalar impurity in a turbulent flow. It is shown that the effectiveness of "advective mixing" for a few degree surpasses the efficiency of conventional diffusion. Noise-induced step-wise growth in the density of ions and free electrons is limited to spatial-temporal clusters that have a fractal structure and covering, therefore, a very small proportion of the actual space-time area. As a result in the considered gradual transition the average conductivity of the medium does not significantly change.

Upon completion of the stage (ii) the process of ionization in the elevated-conductivity areas is determined by the sum of the external field with an induced field of plasma spots in the elevated-conductivity areas. We suggest that elevated-conductivity regions can produce streamer discharges easier than hydrometeors, due to higher polarization charge and field enhancement at their tips. The proposed mechanism of the elevated-conductivity areas appearance provides both amplification of the local electric field in a thundercloud, and self-consistent support of the discharge process under the conditions when the free electrons attachment dominates over their production in ionization process.

As follows from the expressions (4) the output of electrons and ions from the generation area is carried out through the following two mechanisms: because of diffusion flow and flux due to the drift in a stochastic field, whose average magnitude coincides with that of the ambient (external) electric field in the considered cloud region  $\mathbf{E}_a = \langle \mathbf{E}(\mathbf{r}, t) \rangle$ . The drift in the stochastic electric field  $\mathbf{E}(\mathbf{r}, t)$  can be considered as a diffusion process with diffusion coefficient  $D \simeq r_0 \langle \mathbf{V}_e^2(\mathbf{r}, t) \rangle^{1/2}$ , which is many times greater than the diffusion coefficient of electrons:  $\langle \mathbf{V}_e^2(\mathbf{r}, t) \rangle^{1/2} \simeq 10^5$  m/s,  $r_0 \simeq 10^{-2}$  m and  $D \simeq 10^3$  m<sup>2</sup>/s. Therefore, the drift mechanism is much more efficient: during the same time interval, the drift in the stochastic field moves electrons to a distance by two orders of magnitude higher than the normal diffusion. In our case, the advected charged "substance" has a strong effect on the "turbulent" flow itself, by generating local electric fields.

An interesting feature of the mechanism under consideration is the growth of the scales of strong-field regions, and hence the scales of the discharge activity, which precedes the appearance of lightning. In the beginning, the process is determined by supercritical bursts of the stochastic field of charged hydrometeors with characteristic dimensions about and less than 1 cm, then spots of ionic concentration with an effective advective spreading length of about decimetres are involved in the game. It is over the scales  $d$  of the order of a decimeter that a spark breakdown mechanism ( $pd > 4,000$  torr/cm, where  $p$  is the air pressure) begins to work, whereas over the scales of the order of 1 cm the Townsend mechanism is realized [70].

### 3.1 Streamer Formation and Branching from Elevated-Conductivity Regions

The advantage of our lightning initiation scheme is that it organically includes both necessary electric field amplification and sufficient pre-ionization level, which can be realized in a typical thundercloud without any extreme assumptions. In the framework of our approach, the presence of seeding electrons is provided by their detachment from negative ions composing negative ion spots. Electric field overshoots responsible for positive streamers initiation are connected with interactions of ion domains with hydrometeors or with each other and can be realized by a large number of ways, most probable of which are specified below.

Firstly, it may be the case that positive streamers initiation starts from a positive or at the close vicinity of a negative ion spot. It was shown that ion spots evolution may lead to formation of positive and negative ion clusters with peak concentration up to  $10^{17}$  m<sup>-3</sup>. It's clear that such an ion elevated concentration burst amplifies an ambient electric field up to the level when it can trigger an electron avalanche (there is always some amount of free electrons around ion spots provided primarily by their detachment from negative ions). In the case of a negatively charged spot positive streamers enter its interior and, as the ratio of detachment frequency to attachment one dramatically increases for strong electric fields, provoke explosive detachment of electrons from negative ions (the peak value of electric field at a streamer head is at least an order of magnitude greater than the conventional breakdown field). Most likely, this scheme starts to work at ion concentrations, which are much less than mentioned above  $10^{17}$  m<sup>-3</sup>.

Secondly, it may be the case that positive streamers fill the gap between a pair of oppositely charged ion spots. As positive and negative ion spots continuously drift in a local electric field, there must be the cases when two oppositely charged ion domains come together. Then, if they are charged strong enough and (not necessarily) properly posed with respect to an ambient electric field direction, they may initiate positive streamers growing from a positive spot towards a negative one, which facilitates their further development. Note that in this case seeding electrons arise due to the electrons detachment from negative ions of the negative ion spot.

In the third place it may be the case that positive streamers initiation starts from a hydrometeor surface in the presence of an ion spot. Regardless of presence or absence of surface charge, a hydrometeor polarizes at an ambient electric field. It gains additional polarization when approaching a positive or negative ion spot, which may be sufficient to emanate positive streamers from the hydrometeor surface. Note that, as it was mentioned above, streamers viability increases if a hydrometeor approaches a negatively charged ion spot.

Finally, it may be the case that positive streamers initiation starts from a hydrometeor passing between a pair of oppositely charged ion spots. This modification of the previous scheme is even more probable because electric field amplification between a pair of oppositely charged ion domains in the case, when they are properly oriented with respect to an ambient electric field direction, is bigger than in the case of a single ion spot.

### 3.2 Illustrative Example

We consider the thundercloud area with linear dimensions of the order of several meters, i.e. with dimensions perfectly acceptable to initiate lightning, and at the same time compact enough to consider the external field  $\mathbf{E}_a$  as homogeneous one. The full electric field in the considered region can be represented as a sum of two summands  $\mathbf{E}(\mathbf{r}, t) = \mathbf{E}_a + \mathbf{E}_h(\mathbf{r}, t)$ , the second of which represents a strongly inhomogeneous field of charged hydrometeors.

As can be seen from Figure 2, advective spots of positive and negative ions, blurred synchronously in time from one ionization center, diverge in space in the opposite directions along and against the direction of the external field  $\mathbf{E}_a$ . This increases the contrast of the positive  $n_p$  and negative  $n_n$  ion densities and thus reduces the efficiency of both the ion-ion recombination and the electron-ion recombination.

The model system time evolution is represented in Figure 3. Assuming that the negative ions are destroyed in acts of detachment much faster than recombine,  $v_d \gg \beta_{np}n_p$ , it is possible to conclude that the system gradually evolves to the dynamic equilibrium between attachment and detachment processes when the ratio in the electron and ion densities goes to a constant level despite their local variations

$$\frac{n_n}{n_e} \approx \eta = \frac{v_a}{v_d}. \quad (40)$$

Thus, the ion component itself becomes a source of free electrons. As already noted, the presence of water molecules leads to the formation of hydrated clusters with  $\text{NO}_3^-(\text{H}_2\text{O})_n$  [72], which complicates the destruction of negative ions, because with increasing coordination number of the ion  $\text{NO}_3^-(\text{H}_2\text{O})_n$ , the rate of detachment from the cluster is reduced [19]. To demonstrate the robustness of the suggested mechanism we additionally used in calculations the parameter value  $\eta = 10^5$  that is much greater than the estimation  $\eta \approx 370$ , following from the definition (27).

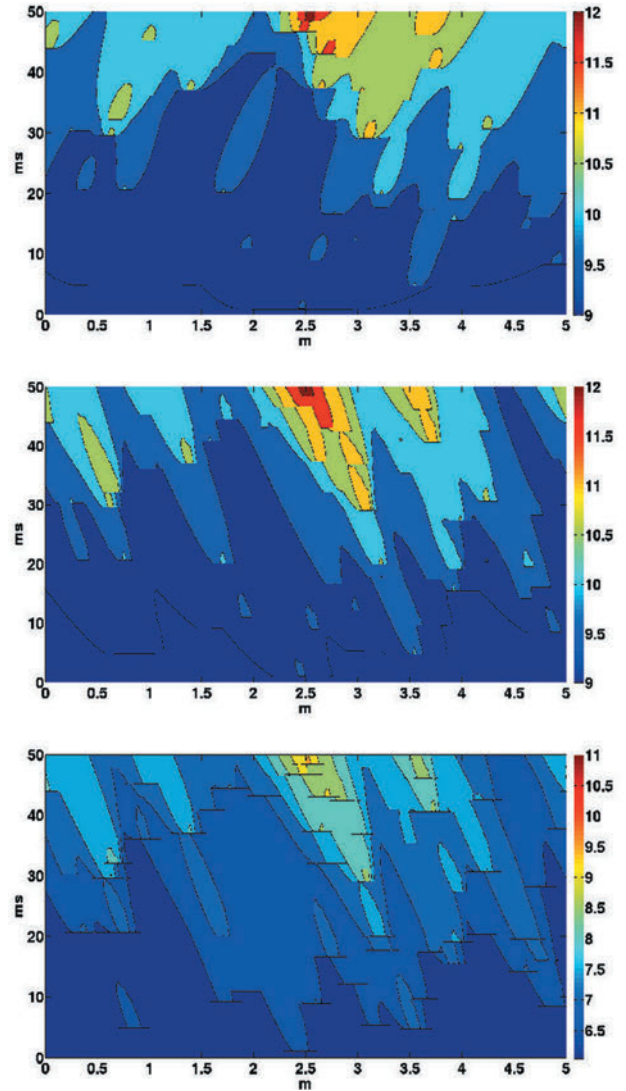


Figure 2. Ion and electron concentration spatiotemporal evolution of the model system: the top panel corresponds to the positive ions, the middle panel corresponds to the negative ions and the bottom panel corresponds to the electrons. The color shows the level of the concentration common logarithm. The vertical axis represents the time; the horizontal axis corresponds to the spatial coordinate. An external electric field is oriented in the positive direction of the spatial axis.

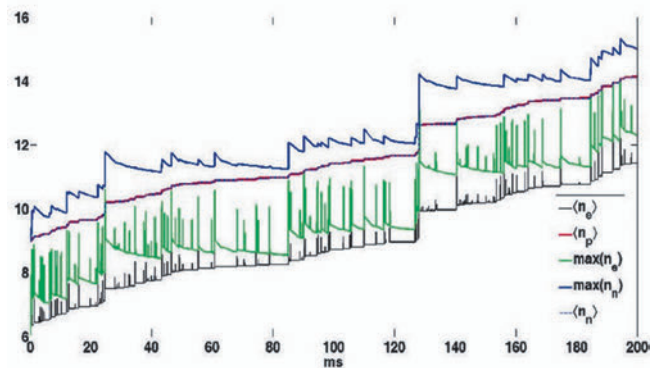


Figure 3. The time evolution of the decimal logarithm values of space average and space maximum of electron and ion concentrations. The concentration of the model system is presented as number per cubic meter.

APPENDIX A. ELECTRIC FIELD FLUCTUATIONS  
PRODUCED BY CHARGED HYDROMETEORS

It is common knowledge that the intracloud electrification process is extremely complex and intricate. Since charges of intracloud particles are the balanced sum of many unobserved random events, the central limit theorem (in its common form) provides a partial explanation for the prevalence of particle charge normal distribution. Therefore one may consider an ensemble of intra-cloud particles as a gas of point charges  $q$  with normal charge distribution function

$$P(q) = \frac{1}{Q\sqrt{2\pi}} \exp\left(-\frac{1}{2}\left(\frac{q}{Q}\right)^2\right), \quad (\text{A1})$$

where the charge distribution average  $\bar{q} = \langle q \rangle \neq 0$  and the charge distribution variance (the charge distribution mean square displacement)  $Q = \langle q^2 \rangle^{1/2}$  may vary in time and space.<sup>1</sup> We start with the assumption that the particles are uniformly distributed in space. The corresponding volume charge density of hydrometeors  $\rho(\mathbf{r}, t)$  can be considered as spatial white noise, which slowly (compared to  $v_a^{-1}$ ) varies in time and satisfies the following ratios:

$$\begin{aligned} \langle \rho(\mathbf{r}_1, t) \rho(\mathbf{r}_2, t) \rangle &= (Q(t))^2 N_h(t) \cdot \delta(\mathbf{r}_1 - \mathbf{r}_2), \\ \langle \rho(\mathbf{r}, t) \rangle &\neq 0, \end{aligned} \quad (\text{A2})$$

where  $N_h$  is the cloud particles concentration and  $\delta(\mathbf{r})$  is Dirac delta function (the product  $Q^2 N_h$  is the spatial white noise source intensity). The second of the relations (A2) characterizes the features of thundercloud large-scale electrical structure. Updrafts drive the less heavy ice crystals upwards, causing the cloud top to accumulate increasing positive charges. While, the gravity causes the heavier negatively charged graupel to fall toward the middle and lower portions of the cloud, building up increasing negative charges. One may consider the intracloud space density of electric charge as a superposition of an irregular part that fluctuates randomly in space and a regular component that depends on altitude. This superposition leads to the formation of charge density vertical profile, which satisfies the self-consistent distribution of the large-scale thundercloud electric field, named ambient field.

The potential of electric field produced by a distribution of charges given by the volume charge density  $\rho(\mathbf{r})$  is obtained by the solution of the Poisson equation  $\nabla^2 \varphi = -\rho(\mathbf{r})/\epsilon_0$ , which, in the dimension of  $d = 3$ , is a superposition of  $1/r$  functions weighted by the source function  $\rho(\mathbf{r})$ :

$$\varphi(\mathbf{r}) = \frac{1}{4\pi\epsilon_0} \int d^3 r' \frac{\rho(\mathbf{r}')}{|\mathbf{r} - \mathbf{r}'|}, \quad (\text{A3})$$

<sup>1</sup>One obtains the same result using either a homogeneous distribution  $P(q) = \frac{1}{2\sqrt{3}Q} - \sqrt{3}Q < q < \sqrt{3}Q$  or a binary one  $P(q) = \frac{1}{2}\delta(q+Q) + \frac{1}{2}\delta(q-Q)$  instead of Gaussian charge distribution

where  $G(\mathbf{r}, \mathbf{r}') = -\frac{1}{|\mathbf{r} - \mathbf{r}'|}$  is the Green function of the Poisson equation.

The ensemble averaging can be performed easily and one obtains that the first moment of potential is  $\langle \varphi(\mathbf{r}) \rangle = 0$ . But the second moment is

$$\langle \varphi(\mathbf{r}_1) \varphi(\mathbf{r}_2) \rangle = \left(\frac{Q}{4\pi\epsilon_0}\right)^2 N_h \cdot \int d^3 r' \frac{1}{|\mathbf{r}_1 - \mathbf{r}'|} \frac{1}{|\mathbf{r}_2 - \mathbf{r}'|}.$$

Therefore, the potential average square is

$$\langle \varphi^2(\mathbf{r}) \rangle = \left(\frac{Q}{4\pi\epsilon_0}\right)^2 N_h \cdot \int d^3 r' \frac{1}{|\mathbf{r} - \mathbf{r}'|^2} = \frac{1}{4\pi} \left(\frac{Q}{\epsilon_0}\right)^2 N_h \cdot r$$

and finally we obtain the root-mean-square value of potential of the following power-law asymptotic behavior:

$$\langle \varphi^2(r) \rangle^{1/2} = \frac{Q}{2\sqrt{\pi\epsilon_0}} \sqrt{N_h r}. \quad (\text{A4})$$

In fact, intracloud particles are not point charges, but have finite sizes. It means that Eq. (A4) remains valid at a distance  $r$  that considerably exceeds a typical particle size  $a$ :  $r \gg a$  (we also bring in mind that  $a \ll N_h^{-1/3}$ ). Since typically  $Q \simeq 10^{-11}$  Q and  $N_h \simeq 10^8$  m<sup>-3</sup>, so that the potential difference fluctuations over an in-cloud linear size  $r \simeq 1$  km reaches the value 100 kV as order-of-magnitude.

Due to the hydrometeors movement and interaction the potential relief  $\varphi(\mathbf{r}, t)$  evolves in time. The above calculations are valid under following quasi-static conditions, when  $Q \left(\frac{\partial Q}{\partial t}\right)^{-1} \gg \frac{L}{c}$ , and  $\frac{N_h^{-1/3}}{u} \gg \frac{L}{c}$  where  $L$  is the characteristic size of the storm cell,  $u$  is the characteristic velocity of the turbulent flow of hydrometeors, and  $c$  is the speed of light. These conditions imply that both the characteristic time of hydrometeors charging and their configuration switching time far exceed the time of propagation of electromagnetic signal through the storm cell. Apart from that, the particles configuration switching time is much less than the Maxwell relaxation time ( $\epsilon_0/\sigma \gtrsim 1$ ,  $\sigma$  is the conductivity of the medium) of charges in the cloud that allows us to neglect both the conduction current and Debye screening of charged hydrometeors.

Similar calculations allow us to estimate the level of electric field fluctuations  $\mathbf{E}(\mathbf{r}, t)$  as a function of spatial scale  $r = |\mathbf{r}|$ .

$$\delta E(r) = \frac{Q}{2\sqrt{\pi\epsilon_0}} \sqrt{\frac{N_h}{r}}. \quad (\text{A5})$$

It is seen that fluctuations of the electric field (A5) depending on the absolute values of the characteristic charge and concentration of hydrometeors, show a power-law distribution and a very slow fall in space with critical exponent  $-1/2$ .

However, the expression (A5) does not account for the effects of clustering of hydrometeors in a turbulent flow of the air environment [42, 43]. From a geometrical point of view, clustering leads to preferential distribution of particles on a fractal subset of three-dimensional space with a fractal dimension  $d_f < 3$ . The formation of clusters in this case is a purely kinematic effect. It is obvious that this feature of particle dynamics completely disappears under averaging over the ensemble of realizations of random velocity fields. However, clustering is of fundamental importance in the lightning initiation, since the kinematic pattern of the hydrometeors distribution remains nearly unchanged at the time of discharge development. Following [9] one can use as fractal subset the skeleton of a vortex cluster with fractal dimension  $d_f \approx 5/3$ . Based on the law of similarity in the distribution of the turbulent eddies in the storm cell with linear size  $L$  we can link the perturbations of hydrometeors density  $\tilde{N}_h$  with its average value of  $N_h$ :

$$\tilde{N}_h \left( \frac{L}{r_0} \right)^{d_f} \approx N_h \left( \frac{L}{r_0} \right)^3. \quad (\text{A6})$$

To account for the hydrometeors clustering effect in the turbulent flow it is necessary to use in the expression (A5) the value of the perturbed density  $\tilde{N}_h$  (A6) instead of the average density of hydrometeors  $N_h$ . Then the estimation of the electric field fluctuations takes the following form

$$\delta E(r) = \frac{Q}{2\sqrt{\pi}\epsilon_0} \sqrt{\frac{N_h}{r}} \cdot \left( \frac{L}{r_0} \right)^{\frac{3-d_f}{2}}. \quad (\text{A7})$$

Let us estimate the volume fraction of the space-time domain occupied by a supercritical field, assuming that the amplitude of Cartesian component of small-scale electric field is normally distributed with a variance of  $E_s$ :

$$dw(\mathbf{E}) = \frac{1}{(2\pi)^{\frac{3}{2}} E_s^3} \exp \left\{ -\frac{E_x^2}{2E_s^2} - \frac{E_y^2}{2E_s^2} - \frac{(E_a - E_z)^2}{2E_s^2} \right\} dE_x dE_y dE_z. \quad (\text{A8})$$

The value  $E_a$  is an average electric field amplitude in the area of thunderstorm  $\mathbf{E}_a = E_a \cdot \mathbf{z}_0 = \langle \mathbf{E}(\mathbf{r}, t) \rangle$ . Transition to spherical coordinates centered at the point  $(0; 0; E_a)$  gives the following distribution of absolute value  $E$  of small-scale electric field:

$$dw(E) = \frac{\sqrt{2/\pi}}{E_s^3} \exp \left\{ -\frac{E^2}{2E_s^2} \right\} E^2 dE. \quad (\text{A9})$$

Computing the variance of the distribution (A9),

$$D(E) = \int_0^\infty E^2 dw(E) = \frac{\sqrt{2/\pi}}{E_s^3} \int_0^\infty \exp \left\{ -\frac{E^2}{2E_s^2} \right\} E^4 dE = 3E_s^2, \quad (\text{A10})$$

we find the value of the mean square field at the scale  $r_0$ :

$$E_{rms}^2 = \langle \mathbf{E}^2 \rangle = \langle \mathbf{E} \rangle^2 + D(E) = E_a^2 + 3E_s^2. \quad (\text{A11})$$

The dimensionless concentration of ionization centers  $\mathfrak{C}$ , which represents the volume fraction of the space-time domain occupied by a supercritical field, can be expressed by the fine-scale electric field distribution function (A9):

$$\mathfrak{C} = \int_{E_b}^\infty dw(E). \quad (\text{A12})$$

Accordingly, for the fine-scale electric field RMS amplitude we obtain

$$E_{rms} = \langle \mathbf{E}^2 \rangle^{\frac{1}{2}} = \sqrt{3E_s^2 + E_a^2}. \quad (\text{A13})$$

Let us parameterize the relationship of the distribution (A8) standard deviation  $E_s$  with the value of breakdown field  $E_b$ :

$$E_s \approx E_b/\Upsilon, \quad (\text{A14})$$

and consider that in line with observations  $E_a = E_b/10$ , then

$$E_{rms} = \langle \mathbf{E}^2 \rangle^{\frac{1}{2}} = \sqrt{3E_s^2 + E_a^2} = E_b \cdot \sqrt{3/\Upsilon^2 + 0.01}. \quad (\text{A15})$$

Figure A1 shows the case  $\Upsilon = 5$  for which  $E_{rms} \approx 0.36E_b$  and  $\mathfrak{C} = \int_{E_b}^\infty dw(E) \approx 1.55 \cdot 10^{-5}$ . Slight in-

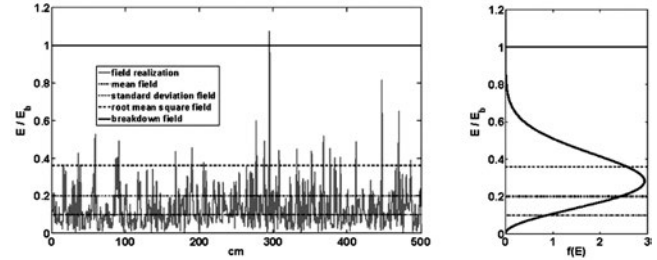


Figure A1. The absolute value of the fine-scale electric field typical implementation, normalized by the value of breakdown field  $E_b$ , and the corresponding distribution of the probability density  $\frac{dw(E)}{dE}$ . The distribution is constructed for the case  $\Upsilon = 5$ .

crease of  $\Upsilon$  leads to a sharp decrease in the dimensionless concentration of ionization centers  $\mathfrak{C}$ . Meanwhile the fine-scale electric field RMS amplitude changes slightly: for example, for  $\Upsilon = 5.54$  we get  $E_{rms} \approx 0.33E_b$  and  $\mathfrak{C} = \int_{E_b}^\infty dw(E) \approx 10^{-6}$ , and for  $\Upsilon = 5.95$  one obtains  $E_{rms} \approx 0.31E_b$  and  $\mathfrak{C} = \int_{E_b}^\infty dw(E) \approx 10^{-7}$ .

Concluding the analysis of the field distribution it is possible to draw the following conclusions. The fine-scale electric field RMS amplitude considerably exceeds the amplitude  $E_a$  of the average field. This has an important implication for the energy balance on a small scale, because the fine-scale electric field RMS amplitude  $\langle \mathbf{E}^2 \rangle^{\frac{1}{2}}$  is responsible for the Joule heating. Another very important conclusion is that the appearance of the ionization center with electric field amplitude  $E \gtrsim E_b$  is the very rarest or, rather an exponentially rare event.

In [59], the approximation of experimental data for the ionization frequency was found, according to which

$$\frac{v_i(E)}{v_a} \simeq \left(\frac{E}{E_b}\right)^\zeta, \quad (\text{A16})$$

where  $\zeta = 5.34$ . In other words, ten times decrease of the uniform electric field in relation to the breakdown level leads to more than five orders decline of ionization frequency in relation to the electron attachment frequency:

$$\langle v_i(E_a)/v_a \rangle = \langle v_i(0.1 \cdot E_b)/v_a \rangle \simeq 4.57 \cdot 10^{-6}. \quad (\text{A17})$$

Now let us find the average of ionization frequency taking into account the electric field fine structure variations. To do this we use along with the parameterization (A14) the distribution density (A9) of absolute value  $E$  of small-scale electric field:

$$\begin{aligned} \left\langle \frac{v_i(\mathbf{r}, t)}{v_a} \right\rangle &= \frac{\sqrt{2/\pi}}{E_s^3} \int_0^\infty \exp\left\{-\frac{E^2}{2E_s^2}\right\} \left(\frac{E}{E_b}\right)^\zeta E^2 dE = \\ &= \frac{(2E_s^2)^{\frac{\zeta+3}{2}}}{\sqrt{2\pi} \cdot E_s^3 \cdot E_b^\zeta} \Gamma\left(\frac{\zeta+3}{2}\right) = \frac{2^{\frac{\zeta+2}{2}}}{\sqrt{\pi}} \Upsilon^{-\zeta} \Gamma\left(\frac{\zeta+3}{2}\right) \end{aligned} \quad (\text{A18})$$

where  $\Gamma(x)$  is gamma function. For  $\Upsilon = 5$  we get  $\langle v_i(\mathbf{r}, t)/v_a \rangle \simeq 0.01$ . The last value is much greater than the estimation obtained in (A17) for homogeneous field.

#### APPENDIX B. BASIC PRINCIPLES AND PREDICTIONS OF PERCOLATION THEORY

In 1957 mathematicians S.R. Broadbent and J.M. Hammersley published an article [57], in which they shared their idea of a possibility to describe a process of coffee flowing through the grounds in a percolator. Their approach was an alternative to a classical diffusion description of one physical substance, conventionally called liquid, flowing in the other, conventionally called medium. In this way a new theory had appeared that later was called a theory of percolation. To be fair, we should mention that originally percolation ideas were first formulated by P.J. Flory [19] as early as 1941 during his study of the processes of polymerization and gelation. Percolation represents the basic model of a structurally disordered medium.

**Lattice Percolation Problem.** Simple lattice problems of the percolation theory may be presented in the following way. Let us consider a square lattice, where each site is occupied with probability  $p$  or is empty with probability  $1-p$  (see Figure B1). The probability  $p$  may be interpreted as concentration of the randomly occupied sites on the lattice. The empty and occupied sites may stand for very different physical properties. For instance, the occupied sites may be considered electrical conductors and the empty sites – insulators. Naturally, we may also assume that electrical current can only flow between nearest-neighbour conductor sites having a common edge. At lower concentrations  $p \ll 1$  the conductor sites are either isolated from each other or form small clusters of nearest neighbour sites. Two conductor sites belong to the same cluster if and only if they are connected by (linked by) a path of nearest-neighbour conductor sites joining them. At  $p \ll 1$  the whole system has dielectric properties, as there are no continuous conductive paths connecting the

lattice has become conductive, since the occupied sites form a giant conductive cluster for electrical current to flow from one side of the system to the other. In the limit of an infinite lattice there exists a well-defined threshold probability  $p_c$  above which there suddenly emerges an infinitely large cluster that spans the system (Fig. B2) and transition occurs from a dielectric phase (at  $p < p_c$ ) to a conductive phase ( $p > p_c$ ). The critical value  $p = p_c$  is called the percolation threshold.

For the square lattice the percolation threshold is about  $p_c \approx 0.59$  (for the cubic lattice the percolation threshold is equal to  $p_c \approx 0.33$ ). The percolation illustrated in Fig. B2 is near the threshold. Contrary to the usual phase transitions occurring at a certain critical

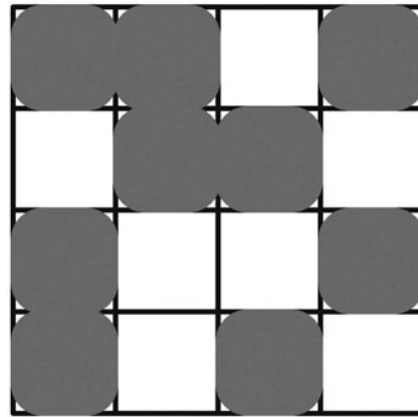


Figure B1: Site percolation problem on a square lattice. Occupied (conductor) sites are marked in grey. Electrical contact exists only between the nearest conductive sites having a common edge.

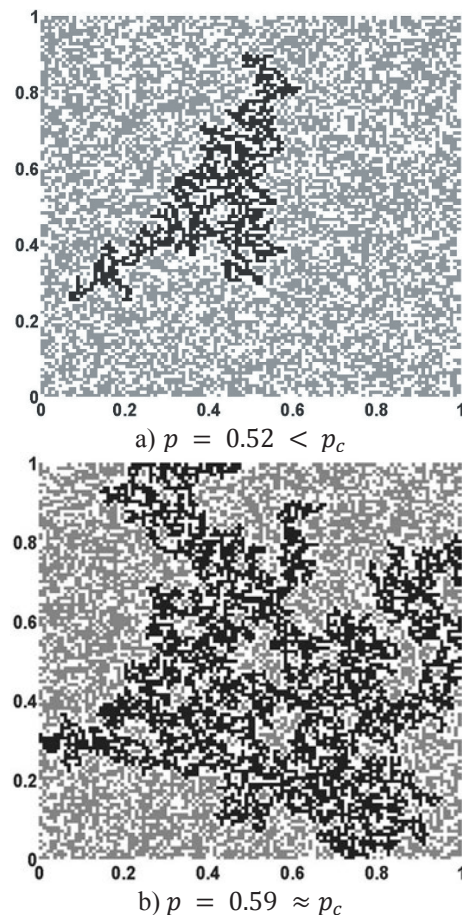


Figure B2: Site percolation on a square lattice: a) the concentration  $p$  of occupied sites is less than the percolation threshold; b) the concentration of occupied sites is equal to the threshold probability  $p_c$ . The sites belonging to the largest cluster are highlighted in black.

**Off-Lattice Percolation Problem.** A simple off-lattice percolation problem may be presented in the following way. Let us assume that equal discs of radius  $R$  are randomly (i.e. chaotically and in average evenly) distributed on a plane. In other words, both coordinates of the discs centres are defined by random numbers uniformly distributed in the interval from zero to  $L$ , where  $L$  is a very large (as compared with  $R$ ) length characterizing the size of the system concerned. An important feature of the problem is that the discs may overlap with one another to any extent. The mean number of the centres of the discs per unit area (discs centres concentration) equals  $\mathfrak{M}$ . Two discs are considered connected, if they have common points, i.e. overlap. If the disc **A** is connected to the disc **B**, and the disc **B** is connected to the disc **C**, then **A** is connected to **C**. Thus, remote discs may be connected by a chain of overlapping discs (Fig. B3). Our task is to find the critical concentration  $\mathfrak{M}_0$  which leads to the percolation through the connected discs, i.e. to the onset of paths running through the entire system and consisting of the overlapping discs. (In other words, there occurs an infinite cluster of connected discs. In Fig. B3 the maximum cluster of the overlapping discs is marked in black). Generally speaking, only two parameters the concentration  $\mathfrak{M}$  and the radius  $R$  have been introduced in to the problem. (Though there is also the size of the system  $L$ , it is clear that if the system is large enough, the critical value  $\mathfrak{M}$  depends little on  $L$ ). Meanwhile, it is easy to see that the absence or presence of the percolation depends just on one parameter, which is the average number of disc centres located within one disc. It is equal to:

$$\mathfrak{G} = \pi R^2 \mathfrak{M}. \quad (\text{B19})$$

One may most easily ascertain that the percolation appears at a certain  $\mathfrak{G}$ -value and does not depend on the values  $\mathfrak{M}$  and  $R$  in the following way. Suppose there is a plane with drawn circles. Let us enlarge the picture several times, for example, with the help of a projector. Altering  $\mathfrak{M}$  and  $R$ , this transformation does not change  $\mathfrak{G}$ , since the average number of the circles centres in a circle does not change with magnification. It is also easy to understand that this transformation has no effect on the percolation. If there was no percolation in the initial image, then it is absent in the magnified one, and vice versa, if the percolation through the overlapped circles existed in the initial image, it would not disappear after magnification. Thus, the magnification, that changes  $\mathfrak{M}$  and  $R$ , but not  $\mathfrak{G}$ , does not control the percolation. Therefore, the presence or absence of the percolation in the system depends only on the  $\mathfrak{G}$ -value. At the large  $\mathfrak{G}$ -values the percolation exists, and at the small values of this parameter there is no percolation.

The problem has thus formulated, and is called a problem of discs or ellipses. Its three-dimensional analogue is called a problem of spheres or ellipsoids and can be formulated as follows. In a three-dimensional space the coordinates of the centres of  $R$ -radius spheres are defined with the help of a random number generator. Two crossing spheres are considered to be connected.

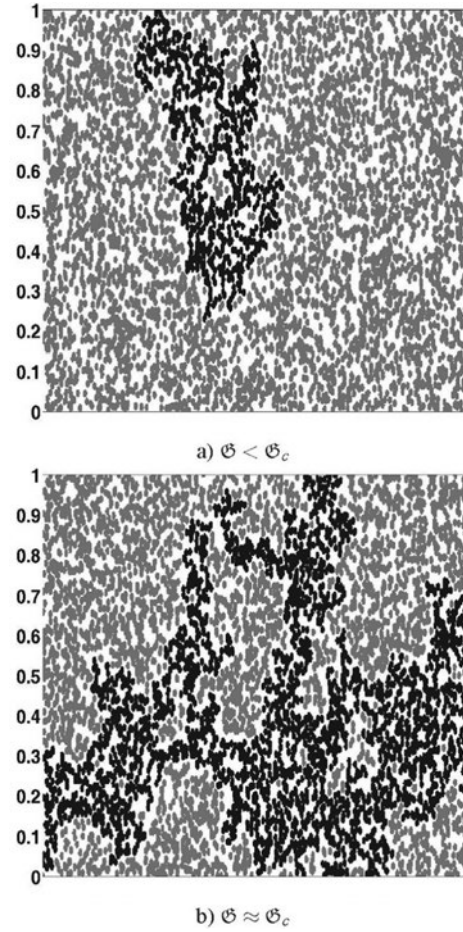


Figure B3: Percolation problem of ellipses: a) dimensionless concentration of ellipses  $\mathfrak{G} = \pi R \parallel R \perp \mathfrak{M}$  is less than critical one; b) dimensionless concentration of ellipses is equal to threshold concentration. The maximum cluster of the overlapping ellipses is marked in black

The task is to define the critical concentration of the centres that leads to the sphere percolation. It is easy to understand that alike the 2-D case the percolation is controlled only by the parameter, which is the average number of sphere centres within one sphere:

$$\mathfrak{G} = \frac{4\pi}{3} R^3 \mathfrak{M}, \quad (\text{B20})$$

or average number of ellipse centres within one ellipse:

$$\mathfrak{G} = \frac{4\pi}{3} R_{\parallel} R_{\perp}^2 \mathfrak{M}, \quad (\text{B21})$$

where  $\mathfrak{M}$  is the average number of spheres/ellipse centres per unit volume. The problem of spheres is important for the theory of electrical conductivity of semiconductors at low temperatures. Therefore, many authors have investigated the problem by a number of various methods. The critical value of the total volume  $\mathfrak{G}_0$  at which the sphere percolation occurs is equal to 0.341889(3) [58]. The correspondent critical volume fraction (occupied by overlapping spheres of radius  $R$  in 3D) is  $\Phi_c = 0.289573(2)$ . For the problem of discs we have  $\mathfrak{G}_0 = 1.12808737(6)$  [63]. The correspondent critical area fraction is  $\Phi_c = 0.6763475(6)$  [68]. For overlapping hyperspheres in 4D we have for the critical volume fraction  $\Phi_c = 0.1223(4)$  and  $\mathfrak{G}_0 = 0.1304(5)$  [80]. The data are summarized in Table 1.

Table 1. Continuum percolation problems: total volume  $\mathfrak{G}$  and critical volume fraction  $\Phi_c$

Percolation type	$\mathfrak{G}$	$\mathfrak{G}_c$	$\Phi_c = 1 - \exp(-\mathfrak{G}_c)$
2D discs	$\pi R^2 \mathfrak{M}$	1.12808737(6)	0.6763475(6)
3D spheres	$\frac{4\pi}{3} R^3 \mathfrak{M}$	0.341889(3)	0.289573(2)
4D hyperspheres	$\frac{\pi^2}{3} R^4 \mathfrak{M}$	0.1304(5)	0.1223(4)

This quantity is denoted by letter  $\mathfrak{F}$  and referred to as filling factor. The filling factor equals the fraction of volume occupied by the spheres constructed around each lattice site and having a radius equal to half the distance to the nearest neighbor. Filling factor essentially depends on lattice type and must be calculated for each specific lattice. For square lattice we have  $\mathfrak{F}_{2D} = \pi/4$ , for simple cubic  $\mathfrak{F}_{3D} = \pi/6$ , for 4D hypercubic lattice  $\mathfrak{F}_{4D} = \pi^2/32$ . Thresholds:  $p_{s2D} \approx 0.59274601(2)$  [41];  $p_{s3D} \approx 0.31160768(15)$  [83];  $p_{s4D} \approx 0.1968861(14)$  [27];

The fraction of occupied volume is found by multiplying the filling factor  $\mathfrak{F}$  by the fraction of occupied sites, that is, by  $p$ . The fraction of filled volume is thus  $\mathfrak{F} \cdot p$ . At percolation threshold it equals  $\mathfrak{F} \cdot p_s$ .

$\mathfrak{F}_{2D} \cdot p_s \approx 0.4655$ ;  $\mathfrak{F}_{3D} \cdot p_s \approx 0.1632$ ;  $\mathfrak{F}_{4D} \cdot p_s \approx 0.0607$ .

**Directed Percolation.** Directed (or oriented) percolation (DP) is a fundamental model in non-equilibrium statistical mechanics. Directed percolation introduced in [5], is an anisotropic variant of standard isotropic percolation which introduces a specific direction in space. A variety of natural phenomena can be modeled by DP, including spreading phenomena like forest fires [35], and large-scale mesospheric electrical discharges named sprites [31]. For this model, the percolation can only occur along a given spatial direction. Regarding this direction as a temporal degree of freedom, directed percolation can then be viewed as a dynamical process in  $d + 1$  dimensions. Starting from a source active (occupied) site at  $t = 0$  on a tilted hypercubic lattice, directed site percolation, as a dynamical process, can be interpreted as follows. As illustrated in Fig. B4, at the next time step, each of the sites emanating from the source site is randomly occupied by an arrow with probability  $p$  which corresponds to the destination site to become active. There exists a critical threshold  $p_c$ , that for  $p < p_c$  the average number of active sites grows for a short time and then decays exponentially. For  $p > p_c$  there is a finite probability that the number of active sites diverges as  $t \rightarrow \infty$ . In this case activity spreads within a so-called spreading cone. Note that, in directed percolation each source site generates an individual cluster, so the lattice in this case cannot be decomposed into disjoint clusters.

Considering the density  $\zeta(t)$  of active sites as an order parameter of a spreading process, observations justify that in the active phase  $\zeta(t)$  decays and eventually saturates at some stationary value  $\zeta_s(t)$ . Near the critical point, the stationary density is then turned out to

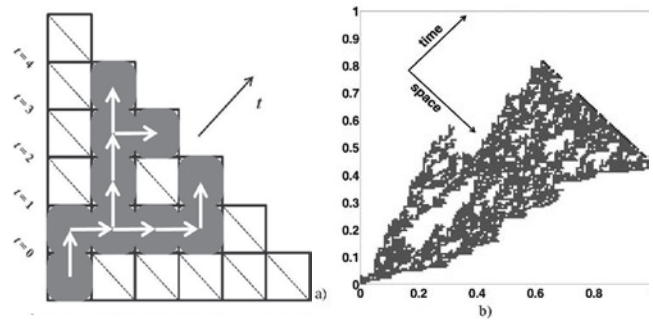


Figure B4. 1 + 1D directed percolation on square lattice: a) schematic representation of directed site percolation that started from a source active site at  $t = 0$  on a tilted square lattice. Each site is activated with probability  $p$ , shown by solid arrows. The cluster of active sites connected by a directed path to the source site is indicated in gray. The dashed lines identify the sets of available sites at time  $t$ ; b) 1 + 1D directed percolation on square lattice. Black sites correspond to the time  $t = 214$  from the beginning of the process.

Table 2: Parameters of percolation problems

Lattice type	Filling $\mathfrak{F}$	Threshold $p_c$	$\mathfrak{F} \cdot p_c$
Square	$\pi/4$	0.59274601(2)	0.4655
Simple cubic	$\pi/6$	0.31160768(15)	0.1632
Hypercubic	$\pi^2/32$	0.1968861(14)	0.0607
Directed 1+1	$\pi/4$	0.705489(4)	0.5541
Directed 2+1	$\pi/4$	0.43531(1)	0.2279
Directed 3+1	$\pi^2/32$	0.231046861(3)	0.0713

satisfy a power-law relation  $\zeta_s \sim (p - p_c)^\beta$ , where  $\beta$  is a universal critical exponent that only depends on dimensionality. The other important quantity is the correlation length whose definition needs a special care, since in this case, time is an additional dimension which should be distinguished from the spatial dimensions. Let us denote the temporal and spatial correlation lengths by the indices  $\xi_{||}$  and  $\xi_{\perp}$ , respectively, which are independent of each other. Then close to the transition, these length scales are expected to diverge as  $\xi_{||} \sim |p - p_c|^{v_{||}}$  and  $\xi_{\perp} \sim |p - p_c|^{v_{\perp}}$  with generally different critical exponents  $v_{||}$  and  $v_{\perp}$ . The two correlation lengths are related in the scaling regime by  $\xi_{||} \sim \xi_{\perp}^z$  where  $z = v_{||}/v_{\perp}$  denotes for the so-called dynamic exponent. In many models, the universality class is given by the three exponents  $\beta$ ,  $v_{||}$  and  $v_{\perp}$ .

(1+1)-d square, diagonal direction  $p_s \approx 0.705489(4)$  [53];

$\mathfrak{F}_{1+1} \cdot p_s \approx 0.5541$ .

(2+1)-d simple cubic, diagonal planes  $p_s \approx 0.43531(1)$  [26];

$\mathfrak{F}_{2+1} \cdot p_s \approx 0.2279$ .

(3+1)-d hypercubic, diagonal planes  $p_s \approx 0.231046861(3)$  [82];

$\mathfrak{F}_{3+1} \cdot p_s \approx 0.0713$ .

## REFERENCES

- [1] Arabshahi S., J.R.Dwyer, A.Nag, et al. (2014), *J. Geophys. Res. Space Phys.*, 119, 479.
- [2] Babich, L. P., E. I. Bochkov, I. M. Kutsyk, T. Neubert, and O. Chanrion (2016), Positive streamer initiation from raindrops in thundercloud fields, *J. Geophys. Res.*, 121, 11, 63936403, doi:10.1002/2016JD024901.
- [3] Bazelyan, J. M., and Yu. P. Raizer, (1998), *Spark Discharge*, CRC Press, Boca Raton, New York.
- [4] Baselyan, J. M., and Yu. P. Raizer, *Spark Dis-charge*, CRC Press, Boca Raton, New York, 1998.
- [5] Bateman, M.G., Rust, W.D., and Marshall, T.C. (1994). A balloon- borne instrument for measuring the charge and size of precipitation particles inside thunderstorms. *J. Atmos. Oceanic Technol.* 161–9.
- [6] Bateman, M.G., Rust, W.D., Smull, B.F., and Marshall, T.C. (1995). Precipitation charge and size measurements in the strati form region of two mesoscale convective systems. *J. Geophys. Res.* 16 341–56.
- [7] Bateman, M.G., Marshall, T.C., Stolzenburg, M., and Rust, W.D. (1999). Precipitation charge and size measurements inside a New Mexico mountain thunderstorm, *J. Geophys. Res.* 104: 9643–53.
- [8] Beale, P. D., and P. M. Duxbury. (1988). Dielectric breakdown in metal-loaded dielectrics. *Phys. Rev.* 37, pp. 2785–2791.
- [9] Bershadskii A.G. (1990), Large-scale fractal structure in laboratory turbulence, astrophysics, and the ocean // *Phys. Usp.* 33 (12) 10731075
- [10] Bowman D. R., D. Stroud. (1989). Model for dielectric breakdown in metal-insulator composites. *Phys. Rev. B* 40, pp. 4641–4650.
- [11] Brown, K. A., P. R. Krehbiel, C. B. Moore, and N. Sargent (1971), Electrical screening layers around charged clouds, *J. Geophys. Res.*, 76, 2825–2835.
- [12] Bunde A., Halvin S. (1995), *Fractals and Disordered Systems*. - Berlin: Springer-Verlag, 1995. 408 p.
- [13] Cai Q., J. Jansk'y, and V. P. Pasko (2017), Initiation of Positive Streamer Corona in Low Thundercloud Fields, *J. Geophys. Res.*, coming soon.
- [14] Dwyer, J. R. (2005), The initiation of lightning by runaway air breakdown, *Geophys. Res. Lett.*, 32, L20808, doi:10.1029/2005GL023975.
- [15] Dwyer J.R. and L.P. Babich, (2011), *J. Geophys. Res.*, 116, A09301.
- [16] Duxbury, P. M., P. D. Beale, H. Bak and P. Schroeder. (1990). Capacitance and dielectric breakdown of metal-loaded dielectrics. *J. Phys. D* 23, pp. 1546–1553.
- [17] Dutton J. (1975), A Survey of Electron Swarm Data // *J. Phys. Chem. Ref. Data*, Vol. 4, No. 3
- [18] Dye, J.E., Jones, J.J., Weinheimer, A.J., and Winn, W.P. (1988). Observations within two regions of charge during initial thunderstorm electrification. *Q.J.R. Meteor. Soc.* 114: 1271 90.
- [19] Fehsenfeld F.C., Ferguson E.E. (1974). // *J. Chem. Phys.* V. 61. 8. P. 3181.
- [20] Femia, N., L. Niemeyer, and V. Tucci, (1993), Fractal characteristics of electrical discharges: experiments and simulations, *J. Phys. D: Appl. Phys.*, vol. 26, 619-627.
- [21] Gallimberti, I., G. Bacchiega, A. Bondiou-Glergerie, and P. Lalande (2002), Fundamental processes in long air gap discharges, *C. R. Phys.*, 3(10), 13351359, doi:10.1016/S1631-0705(02) 01414-7.
- [22] Gardiner, B., Lamb, D., Pitter, R.L., Hallett, J., and Saunders, C.P.R. (1985). Measurements of initial potential gradient and particle charges in a Montana summer thunderstorm. *J. Geophys. Res.* 90: 607986.
- [23] Gou, X. M. Chen, Y. Du, and W. Dong (2010), Fractal dynamics analysis of the VHF radiation pulses during initial breakdown process of lightning, *Geophysical Research Letters*, vol. 37, L11808, doi:10.1029/2010GL043178, 2010.
- [24] Gomes, C., V. Cooray, M. Fernando, R. Montano, and U. Sonnadara (2004), Characteristics of chaotic pulse trains generated by lightning flashes, *J. Atmos. Solar-terr. Phys.*, vol. 66, 1733-1743, 2004.
- [25] Gou, X. M. Chen, Y. Du, and W. Dong (2010), Fractal dynamics analysis of the VHF radiation pulses during initial breakdown process of lightning, *Geophysical Research Letters*, vol. 37, L11808, doi:10.1029/2010GL043178, 2010.
- [26] Grassberger, P.; Y.-C. Zhang (1996). "Self-organized" formulation of standard percolation phenomena". *Physica A.* 224: 169179.
- [27] Grassberger, Peter (2003). "Critical percolation in high dimensions". *Physical Review E.* 67 (3): 4.
- [28] Griffiths, R. and C. Phelps (1976), A model for lightning initiation arising from positive corona streamer development. *J. Geophys. Res.*, 31, 3671-3676
- [29] Gurevich, A. V., G. M. Milikh, and R. Roussel-Dupre (1992), Runaway electron mechanism of air breakdown and preconditioning during a thunderstorm, *Phys. Lett. A*, 165, 463 468.
- [30] Gurevich, A. V., K. P. Zybin, and R. A. Roussel-Dupre (1999), Lightning initiation by simultaneous effect of runaway breakdown and cosmic ray showers, *Phys. Lett. A*, 254, 7987.
- [31] Hayakawa M., D. Iudin, E. Mareev, V. Trakhtengerts (2007), Cellular automaton modeling of mesospheric optical emissions: Sprites, *Phys. Plasmas*, 14, 042902.
- [32] Hayakawa, M., D. I. Iudin, and V. Y. Trakhtengerts, (2008), Modeling of thundercloud VHF/UHF radiation on the lightning preliminary breakdown stage, *J. Atmos. Solar-terr. Phys.*, vol. 70, 1660-1668, doi:10.1016/j. jastp.2008.06.011.
- [33] Horsthemke W., and R. Lefever (1984), *Noise-induced transitions*. Springer, Berlin.
- [34] Iudin, D.I., V.Y. Trakhtengertz, and M. Hayakawa (2003), Fractal dynamics of electric discharges in a thundercloud, *Phys. Rev. E*, vol. 68, 016601, doi:10.1103/PhysRevE.68.016601, 2003.
- [35] Iudin D.I., Sergeev Ya.D., Hayakawa M. (2015), Infinity computations in cellular automaton forest-fire model // *Communications in Nonlinear Science and Numerical Simulation*, 20(3), 861-870.
- [36] Iudin, D.I., E.A. Mareev, D.I. Budaragin, R.M. Dmitrienko, V.Y. Klimashov, and S.A. Savikhin (2011), Self-organized charge gathering system and lightning discharge characteristics, *Proceedings of XIV International Conference on Atmo-spheric Electricity*, August 08-12, Rio de Janeiro, Brazil.

- [37] Iudin D. I., F. D. Iudin, and M. Hayakawa, (2015), Modeling of the intracloud lightning discharge radio emission, *Radiophysics and Quantum Electronics*, Vol.58, No.03, August, doi: 10.1007/s11141-015-9591-4.
- [38] Iudin D. I. and S. S. Davydenko, (2015), Fractal model of a compact intracloud discharge. I. Features of the structure and evolution, *Radiophysics and Quantum Electronics*, Vol.58, No.7, December, pp. 477–496, doi: 10.1007/s11141-015-9621-2.
- [39] Iudin D. I. (2017), Lightning-discharge initiation as a noise-induced kinetic transition. *Radiophysics and Quantum Electronics*, Vol.60, No.05, October, doi: 10.1007/s11141-017-9807-x.
- [40] Jensen H.J. (1998), *Self-Organized Criticality*, Cambridge university press.
- [41] Jacobsen, J. L. (2014). "High-precision percolation thresholds and Potts-model critical manifolds from graph polynomials". *J. Phys. A: Math. Theor.* 47 (13): 135001.
- [42] Klyatskin V.I. (1994), Statistical description of the diffusion of a passive tracer in a random velocity field // *Phys. Usp.* 37 501513.
- [43] Klyatskin V.I. (2003), Clustering and diffusion of particles and passive tracer density in random hydrodynamic flows // *Phys. Usp.* 46 667688.
- [44] Kozlov S. I., Vlaskov V. A. and Smirnova N. V., (1988) *Sou. Space Res.* 26 pp. 738-45.
- [45] I. A. Kossyi, A. Yu. Kostinsky, A. A. Matveyev and V. P. Silakov (1992), Kinetic scheme of the non-equilibrium discharge in nitrogen-oxygen mixtures. *Plasma Sources Sci. Technol.* 1 pp. 207-220.
- [46] Krehbiel P.R. (1986), The electrical structure of thunderstorms. In R.L. Gardner, editor, *The Earth's Electrical Environment*, pp. 90–113. National Academy Press, Washington, D.C.
- [47] Krehbiel P.R., J.A. Rioussset, V.P. Pasko, R.J. Thomas, W. Rison, M.A. Stanley and H.E. Edens (2008), Upward electrical discharges from thunderstorms // *Nature*, doi:10.1038/ngeo162.
- [48] Kupershtokh A. L., V. Charalambakos, D. Agoris, and D. I. Karpov (2001), Simulation of break-down in air using cellular automata with streamer to leader transition // *J. Phys. D: Appl. Phys.* 34, 936946.
- [49] Landa P.S., and P.V.E. McClintock (2000), Changes in the dynamical behavior of nonlinear systems induced by noise // *Phys. Repts* 323, p. 1-80 (2000).
- [50] Liu, N.Y., B. Kosar, S. Sadighi, J.R. Dwyer and H.K. Rassoul (2012), Formation of streamer discharges from an isolated ion-ization column at subbreakdown conditions, *Phys. Rev. Lett.*, 109(2),25,002, doi:10.1103/PhysRevLett.109.025002.
- [51] Loeb, L. B. (1966), The mechanisms of stepped and dart leaders in cloud-to-ground lightning strokes, *J. Geophys. Res.*, 71, 4711.
- [52] Lowke, J. J. (2015), The initiation of lightning in thunderclouds: The possible influence of metastable nitrogen and oxygen molecules in initiating lightning streamers, *J. Geophys. Res. Atmos.*, 120, 3183 3190, doi:10.1002/2014JD022223.
- [53] Lubeck, S.; R. D. Willmann (2002). "Universal scaling behaviour of directed percolation and the pair contact process in an external field". *J. Phys. A.* 35 (48): 10205.
- [54] LeVine, D. M., and R. Meneghini (1978), Simulation of radiation from lightning return strokes: the effect of tortuosity, *Radio Sci.*, vol. 13(5), 801-809.
- [55] Liu, N., and V. P. Pasko (2004), Effects of photoionization on propagation and branching of positive and negative streamers in sprites, *J. Geophys. Res.*, 109, A04301, doi:10.1029/2003JA010064.
- [56] Liu, N.Y., B. Kosar, S. Sadighi, J.R. Dwyer, and H.K. Rassoul (2012), Formation of streamer discharges from an isolated ionization column at subbreakdown conditions, *Phys. Rev. Lett.*, 109(2), 25,002, doi:10.1103/PhysRevLett.109.025002.
- [57] Lorenz, C. D.; R. M. Ziff (1998). "Universality of the excess number of clusters and the crossing probability function in three-dimensional percolation". *Journal of Physics A.* 31 (40): 81478157.
- [58] Lorenz, C. D.; R. M. Ziff (2000). "Precise determination of the critical percolation threshold for the three dimensional Swiss cheese model using a growth algorithm". *J. Chem. Phys.* 114 (8): 3659. doi:10.1063/1.1338506
- [59] Mayham I.T., Fante R.L. (1971) // *J. Appl. Phys.* Vol. 42. No 13. P. 5362.
- [60] Marshall, T.C., M.P. McCarthy, and W.D. Rust (1995), Electric field magnitudes and lightning initiation in thunderstorms, *J. Geophys Res.*, V. 100, No. D4, pp. 7097-7103.
- [61] Marshall, T.C., M.P. McCarthy, and W.D. Rust (1995), Electric field magnitudes and lightning initiation in thunderstorms, *J. Geophys Res.*, V. 100, No. D4, pp. 7097-7103.
- [62] Marshall, T. C., and M. Stolzenburg (1998), Estimates of cloud charge densities in thunderstorms, *J. Geophys. Res.*, 103, 19,769 – 19,775, doi:10.1029/98JD01674.
- [63] Mertens, Stephan; Cristopher Moore (2012). "Continuum percolation thresholds in two dimensions". *Physical Review E.* 86: 061109.
- [64] Mikhailov A. S. and I. V. Uporov (1980), Noise-induced phase transition and the percolation problem for fluctuating media with diffusion, *Sov. Phys. JETP* 52(5), Nov. 1980
- [65] D.J. Malan. (1963) *Physics of Lightning*. The English Universities Press, 1963. 176 pp.
- [66] Petersen, D., M. Bailey, W.H. Beasley, and J. Hallett (2008). A brief review of the problem of lightning initiation and a hypothesis of initial lightning leader formation, *JOURNAL OF GEOPHYSICAL RESEARCH*, vol. 113, D17205, doi:10.1029/2007JD009036.
- [67] Phelps, C. T., and R. F. Griffiths (1976), Dependence of positive corona streamer propagation on air pressure and water vapour content, *J. Appl. Phys.*, 47(7), 29292934.
- [68] Quintanilla, John A.; R. M. Ziff (2007). "Near symmetry of percolation thresholds of fully penetrable disks with two different radii". *Physical Review E.* 76 (5): 051115

- [69] Rison, W., P. R. Krehbiel, M. G. Stock, H. E. Edens, X. Shao, R. J. Thomas, M. A. Stanley & Y. Zhang (2016), Observations of narrow bipolar events reveal how lightning is initiated in thunder-storms. 7:10721 doi: 10.1038/ncomms10721.
- [70] Raizer, Y. P. (1991), *Gas Discharge Physics*, Springer, New York.
- [71] Rakov, V. A., and M. A. Uman (2003), *Lightning: Physics and Effects*, Cambridge Univ. Press, New York.
- [72] Popov N. A. (2010), Evolution of the Negative Ion Composition in the Afterglow of a Streamer Discharge in Air // *Plasma Physics Reports*, Vol. 36, No. 9, pp. 812818.
- [73] Sadighi, S., N. Liu, J. R. Dwyer, and H. K. Rassoul (2015), Streamer formation and branching from model hydrometeors in subbreakdown conditions inside thunderclouds, *J. Geophys. Res. Atmos.*, 120, 36603678, doi:10.1002/2014JD022724.
- [74] Said R. K., M. B. Cohen, and U. S. Inan (2013). Highly intense lightning over the oceans: Estimated peak currents from global GLD360 observations, *J. Geophys Res.: Atmospheres*, Vol. 118, 69056915, doi:10.1002/jgrd.50508.
- [75] Sancho J.M., and J. Garcia-Ojalvo, Noise-induced order in extended systems: a tutorial / In: *Stochastic processes in physics, chemistry and biology*. Springer, Berlin (2000), p. 235-246.
- [76] Shishkin, N.S.(1968), Some problems of theory of natural and artificial precipitation, *Bull. Am. Meteorol. Soc.*, 49(5P2), 622.
- [77] Shraiman B.I. and E.D. Siggia (2000). Scalar turbulence *NATURE* Vol. 405, 8 June 2000, p. 639-646.
- [78] Sinkevich A.A., Dovgalyuk Yu. A. (2013) // *Radiophysic. T.* 56, No. 11-12. P. 908.
- [79] Tennekes, H. Lumley, J. A. (1972), *First Course in Turbulence* (MIT Press, Cambridge).
- [80] Torquato, S.; Y. Jiao (2012). "Effect of dimensionality on the continuum percolation of over-lapping hyperspheres and hypercubes. II. Simulation results and analyses". *J. Chem. Phys.* 137 (7): 074106. doi:10.1063/1.4742750
- [81] Vecchi G., D. Labate, and F. Canavero (1994), Fractal approach to lightning radiation on a tortuous channel, *Radio Science*, V. 29, No 4, pp. 691– 704.
- [82] Wang J., Z. Zhou, Q. Liu, T.M. Garoni, and Y. Deng (2013), High-precision Monte Carlo study of directed percolation in (d+1) dimensions, *Phys. Rev. E* 88 042102.
- [83] Xu, Xiao; Junfeng Wang, Jian-Ping Lv, Youjin Deng (2014). "Simultaneous analysis of three-dimensional percolation models". *Frontiers of Physics.* 9 (1): 113119.
- [84] Ziegler, C.L., MacGormam, D.R., Dye, J.E., and Ray, P.S. (1991). A model evaluation of no inductive graupelice charging in the early electrification of a mountain thunderstorm. *J. Geophys. Res.* 96: 12 83355.
- [85] Ziegler, C.L., and MacGorman, D.R. (1994). Observed lightning morphology relative to modeled space charge and electric field distributions in a tornadic storm. *J. Atmos. Sci.* 51: 83351.

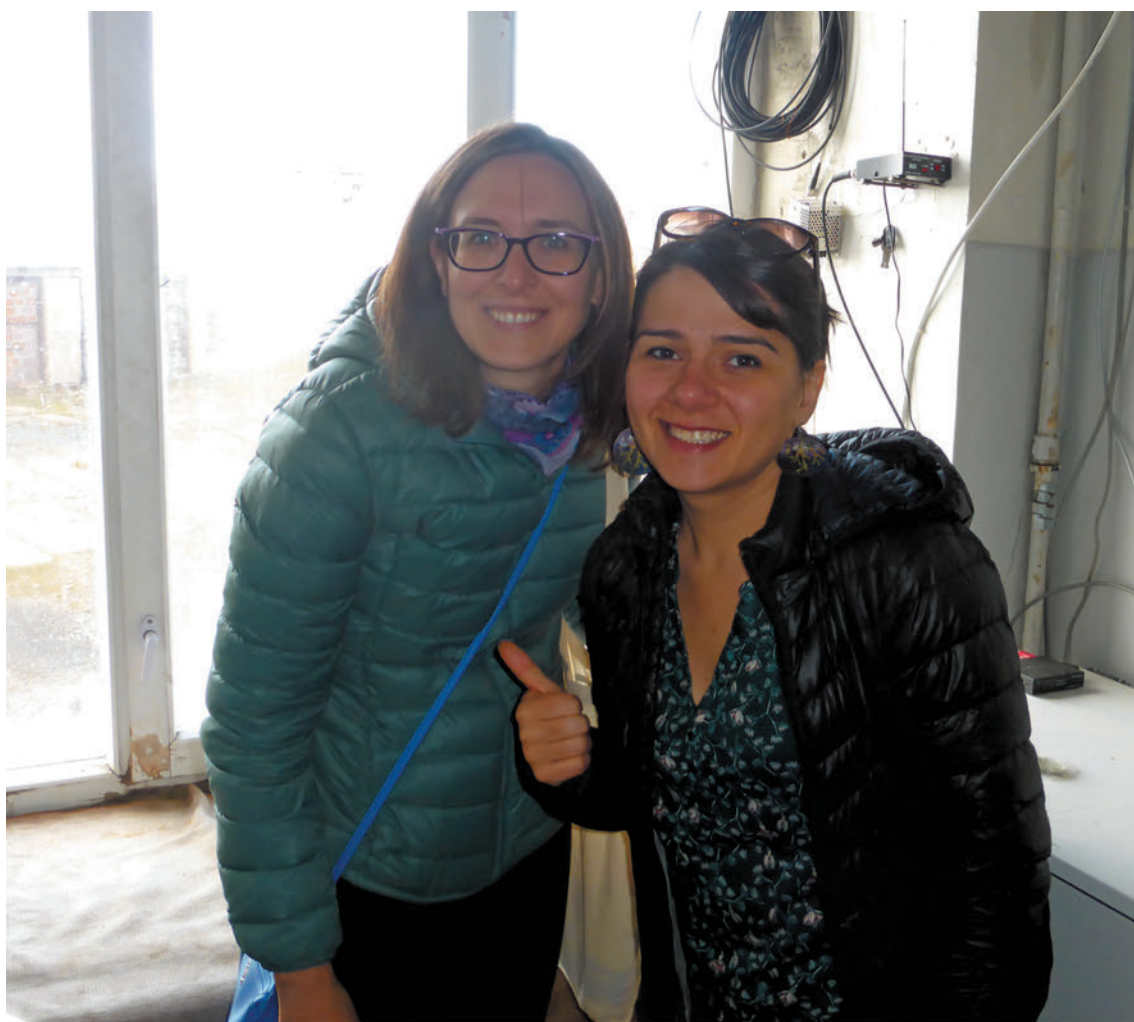
## List of Participants

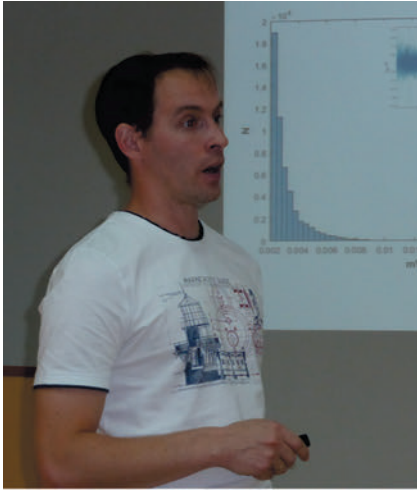
1	Ekaterina Svechnikova, Institute of Applied Physics of the Russian Academy of Sciences (IAP RAS)	ktts@mail.ru
2	Arsen Ghalumyan, A Alikhanyan National Lab (Yerevan Physics Institute)	ghalumyan@yandex.ru
3	Pavel Kovář, Czech Technical University in Prague, Czech Rep.	kovar@fel.cvut.cz
4	Jan Mikes, Czech Technical University in Prague, Czech Rep.	mikes.jan@cvut.cz
5	Suren Soghomonyan, A Alikhanyan National Lab (Yerevan Physics Institute)	surensog@gmail.com
6	Yeghia Khanikyants, A Alikhanyan National Lab (Yerevan Physics Institute)	khanikyanc@yerphi.am
7	Yuuki Wada, The University of Tokyo	wada@juno.phys.s.u-tokyo.ac.jp
8	Roberta Colalillo, INFN, Napoli, Italy	colalillo@na.infn.it
9	Jakub Slegl, Nuclear Physics Institute of CAS, Czech Rep.	slegl@ujf.cas.cz
10	Garik Garipov. SINP, MSU, RF	ggkmsu@gmail.com
11	Aleksandr Kiselev. IKI, RS, RF	aleksandr.kiselyov@gmail.com
12	Onrej Ploc. Nuclear Physics Institute of CAS, Czech Rep	ploc@ujf.cas.cz
13	David Aslanyan, A. Alikhanyan National Lab (Yerevan Physics Institute)	davitAslanyan@yerphi.am
14	Egor Stadnichuk, MIPT/INR RAS, RF	egrstadnichuk@yandex.ru
15	Maxim Dolgonsoov, IKI of RAS/HSE, RF	maxim.dolgonosov@gmail.com
16	Ashot Chilingarian, A. Alikhanyan National Lab (Yerevan Physics Institute)	chili@aragats.am
17	Tigran Karapetyan, A Alikhanyan National Lab (Yerevan Physics Institute)	ktigran79@gmail.com
18	Albert Avetisyan, A. Alikhanyan National Lab (Yerevan Physics Institute)	albert@yerphi.am
19	Balabek Sargsyan, A Alikhanyan National Lab (Yerevan Physics Institute)	balabek.sargsyan@yerphi.am
20	Bagrat Mailyan, The University of Alabama, Huntsville, USA	bagrat.mailyan@uah.edu
21	Hripsime Mkrtychyan, A Alikhanyan National Lab (Yerevan Physics Institute)	hripsime@yerphi.am
22	Gagik Hovsepyan, A Alikhanyan National Lab (Yerevan Physics Institute)	hgg@yerphi.am
23	Gayane Karapetyan, A Alikhanyan National Lab (Yerevan Physics Institute)	gayanek77@yerphi.am
24	Suren Hovakimyan, Ministry of Emergency Situation of RA	suren.hovakimyan@gmail.com
25	Lev Kozliner, A Alikhanyan National Lab (Yerevan Physics Institute)	kozliner@yerphi.am
26	Mary Zazyan, A Alikhanyan National Lab (Yerevan Physics Institute)	mary@yerphi.am
27	Dmitry Iudin, Institute of Applied Physics of Russian Academy of Science	iudin@ipfran.ru
28	David Pokhsaryan, A Alikhanyan National Lab (Yerevan Physics Institute)	davitpo@gmail.com
29	Sergey Abovyan, A Alikhanyan National Lab (Yerevan Physics Institute)	sergey.abovyan@gmail.com
30	Stanislav Davidenko, Institute of Applied Physics of Russian Academy of Science	david@ipfran.ru
31	Leonid Sorokin, Peoples' Friendship University of Russia	leonid.plasma@gmail.com
32	Ashkhen Eghiazaryan, A. Alikhanyan National Lab (Yerevan Physics Institute)	ashkhen@mail.yerphi.am























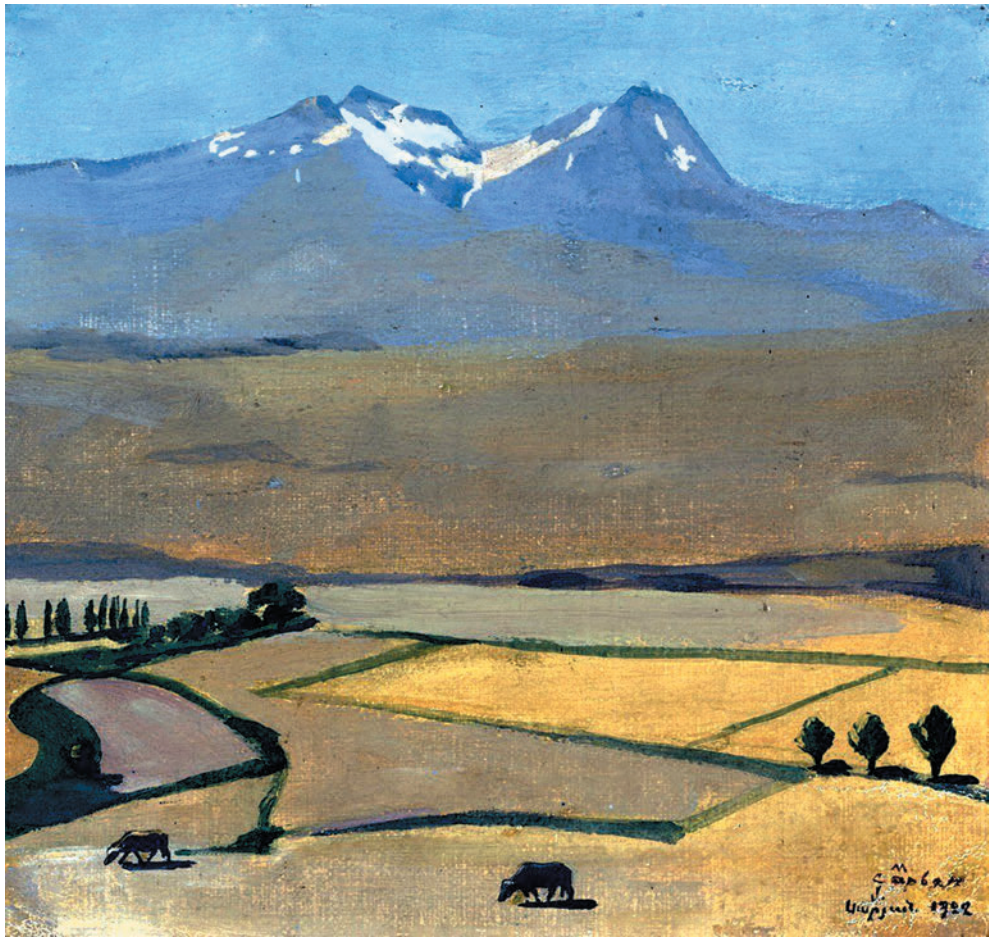




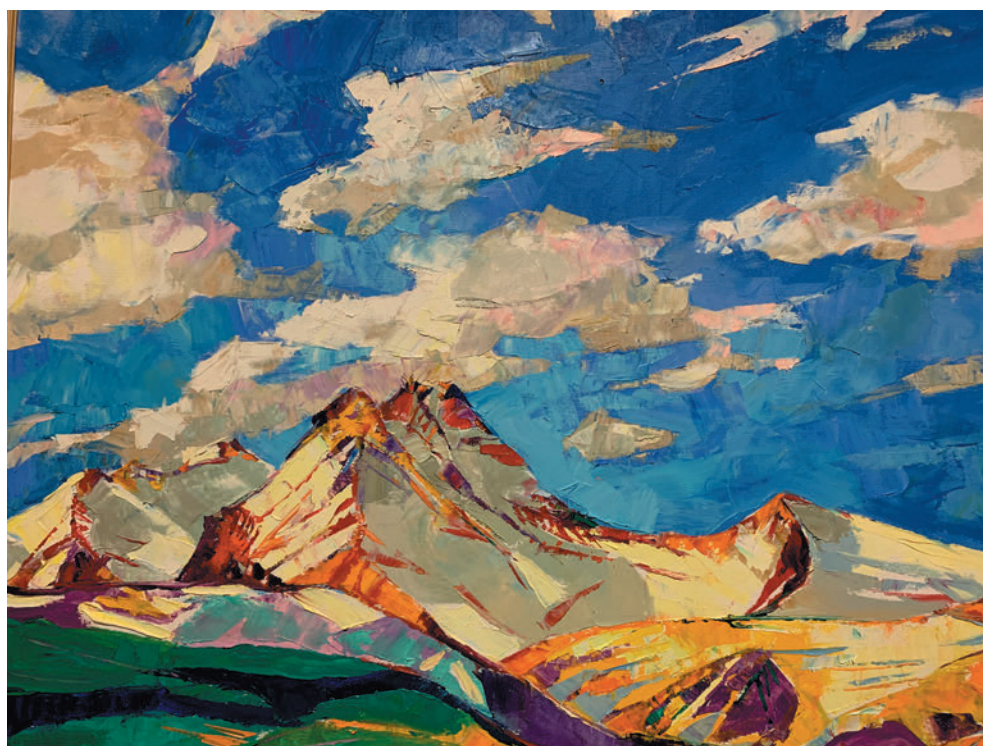


ARARAT AND ARAGATS MOUNTAINS IN MARTIROS SARYAN'S ART WORKS

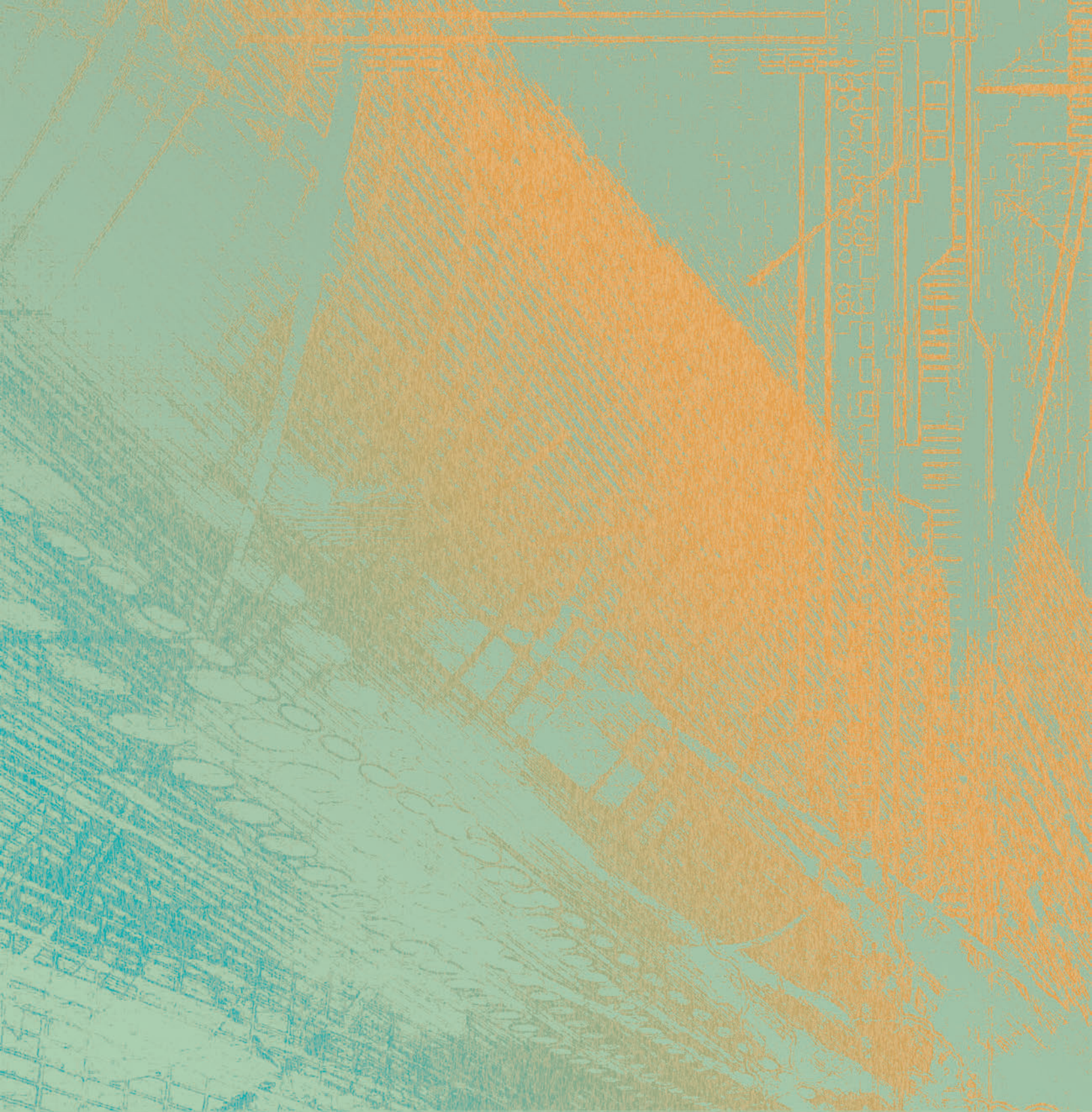




ARAGATS MOUNTAIN IN MARTIN AKOGHLYAN'S ART WORKS







[http://crd.yerphi.am/TEPA\\_2018](http://crd.yerphi.am/TEPA_2018)

